

## The $^{12}\text{C}(\alpha,\gamma)^{16}\text{O}$ reaction and its implications for stellar helium burning

R. J. deBoer,<sup>\*</sup> J. Görres, and M. Wiescher

*The Joint Institute for Nuclear Astrophysics, Department of Physics,  
University of Notre Dame, Notre Dame, Indiana 46556 USA*

R. E. Azuma<sup>†</sup>

*Department of Physics, University of Toronto, Toronto, Ontario M5S 1A7, Canada,  
and The Joint Institute for Nuclear Astrophysics, Department of Physics,  
University of Notre Dame, Notre Dame, Indiana 46556 USA*

A. Best<sup>‡</sup>

*INFN, Laboratori Nazionali del Gran Sasso, 67100 Assergi, Italy*

C. R. Brune

*Edwards Accelerator Laboratory, Department of Physics and Astronomy,  
Ohio University, Athens, Ohio 45701, USA*

C. E. Fields<sup>§</sup>

*The Joint Institute for Nuclear Astrophysics, Department of Physics and Astronomy,  
Michigan State University, East Lansing, Michigan 48824, USA*

S. Jones

*Heidelberg Institute for Theoretical Studies, Schloss-Wolfsbrunnengasse 35,  
D-69118 Heidelberg, Germany, and the NuGrid Collaboration, <http://nugridstars.org>*

M. Pignatari

*E. A. Milne Centre for Astrophysics, Department of Physics & Mathematics,  
University of Hull, HU6 7RX, United Kingdom,  
and Konkoly Observatory, Research Centre for Astronomy and Earth Sciences,  
Hungarian Academy of Sciences, Konkoly Thege Miklos ut 15-17, H-1121 Budapest,  
Hungary, and the NuGrid Collaboration, <http://nugridstars.org>*

D. Sayre

*Lawrence Livermore National Laboratory, Livermore, California 94550, USA*

K. Smith

*Department of Physics & Astronomy, University of Tennessee Knoxville,  
Knoxville, Tennessee 37996 USA<sup>||</sup>*

F. X. Timmes

*The Joint Institute for Nuclear Astrophysics, School of Earth and Space Exploration,  
Arizona State University, Tempe, Arizona, USA*

E. Uberseder

*Cyclotron Institute, Texas A&M University, College Station, Texas 77843, USA*<sup>†</sup>

(published 7 September 2017)

The creation of carbon and oxygen in our Universe is one of the forefront questions in nuclear astrophysics. The determination of the abundance of these elements is key to our understanding of both the formation of life on Earth and to the life cycles of stars. While nearly all models of different nucleosynthesis environments are affected by the production of carbon and oxygen, a key ingredient, the precise determination of the reaction rate of  $^{12}\text{C}(\alpha, \gamma)^{16}\text{O}$ , has long remained elusive. This is owed to the reaction's inaccessibility, both experimentally and theoretically. Nuclear theory has struggled to calculate this reaction rate because the cross section is produced through different underlying nuclear mechanisms. Isospin selection rules suppress the  $E1$  component of the ground state cross section, creating a unique situation where the  $E1$  and  $E2$  contributions are of nearly equal amplitudes. Experimentally there have also been great challenges. Measurements have been pushed to the limits of state-of-the-art techniques, often developed for just these measurements. The data have been plagued by uncharacterized uncertainties, often the result of the novel measurement techniques that have made the different results challenging to reconcile. However, the situation has markedly improved in recent years, and the desired level of uncertainty  $\approx 10\%$  may be in sight. In this review the current understanding of this critical reaction is summarized. The emphasis is placed primarily on the experimental work and interpretation of the reaction data, but discussions of the theory and astrophysics are also pursued. The main goal is to summarize and clarify the current understanding of the reaction and then point the way forward to an improved determination of the reaction rate.

DOI: [10.1103/RevModPhys.89.035007](https://doi.org/10.1103/RevModPhys.89.035007)**CONTENTS**

I. Introduction	3	B. The push to lower energies (1974–1993)	27
II. Helium Burning and Its Astrophysical Significance	3	C. Return to indirect techniques (1993–present)	28
A. Helium burning in low- and intermediate-mass stars	5	D. Upcoming experiments	32
B. Helium burning in massive stars	5	E. World data set	33
C. Helium burning in first stars	6	VI. $R$ -matrix Analysis of $^{12}\text{C}(\alpha, \gamma)^{16}\text{O}$	34
D. Uncertainty considerations	7	A. “Best fit” procedure	35
E. The nuclear reaction rate	8	1. Systematic uncertainty $\chi^2$ term	36
III. Nuclear Physics Aspects	9	2. Corrections for experimental effects	38
A. The experimental situation	10	B. Ground state transition	39
B. Cluster models	11	C. Cascade transitions	41
C. Phenomenological models	12	D. $\beta$ -delayed $\alpha$ emission	44
IV. $R$ -matrix Theory	12	E. $\alpha$ scattering	47
A. General $R$ -matrix theory	12	F. Subthreshold states	47
B. Physical interpretation of the $R$ -matrix parameters	15	VII. Uncertainty Analysis	49
C. Parameter transformations	16	A. Sensitivity to different data sets	50
D. Radiative capture	16	B. Limiting interference solutions	50
E. $\beta$ -delayed particle emission	20	C. Channel radius and background poles	52
F. $R$ -matrix phenomenology	20	D. Different fitting methods	54
G. $R$ -matrix strategy	21	E. Monte Carlo uncertainty analysis	55
V. Experimental Measurements	22	F. Summary and total uncertainty estimate	56
A. First measurements (1955–1974)	23	VIII. Discussion of Recent Works	57
		A. Schürmann <i>et al.</i> (2011)	57
		B. Oulebsir <i>et al.</i> (2012)	58
		C. Xu <i>et al.</i> (2013) (NACRE2)	59
		D. An <i>et al.</i> (2015)	59
		IX. Stellar Reaction Rate and Implications	60
		X. Astrophysics Implications	60
		A. Aspects of $^{12}\text{C}(\alpha, \gamma)^{16}\text{O}$ on $3 M_{\odot}$ stellar models	61
		B. Aspects of $^{12}\text{C}(\alpha, \gamma)^{16}\text{O}$ on $15 M_{\odot}$ and $25 M_{\odot}$ models	62
		XI. Summary and Outlook	63
		Acknowledgments	64
		Appendix A: $R$ -matrix Fit Parameters	64
		Appendix B: Tabulated Reaction Rate	68
		References	69

\*rdeboer1@nd.edu.

†Deceased.

‡Present address: Università degli Studi di Napoli “Federico II” and INFN, Napoli, Italy.

§Ford Foundation Predoctoral Fellow.

||Present address: Los Alamos National Laboratory, Los Alamos, NM 87545, USA.

¶Present address: Nuclear Engineering and Radiological Sciences, University of Michigan, Ann Arbor, MI 48109, USA.

## I. INTRODUCTION

The baryonic matter that is a product of the big bang takes the form of hydrogen, helium, and very small amounts of lithium. This is the seed material that has fueled the chemical evolution of our Universe. Through the many generations of stars their life cycles have been governed by myriads of microscopic interactions driven by the short range strong and weak forces and the long range electromagnetic force. Chemical reactions define the molecular configurations of elements in our environment, while nuclear processes are responsible for the formation of the chemical elements themselves. The history and environments where the formation processes occur dictate the elemental and isotopic abundance distributions that we observe today.

The nuclear reactions necessary for the formation of the elements can take place only at conditions of high density and temperature. These conditions occur only in special settings in the Universe, such as the center of stars and during stellar explosions. Tens of thousands of nuclear reactions can participate in a specific nucleosynthesis scenario, depending on the various environmental conditions. However, only a small fraction of these reactions have a strong impact on the overall chemical evolution of the elements. These few reactions have far reaching consequences for the chemistry and the subsequent molecular evolution of baryonic matter. There is one reaction of particular relevance  $^{12}\text{C}(\alpha, \gamma)^{16}\text{O}$  that influences the  $^{12}\text{C}/^{16}\text{O}$  ratio in our Universe. This reaction, together with the  $3\alpha$  process, the fusion of three  $^4\text{He}$  nuclei into one  $^{12}\text{C}$  nucleus, defines the carbon and oxygen abundance that is the fundamental basis for all organic chemistry and for the evolution of biological life in our Universe. As Willy Fowler wrote in his 1983 Nobel Prize lecture (Fowler, 1984), “The human body is 65% oxygen by mass and 18% carbon with the remainder mostly hydrogen. Oxygen (0.85%) and carbon (0.39%) are the most abundant elements heavier than helium in the Sun and similar main sequence stars. It is little wonder that the determination of the ratio  $^{12}\text{C}/^{16}\text{O}$ , produced during helium burning, is a problem of paramount importance in nuclear astrophysics.” As a consequence, the reaction has been dubbed “the holy grail of nuclear astrophysics.”

The significance of the  $^{12}\text{C}(\alpha, \gamma)^{16}\text{O}$  reaction for energy production and nucleosynthesis in stars is closely tied to that of the  $3\alpha$  process. The simultaneous fusion of three  $\alpha$  particles was discussed by Bethe (1939), but it was not until preliminary measurements of the long lifetime of the  $^8\text{Be}$  were made that it was realized by Salpeter (1952) that a much more efficient two-step reaction was possible. Finally it was Hoyle (1954) who deduced that there must be an actual resonance in the  $^8\text{Be}(\alpha, \gamma)^{12}\text{C}$  reaction, the famous Hoyle state in  $^{12}\text{C}$ , that enhances the cross section even further (Salpeter, 2002). The experimental work of Cook *et al.* (1957) rather quickly established the rate of the  $3\alpha$  process since it depends mainly on the strength of the Hoyle state [see Freer and Fynbo (2014) for a recent review]. Current estimates of the uncertainty in the  $3\alpha$  rate are at about the 10% level over the regions of typical astrophysical interest. However, at lower temperatures ( $< 0.1$  GK), the uncertainty is likely much larger, because

other reaction mechanisms become significant [see, e.g., Suno, Suzuki, and Descouvemont (2016) and references therein].

Nature is not so kind to us with the  $^{12}\text{C}(\alpha, \gamma)^{16}\text{O}$  reaction. Here the cross section enhancement is not the result of a single narrow resonance or even several such resonances, but stems from the very delicate (and seemingly devious) interferences between broad overlapping resonances and nonresonant reaction components, properties which are much more difficult to determine accurately. Originally only the  $E1$  contribution to the cross section was thought to dominate and the reaction rate and estimates were based purely upon the properties of the  $1^-$  subthreshold state in  $^{16}\text{O}$ . At that time, since no direct measurements had been made, only very rough predictions of the cross section, based on theory and indirect measurements, were possible. For example, in the seminal work of Burbidge *et al.* (1957) ( $\text{B}^2\text{FH}$ ), the ground state  $\gamma$  width of the  $1^-$  subthreshold level at  $E_x = 7.12$  MeV had been measured by Swann and Metzger (1956) as  $\Gamma_{\gamma_0} = 130_{-80}^{+90}$  meV but no experimental information was available for the reduced  $\alpha$  width, which had to be calculated based on rudimentary nuclear theory. The significance of the comparable  $E2$  contribution was not realized for another 30 years (Redder *et al.*, 1987).

This review provides an overview of the astrophysical significance of the  $^{12}\text{C}(\alpha, \gamma)^{16}\text{O}$  reaction, the particular role it plays in nuclear physics, and a review of the interpretation and analysis of the experimental nuclear physics data that provide the basis for the presently used nuclear reaction rate in astrophysical simulations. In this work we seek to employ as comprehensive a study of the  $^{12}\text{C}(\alpha, \gamma)^{16}\text{O}$  reaction as possible by including other measurements that provide important information on the  $^{16}\text{O}$  compound nucleus for our interpretation of the reaction mechanism. This is implemented using a state-of-the-art  $R$ -matrix analysis, whose theoretical basis and implementation is explored in detail. Based on this complementary information a reaction rate analysis is performed that includes all available reaction and decay data associated with the  $^{16}\text{O}$  compound nucleus. The goal is to investigate the uncertainties associated with the low-energy extrapolation of the existing laboratory data into the stellar energy range. The uncertainties in the reaction rate are determined by Monte Carlo (MC) simulation techniques and a detailed investigation of the systematic uncertainties in both data and model. Finally, the impact of these uncertainties will be investigated in the framework of stellar model simulations.

## II. HELIUM BURNING AND ITS ASTROPHYSICAL SIGNIFICANCE

The  $^{12}\text{C}(\alpha, \gamma)^{16}\text{O}$  reaction plays a major role in key nuclear burning phases driving the evolution and the associated nucleosynthesis in low mass and massive stars. This includes main-sequence hydrogen burning, where  $^{12}\text{C}$  and  $^{16}\text{O}$  formed by the  $^{12}\text{C}(\alpha, \gamma)^{16}\text{O}$  reaction in previous generations of stars can play a critical role. On the main sequence, hydrogen burning fuses four hydrogen nuclei into helium releasing about 25 MeV of energy. This energy release generates the internal pressure conditions for maintaining the stability of the

stellar core against gravitational contraction. For low mass stars with initial masses  $M \lesssim 1.5M_{\odot}$  the fusion process is facilitated by the  $pp$  chains, a sequence of light ion capture reactions building upon the fusion of two protons into a deuteron by the weak interaction. In more massive stars  $M \gtrsim 1.5M_{\odot}$ , the importance of the  $pp$  chains is diminished and the fusion process is dominated by a catalytic reaction sequence, the CNO cycles that are characterized by four proton capture reactions and two  $\beta^+$  decays on carbon and oxygen forming a cycle by emitting an  $\alpha$  particle. The result of CNO nucleosynthesis is the conversion of hydrogen to  $^4\text{He}$  and enrichment of  $^{14}\text{N}$  based on the depletion of the initial  $^{12}\text{C}$  and  $^{16}\text{O}$  nuclei.

With the depletion of hydrogen in the stellar core, hydrogen burning continues only in a shell surrounding the inert core. The hydrogen depleted core contracts gravitationally, increasing the density and temperature of the core matter. This contraction is halted with the ignition of helium burning as a new energy source. Helium burning is triggered by the  $3\alpha$  process releasing 7.5 MeV in fusion energy and producing  $^{12}\text{C}$ . This is a rather unique process, setting stringent conditions for the ignition of helium burning in stars. The  $3\alpha$  process is followed by the subsequent  $\alpha$  capture reaction  $^{12}\text{C}(\alpha, \gamma)^{16}\text{O}$ , converting the  $^{12}\text{C}$  into  $^{16}\text{O}$ . These two isotopes are the principal products of helium burning. The ratio of these products affects not only their own nucleosynthesis but the future evolution of the star in its subsequent burning phases. The ratio of  $^{12}\text{C}/^{16}\text{O}$  is determined by the competition between the  $3\alpha$  and  $^{12}\text{C}(\alpha, \gamma)^{16}\text{O}$  reaction rates at a given temperature. The time evolution of the molar abundances  $Y(^{12}\text{C})$  and  $Y(^{16}\text{O})$  can be calculated as a function of the helium seed abundance  $Y(^4\text{He})$ , the reaction rates  $\lambda_{\text{reaction}}$  of the helium burning processes, and the density  $\rho$  using the following equations:

$$\begin{aligned} \frac{dY(^{12}\text{C})}{dt} &= \frac{1}{3!} Y^3(^4\text{He}) \rho^2 \lambda_{(3\alpha)} - Y(^4\text{He}) Y(^{12}\text{C}) \rho \lambda_{^{12}\text{C}(\alpha, \gamma)^{16}\text{O}}, \\ \frac{dY(^{16}\text{O})}{dt} &= Y(^4\text{He}) Y(^{12}\text{C}) \rho \lambda_{^{12}\text{C}(\alpha, \gamma)^{16}\text{O}} \\ &\quad - Y(^4\text{He}) Y(^{16}\text{O}) \rho \lambda_{^{16}\text{O}(\alpha, \gamma)^{20}\text{Ne}}, \end{aligned} \quad (1)$$

where the stoichiometric factor of  $1/3!$  accounts for indistinguishable  $\alpha$  particles.

Figure 1 illustrates a typical evolution of Eq. (1) at constant temperature and density. Putting helium on the  $x$  axis instead of time makes the evolution largely independent of the exact thermodynamic conditions. The feeding of  $^{12}\text{C}$ , driven by the  $3\alpha$  process, occurs early in the evolution when the abundance of carbon is low and helium is high. Oxygen production occurs later by  $\alpha$  capture on the freshly produced  $^{12}\text{C}$ . This shows the sensitivity of the  $^{12}\text{C}/^{16}\text{O}$  ratio to the strengths of the  $^{12}\text{C}(\alpha, \gamma)^{16}\text{O}$  and  $^{16}\text{O}(\alpha, \gamma)^{20}\text{Ne}$  rates in addition to the  $3\alpha$  process that facilitates the feeding of these isotopes. Both reactions are therefore critical for our understanding of the emergence of  $^{12}\text{C}$  and the evolution of its abundance.

In typical helium burning environments the reaction rate  $\lambda_{^{16}\text{O}(\alpha, \gamma)^{20}\text{Ne}}$  is considerably smaller than  $\lambda_{^{12}\text{C}(\alpha, \gamma)^{16}\text{O}}$ . Both

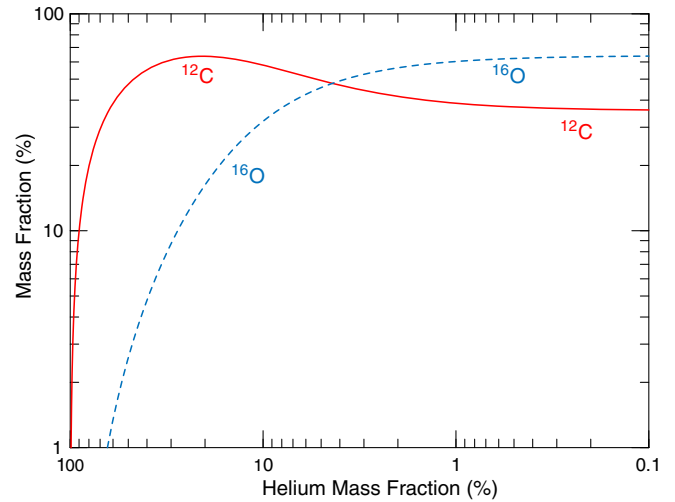


FIG. 1. Typical evolution of  $^{12}\text{C}$  and  $^{16}\text{O}$  mass fractions as a function of the  $^4\text{He}$  mass fraction at constant temperature and density. A mass fraction  $X_i$  of isotope  $i$  is related to the molar abundance  $Y_i$  of Eq. (1) by  $X_i = W_i Y_i$ , where  $W_i$  is the atomic weight. The oxygen mass fraction rises above the carbon mass fraction only when the helium abundance is relatively small.

the  $3\alpha$  process and the  $^{12}\text{C}(\alpha, \gamma)^{16}\text{O}$  reaction burn with high efficiency through pronounced resonance mechanisms. In contrast, the  $^{16}\text{O}(\alpha, \gamma)^{20}\text{Ne}$  reaction lacks any such resonance enhancement in the stellar energy range making its rate comparatively much lower (Costantini *et al.*, 2010). This essentially prohibits further helium burning beyond  $^{16}\text{O}$  and maintains the  $^{12}\text{C}/^{16}\text{O}$  balance as we observe it today. This effect of a sensitive balance between these three reactions is frequently discussed as an example for the anthropic principle, a prerequisite for the evolution of biological life as we know it in our Universe (Carr and Rees, 1979). These deliberations dominated the discussion of the importance of the interplay between these three reactions in the early second half of the 20th century (Kragh, 2010).

With the emergence of more sophisticated stellar modeling and nucleosynthesis simulation techniques, a number of more intricate questions emerged that underlined the importance of the  $^{12}\text{C}(\alpha, \gamma)^{16}\text{O}$  reaction. It plays a crucial role for stellar evolution and the associated nucleosynthesis during later stages. The aspects and consequences of the  $^{12}\text{C}(\alpha, \gamma)^{16}\text{O}$  rate have been investigated in detail by performing extensive modeling of the evolution and nucleosynthesis patterns in stars over a wide range of stellar masses. These simulations were performed using tabulated reaction rates (Caughlan and Fowler, 1988; Angulo *et al.*, 1999), or later (Buchmann and Barnes, 2006), with variations based on the predicted uncertainty ranges. There are pronounced differences with respect to the role of the reaction rate for nucleosynthesis in low- and intermediate-mass stars  $M \leq 8M_{\odot}$  that develop into asymptotic giant branch (AGB) stars with subsequent mass loss, ending as white dwarfs and massive stars  $M \geq 8M_{\odot}$  that develop toward their final fate as core-collapse supernova. The outcome of these studies is discussed in the following sections.

### A. Helium burning in low- and intermediate-mass stars

When a single star on the main sequence exhausts the supply of hydrogen in its core, the core contracts and its temperature increases, while the outer layers of the star expand and cool. The star becomes a red giant (Iben, 1991; Stancliffe *et al.*, 2009; Karakas and Lattanzio, 2014). The subsequent onset of helium burning in the core, for stars with initial masses  $M \gtrsim 0.5M_{\odot}$ , causes the star to populate the horizontal branch in the Hertzsprung-Russell diagram for more metal-poor stars or the red clump for more metal-rich stars (Cannon, 1970; Faulkner and Cannon, 1973; Seidel, Demarque, and Weinberg, 1987; Castellani, Chieffi, and Straniero, 1992; Girardi, 1999). After the star depletes the supply of helium in its core, the carbon-oxygen (CO) core contracts while the envelope once again expands and cools along a path that is aligned with its previous red-giant track. The star becomes an AGB star (Hansen, Kawaler, and Trimble, 2004; Herwig, 2005; Kippenhahn, Weigert, and Weiss, 2012; Fishlock *et al.*, 2014; Salaris *et al.*, 2014).

A variation of the  $^{12}\text{C}(\alpha, \gamma)^{16}\text{O}$  rate affects the core helium burning lifetime which in turn impacts the mass of the resulting He-exhausted core at the onset of the AGB phase. This mass is an important quantity that affects many of the star's properties during the AGB phase. Low- and intermediate-mass stars enter the AGB phase with hydrogen and helium fusion continuing in shells around a hot core composed primarily of carbon and oxygen and a trace amount of the neutron-rich isotope  $^{22}\text{Ne}$ . The precise influence of the  $^{12}\text{C}(\alpha, \gamma)^{16}\text{O}$  rate on the nucleosynthesis in AGB stars is challenging to accurately evaluate in the framework of present models due to multiple uncertainties (e.g., mixing processes). Yet, the reaction does play a key role for the nucleosynthesis during the AGB phase affecting the ejected abundances as well as the  $^{12}\text{C}/^{16}\text{O}$  ratio in the white dwarf remnant.

During the AGB phase helium ignites in the He shell under electron degenerate conditions, whose energy release triggers a sequence of convective thermal pulses, often called He-shell flashes. Depending on mass and composition, there may be a few to several hundred thermal pulses. During a He-shell flash the  $3\alpha$  process is the dominant source of energy and a producer of  $^{12}\text{C}$ . The  $^{12}\text{C}(\alpha, \gamma)^{16}\text{O}$  reaction creates  $^{16}\text{O}$ , whose mass fraction increases with depth. However, the duration of a He-shell flash is relatively short. Simulations suggest the  $^{16}\text{O}$  mass fraction in the intershell rises to  $\approx 0.2$ , the  $^{12}\text{C}$  mass fraction to 0.2–0.45, and the remaining material is mainly  $^4\text{He}$  (Werner and Herwig, 2006; Battino *et al.*, 2016).

The energy release from the thermal pulses also temporarily reduces or extinguishes H burning in the layers beneath the stellar envelope and causes convection to pull material from the central regions of the star toward its surface (Herwig, 2005; Straniero, Gallino, and Cristallo, 2006; Karakas and Lattanzio, 2014). This dredged-up material is enriched in carbon, oxygen, and *s*-process elements from the helium intershell, modifying the surface composition (Gallino *et al.*, 1998). This phenomenon is confirmed by the spectroscopic analysis of AGB stars (Abia *et al.*, 2001; Zamora *et al.*, 2009), post-AGB stars (Delgado-Inglada *et al.*, 2015), measurements of presolar grains (Lugaro *et al.*, 2003), and planetary nebula

as the dredged-up material is blown into the interstellar medium by stellar winds (Van Winckel and Reyniers, 2000).

For stars with an initial mass less than  $\approx 6M_{\odot}$  the temperature in the stellar core is too low to ignite  $^{12}\text{C}$  fusion, and the post-AGB evolution leads to a white dwarf. The  $^{12}\text{C}(\alpha, \gamma)^{16}\text{O}$  reaction rate has a large influence on the mass fraction profiles of  $^{12}\text{C}$  and  $^{16}\text{O}$  in the white dwarf remnant (Herwig, Austin, and Lattanzio, 2006; Fields *et al.*, 2016). For example, properties of white dwarf models derived from Monte Carlo stellar evolution surveys suggest a variation of  $^{12}\text{C}(\alpha, \gamma)^{16}\text{O}$  within the experimental uncertainties causes a  $\approx 50\%$  spread in the central carbon and oxygen mass fractions. Surveys of planetary nebulae find cases of oxygen enrichment by nearly a factor of 2 relative to carbon (Delgado-Inglada *et al.*, 2015), which may be due to an enhanced  $^{12}\text{C}(\alpha, \gamma)^{16}\text{O}$  rate or mixing processes (Pignatari *et al.*, 2016). Asteroseismology studies of white dwarfs seek to determine the  $^{12}\text{C}/^{16}\text{O}$  profile and infer the reaction rate from the transition of the white dwarfs inner oxygen-rich region to the carbon-rich region in the outer layers (Metcalf, 2003).

For stars with an initial mass above  $\approx 7M_{\odot}$  the temperatures in the stellar core are high enough to ignite carbon, and the minimum mass for neon ignition is  $\approx 10M_{\odot}$ . Stars with initial masses between  $\approx 7M_{\odot}$  and  $\approx 10M_{\odot}$  are designated as super-AGB stars. Depending primarily on the initial mass,  $^{12}\text{C}/^{16}\text{O}$  profile, and composition mixing model, the ignition of carbon may not occur at all (for stars  $\lesssim 7M_{\odot}$ ), occur at the center of the star (for stars  $\gtrsim 10M_{\odot}$ ), or occur somewhere off center (Siess, 2007, 2009; Poelarends *et al.*, 2008; Jones *et al.*, 2013; Doherty *et al.*, 2015; Farmer, Fields, and Timmes, 2015). In the off-center case, ignition is followed by the inward propagation of a subsonic burning front (Nomoto and Iben, 1985; Timmes, Woosley, and Taam, 1994; García-Berro, Ritossa, and Iben, 1997; Lecoanet *et al.*, 2016). The ignition conditions depend on the  $^{12}\text{C}/^{16}\text{O}$  ratio determined by the  $^{12}\text{C}(\alpha, \gamma)^{16}\text{O}$  rate and may vary by a factor of  $\approx 13$  at ignition (Straniero *et al.*, 2003).

The  $^{12}\text{C}/^{16}\text{O}$  profile in the remnant white dwarf impacts the ignition of type Ia supernovae, one of the premier probes for measuring the cosmological properties of the Universe (Riess *et al.*, 1998; Perlmutter *et al.*, 1999). The carbon mass fraction impacts the overall energy release, expansion velocity, and silicon-group and iron-group ejecta profiles (Höflich, Wheeler, and Thielemann, 1998; Röpke *et al.*, 2006; Calder *et al.*, 2007; Raskin *et al.*, 2012; Miles *et al.*, 2016; Seitzzahl *et al.*, 2016) in progenitor systems involving either one white dwarf (single degenerate channel) or two white dwarfs (double degenerate channel).

### B. Helium burning in massive stars

Most of a main sequence star's initial metallicity comes from the CNO and  $^{56}\text{Fe}$  nuclei inherited from its ambient interstellar medium. The slowest step in the hydrogen burning CNO cycle is proton capture onto  $^{14}\text{N}$ . This results in all the CNO catalysts piling up into  $^{14}\text{N}$  when hydrogen burning is completed. During the early onset of core helium burning, the reaction sequence  $^{14}\text{N}(\alpha, \gamma)^{18}\text{F}(\beta^+ \nu_e)^{18}\text{O}(\alpha, \gamma)^{22}\text{Ne}$  converts all of the  $^{14}\text{N}$  into  $^{22}\text{Ne}$ . For the first time, the stellar core has a

net neutron excess. As detailed later, this neutronization is important for the slow neutron capture (*s*) process in massive stars.

Helium burning in massive stars with initial masses  $M \gtrsim 8M_{\odot}$  has a lifetime of  $\approx 10^6$  yr. Typical core temperatures and densities in solar metallicity stellar models are  $\approx 2 \times 10^8$  K and  $\approx 1 \times 10^3$  g cm $^{-3}$ , respectively (Iben, 1966; Woosley, Heger, and Weaver, 2002; Limongi and Chieffi, 2003; Nomoto, Kobayashi, and Tominaga, 2013). As the convective helium core evolves the temperature and density rise significantly and thus so does the energy generation due to the  $3\alpha$  process and  $^{12}\text{C}(\alpha, \gamma)^{16}\text{O}$  reactions. Carbon production is favored by larger densities and smaller  $\lambda_{^{12}\text{C}(\alpha, \gamma)^{16}\text{O}}$ , while oxygen production is favored for smaller densities [see Eq. (1)] and larger  $\lambda_{^{12}\text{C}(\alpha, \gamma)^{16}\text{O}}$ . Figure 1 shows that the last remnants of helium fuel are the most important in setting the final  $^{12}\text{C}/^{16}\text{O}$  ratio.

In addition, during the final stages of helium burning, when the temperature and density are larger, the three reactions  $^{12}\text{C}(\alpha, \gamma)^{16}\text{O}$ ,  $^{22}\text{Ne}(\alpha, n)^{25}\text{Mg}$ , and  $^{16}\text{O}(\alpha, \gamma)^{20}\text{Ne}$  compete for those last few  $\alpha$  particles. The  $^{22}\text{Ne}(\alpha, n)^{25}\text{Mg}$  reaction is the dominant neutron source of the *s* process in massive stars (Raiteri *et al.*, 1991; Käppeler *et al.*, 1994; The, El Eid, and Meyer, 2007; Tur, Heger, and Austin, 2009; Pignatari *et al.*, 2010), producing about eight neutrons per iron seed nuclei. Therefore, the  $^{12}\text{C}(\alpha, \gamma)^{16}\text{O}$  reaction has an impact on *s*-process nucleosynthesis, where a larger rate translates into a smaller production of neutrons. For temperatures larger than  $\approx 4 \times 10^8$  K, the  $^{16}\text{O}(\alpha, \gamma)^{20}\text{Ne}$  rate becomes larger than the  $^{12}\text{C}(\alpha, \gamma)^{16}\text{O}$  rate, converting some of the abundant  $^{16}\text{O}$  into  $^{20}\text{Ne}$ .

The neutronization, entropy profile, and  $^{12}\text{C}/^{16}\text{O}$  ratio that emerges from core helium burning influence the subsequent evolution of a massive star. The uncertainty of the  $^{12}\text{C}(\alpha, \gamma)^{16}\text{O}$  rate propagates to the subsequent carbon, neon, oxygen, and silicon burning stages (Imbriani *et al.*, 2001; El Eid, Meyer, and The, 2004). For example, upon helium depletion the core again contracts and heats to conditions conducive to carbon burning by the  $^{12}\text{C} + ^{12}\text{C}$  reaction. Ignition of carbon depends on the fusion cross section of this heavy-ion reaction and on the square of the carbon fuel abundance that is chiefly set by the  $^{12}\text{C}(\alpha, \gamma)^{16}\text{O}$  reaction. Tur, Heger, and Austin (2007, 2010) considered the influence of uncertainties in the  $3\alpha$  and  $^{12}\text{C}(\alpha, \gamma)^{16}\text{O}$  reactions on the evolution and nucleosynthesis of massive stars. Using a reference  $^{12}\text{C}(\alpha, \gamma)^{16}\text{O}$  rate of 1.2 times that of Buchmann *et al.* (1996), they concluded that variations of this rate induced variations in the final abundances ejected by the supernova explosion including  $^{12}\text{C}$ , the key radionuclides  $^{26}\text{Al}$ ,  $^{44}\text{Ti}$ , and  $^{60}\text{Fe}$ , and the final mass of the remnant.

These later evolutionary phases are a rich site of challenges that include the interplay between nuclear burning (Couch *et al.*, 2015; Farmer *et al.*, 2016; Müller *et al.*, 2016; Jones *et al.*, 2017), convection (Meakin and Arnett, 2007; Viallet *et al.*, 2013), rotation (Heger, Langer, and Woosley, 2000; Rogers, 2015; Chatzopoulos *et al.*, 2016), radiation transport (Jiang *et al.*, 2015, 2016), instabilities (Garraud *et al.*, 2015; Wheeler, Kagan, and Chatzopoulos, 2015), mixing

(Maeder and Meynet, 2012; Martins *et al.*, 2016), waves (Rogers *et al.*, 2013; Aerts and Rogers, 2015; Fuller *et al.*, 2015), eruptions (Humphreys and Davidson, 1994; Kashi, Davidson, and Humphreys, 2016; Quataert *et al.*, 2016), and binary partners (Justham, Podsiadlowski, and Vink, 2014; Marchant *et al.*, 2016; Pavlovskii *et al.*, 2017). This bonanza of physical puzzles is closely linked with compact object formation by core-collapse supernovae (Timmer, Woosley, and Weaver, 1996; Eldridge and Tout, 2004; Özel *et al.*, 2010; Perego *et al.*, 2015; Suwa *et al.*, 2015; Sukhbold *et al.*, 2016) and the diversity of observed massive star transients (Van Dyk *et al.*, 2000; Ofek *et al.*, 2014; Smith *et al.*, 2016). Recent observational clues that challenge conventional wisdom (Zavagno *et al.*, 2010; Vreeswijk *et al.*, 2014; Boggs *et al.*, 2015; Jerkstrand *et al.*, 2015; Strotjohann *et al.*, 2015) coupled with the expectation of large quantities of data from upcoming surveys (Creevey *et al.*, 2015; Papadopoulos *et al.*, 2015; Sacco *et al.*, 2015; Yuan *et al.*, 2015), new measurements of key nuclear reaction rates and techniques for assessing reaction rate uncertainties (Wiescher, Käppeler, and Langanke, 2012; Sallaska *et al.*, 2013; Iliadis *et al.*, 2016), and advances in 3D pre-supernova modeling (Couch *et al.*, 2015; Müller *et al.*, 2016; Jones *et al.*, 2017) offer significant improvement in our quantitative understanding of the end states of massive stars.

### C. Helium burning in first stars

After the photons of the cosmic microwave background were released, the Universe exhibited a uniform structure with no point sources of light. As gravitational perturbations grew, dark matter and gas aggregated. No metals existed to facilitate the cooling and further condensation of gas into stars, as in later generations. Primordial star formation was instead driven by cooling through molecular hydrogen line emission (Palla, Salpeter, and Stahler, 1983). The first stars—referred to as H-He, pregalactic, population III, or zero metallicity stars—are thought to have initially formed at redshifts  $z \approx 20$  in small dark matter haloes of mass  $\approx 10^6 M_{\odot}$  (Abel, Bryan, and Norman, 2002; McKee and Tan, 2008; Turk, Abel, and O’Shea, 2009). Simulations suggest that fragmentation of the central gas configuration allows for a range of stellar masses  $1M_{\odot} \lesssim M \lesssim 1000M_{\odot}$ , depending on the dimensionality, spatial resolution, and local physics used in the simulations (Truran and Cameron, 1971; Fuller, Woosley, and Weaver, 1986; Hosokawa *et al.*, 2016; Stacy, Bromm, and Lee, 2016).

The  $^{12}\text{C}(\alpha, \gamma)^{16}\text{O}$  reaction impacts the early nucleosynthesis steps of the first generation of stars. In sufficiently massive first generation stars  $M \gtrsim 10M_{\odot}$ , the *pp* chains have too weak a temperature dependence to provide enough energy generation to halt gravitational contraction. Such stars continue to get denser and hotter until the central temperature reaches  $\approx 10^8$  K, where the  $3\alpha$  reaction synthesizes  $^{12}\text{C}$  (Ezer and Cameron, 1971). This self-production of carbon is followed by the  $^{12}\text{C}(\alpha, \gamma)^{16}\text{O}$  reaction to produce oxygen. The zero metallicity star thus makes enough of its own CNO elements to power the catalytic, hydrogen burning CNO cycles, halt gravitational contraction, and proceed onto the main

sequence. The evolution of the first stars from the main sequence to their final fate continues to be investigated across the entire initial mass spectrum (D'Antona, 1982; El Eid, Fricke, and Ober, 1983; Guenther and Demarque, 1983; Bond, Arnett, and Carr, 1984; Umeda, Nomoto, and Nakamura, 2000; Weiss *et al.*, 2000; Marigo *et al.*, 2001; Heger and Woosley, 2002, 2010; Ritter *et al.*, 2016). In stars sufficiently massive to burn helium, the  $^{12}\text{C}(\alpha, \gamma)^{16}\text{O}$  reaction establishes the  $^{12}\text{C}/^{16}\text{O}$  profile which impacts the subsequent evolution.

Indeed, the most metal-poor stars that we observe today carry signatures of the first core-collapse supernovae, characterized by enhancements of carbon and oxygen relative to iron,  $[\text{C}/\text{Fe}] \sim [\text{O}/\text{Fe}] \sim +3.0$  (Bond, 1981; Bessell and Norris, 1984; Beers, Preston, and Shtetman, 1985, 1992; Frebel *et al.*, 2005, 2015; Christlieb, 2008; Keller *et al.*, 2014; Hansen *et al.*, 2016; Yoon *et al.*, 2016). A large fraction of these stars show  $[\text{C}/\text{Fe}]$  and  $[\text{O}/\text{Fe}]$  ratios larger than those in the Sun (Bonifacio *et al.*, 2015; Hansen *et al.*, 2015). The full potential of stellar archaeology can likely be reached in ultrafaint dwarf galaxies, where the simple formation history may allow for straightforward identification of second-generation stars (Ji, Frebel, and Bromm, 2015). These observations confirm the important role of the  $^{12}\text{C}(\alpha, \gamma)^{16}\text{O}$  reaction for interpreting the onset of nucleosynthesis in the first stars.

#### D. Uncertainty considerations

The reliability of nucleosynthesis predictions depends on the quality of the stellar models and the nuclear reaction input parameters. The interplay between these two components defines the overall uncertainty in the model predictions. The quality of stellar model simulations has seen a rapid improvement over the last two decades due to the enormous increase in computational power. This has effectively reduced the traditional uncertainties associated with the model parameters, putting larger demands on the uncertainties associated with the reaction cross section.

An unprecedented effort has also been invested into improved experimental data and extrapolation techniques. While there have been significant advances, cross section measurements toward lower energies represent a staggering experimental challenge. The exponential decline of the cross section can translate a few tens of keV steps toward lower energies into an order of magnitude reduction in reaction yield. This needs to be compensated by either a significant increase in beam current, a significant increase in detection efficiency, and/or a significant decrease in the experimental background. Past experiments have pushed the measurements to the limit of the practical amount of time and effort that is achievable with current resources. However, advances in detector technology and high current, low background accelerator facilities offer renewed chances to move forward.

Improvements in the extrapolation technique are also possible. One major step forward can be made by making a more complete and consistent treatment of all reaction parameters and data using  $R$ -matrix theory. The overall uncertainty in the cross section evaluations, however, is difficult to assess. In addition, the propagation of the rate through the stellar models is also open to interpretation. An

attempt based on statistical means was suggested by Iliadis *et al.* (2015). This was adopted by Fields *et al.* (2016) to provide uncertainty ranges for different quantities predicted by a stellar model (e.g., density or mass fraction of  $^{12}\text{C}$ ) as they are sensitive to the uncertainty in the rate of the  $^{12}\text{C}(\alpha, \gamma)^{16}\text{O}$  reaction given by Kunz *et al.* (2002).

The long-standing large uncertainties associated with the  $^{12}\text{C}(\alpha, \gamma)^{16}\text{O}$  reaction rate and the difficulties in providing a reliable extrapolation of laboratory data to the stellar energy range triggered initiatives to deduce the reaction rate from nucleosynthesis simulations for massive stars and the comparison with observational abundance distributions. The first attempt utilized a set of massive star models ranging from  $12M_{\odot}$  to  $40M_{\odot}$ , following nuclear burning through all phases of stellar evolution up to the point of iron core collapse (Weaver and Woosley, 1993). Within the uncertainties of the model simulations, the results indicated a reaction rate that is in good agreement with that suggested later by Buchmann and Barnes (2006) on the basis of an  $R$ -matrix analysis. A similar approach was taken by Garnett (1997), who used the C/O abundance ratio in the ionized interstellar gas of galaxies, with very low heavy element abundances, to constrain the  $^{12}\text{C}(\alpha, \gamma)^{16}\text{O}$  rate. This study confirmed the results of the former analysis by Weaver and Woosley (1993).

A similar analysis on the impact of the  $^{12}\text{C}(\alpha, \gamma)^{16}\text{O}$  reaction rate on the nucleosynthesis of heavier element yields during presupernova evolution and supernova explosions was performed by Tur, Heger, and Austin (2007). They considered the nucleosynthesis in stars with initial masses ranging from  $13M_{\odot}$  to  $27M_{\odot}$  calculated from the implicit, one-dimensional, hydrodynamical stellar evolution code KEPLER (Woosley, Heger, and Weaver, 2002). They varied the  $^{12}\text{C}(\alpha, \gamma)^{16}\text{O}$  reaction rate by scaling the  $S$  factor of  $S(300 \text{ keV}) = 146 \text{ keV b}$  as suggested by Buchmann and Barnes (2006) by a factor of 0.6 to 1.9, probing the impact on the production factors of light elements and, in particular, the carbon/oxygen mass fraction at carbon ignition at the center of these massive stars. The results again suggested good agreement with the prediction by Buchmann and Barnes (2006), confirming the earlier results of Weaver and Woosley (1993) and Garnett (1997). The study concluded that for a reliable nucleosynthesis simulation for massive stars, the  $^{12}\text{C}(\alpha, \gamma)^{16}\text{O}$  reaction rate needs to be known to an uncertainty of 10%.

This work was followed more recently by a more expanded study (West, Heger, and Austin, 2013), where the sensitivity of presupernova evolution and supernova nucleosynthesis yields of massive stars was considered in dependence of variations in the  $3\alpha$  and the  $^{12}\text{C}(\alpha, \gamma)^{16}\text{O}$  rates. These variations were kept within an uncertainty range of  $\pm 2\sigma$ . A grid of 12 initial stellar masses between  $12M_{\odot}$  and  $30M_{\odot}$ , using 176 models per stellar mass, were computed to explore the effects of the two independently varying rates on the production of intermediate-mass elements  $A = 16\text{--}40$  and the  $s$ -only isotopes produced efficiently by the weak  $s$  process ( $^{70}\text{Ge}$ ,  $^{76}\text{Se}$ ,  $^{80}\text{Kr}$ ,  $^{82}\text{Kr}$ ,  $^{86}\text{Sr}$ , and  $^{87}\text{Sr}$ ) in comparison to the solar abundance distribution. The study found a close correlation between the two rates for an optimal fit of the abundances, as to be expected by Eq. (1), indicating that

TABLE I. Astrophysical environments and burning stages where the  $^{12}\text{C}(\alpha, \gamma)^{16}\text{O}$  reaction plays an important role. The temperatures of these environments dictate the energy ranges where the  $^{12}\text{C}(\alpha, \gamma)^{16}\text{O}$  cross section must be well known for an accurate calculation of the reaction rate.

Burning stages	Astrophysical sites	Temperature range (GK)	Gamow energy range (MeV)
Core helium burning	AGB stars and massive stars	0.1–0.4	0.15–0.65
Core carbon and oxygen burning	Massive stars	0.6–2.7	0.44–2.5
Core silicon burning	Massive stars	2.8–4.1	1.1–3.4
Explosive helium burning	Supernovae and x-ray bursts	$\approx 1$	0.6–1.25
Explosive oxygen and silicon burning	Supernovae	$> 5$	$> 1.45$

an increase of the  $^{12}\text{C}(\alpha, \gamma)^{16}\text{O}$  rate requires an increase in the  $3\alpha$  rate.

### E. The nuclear reaction rate

While these model based studies are certainly of great interest, they depend on the reliability of the stellar models, the model parameters, and the numerical treatment of the hydrodynamic aspects of stellar evolution. Depending on the internal burning conditions in the specific environments the stellar reaction rate needs to be well known over a wide energy range.

The nuclear reaction rate can be calculated from the total reaction cross section  $\sigma(E)$  by integration over the Maxwell-Boltzmann distributions of the interacting particles in a stellar environment of temperature  $T$ . The reaction rate per particle pair is given by

$$N_A \langle \sigma v \rangle = \left( \frac{8}{\pi \mu} \right)^{1/2} \frac{N_A}{(k_B T)^{3/2}} \int_0^\infty \sigma(E) E e^{-E/k_B T} dE, \quad (2)$$

where  $\mu$  is the reduced mass,  $E = \mu v^2/2$  is the center-of-mass energy,  $N_A$  is Avogadro's number, and  $k_B$  is Boltzmann's constant. The energy-dependent cross section is the key input for determining the reaction rate. This is determined by various reaction contributions and mechanisms.

Traditionally, the charged-particle reaction cross section is expressed in terms of the astrophysical  $S$  factor

$$S(E) = \sigma(E) E e^{2\pi\eta}. \quad (3)$$

The exponential term  $e^{2\pi\eta}$  approximately accounts for the influence of the Coulomb barrier on the cross section, where  $\eta$  is the Sommerfeld parameter ( $\sqrt{\mu/2E} Z_1 Z_2 e^2 / \hbar^2$ ). Therefore  $S(E)$  essentially describes the nuclear and centrifugal barrier components of the reaction mechanism and is also more convenient for plotting and extrapolation. The reaction rate scales with the  $S$  factor at the stellar energy range, and the literature therefore often quotes the  $S$  factor at a typical stellar energy. For the  $^{12}\text{C}(\alpha, \gamma)^{16}\text{O}$  reaction this is at  $E_{\text{c.m.}} = 300$  keV. Thus the value of  $S(300 \text{ keV})$  is often given for ease of comparison of the impact of the nuclear reaction data on the extrapolation.

Equation (2) can be approximated when either of two extreme cases dominate the  $S$  factor. First, some  $S$  factors are dominated by nonresonant processes (e.g., direct capture) and are often characterized by a nearly energy-independent  $S$  factor. In this case, the energy range of interest for a specific burning temperature  $T$  is traditionally defined in terms of the

Gamow window, which is defined by the integrand in Eq. (2). For a constant  $S$  factor, the integrand can be approximated by a Gaussian distribution around the mean center-of-mass energy  $E_0$  (in units of MeV) of

$$E_0 = 0.122 (Z_1^2 Z_2^2 \hat{\mu} T_9^2)^{1/3}, \quad (4)$$

with  $Z_1$  and  $Z_2$  being the charges of the interacting particles,  $\hat{\mu}$  is the reduced mass in atomic mass units, and  $T_9$  is the temperature in GK. Using the same notation, the width  $\Delta E$  of the Gamow range is given by

$$\Delta E = 0.236 (Z_1^2 Z_2^2 \hat{\mu} T_9^5)^{1/6}. \quad (5)$$

The reader is cautioned that this Gaussian distribution concept may break down in the case of resonances or as one moves above the Coulomb barrier (i.e., at higher temperatures) (see Fig. 28).

This simple formalism facilitates the quick identification of the energy range over which the reaction cross section needs to be determined to provide a reaction rate for stellar burning simulations. Table I summarizes the energy ranges corresponding to the characteristic temperatures of the various stellar environments discussed in Sec. II. A purely experimentally determined reaction rate would require experimental cross section data covering the full range of these energies ( $0.15 < E_{\text{c.m.}} < 3.4$  MeV). Since this has not been achieved for the lower energies, the reaction rate for  $^{12}\text{C}(\alpha, \gamma)^{16}\text{O}$  has to rely on the extrapolation of experimental data obtained at higher energies.

The second case is when the  $S$  factor is dominated by narrow isolated resonances (i.e., such that the resonance width is small compared to the resonance energy and interference effects can be neglected). Ignoring all energy dependences except the Lorentzian approximation of the Breit-Wigner cross section, Eq. (2) can then be integrated analytically. This yields an expression for the reaction rate in terms of resonance strengths  $\omega\gamma_i$ :

$$N_A \langle \sigma v \rangle = 1.5394 \times 10^{11} (\hat{\mu} T_9)^{-3/2} \times \sum_i \omega\gamma_i \exp\left(\frac{-11.605 E_{R_i}}{T_9}\right) \left[ \frac{\text{cm}^3}{\text{s mol}} \right], \quad (6)$$

where  $\omega\gamma_i$  and  $E_{R_i}$  are the resonance strength and resonance energy of the  $i$ th resonance in MeV, respectively.

The resonance strengths are proportional to the production and decay widths,  $\Gamma_{\text{in}}$  and  $\Gamma_{\text{out}}$ :

$$\omega\gamma = \frac{(2J+1)}{(2J_1+1)(2J_2+1)} \frac{\Gamma_{\text{in}}\Gamma_{\text{out}}}{\Gamma}, \quad (7)$$

where  $J$  is the spin of the resonance,  $J_1$  and  $J_2$  are the spins of the nuclei in the entrance channel, and  $\Gamma$  is the total width of the resonance. In the case of radiative  $\alpha$  capture reactions,  $\Gamma_{\text{in}}$  and  $\Gamma_{\text{out}}$  correspond to the  $\alpha$  and  $\gamma$  partial widths  $\Gamma_\alpha$  and  $\Gamma_\gamma$ , respectively.

Complicating matters, the energy dependence of the  $^{12}\text{C}(\alpha, \gamma)^{16}\text{O}$  reaction does not fall into either of these two specialized categories. Instead, the  $S$  factor is dominated by broad resonances which interfere with one another, a regime in between the two extreme cases discussed. Therefore the reaction rate must be determined through numerical integration of Eq. (2). However, in addition to these broad resonances there are also a few narrow resonances that are superimposed upon them. Because of practical experimental considerations (i.e., target thickness and accelerator energy resolution), the strengths of these narrow resonances are much easier quantities to measure accurately than the individual widths or actual cross sections over them. Therefore, in practice, numerical integration of Eq. (2) is used in conjunction with the narrow resonance specific form of Eq. (6) to calculate the total rate of the  $^{12}\text{C}(\alpha, \gamma)^{16}\text{O}$  reaction. This process is described in more detail in Sec. IX.

The following section is dedicated to outlining our present knowledge of the reaction mechanisms and the underlying

nuclear structure and reaction phenomena that are needed for an accurate calculation of the reaction rate. For an informed extrapolation it is important to treat and determine the  $^{12}\text{C}(\alpha, \gamma)^{16}\text{O}$  cross section as a nuclear physics problem that can be solved only by understanding the complex quantum mechanics of the reaction mechanism. Further, nuclear theory, as discussed in Secs. III and IV, independently calculates the different multiplicities of the reaction. Thus for the extrapolation to be made, it is necessary to not only measure the total cross section as a function of energy  $\sigma(E)$ , but also to understand its composition in terms of photon multiplicities and  $^{16}\text{O}$  final states.

### III. NUCLEAR PHYSICS ASPECTS

The reaction mechanism of  $^{12}\text{C}(\alpha, \gamma)^{16}\text{O}$ , and therefore its cross section or  $S$  factor, is characterized by strong resonant and nonresonant contributions and the interference effects between these components. The strength of these components is directly associated with the nuclear structure of the  $^{16}\text{O}$  nucleus. Being doubly magic it has been the subject of numerous studies and its unique level structure has provided a long-standing challenge for theoretical descriptions.

The  $^{16}\text{O}$  compound nucleus is represented schematically in Fig. 2. It has four particle bound excited states at excitation energies  $E_x = 6.05, 6.13, 6.92,$  and  $7.12$  MeV. As an even-even nucleus, the spin of the ground state is  $J^\pi = 0^+$  and the

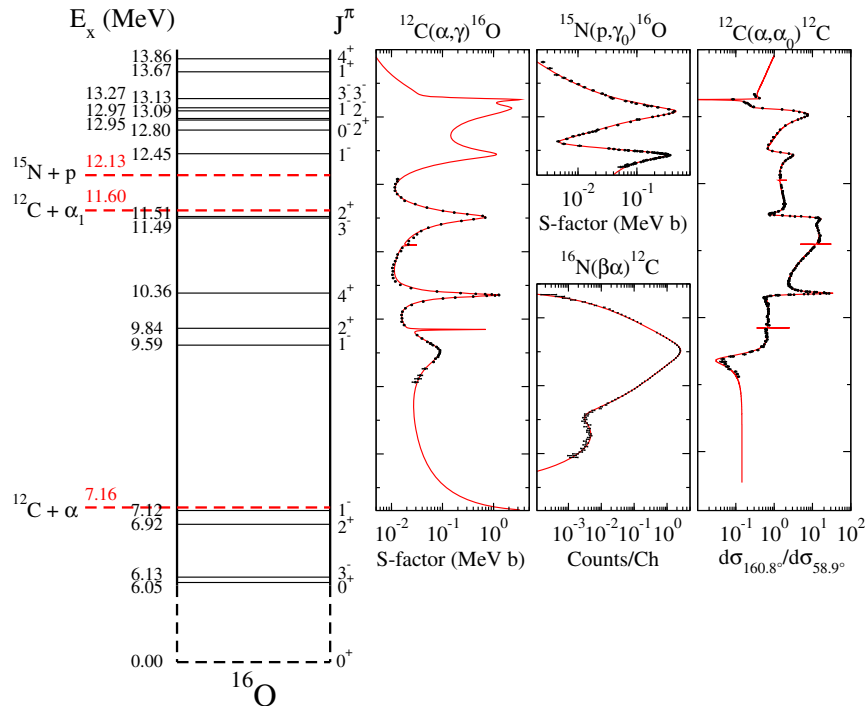


FIG. 2. Level diagram of the  $^{16}\text{O}$  compound nucleus. Levels that are irrelevant to the analysis are omitted, for example, unnatural parity states below the proton separation energy. Several reactions that populate the CN are shown where their energy axis has been converted to excitation energy. At low energy only  $^{12}\text{C} + \alpha_0$ ,  $^{16}\text{O} + \gamma$ , and  $^{16}\text{N}(\beta\alpha)^{12}\text{C}$  partitions are considered. At higher energies, the  $^{15}\text{N} + p$  and  $^{12}\text{C} + \alpha_1$  partitions are also included. Representative experimental cross section measurements that populate the CN are shown on the right. The total cross section data for the  $^{12}\text{C}(\alpha, \gamma)^{16}\text{O}$  reaction are those of Schürmann *et al.* (2005), the  $^{15}\text{N}(p, \gamma)^{16}\text{O}$  those of LeBlanc *et al.* (2010), the  $^{16}\text{N}(\beta\alpha)^{12}\text{C}$  spectrum is from Buchmann *et al.* (1993), and the  $^{12}\text{C}(\alpha, \alpha_0)^{12}\text{C}$  data are from Tischhauser *et al.* (2002). The solid red curves represent the phenomenological  $R$ -matrix fits described in this work.

four excited states are  $0^+$ ,  $3^-$ ,  $2^+$ , and  $1^-$ , respectively. The two odd parity states are considered to be single-particle configurations that can be described well in the framework of the shell model, while the two of even parity have been characterized as cluster configurations that require a microscopic potential or cluster model approach (Langanke and Friedrich, 1986). From the following cluster model discussions in Sec. III.B, one might expect that the separation energy  $S_{\alpha_0}$  of the  $^{16}\text{O}$  CN into an  $\alpha$  particle and the ground state configuration of  $^{12}\text{C}$  is at  $E_x = 7.16$  MeV. It will become of utmost relevance for the reaction rate that  $S_{\alpha_0}$  is only a few hundred keV above the  $2^+$  and  $1^-$  bound states. It is useful to note that all of the excited bound states that  $\gamma$  decay do so to the ground state with nearly 100% probability. Angular momentum and spin selection rules dictate that if the  $^{16}\text{O}$  compound nucleus is formed by a  $^{12}\text{C} + \alpha_0$  reaction (intrinsic spins both equal to 0), then only states with  $J = l$  and  $\pi = (-1)^l$  (natural parity states), where  $J$  is the total spin and  $l$  is the relative orbital angular momentum, can be populated. With the limitation to only natural parity states, the  $\gamma$ -ray decay selection rules allow only electric transitions to the  $0^+$  ground state to occur. Further,  $\gamma$ -ray decays from  $0^+$  to  $0^+$  states are strictly forbidden.

The  $^{12}\text{C}(\alpha, \gamma)^{16}\text{O}$  cross section is greatly influenced by the isospin of the states in  $^{16}\text{O}$ . The two  $1^-$  levels that most influence the low-energy cross section, those at  $E_x = 7.12$  MeV (bound) and 9.59 MeV (unbound), are  $T = 0$ , for which  $E1$   $\gamma$ -ray decays would be strictly forbidden to the ground state if the states were isospin pure. However, the Coulomb interaction breaks isospin symmetry, causing the states to become isospin mixed, allowing for such transitions to take place, albeit at a reduced strength. This is the primary reason that the  $E1$  and  $E2$  multipolarity components of the  $^{12}\text{C}(\alpha, \gamma_0)^{16}\text{O}$  cross section are of nearly equal strength. In fact, the earliest studies of the  $^{12}\text{C}(\alpha, \gamma)^{16}\text{O}$  reaction were made primarily to study the effects of isospin symmetry breaking. At higher energies, the next  $T = 0$  state is at  $E_x = 12.45$  MeV and the first  $T = 1$  state is at  $E_x = 13.09$  MeV. Reproducing the properties of these states, especially the  $\gamma$ -ray decay widths, has proven challenging for nuclear models as discussed further in Sec. III.B.

The level structure of  $^{16}\text{O}$  results in very different reaction mechanisms favored by the  $\gamma$ -ray deexcitations to the ground state versus those to higher-lying excited states. As discussed in more detail in Sec. IV.D,  $E1$  direct capture to the ground state is greatly suppressed. On the other hand, the large  $Q$  value for the ground state transition favors resonance decays. This results in resonances, including those of the subthreshold states, dominating over the direct capture. It should also be noted that while the  $E1$  direct capture strength is negligible, there is the possibility that  $E2$  direct capture could be a significant component to the cross section in off-resonance regions. In contrast, resonant deexcitations to the high-lying excited states in  $^{16}\text{O}$  are suppressed because of their smaller  $Q$  values. This then puts the strength of resonance decays on par with that of the direct capture, with direct capture even dominating in several cases (see Sec. VI.C). Therefore, the cascade transition cross sections are expected to be small compared with those of the ground

state. This then makes the determination of asymptotic normalization coefficients for the corresponding final states critical for modeling the external capture component of the capture cross sections for these transitions (see Secs. IV.D and VI.C).

The essential goal is to obtain an accurate value of the cross section over the energy range that contributes significantly to the reaction rate calculation (see Sec. IX). Ideally the cross section could simply be measured directly in the laboratory, but this is not a viable option since the Coulomb repulsion between the two charged particles makes the cross sections over the Gamow energy region extremely small. For the  $^{12}\text{C}(\alpha, \gamma)^{16}\text{O}$  reaction, the cross section at  $E_{c.m.} = 300$  keV is estimated to be about  $2 \times 10^{-17}$  b. This is still about 5 orders of magnitude below the sensitivity, a few picobarns, achieved by the most state-of-the-art measurements. For this reason, nuclear reaction theories must be used to aid in the *extrapolation* of the cross section to the astrophysically relevant region. This is the crux of the problem.

Several different approaches have been investigated. The cluster model approach provides guidance for interpreting the level structure of the  $^{16}\text{O}$  compound nucleus, but so far they are not a sufficiently reliable method for predicting reaction cross sections or for extrapolating existing experimental data from laboratory studies into the stellar energy range. Phenomenological models, fit to experimental data and extrapolated to low energy, are more accurate and have been the mainstay for many years. The remainder of this section is devoted to an introduction to the experimental data and the status of the cluster and phenomenological models used to interpret it.

### A. The experimental situation

A host of experimental measurements have been made to study the  $^{12}\text{C}(\alpha, \gamma)^{16}\text{O}$  reaction over the years. Because of its incredible importance to the field of nuclear astrophysics and the extreme challenge of its measurement, nearly every kind of technique in the experimental nuclear physicist's tool box has been brought to bear. Experiments have ranged from the most sophisticated, brute force, high beam current, direct measurements, to techniques as indirect as the study of the  $\beta$ -delayed  $\alpha$  emission of  $^{16}\text{N}$  and Coulomb excitation. These extensive and diverse efforts have aimed either at the direct study of the low-energy cross section or at the study of the nuclear properties of the levels near the  $\alpha$  threshold in the  $^{16}\text{O}$  compound nucleus.

Direct methods have evolved from measuring reaction yields in close geometry where only faint signals were observed, and are difficult to interpret, to measuring high statistics detailed angular distributions in far geometry that approach direct observation of the differential cross sections. Most experiments have focused on a limited low-energy region in the range  $1 < E_{c.m.} < 3$  MeV for two primary reasons. First, a broad  $1^-$  resonance (corresponding to the level at  $E_x = 9.59$  MeV in Fig. 2) enhances the cross section in this region making measurements more viable. This state then serves as a touch stone for measurements toward lower energies. Second, measurements are greatly hindered by the increasing, and very high cross section,  $^{13}\text{C}(\alpha, n)^{16}\text{O}$

background reaction. The large amount of neutrons it creates causes several serious experimental difficulties. The neutrons themselves cause damage to the delicate lattice structure of solid state detectors. Further, secondary  $\gamma$  rays are created through inelastic neutron scattering and neutron capture on both surrounding material and the detectors themselves. They create  $\gamma$  rays over a wide energy range that hinder the measurements of all the transitions of the  $^{12}\text{C}(\alpha, \gamma)^{16}\text{O}$  reaction (Makii *et al.*, 2005).

In recent years, the vast improvements in experimental techniques have expanded the accessible energy range, to both lower and higher energies. This effort, coupled with substantial improvements in the phenomenological description of the reaction contributions and the overall reaction mechanism through  $R$ -matrix theory, leads to a substantially improved confidence in the low-energy extrapolation of the cross section. Before entering into a detailed discussion of the experimental data and its phenomenological interpretation in Secs. V and VI, the following sections provide a summary of past utilization of both cluster models and  $R$ -matrix theory for interpreting the  $^{12}\text{C}(\alpha, \gamma)^{16}\text{O}$  cross sections.

## B. Cluster models

Since the pioneering work of Wheeler (1937a), it has been argued that individual nucleons should often be found in tightly bound  $\alpha$ -particle cluster configurations [see, e.g., Beck (2010, 2012, 2014) for a series of recent reviews]. It follows then that for nuclei that are integer multiples of the  $\alpha$  particle, many of the nuclear excitations in the compound nucleus can be interpreted as the molecular configurations of  $\alpha$  particle clusters. This then strongly influences the strength of the associated resonance states and the strength of direct capture transitions, which usually dominate the reaction mechanism. This idea is particularly interesting when played out using the theoretical framework of the Ikeda model (Ikeda, Takigawa, and Horiuchi, 1968), which predicts pronounced  $\alpha$ -clustering configurations near the  $\alpha$  threshold. Thus the effect of  $\alpha$  clustering is particularly critical for reactions in stellar helium burning, where the  $3\alpha$  process and the subsequent  $^{12}\text{C}(\alpha, \gamma)^{16}\text{O}$  reaction dominate (Freer, 2007).

For modeling the radiative capture cross section of the  $^{12}\text{C}(\alpha, \gamma)^{16}\text{O}$  reaction, a number of cluster models of varying levels of sophistication have been applied to investigate the impact of these effects on the various transition components. This is, in particular, important for the  $E_2$  ground state transition due to the fact that the subthreshold  $2^+$  state at  $E_x = 6.92$  MeV represents a high degree of  $\alpha$  clustering (Brown and Green, 1966). In the  $E_1$  ground state component, the cluster contribution of the  $E_x = 7.12$  MeV subthreshold state and its interference with the resonance corresponding to the broad  $E_x = 9.59$  MeV cluster state add significantly to the reaction strength.

Most of the cluster models applied to the study of this reaction have their roots in the resonating group method (RGM) originally proposed by Wheeler (1937b). Microscopic potential models (PMs) have been presented by Langanke and Koonin (1983, 1985) and Funck, Langanke, and Weiguny (1985) and are summarized by Langanke and Friedrich

(1986). Single-channel and multichannel generator coordinate method (which is equivalent to the RGM) calculations have also been developed (Descouvemont, Baye, and Heenen, 1984; Descouvemont and Baye, 1987; Descouvemont, 1993; Dufour and Descouvemont, 2008). Many of these works have also included calculations of the strengths of the  $^{12}\text{C}(\alpha, \gamma)^{16}\text{O}$  cascade transitions (Descouvemont, Baye, and Heenen, 1984; Langanke and Koonin, 1985; Descouvemont and Baye, 1987; Dufour and Descouvemont, 2008). Since none of these models allow for all of the degrees of freedom associated with 16 nucleons, the use of effective interactions is required along with some phenomenological adjustment of parameters to agree with experimental inputs such as separation thresholds and resonance energies.

Despite the long-standing theoretical development, precision  $\alpha$ -cluster modeling is still challenging. As a recent example, the  $\alpha$ -cluster configuration of the  $^{16}\text{O}$  nucleus was studied using a modified shell-model approach built on a cluster-nucleon configuration interaction model with advanced realistic shell-model Hamiltonians. The model was constructed in order to investigate the strength of clustering phenomena in the harmonic oscillator basis (Volya and Tchuvil'sky, 2015). This study provides a comprehensive description of the  $\alpha$ -cluster structure of the  $^{16}\text{O}$  nucleus up to a very high excitation energy range based on the  $^{12}\text{C}$  ground state configuration. The study demonstrates the possible existence of pronounced  $\alpha$ -cluster configurations, in particular, for the energy range near the  $\alpha$  threshold where large  $\alpha$  spectroscopic factors are predicted for natural parity resonance and subthreshold levels in the range  $6.0 < E_x < 8.5$  MeV. These theoretical results are in general agreement with the tabulated values obtained by  $\alpha$  transfer and capture reactions (Tilley, Weller, and Cheves, 1993).

In principle these models are highly constrained and consequently have great predictive power. However, the cluster models are challenged to describe all of the available experimental data with the precision required for nuclear astrophysics applications. This is largely because they take only certain cluster components in the reaction mechanism into account. For example, there are difficulties in correctly describing the width of the narrow  $2^+$  state at  $E_x = 9.84$  MeV with this approach, as it is predominantly not an  $\alpha$ -cluster state (Dufour and Descouvemont, 2008). The new approach of coupling the cluster model with modern shell-model techniques offers new opportunities for a more comprehensive theoretical description of the level structure of the  $^{16}\text{O}$  compound nucleus that is necessary for a reliable theoretical prediction of the  $^{12}\text{C}(\alpha, \gamma)^{16}\text{O}$  reaction cross section (Volya and Tchuvil'sky, 2015). Another state-of-the-art example is the calculation of Epelbaum *et al.* (2014), where binding energies, charge radii, quadrupole moment (for the  $2^+$  state), and electromagnetic transition strengths are provided for the even-parity bound states of  $^{16}\text{O}$ . As theoretical approaches become truly *ab initio*, they will significantly further our understanding of the  $^{12}\text{C}(\alpha, \gamma)^{16}\text{O}$  reaction. Already cluster models can be very useful for making theoretical calculations of asymptotic normalization coefficients (ANCs) for the bound states of  $^{16}\text{O}$  and this should see further attention.

However, because of the limitations described, phenomenological approaches must still be employed.

### C. Phenomenological models

A strong point of phenomenological reaction models is that, while remaining ignorant of more fundamental nuclear physics (i.e., internal nuclear wave functions), well-established quantum-mechanical symmetries and conservation laws, such as angular momentum conservation and unitarity, can still be enforced. This allows the model to remain flexible, while still providing many stringent constraints. On the other hand, phenomenological models have little predictive power without data and the quality of their constraints or predictions is very much dependent upon the quality of the supporting experimental data.

The most long-standing and pervasive phenomenological model for the resolved resonance region is the  $R$ -matrix theory of Wigner and Eisenbud (1947), which was further developed by Bloch (1957) and Lane and Thomas (1958). It has been used by many in the field for the analysis of the  $^{12}\text{C}(\alpha, \gamma)^{16}\text{O}$  reaction as well as many other reactions. The  $R$ -matrix model, as described in more detail in Sec. IV, offers the best approach to phenomenological analysis of the  $^{12}\text{C}(\alpha, \gamma)^{16}\text{O}$  reaction at this time. Some of the other alternatives, and justification for this assertion, are discussed later.

One extension of the  $R$ -matrix method that has been applied to the  $^{12}\text{C}(\alpha, \gamma)^{16}\text{O}$  reaction is the “hybrid”  $R$ -matrix-optical model (Johnson, 1973; Koonin, Tombrello, and Fox, 1974). In this approach, the broad  $1^-$  state at  $E_x = 9.85$  MeV and higher-energy background levels are modeled using an optical potential, with the subthreshold  $1^-$  state being introduced as a separate  $R$ -matrix level. Refinements have been provided in subsequent publications (Langanke and Koonin, 1983, 1985). This method has the attractive feature that the optical model should reproduce many of the higher-lying broad resonances. If this can replace the need for additional background pole terms, the number of free parameters could be greatly reduced and an improved constraint on the extrapolated  $S$  factor could be achieved. However, these models have difficulties describing, over a broad energy range, the high-precision  $^{12}\text{C}(\alpha, \alpha)^{12}\text{C}$  elastic scattering data that are now available (Plaga *et al.*, 1987; Tischhauser *et al.*, 2009). These difficulties are not present in the standard  $R$ -matrix approach due to the greater flexibility. Nevertheless, the hybrid model may still be interesting for investigating the effects of the nuclear interaction beyond the channel radius.

An alternative to the  $R$  matrix is the  $K$  matrix, as developed by Jean Humblet (Humblet, Dyer, and Zimmerman, 1976; Humblet, 1990).  $K$ -matrix theory is based upon a pole expansion (Mittag-Leffler series) of a meromorphic function, rather than the properties of eigenfunctions satisfying boundary conditions as in  $R$ -matrix theory. Some advantages of the  $K$ -matrix approach are that there is no channel radius and the computation of Coulomb wave functions is not needed. The fitting of experimental data is in general quite similar to the  $R$ -matrix approach, with equal numbers of free parameters leading to similar quality fits,  $S$ -factor extrapolations, and uncertainties. A detailed comparison of the  $K$ - and  $R$ -matrix

approaches for  $^{12}\text{C}(\alpha, \gamma)^{16}\text{O}$  has been given by Azuma *et al.* (1994). A disadvantage of the  $K$ -matrix method is that the background remaining in addition to the explicitly included levels has a complicated and generally uncertain functional form, including the possibility of subthreshold poles (echo poles) and complex-energy poles; see Barker (1994b), Brune (1996), and Humblet, Csötò, and Langanke (1998). The situation is much clearer in the  $R$ -matrix approach, where the remaining background can consist only of real pole terms at higher energies.

Recently, several researchers have investigated new approaches for obtaining bound-state ANC’s from elastic scattering data (Safronov, 2009; Sparenberg, Capel, and Baye, 2010; König, Lee, and Hammer, 2013), but it is not clear if these methods offer any advantages over the phenomenological  $R$ -matrix approach.

With these considerations, a phenomenological  $R$ -matrix approach will be used to interpret the experimental data and perform the interpolation and extrapolation of the  $^{12}\text{C}(\alpha, \gamma)^{16}\text{O}$  cross section over the entire range of astrophysical interest. The following section details the critical aspects of this theoretical framework.

## IV. R-MATRIX THEORY

Since the first analysis of the  $^{12}\text{C}(\alpha, \gamma)^{16}\text{O}$  reaction by Barker (1971),  $R$ -matrix theory has been used to model the experimental data. Over the intervening years many different approaches have been used (see Table IV), but for the reasons discussed, the  $R$  matrix has been the most common method and is the choice adopted for the present analysis. In many previous works, the  $R$ -matrix formalism has been specialized to the  $^{12}\text{C}(\alpha, \gamma)^{16}\text{O}$  case in order to simplify the formulas. In this more global analysis, that considers several other reaction partitions in addition to  $^{12}\text{C} + \alpha$  and  $^{16}\text{O} + \gamma$ , the complete formalism is required. Sections IV.A–IV.E cover the  $R$ -matrix theory in a general manner, keeping in mind that the  $R$ -matrix approach is a useful tool for many applications besides the phenomenological analysis of nuclear reactions. Section IV.F discusses considerations that are specific to the phenomenological analysis of nuclear reaction data and finally Sec. IV.G covers our specific application to  $^{12}\text{C}(\alpha, \gamma)^{16}\text{O}$ .

### A. General $R$ -matrix theory

$R$ -matrix theory has been explained in detail in previous reviews (Lane and Thomas, 1958; Hale and Dodder, 1980; Azuma *et al.*, 2010; Descouvemont and Baye, 2010), and only certain details will be described here. For the most part, we utilize the approach and notation of Lane and Thomas (1958) (LT); an important alternative is the Bloch operator formalism (Bloch, 1957; Lane and Robson, 1966).

The most basic premise of  $R$ -matrix theory divides the nuclear configuration space into two distinct regions: the nuclear interior where the many-body nuclear interactions are complicated, and the exterior where it is assumed there are two clusters in each channel that can be treated as separate and noninteracting (except for the Coulomb potential). Channels are assumed to be orthogonal and are labeled by the indices  $\alpha s \equiv c$ , where  $\alpha$  defines a particular pair of nuclei,  $s$  is the

coupled spin (channel spin) of the pair, and  $l$  is the relative orbital angular momentum. We work in the nuclear center-of-mass system; the quantities  $\mu_\alpha$ ,  $k_\alpha$ ,  $v_\alpha$ , and  $r_\alpha$  are the reduced mass, wave number, relative velocity, and radial separation for pair  $\alpha$ . Channel spin wave functions are defined by

$$|\psi\rangle_{\alpha\nu} = [|\psi\rangle_{\alpha 1} \otimes |\psi\rangle_{\alpha 2}]_{\nu}, \quad (8)$$

where  $|\psi\rangle_{\alpha 1}$  and  $|\psi\rangle_{\alpha 2}$  are the internal wave functions of the nuclei 1 and 2 making up pair  $\alpha$ , and  $\nu$  is the channel spin projection.

For each channel, the dividing surface between the regions is taken to be a sphere of radius  $r_\alpha = a_c$ . This radius is known as the *channel radius* and may be different for different channels. It is convenient to utilize the ‘‘channel surface functions’’ introduced by Hale and Dodder (1980) which have total angular momentum  $J$  with component  $M$ :

$$|\mathcal{S}cJM\rangle = \left(\frac{\hbar^2}{2\mu_\alpha a_c}\right)^{1/2} \frac{\delta(r_\alpha - a_c)}{a_c} [|\psi\rangle_{\alpha\nu} \otimes i^l Y_{lm}(\hat{r}_\alpha)]_{JM}, \quad (9)$$

where  $Y_{lm}$  are the spherical harmonics. These functions can be used to project a total wave function into a well-defined angular momentum state on a particular channel surface.

In the internal region, we take the basis vectors  $|\lambda JM\rangle$  to be the solutions to the nuclear Hamiltonian with energy eigenvalues  $E_\lambda$  that satisfy boundary conditions (LT, Eq. V.2.1)

$$\langle \mathcal{S}cJM | \frac{\partial}{\partial r_\alpha} r_\alpha | \lambda JM \rangle = B_c \langle \mathcal{S}cJM | \lambda JM \rangle, \quad (10)$$

where  $B_c$  are real energy-independent boundary condition constants. They are orthogonal and normalized over the internal region such that

$$\langle \lambda' J' M' | \lambda JM \rangle = \delta_{\lambda\lambda'} \delta_{J'J} \delta_{M'M}. \quad (11)$$

They are also understood to be complete, provided that all basis vectors satisfying the boundary condition (an infinite number) are included. Under time reversal these basis vectors transform according to (LT, Eq. III.3.4)

$$K|\lambda JM\rangle = (-1)^{J-M} |\lambda J - M\rangle, \quad (12)$$

where  $K$  is the time-reversal operator. The real  $M$ -independent reduced-width amplitudes are given by (LT, Eq. III.4.8a)

$$\gamma_{\lambda c J} = \langle \mathcal{S}cJM | \lambda JM \rangle, \quad (13)$$

i.e., by the amplitude of the eigenfunction at the nuclear surface.

In the external region wave functions can be expressed in terms of (LT, Eq. III.2.19)

$$|\mathcal{I}cJM\rangle = \frac{I_{\alpha l}(r_\alpha)}{v_\alpha^{1/2} r_\alpha} [|\psi\rangle_{\alpha\nu} \otimes i^l Y_{lm}(\hat{r}_\alpha)]_{JM}, \quad (14a)$$

$$|\mathcal{O}cJM\rangle = \frac{O_{\alpha l}(r_\alpha)}{v_\alpha^{1/2} r_\alpha} [|\psi\rangle_{\alpha\nu} \otimes i^l Y_{lm}(\hat{r}_\alpha)]_{JM}, \quad (14b)$$

where the incoming and outgoing Coulomb functions  $I_{\alpha l}$  and  $O_{\alpha l}$  are defined by LT, Eq. III.2.13. For closed channels the outgoing solution  $O_{\alpha l}$  is taken to be the exponentially decaying Whittaker function (LT, Eq. III.2.17) and  $v_\alpha$  for negative energies is a positive real quantity as defined by LT (Sec. III.1). In addition one defines

$$L_c = \left(\frac{r_\alpha}{O_{\alpha l}} \frac{\partial O_{\alpha l}}{\partial r_\alpha}\right)_{a_c} = S_c + iP_c, \quad (15)$$

where the shift factor  $S_c$  and penetration factor  $P_c$  are real quantities. Other Coulomb surface quantities are given by  $O_c = O_{\alpha l}(a_c)$ ,  $I_c = I_{\alpha l}(a_c)$ , and  $\Omega_c = (I_c/O_c)^{1/2}$ . The relative Coulomb phase shift  $\omega_{\alpha l}$  is defined by LT, Eq. III.2.13c. From this point forward, we suppress the angular momentum labels  $J$  and  $M$  where it introduces no ambiguity and denote  $|\mathcal{S}cJM\rangle$  by  $|c\rangle$  in order to simplify the presentation.

By expanding an arbitrary wave function  $|\Psi\rangle$  in the internal region in terms of the basis  $|\lambda\rangle$  and applying Green’s theorem, it can be shown (LT, Eq. V.2.7) that

$$\langle c | \Psi \rangle_{\text{int}} = \sum_{c'} R_{cc'} \langle c' | \frac{\partial}{\partial r_{c'}} r_{c'} - B_{c'} | \Psi \rangle_{\text{int}}, \quad (16)$$

where  $R_{cc'}$  are elements of the  $\mathbf{R}$  matrix. It is a function of the energy  $E$  and can be expressed in terms of the reduced-width amplitudes and energy eigenvalues as

$$R_{c'c} = \sum_{\lambda} \frac{\gamma_{\lambda c'} \gamma_{\lambda c}}{E_\lambda - E}. \quad (17)$$

Essentially,  $\mathbf{R}$  defines the logarithmic derivative of the radial wave function at the channel surface(s) as a function of energy.

The general wave function  $|\Psi\rangle$  may be expanded in the external region (i.e., outside the channel radii) via

$$|\Psi\rangle_{\text{ext}} = \sum_{cJM} z_{cJM} \left[ |\mathcal{I}cJM\rangle - \sum_{c'} U_{c'c}^J |\mathcal{O}c'JM\rangle \right], \quad (18)$$

where the expansion coefficients  $z_{cJM}$  specify the incoming flux which can only be nonzero for open channels and  $U_{c'c}$  are elements of the scattering matrix  $\mathbf{U}$  (also called the collision matrix). By evaluating  $\langle c | \Psi \rangle_{\text{ext}}$  and  $\langle c | (\partial/\partial r_\alpha) r_\alpha | \Psi \rangle_{\text{ext}}$  and comparing the results to Eq. (16) considering the continuity of the logarithmic radial derivative at the channel radius,  $\mathbf{U}$  can be related to  $\mathbf{R}$  and the external Coulomb functions evaluated at the channel radii. The result is (LT, Eqs. VII.1.5 and VII.1.6a)

$$U = \Omega\{\mathbf{1} + 2i\mathbf{P}^{1/2}[\mathbf{I} - \mathbf{R}(\mathbf{L} - \mathbf{B})]^{-1}\mathbf{R}\mathbf{P}^{1/2}\}\Omega, \quad (19)$$

where  $\Omega$ ,  $\mathbf{P}$ ,  $\mathbf{L}$ , and  $\mathbf{B}$  are purely diagonal with elements  $\Omega_c$ ,  $P_c$ ,  $L_c$ , and  $B_c$ , respectively;  $\mathbf{1}$  is the unit matrix. Alternatively, the elements of the scattering matrix can be expressed as

$$U_{c'c} = \Omega_{c'}\Omega_c \left[ \delta_{c'c} + 2i(P_{c'}P_c)^{1/2} \sum_{\lambda\mu} A_{\lambda\mu} \gamma_{\lambda c'} \gamma_{\mu c} \right], \quad (20)$$

where  $A_{\lambda\mu}$  are elements of the level matrix  $\mathbf{A}$  that is defined in level space by its inverse

$$[\mathbf{A}^{-1}]_{\lambda\mu} = (E_\lambda - E)\delta_{\lambda\mu} - \sum_c \gamma_{\lambda c} \gamma_{\mu c} (L_c - B_c). \quad (21)$$

We also define a matrix  $\mathbf{M}$  that is closely related to the scattering matrix  $\mathbf{U}$ :

$$U = \Omega[\mathbf{1} + 2i\mathbf{P}^{1/2}\mathbf{M}\mathbf{P}^{1/2}]\Omega, \quad (22)$$

$$M_{c'c} = \{[\mathbf{1} - \mathbf{R}(\mathbf{L} - \mathbf{B})]^{-1}\mathbf{R}\}_{c'c} \quad (23)$$

$$= \sum_{\lambda\mu} A_{\lambda\mu} \gamma_{\lambda c'} \gamma_{\mu c}. \quad (24)$$

The matrix  $\mathbf{M}$  may be interpreted physically as the projection of the outgoing-wave Green's function onto the channel surfaces [(Lane and Robson, 1966, Eq. (65)].

If the scattering matrix is diagonal, the nuclear phase shifts  $\delta_c$  may be defined via

$$U_{cc} = e^{2i\delta_c}. \quad (25)$$

The  $\Omega_{c'}\Omega_c\delta_{c'c}$  term provides a so-called hard-sphere contribution to  $U_{c'c}$ ; it is present only for elastic scattering. While the phase shift corresponding to this term is mathematically identical to that resulting from an infinite repulsive core at the channel radius, one should avoid placing too much physical significance on it since the total phase shift has contributions both from this term and from the  $\mathbf{R}$  matrix. Note also that the hard-sphere term is present even if the nuclear interactions vanish.

The solution corresponding to Eq. (18) in the internal region can be found using (LT, Eq. IX.1.31)

$$|\Psi\rangle_{\text{int}} = -i \sum_{cJM} \Omega_c (2\hbar P_c)^{1/2} z_{cJM} \sum_{\lambda\mu} A_{\lambda\mu} \gamma_{\mu c} |\lambda JM\rangle. \quad (26)$$

With the particular choice

$$z_{\xi JM} = i \left[ \frac{\pi\hbar(2l+1)}{\mu_\alpha k_\alpha} \right]^{1/2} (s\nu 0 | JM), \quad (27)$$

where  $\xi \equiv \alpha s l$  and  $z_{cJM} = 0$  for  $c \neq \xi$ ,  $|\Psi\rangle_{\text{ext}}$  is asymptotically equal to  $\exp[i\{k_\alpha z_\alpha + \eta_\alpha \log k(r_\alpha - z_\alpha)\}] |\psi\rangle_{\alpha s \nu}$  plus outgoing waves. In this case, noting that  $\mathbf{M} = \nu$  only,  $|\Psi\rangle$  becomes

$$|\alpha s \nu\rangle_{\text{ext}} = \sum_{IJ} i \left[ \frac{\pi\hbar(2l+1)}{\mu_\alpha k_\alpha} \right]^{1/2} (s\nu 0 | J\nu) \times \left[ \mathcal{I}_\xi J\nu - \sum_c U_{c\xi}^J |\mathcal{O}c J\nu\rangle \right], \quad (28a)$$

$$|\alpha s \nu\rangle_{\text{int}} = \sum_{IJ} \hbar \Omega_\xi \left[ \frac{2\pi P_\xi(2l+1)}{\mu_\alpha k_\alpha} \right]^{1/2} (s\nu 0 | J\nu) \sum_{\lambda\mu} A_{\lambda\mu} \gamma_{\mu\xi} |\lambda J\nu\rangle. \quad (28b)$$

The wave function  $|\alpha s \nu\rangle$  corresponds to an incident plane wave in partition  $\alpha$  with channel spin  $s$  and projection  $\nu$ ; the asymptotic form of Eq. (28a) may be used to define scattering amplitudes. These equations are also useful for calculating radiative capture in perturbation theory, as described later. In addition, the plane wave states can be expressed in terms of partial waves:

$$|\alpha s \nu\rangle = \frac{i\pi^{1/2}}{k_\alpha} \sum_{IJ} (2l+1)^{1/2} (s\nu 0 | J\nu) |\alpha s l J\nu\rangle, \quad (29)$$

where the internal and external representations of  $|\alpha s l J\nu\rangle$  can be read off by inspection of Eq. (28).

For the calculation of observables, formulas from general reaction theory may be utilized. Defining the transition matrix to be

$$T_{c'c} = e^{2i\omega_c} \delta_{c'c} - U_{c'c}, \quad (30)$$

the angle-integrated cross section can then be computed via (LT, Eq. VIII.3.2b)

$$\sigma_{\alpha\alpha'} = \frac{\pi}{k_\alpha^2} \sum_{JlJ's's'} g_J |T_{c'c}|^2, \quad (31)$$

where the case of elastic scattering of charged particles is excluded. The statistical factor is given by

$$g_J = \frac{2J+1}{(2J_{\alpha 1}+1)(2J_{\alpha 2}+1)}, \quad (32)$$

where  $J_{\alpha 1}$  and  $J_{\alpha 2}$  are the individual particle spins for the pair  $\alpha$ .

While the angle integrated cross section is related in a rather simple way to the transition matrix via Eq. (30), the unpolarized differential cross section takes on a more complicated form because different partial waves may interfere:

$$\frac{d\sigma_{\alpha\alpha'}}{d\Omega_{\alpha'}} = \frac{1}{(2J_{\alpha 1}+1)(2J_{\alpha 2}+1)} \sum_{s's'} (2s+1) \frac{d\sigma_{\alpha s, \alpha' s'}}{d\Omega_{\alpha'}}, \quad (33)$$

where

$$\begin{aligned}
 & (2s+1) \frac{k_\alpha^2}{\pi} \frac{d\sigma_{\alpha s, \alpha' s'}}{d\Omega_{\alpha'}} \\
 &= (2s+1) |C_{\alpha'}(\theta_{\alpha'})|^2 \delta_{\alpha s, \alpha' s'} \\
 &+ \frac{1}{\pi} \sum_L B_L(\alpha s, \alpha' s') P_L(\cos \theta_{\alpha'}) + \delta_{\alpha s, \alpha' s'} (4\pi)^{-1/2} \\
 &\times \sum_{Jl} (2J+1) 2\text{Re}[i(T_{c'c}^J)^* C_{\alpha'}(\theta') P_l(\cos \theta_{\alpha'})], \quad (34)
 \end{aligned}$$

with

$$\begin{aligned}
 B_L(\alpha s, \alpha' s') &= \frac{(-1)^{s-s'}}{4} \sum_{J_1 J_2 l_1 l_2 l_1' l_2'} \bar{Z}(l_1 J_1 l_2 J_2, sL) \\
 &\times \bar{Z}(l_1' J_1' l_2' J_2', s'L) (T_{\alpha' s' l_1', \alpha s l_1}^{J_1}) (T_{\alpha' s' l_2', \alpha s l_2}^{J_2})^* \quad (35)
 \end{aligned}$$

and

$$\begin{aligned}
 \bar{Z}(l_1 J_1 l_2 J_2, sL) &= [(2l_1+1)(2l_2+1)(2J_1+1)(2J_2+1)]^{1/2} \\
 &\times (l_1 l_2 00 | L 0) W(l_1 J_1 l_2 J_2; sL). \quad (36)
 \end{aligned}$$

Here the  $P_L(\cos \theta_\alpha)$  are the Legendre polynomials and  $W$  is the Racah coefficient. The  $C_\alpha(\theta_\alpha)$  are the Coulomb amplitudes that are present only for charged-particle elastic scattering. They are given by

$$C_\alpha(\theta_\alpha) = (4\pi)^{-1/2} \eta_\alpha \csc^2\left(\frac{\theta_\alpha}{2}\right) \times \exp\left\{-2i\eta_\alpha \ln\left[\sin\left(\frac{\theta_\alpha}{2}\right)\right]\right\}, \quad (37)$$

where  $\eta_\alpha$  is the Sommerfeld parameter for the partition  $\alpha$ . The differential cross section for polarized particles, which is not utilized in this analysis, can be found in [Patz gen. Schieck \(2012\)](#), for example.

## B. Physical interpretation of the $R$ -matrix parameters

Following [Thomas \(1951\)](#), it is instructive to make a one level approximation to the level matrix  $A$ . This leads (ignoring the hard-sphere contribution if  $c = c'$ ) to

$$|T_{cc'}|^2 = \frac{\Gamma_{\lambda c} \Gamma_{\lambda c'}}{(E_\lambda - E + \Delta_\lambda)^2 + (1/4)(\sum_{c''} \Gamma_{\lambda c''})^2}, \quad (38)$$

where  $\Gamma_{\lambda c} = 2P_c \tilde{\gamma}_{\lambda c}^2$  is the formal partial width for channel  $c$  and  $\Delta_\lambda$  is the energy-dependent level shift:

$$\Delta_\lambda = -\sum_c \tilde{\gamma}_{\lambda c}^2 [S_c(E) - B_c]. \quad (39)$$

This form is functionally quite similar to the expression of [Breit and Wigner \(1936\)](#) for a single resonance level, with the exception of the level shift. Considering that the boundary condition constants  $B_c$  are arbitrary real parameters, the correspondence to the Breit-Wigner formula may be made closer by choosing

$$B_c = S_c(E_\lambda), \quad (40)$$

i.e., such that the level shift vanishes at  $E_\lambda$ . In this situation, we may associate  $E_\lambda$  with the resonance energy. When the boundary conditions satisfy Eq. (40), we denote the corresponding  $R$ -matrix parameters with tildes, i.e., as  $\tilde{E}_\lambda$  and  $\tilde{\gamma}_{\lambda c}$ .

Further following [Thomas \(1951\)](#), one may make a linear approximation to the level shift

$$\Delta_\lambda \approx (\tilde{E}_\lambda - E) \sum_c \tilde{\gamma}_{\lambda c}^2 \frac{dS_c}{dE}(\tilde{E}_\lambda) \quad (41)$$

and Eq. (38) becomes (LT, Eq. VII.3.2)

$$|T_{cc'}|^2 = \frac{\tilde{\Gamma}_{\lambda c} \tilde{\Gamma}_{\lambda c'}}{(\tilde{E}_\lambda - E)^2 + (1/4)(\sum_{c''} \tilde{\Gamma}_{\lambda c''})^2}, \quad (42)$$

where (LT, Eqs. XII.3.5 and XII.3.6)

$$\tilde{\Gamma}_{\lambda c} = \frac{2P_c \tilde{\gamma}_c^2}{1 + \sum_{c''} \tilde{\gamma}_{\lambda c''}^2 (dS_{c''}/dE)(\tilde{E}_\lambda)}. \quad (43)$$

With this definition, Eq. (42) is now formally identical to the Breit-Wigner expression. One may expect the Breit-Wigner formula to be a particularly good approximation to  $R$ -matrix theory in the case of an isolated narrow resonance, such that the importance of other resonances and any nonlinear energy dependence of  $S_c(E)$  is minimal.

The partial width for decay into channels which are closed (or bound) is zero. In this case, one defines instead the ANC, which are real quantities that can be related to the reduced width via (LT, Eqs. IV.7.1–IV.7.4), [([Barker, 1995](#)), Eqs. (8) and (16)], [([Mukhamedzhanov and Tribble, 1999](#)), Eqs. (60) and (63)]

$$C_{\lambda c} = \frac{(2\mu_\alpha a_c)^{1/2}}{\hbar W_c(a_c)} \frac{\tilde{\gamma}_{\lambda c}}{[1 + \sum_{c''} \tilde{\gamma}_{\lambda c''}^2 (dS_{c''}/dE)(\tilde{E}_\lambda)]^{1/2}}, \quad (44)$$

where  $W_c(a_c)$  is the exponentially decaying Whittaker function evaluated at the channel radius. Note that the square of this equation  $C_{\lambda c}^2$  is very similar in structure to Eq. (43) that describes the partial widths in unbound channels. If the level in question is bound in all channels, it can be shown (LT, Eq. A.29) that the factor of

$$\left[1 + \sum_{c''} \tilde{\gamma}_{\lambda c''}^2 \frac{dS_{c''}}{dE}(\tilde{E}_\lambda)\right]^{1/2}$$

in the denominator of Eq. (44) is exactly what is required to change the normalization volume of the eigenfunction from the interior region [see Eq. (11)] to all space.

Based on the correspondence of Eq. (42) to the Breit-Wigner formula, the quantities  $\tilde{E}_\lambda$  and  $\tilde{\Gamma}_{\lambda c}$  previously defined are often called the observed resonance energy and partial widths corresponding to an  $R$ -matrix level; in addition, [Azuma \*et al.\* \(2010\)](#) used the terminology ‘‘physical  $R$ -matrix

parameters” for  $\tilde{E}_\lambda$  and  $\tilde{\gamma}_{\lambda c}$ . The reader is cautioned, however, that many conventions have been used in the past to define “resonance energies” and “partial widths.” Some workers also go on to define “observed” reduced widths, which provides an additional opportunity for confusion (such parameters are not used in this work). In addition,  $\tilde{E}_\lambda$  and  $\tilde{\Gamma}_{\lambda c}$  are somewhat dependent upon the channel radius that is used. A more fundamental and unambiguous definition of resonance energies and partial widths is provided by the poles and residues of the scattering matrix which may be extracted from an  $R$ -matrix parametrization (Hale, Brown, and Jarmie, 1987). This approach brings with it complications, including the fact that these poles and residues are generally complex quantities. However, for the case of a bound state, the relation is simple:  $\tilde{E}_\lambda$  is a pole of the scattering matrix and its residues are proportional to  $C_{\lambda c} C_{\lambda c'}$ .

In order to give a more intuitive measure of the strength of the reduced width, it is often divided by the Wigner limit (Wigner and Eisenbud, 1947) to give the dimensionless reduced width

$$\theta_{\lambda c}^2 = \frac{\tilde{\gamma}_{\lambda c}^2}{\gamma_{\text{W}}^2}, \quad (45)$$

where

$$\gamma_{\text{W}}^2 = \frac{3}{2} \frac{\hbar^2}{\mu_\alpha a_c^2} \quad \text{or} \quad \frac{\hbar^2}{\mu_\alpha a_c^2} \quad (46)$$

is the Wigner limit. Unfortunately different conventions have been used for the Wigner limit that has led to some confusion in the literature. The quantity  $\gamma_{\text{W}}^2$  may be thought of as a crude estimate for the reduced width corresponding to a “single-particle” assumption for channel  $c$ . Consequently,  $\theta_{\lambda c}^2$  is similar to the spectroscopic factor and can be interpreted physically as a dimensionless measure of the strength of a level relative to the single-particle case. We generally avoid the use of  $\theta_{\lambda c}^2$  in this work because of its ambiguous definition and dependence on channel radius. We have, however, included some discussion in order to allow comparison with previous work.

### C. Parameter transformations

The tilde notation implies that the parameters are relative to the choice of boundary condition given by Eq. (40), i.e., that the level shift vanishes at the resonance energy. It is only for this choice of  $B_c$  that the  $R$ -matrix parameters have a simple physical interpretation. Since the  $B_c$  are energy independent, this implies that only one level of a given spin and parity can satisfy Eq. (40) and thus the parameters corresponding to other levels will not have a simple physical interpretation. Barker (1972) showed that the scattering matrix is invariant with respect to changes in the  $B_c$ , provided the  $R$ -matrix parameters are adjusted using a transformation that was also given. That this result holds even when the number of levels is finite is rather remarkable and unexpected and is the likely reason why it took nearly 30 years after the formulation of  $R$ -matrix theory for this to be noticed. It is possible via iterative searching to

find the transformations which yield Eq. (40) for all channels simultaneously and thus deduce a physical interpretation for all of the levels.

Brune (2002) showed that the number of independent transformations yielding Eq. (40) in all channels is equal to the original number of  $R$ -matrix levels, provided that  $dS_c/dE > 0$  (which appears to be true in practice, although it remains in general unproven). This work further showed that the  $R$ -matrix formalism could be cast in a form such that the scattering matrix is given directly in terms of the  $\tilde{E}_\lambda$  and  $\tilde{\gamma}_{\lambda c}$  for all of the levels. In this approach, the  $B_c$  do not appear and all of the parameters have a simple physical interpretation. We call  $\tilde{E}_\lambda$  and  $\tilde{\gamma}_{\lambda c}$  the alternative  $R$ -matrix parameters. The alternative level matrix may be defined via

$$\begin{aligned} (\tilde{A}^{-1})_{\lambda\mu} &= (\tilde{E}_\lambda - E)\delta_{\lambda\mu} - \sum_c \tilde{\gamma}_{\lambda c} \tilde{\gamma}_{\mu c} (S_c + iP_c) \\ &+ \sum_c \begin{cases} \tilde{\gamma}_{\lambda c}^2 S_{\lambda c} & \lambda = \mu, \\ \tilde{\gamma}_{\lambda c} \tilde{\gamma}_{\mu c} \frac{S_{\lambda c}(E - \tilde{E}_\mu) - S_{\mu c}(E - \tilde{E}_\lambda)}{E_\lambda - E_\mu} & \lambda \neq \mu, \end{cases} \quad (47) \end{aligned}$$

where  $S_{\lambda c} \equiv S_c(\tilde{E}_\lambda)$ . The  $M$  matrix, which via Eq. (22) determines the scattering matrix and thus the observables, is then given by

$$M_{c'c} = \sum_{\lambda\mu} \tilde{A}_{\lambda\mu} \tilde{\gamma}_{\lambda c'} \tilde{\gamma}_{\mu c}. \quad (48)$$

It is important to note that this formalism is mathematically equivalent to the original  $R$ -matrix theory. This approach is used exclusively in the present analysis.

### D. Radiative capture

$R$ -matrix theory as described does not include reactions involving photons and the channel label  $c$  used in the previous equations do not include such channels. As is the case for most theoretical treatments, we include photon channels in  $R$ -matrix calculations via perturbation theory, where the transition matrix is given by the matrix element of the electromagnetic interaction Hamiltonian evaluated between initial and final nuclear states. The interaction Hamiltonian is decomposed into a sum of transition operators corresponding to particular multipoles which are classified as electric ( $EL$ ) or magnetic ( $ML$ ). The  $R$ -matrix formalism is then used to define the nuclear states. We assume here that the final state is bound in all nuclear decay channels, although an extension to unbound final states is possible. The matrix elements can be evaluated in coordinate space by separately considering the contributions from inside and outside the channel radii of the initial scattering state. In the internal region, the key quantities are the matrix elements of the transition operators between the  $R$ -matrix basis states  $|\lambda\rangle$  and the final state, which are defined to be the (internal) reduced widths for photons. In the external region, the Coulomb functions can be used for both the initial and final state. Importantly, a bound final state may be parametrized completely in the external region by its ANCs. In the external region, we consider only electric transitions and utilize the simple Siegert form of the transition

operators in the long-wavelength approximation. This contribution to the transition matrix has been traditionally referred to as *external capture* and depends only on the  $R$ -matrix parameters for nuclear channels and the final-state ANCs.

There are different nomenclatures that have been used in the literature to describe the direct (one-step) process that can occur for a capture reaction. Since this has led to considerable confusion, a moment is taken here to better define the terminology surrounding the direct capture process. In this work “direct capture” always refers to transitions from an initial state to a final state in a nonresonant manner, where no obvious intermediate compound nucleus resonance is populated. It does not refer to any particular model, including the direct capture model developed by Rolfs (1973). In fact, it should be noted that Rolfs (1973) made a careful distinction between the direct capture model that was being used and the more general concept of a direct capture process. From a quantum-mechanical point of view there is no completely unambiguous way to separate resonant and nonresonant processes, which implies that the concept of direct capture is likewise somewhat ambiguous. In the  $R$ -matrix approach, the physical process of direct capture is described by a combination of external capture and background poles. From this point of view, the ambiguity is related to the somewhat arbitrary choice of channel radius, which affects the strength of background poles and the division between internal and external capture. Another point which has caused confusion is that direct capture is not synonymous with external capture in the  $R$ -matrix approach where resonances also contribute to external capture. However, the two concepts do have considerable overlap and much of the important early work in this area used direct capture models that included only external capture (or extranuclear capture) (Christy and Duck, 1961; Tombrello and Parker, 1963).

The importance of external radiative capture in the  $R$ -matrix approach was first considered by Thomas (1952). The general formalism was presented by Azuma *et al.* (2010), which is based upon the work of Lane and Thomas (1958), Lane and Lynn (1960), Lynn (1968), Holt *et al.* (1978), Barker and Kajino (1991), and Angulo and Descouvemont (2001). We largely follow Azuma *et al.* (2010) which employs the general notation of Barker and Kajino (1991) but utilizes ANCs to parametrize the strength of the final states.

We utilize the label  $p \equiv \epsilon L \lambda_f$  for photon channels, where  $\epsilon$  indicates the transition type ( $\epsilon = 0$  for magnetic,  $\epsilon = 1$  for electric),  $L$  is the multipolarity, and  $\lambda_f$  characterizes the final nuclear state by its total angular momentum  $J_f$ , parity, energy, and possibly its ANCs. Note that  $\lambda_f$  is analogous to the label  $\alpha$  used for nuclear partitions.

The differential radiative capture cross section may be calculated in first-order perturbation theory via (Knutson, 1999)

$$\frac{d\sigma_{\alpha \rightarrow \lambda_f}}{d\Omega_\gamma} = \frac{k_\gamma}{2\pi \hbar v_\alpha} \frac{1}{(2J_{\alpha 1} + 1)(2J_{\alpha 2} + 1)} \times \sum_{svqM_f} |\langle \lambda_f M_f | H_e(\vec{k}_\gamma, q) | \alpha s \nu \rangle|^2, \quad (49)$$

where  $|\lambda_f M_f\rangle$  is the final-state wave function with total angular momentum projection  $M_f$ ;  $\vec{k}_\gamma$  is the photon wave vector with magnitude  $k_\gamma = (E - E_f)/\hbar c$  with  $E_f$  the final-state energy;  $H_e(\vec{k}_\gamma, q)$  is the photon emission Hamiltonian, with  $q$  the photon circular polarization; and  $|\alpha s \nu\rangle$  are plane wave states with outgoing boundary conditions, normalized to unit magnitude, and are described within the  $R$ -matrix approach by Eq. (28). The final-state wave function is normalized over all space such that  $\langle \lambda_f M_f | \lambda_f M_f \rangle = \delta_{M_f M_f'}$  and it behaves under time reversal according to

$$K|\lambda_f M_f\rangle = (-1)^{J_f - M_f} |\lambda - M_f\rangle. \quad (50)$$

The photon emission Hamiltonian is given by  $H_e(\vec{k}_\gamma, q) = [H_a(\vec{k}_\gamma, q)]^\dagger$ , where  $H_a(\vec{k}_\gamma, q)$  is the photon absorption Hamiltonian (Rose and Brink, 1967; Knutson, 1999; Dohet-Eraly and Baye, 2013)

$$H_a(\vec{k}_\gamma, q) = -\sum_{\epsilon L \mu} q^{1-\epsilon} \alpha_{\epsilon L} \mathcal{M}_\mu^{\epsilon L} D_{\mu q}^L(-\phi_\gamma, -\theta_\gamma, 0), \quad (51)$$

with

$$\alpha_{\epsilon L} = -\left[ \frac{2\pi(L+1)(2L+1)}{L} \right]^{1/2} \frac{i^{L+1-\epsilon} k_\gamma^L}{(2L+1)!!}. \quad (52)$$

Here  $D_{\mu q}^L$  is the Wigner rotation matrix,  $\theta_\gamma$  and  $\phi_\gamma$  describe the photon emission angles,  $\mathcal{M}_\mu^{\epsilon L}$  are the multipole operators, and  $\mu$  is the projection of  $L$ .

The transition matrix connecting nuclear and photon channels may be defined as

$$T_{c \rightarrow p}^J = \left[ \frac{8\pi(L+1)}{\hbar v_\alpha L} \right]^{1/2} \frac{k_\gamma^{L+1/2}}{(2L+1)!!} \langle \alpha s I J || i^{L+1-\epsilon} \mathcal{M}^{\epsilon L} || \lambda_f \rangle^*, \quad (53)$$

where the definition of the reduced matrix element is

$$\begin{aligned} & \langle \alpha s I J M || i^{L+1-\epsilon} \mathcal{M}_\mu^{\epsilon L} || \lambda_f M_f \rangle \\ & \equiv (L J_f \mu M_f | J M) \langle \alpha s I J || i^{L+1-\epsilon} \mathcal{M}^{\epsilon L} || \lambda_f \rangle, \end{aligned} \quad (54)$$

and  $|\alpha s I J \nu\rangle$  are the partial-wave components of  $|\alpha s \nu\rangle$  defined by Eq. (29). With this definition of the transition matrix, the angle-integrated radiative capture cross section corresponding to Eq. (49) can be written as

$$\sigma_{\alpha \rightarrow \lambda_f} = \frac{\pi}{k_\alpha^2} \sum_{J L S L_e} g_J |T_{c \rightarrow p}^J|^2, \quad (55)$$

which is analogous to Eq. (31) for the cross section connecting nuclear partitions. The expression for the differential cross section in terms of  $T_{c \rightarrow p}^J$  is given by Eq. (36) of Azuma *et al.* (2010).

We now specify our approach to  $R$ -matrix theory, where the internal and external contributions to the matrix element  $\langle \alpha s I J || \mathcal{M}^{\epsilon L} || \lambda_f \rangle$  are considered separately and we can define

the total transition matrix to be the sum of internal and external contributions:

$$T_{c \rightarrow p}^J = T_{c \rightarrow p}^J(\text{int}) + T_{c \rightarrow p}^J(\text{ext}). \quad (56)$$

Using Eqs. (28b) and (29) the internal contribution to the matrix element is given by

$$\begin{aligned} \langle \lambda_f || i^{L+1-\epsilon} \mathcal{M}^{\epsilon L} || \alpha s l J \rangle_{\text{int}}^* &= -i\Omega_c (2\hbar v_\alpha P_c)^{1/2} \\ &\times \sum_{\lambda\mu} A_{\lambda\mu} \gamma_{\mu c} \langle \lambda || i^{L+1-\epsilon} \mathcal{M}^{\epsilon L} || \lambda_f \rangle_{\text{int}}^*, \end{aligned} \quad (57)$$

where the  $J$  index is suppressed on the right-hand side (rhs) and the reduced matrix element is defined as in Eq. (54). We thus have

$$T_{c \rightarrow p}^J(\text{int}) = -2i\Omega_c (P_c k_\gamma^{2L+1})^{1/2} \sum_{\lambda\mu} A_{\lambda\mu} \gamma_{\mu c} \gamma_{\lambda p}, \quad (58)$$

where the photon reduced-width amplitude is given by

$$\gamma_{\lambda p} = \left[ \frac{4\pi(L+1)}{L} \right]^{1/2} \frac{\langle \lambda || i^{L+1-\epsilon} \mathcal{M}^{\epsilon L} || \lambda_f \rangle_{\text{int}}}{(2L+1)!}. \quad (59)$$

Because of the time-reversal properties of  $|\lambda\rangle$  and  $|\lambda_f\rangle$  given by Eqs. (12) and (50), as well as of the multipole operators, these reduced-width amplitudes are real quantities (Lane and Thomas, 1958; Holt *et al.*, 1978; Knutson, 1999) and hence the complex conjugation symbol on the reduced matrix element has been dropped. We assume there is no residual photon-energy dependence of the multipole operators, as is the case for the long-wavelength approximation, such that the  $\gamma_{\lambda p}$  are constants. Note also that the form of  $T_{c \rightarrow p}^J(\text{int})$  given by Eq. (58) has the same structure as the transition matrix connecting nuclear channels, with the exception that photon channels do not contribute to  $A_{\lambda\mu}$  (or equivalently to the resonance denominators).

In the external region, explicit forms for the wave functions and multipole operators will be utilized. Here the final-state wave function is assumed to consist of two clusters in each channel and may be written as

$$|\lambda_f M_f\rangle_{\text{ext}} = \sum_c C_c \frac{W_c(r_\alpha)}{r_\alpha} [|\psi\rangle_{\alpha s l} \otimes i^l Y_{lm}(\hat{r}_\alpha)]_{J_f M_f}, \quad (60)$$

where the sum is over final-state channels  $c$ ,  $W_c(r_\alpha)$  is the Whittaker function which describes the radial dependence of the final channel  $c$ , and  $C_c$  is the ANC describing the channel's asymptotic strength.

Only the electric multipole operators will be considered in the external region. Assuming that each cluster is represented by a point charge, using the Siegert form of the operators, and making the long-wavelength approximation, the electric multipole operators in partition  $\alpha$  become

$$\mathcal{M}_\mu^{1L} = \bar{e}_\alpha^L r_\alpha^L Y_{L\mu}(\hat{r}_\alpha), \quad (61)$$

where the effective charge is

$$\bar{e}_\alpha^L = e \left[ Z_{\alpha 1} \left( \frac{M_{\alpha 2}}{M_\alpha} \right)^L + Z_{\alpha 2} \left( -\frac{M_{\alpha 1}}{M_\alpha} \right)^L \right] \quad (62)$$

with  $eZ_{\alpha i}$  and  $M_{\alpha i}$  the charges and masses of partition  $\alpha$  and  $M_\alpha = M_{\alpha 1} + M_{\alpha 2}$ . The effective charge factor plays a critical role in  $^{12}\text{C}(\alpha, \gamma)^{16}\text{O}$   $E1$  capture. Because of the nearly equal charge-to-mass ratios of  $^4\text{He}$  and  $^{12}\text{C}$  nuclei,  $\bar{e}_\alpha^L$  nearly vanishes for this case and external capture is strongly suppressed.

The external contribution to the transition matrix can now be calculated using Eqs. (28a) and (29) for the initial state, Eq. (60) for the final state, Eqs. (19) and (22) for the nuclear scattering matrix, Eq. (61) for the multipole operators, and Eq. (53) for the transition matrix. Note that matrix elements of these simple electric multipole operators vanish unless  $\alpha = \alpha_f$  and  $s = s_f$ . One thus obtains

$$\begin{aligned} T_{c \rightarrow p}^J(\text{ext}) &= -2i\Omega_c (P_c k_\gamma^{2L+1})^{1/2} \\ &\times \sum_{c'l_f} \frac{\bar{e}_{\alpha'}^L}{\hbar} (\mu_{\alpha'} a_{c'})^{1/2} V(LL_f J s'; l' J_f) C_{\alpha' s' l_f} \\ &\times [\delta_{cc'} P_c^{-1} J'_{c'l_f L} + M_{cc'} (J''_{c'l_f L} + iJ'_{c'l_f L})], \end{aligned} \quad (63)$$

where the real function  $V$  contains angular momentum factors:

$$\begin{aligned} V(LL_f J s; l J_f) &= \frac{1}{(2L+1)!} \left[ \frac{2(L+1)(2L+1)}{L} \right]^{1/2} \\ &\times i^{l+L-l_f} (iL00|l_f 0)(2l+1)^{1/2} \\ &\times (2J_f+1)^{1/2} W(LL_f J s; l J_f). \end{aligned} \quad (64)$$

When  $c$  is an open channel, the radial integrals  $J'_{c'l_f L}$  and  $J''_{c'l_f L}$  are given by

$$J'_{c'l_f L} = \int_{a_c}^{\infty} \frac{G_c(a_c) F_c(r_\alpha) - F_c(a_c) G_c(r_\alpha)}{F_c^2(a_c) + G_c^2(a_c)} W_{c_f}(r_\alpha) r_\alpha^L dr_\alpha \quad (65)$$

and

$$J''_{c'l_f L} = \int_{a_c}^{\infty} \frac{F_c(a_c) F_c(r_\alpha) + G_c(a_c) G_c(r_\alpha)}{F_c^2(a_c) + G_c^2(a_c)} W_{c_f}(r_\alpha) r_\alpha^L dr_\alpha, \quad (66)$$

where  $c_f \equiv \alpha s l_f$  and  $F_c(r_\alpha)$  and  $G_c(r_\alpha)$  are the regular and irregular Coulomb wave functions, respectively. If channel  $c$  is closed, we take  $J'_{cc_f L} = 0$  and

$$J''_{c'l_f L} = \int_{a_c}^{\infty} \frac{W_c(r_\alpha)}{W_c(a_c)} W_{c_f}(r_\alpha) r_\alpha^L dr_\alpha. \quad (67)$$

Our radial integrals are very similar to those introduced by Barker and Kajino (1991), but use a different normalization and a different convention for closed channels.

As expressed by Eq. (63), the external photon transition matrix consists of two types of terms. The first is proportional to  $\delta_{cc'} J'_{cc'L}$  and thus only receives contributions from the entrance channel. It is also nonresonant and independent of the  $R$ -matrix parameters of the nuclear channels, except for the channel radii. In addition, the radial scattering wave function in the  $J'_{cc'L}$  integral corresponds to elastic scattering by a hard sphere. For these reasons, this contribution has been called hard-sphere capture. The second term is proportional to the  $\mathbf{M}$  matrix and consequently depends on the nuclear  $R$ -matrix parameters and exhibits resonances along with the nuclear channels. This contribution has been called channel capture in the literature. Note that the division of capture strength between the internal contribution, hard-sphere capture, and channel capture is dependent upon the choice of channel radii.

It is possible to write the internal and external contributions to  $T^J_{c \rightarrow p}$  in a different form that emphasizes another aspect of the underlying physics that they share. Considering radiative captures to a particular photon channel  $p$  from nuclear channels of total spin  $J$ , we can write Eq. (58) as

$$T^J_p(\text{int}) = -2i\Omega\mathbf{P}^{1/2}k_\gamma^{L+1/2}\boldsymbol{\gamma}^T\mathbf{A}\boldsymbol{\gamma}_p, \quad (68)$$

where  $T^J_p(\text{int})$  is a column vector in channel space with elements  $T^J_{c \rightarrow p}$ ,  $\boldsymbol{\gamma}$  is a matrix (in general, rectangular) with elements  $\gamma_{\lambda c}$ ,  $\mathbf{A}$  is the level matrix defined by Eq. (21), and  $\boldsymbol{\gamma}_p$  is a column vector in level space with elements  $\gamma_{\lambda p}$ . Using the method described in the appendix of Brune (2002), Eq. (68) can also be written as

$$T^J_p(\text{int}) = -2i\Omega\mathbf{P}^{1/2}k_\gamma^{L+1/2}[\mathbf{I} - \mathbf{R}(\mathbf{L} - \mathbf{B})]^{-1}\mathbf{R}_p, \quad (69)$$

where  $\mathbf{R}_p$  is a column vector in channel space with components

$$[\mathbf{R}_p]_c = \sum_\lambda \frac{\gamma_{\lambda c}\gamma_{\lambda p}}{E_\lambda - E}. \quad (70)$$

Considering now the external region, one can define column vectors  $\mathbf{x}$  and  $\mathbf{y}$  in channel space with components

$$x_c = \sum_{l_f} \frac{\tilde{e}_\alpha^L}{\hbar} (\mu_\alpha a_c)^{1/2} V(Ll_f J_s; lJ_f) C_{\alpha sl_f} J'_{cl_f L} \quad (71)$$

and

$$y_c = \sum_{l_f} \frac{\tilde{e}_\alpha^L}{\hbar} (\mu_\alpha a_c)^{1/2} V(Ll_f J_s; lJ_f) C_{\alpha sl_f} J''_{cl_f L}. \quad (72)$$

Equation (63) can then be written as

$$\begin{aligned} T^J_p(\text{ext}) &= -2i\Omega\mathbf{P}^{1/2}k_\gamma^{L+1/2} \\ &\times \{ \mathbf{P}^{-1}\mathbf{x} + [\mathbf{I} - \mathbf{R}(\mathbf{L} - \mathbf{B})]^{-1}\mathbf{R}(\mathbf{y} + i\mathbf{x}) \} \\ &= -2i\Omega\mathbf{P}^{1/2}k_\gamma^{L+1/2}[\mathbf{I} - \mathbf{R}(\mathbf{L} - \mathbf{B})]^{-1} \\ &\times \{ [\mathbf{I} - \mathbf{R}(\mathbf{L} - \mathbf{B})]\mathbf{P}^{-1}\mathbf{x} + \mathbf{R}(\mathbf{y} + i\mathbf{x}) \}. \end{aligned} \quad (73)$$

We define  $\mathbf{P}_c^{-1}x_c \equiv 0$  for closed channels, since from Eq. (63) it is clear that these values affect only  $T^J_{c \rightarrow p}$  when  $c$  is closed,

which are channels we are not interested in. Defining  $\mathbf{S}$  to be a diagonal matrix in channel space with elements consisting of the shift function  $S_c$ , the quantity in braces in Eq. (73) simplifies to

$$\mathbf{R}_p(\text{ext}) \equiv [\mathbf{I} - \mathbf{R}(\mathbf{S} - \mathbf{B})]\mathbf{P}^{-1}\mathbf{x} + \mathbf{R}\mathbf{y}, \quad (74)$$

which is a real quantity as the complex pieces have canceled.

The total transition matrix can now be written as

$$T^J_p = -2i\Omega\mathbf{P}^{1/2}k_\gamma^{L+1/2}[\mathbf{I} - \mathbf{R}(\mathbf{L} - \mathbf{B})]^{-1}[\mathbf{R}_p + \mathbf{R}_p(\text{ext})]. \quad (75)$$

The important result is that both  $\mathbf{R}_p$  and  $\mathbf{R}_p(\text{ext})$  are real quantities, which implies the complex phases of the  $T^J_{c \rightarrow p}$  are determined entirely by Coulomb interactions and the  $R$ -matrix parameters for nuclear channels—and thus not by the photon emission Hamiltonian. Knutson (1999) pointed out that results such as this are a manifestation of Watson's theorem (Watson, 1954), which is more general than  $R$ -matrix theory. The primary assumptions required for Watson's theorem are first-order perturbation theory for photon emission and time-reversal invariance. A derivation of the analogous result for the single-channel  $R$ -matrix case was given by Barker and Kajino (1991), Eqs. (25)–(27), where the complex phase of the capture matrix element is found to be simply given by the sum of the Coulomb and nuclear elastic scattering phase shifts. As shown by Eq. (55), complex phases do not affect the total cross section. They do, however, significantly impact angular distributions, which has important implications for the  $^{12}\text{C}(\alpha, \gamma)^{16}\text{O}$  reaction, as  $\gamma$ -ray angular distributions are used to separate the  $E1$  and  $E2$  multipole transitions to the  $^{16}\text{O}$  ground state. It has been found that elastic scattering data, which can precisely fix the nuclear  $R$ -matrix parameters, are very helpful for improving the accuracy of the extracted radiative capture multipoles; see Brune (2001) and Gai (2013) for further discussion.

In the case of a narrow resonance or bound state, a single-level approximation again provides for a physical interpretation. We assume the level shift vanishes for level  $\lambda$  and consequently describe it with  $\tilde{E}_\lambda$ ,  $\tilde{\gamma}_{\lambda c}$ , and  $\tilde{\gamma}_{\lambda p}$ . We make a single-level approximation to the matrix  $\mathbf{M}$  appearing in Eq. (63) and ignore the hard-sphere capture term. The cross section can then be put into the Breit-Wigner form as shown before for nuclear channels. It is also useful to define a channel contribution to the  $\gamma$ -ray reduced-width amplitude:

$$\begin{aligned} \tilde{\gamma}_{\lambda p}(\text{ch}) &= \sum_{cl_f} \frac{\tilde{e}_\alpha^L}{\hbar} (\mu_\alpha a_c)^{1/2} V(Ll_f J_s; lJ_f) \\ &\times \gamma_{\lambda c} C_{\alpha sl_f} (J''_{cl_f L} + iJ'_{cl_f L}). \end{aligned} \quad (76)$$

The resulting partial  $\gamma$ -ray width can then be written as

$$\tilde{\Gamma}_{\lambda p} = \frac{2k_\gamma^{2L+1} |\tilde{\gamma}_{\lambda p} + \tilde{\gamma}_{\lambda p}(\text{ch})|^2}{1 + \sum_c \tilde{\gamma}_{\lambda c}^2 (dS_c/dE)(\tilde{E}_\lambda)}. \quad (77)$$

Note that  $\tilde{\gamma}_{\lambda p}$  and  $\tilde{\gamma}_{\lambda p}(\text{ch})$ , which are the internal and external contributions, are combined coherently and that  $\tilde{\gamma}_{\lambda p}(\text{ch})$  is in

general a complex quantity. We should also emphasize here that photon channels do not contribute to the total width in the denominator of the Breit-Wigner formula in this approach.

The radiative capture formalism presented is easily adapted to the alternative  $R$ -matrix parametrization. The alternative photon reduced widths  $\tilde{\gamma}_{\lambda p}$  are defined by the replacements  $\gamma_{\lambda p} \rightarrow \tilde{\gamma}_{\lambda p}$  and  $\langle \lambda | \rightarrow \langle \tilde{\lambda} |$  in Eq. (59). The internal contribution to the transition matrix is calculated using the replacement

$$\sum_{\lambda\mu} A_{\lambda\mu} \gamma_{\mu c} \gamma_{\lambda p} \rightarrow \sum_{\lambda\mu} \tilde{A}_{\lambda\mu} \tilde{\gamma}_{\mu c} \tilde{\gamma}_{\lambda p} \quad (78)$$

in Eq. (58) (Brune, 2002). For the external contribution, one needs only the  $M$  matrix, which is already defined in terms of the alternative parameters by Eq. (48).

### E. $\beta$ -delayed particle emission

As in the case of radiative capture,  $\beta$ -delayed particle spectra can be modeled in the  $R$ -matrix approach using first-order perturbation theory. General formulas were given by Barker and Warburton (1988) and formulas specific to the  $\beta$ -delayed  $\alpha$ -particle spectrum from  $^{16}\text{N}$  were given, for example, by Azuma *et al.* (1994). Note that only allowed transitions are considered, which is roughly analogous to only considering  $E1$  transitions for radiative capture. In addition, we do not consider any external contribution to the transition matrix element. Such contributions are not thought to be significant for the  $^{16}\text{N}$   $\beta$  decays, although they have been found to be important for understanding the  $\beta$ -delayed deuteron spectrum from  $^6\text{He}$  decay (F. Barker, 1994). The reader should be aware that  $\beta$  decays into unbound states have received considerably less theoretical attention, in the  $R$ -matrix context or otherwise, than radiative capture.

The rate of  $\beta$ -delayed particle decay may be written as (Barker and Warburton, 1988)

$$\frac{\ln 2}{t_{1/2}} = \int \sum_{Jc} w_c^J(E) dE, \quad (79)$$

where differential decay rate  $w_c^J$  is summed over the final-state angular momenta  $J$  and channels  $c \equiv \alpha sl$  and  $t_{1/2}$  is the partial half-life for  $\beta$ -delayed particle emission. For example, the total half-life of  $^{16}\text{N}$  is 7.13(2) s (Tilley, Weller, and Cheves, 1993), but the branching ratio for  $\beta$ -delayed  $\alpha$  emission is only  $1.2 \times 10^{-5}$ . Therefore the  $\beta$ -delayed  $\alpha$  emission half-life is  $5.9 \times 10^5$  s.

The  $w_c^J(E)$  describe the  $\beta$ -delayed particle energy spectrum (or possibly spectra) components that do not interfere. These quantities may be written in the  $R$ -matrix formalism as (Barker, 1967, 1969; Barker and Warburton, 1988)

$$w_c^J(E) = C^2 f_\beta P_c \sum_x \left| \sum_{\lambda\mu} g_{\lambda x} \gamma_{\mu c} A_{\lambda\mu} \right|^2, \quad (80)$$

where  $C^2$  is a constant factor,  $f_\beta$  is the integrated Fermi function (the  $\beta$ -decay phase space factor), and the  $g_{\lambda x}$  are the  $\beta$ -decay feeding factors. Here  $x$  is used to indicate either Fermi

or Gamow-Teller transitions. The  $J$  dependence of the  $R$ -matrix quantities  $g_{\lambda x}$ ,  $P_c$ ,  $\gamma_{\mu c}$ , and  $A_{\lambda\mu}$  on the rhs of Eq. (80) has been suppressed. Also note that the  $\beta$ -decay feeding factors are assumed here to take only real values.

In practice it is often convenient to rewrite Eq. (80) as

$$n_c^J(E) = f_\beta P_c \sum_x \left| \sum_{\lambda\mu} B_{\lambda x} \gamma_{\mu c} A_{\lambda\mu} \right|^2, \quad (81)$$

where the feeding factor is now defined to be

$$B_{\lambda x} = C(N t_{1/2} / \ln 2)^{1/2} g_{\lambda x}, \quad (82)$$

where  $n_c^J(E)$  is the number of counts per unity energy, and  $N$  is the total number of counts in the spectrum. Further variations of this formula exist in the literature, including dividing Eq. (81) by  $N$  and redefining  $B_{\lambda x}$  so that it is independent of  $N$ . In addition, some workers, such as Azuma *et al.* (1994), absorbed the reduced width  $\gamma_{\mu c}$  into the definition of the feeding factor.

In the case of  $\beta$  decay to a narrow unbound level, the single-level approximation may be used to relate the measured transition strength to the feeding factor for that level. This approximation results in a Breit-Wigner energy spectrum for the particle decay. We assume the level shift vanishes for the level  $\lambda$  and that its parameters are  $\tilde{E}_\lambda$ ,  $\tilde{\gamma}_{\lambda c}$ , and  $\tilde{B}_{\lambda x}$ . If one then ignores the energy dependences of  $f_\beta$  and  $P_c$  and assumes  $S_c$  is linear in energy, the integral over the resulting Lorentzian energy distribution can be performed analytically to obtain (Barker and Warburton, 1988)

$$(f t_{1/2})_\lambda = \frac{N_\lambda t_{1/2} [1 + \sum_c \tilde{\gamma}_{\lambda c}^2 (dS_c/dE)(\tilde{E}_\lambda)]}{\pi \sum_x |\tilde{B}_{\lambda x}|^2}, \quad (83)$$

where  $N_\lambda$  is the total number of counts observed for the transition. This formula may also be used to define  $\log(f t_{1/2})_\lambda$  values. Also note that this equation becomes exact (in the sense of the  $R$ -matrix approach) if the final state is bound; see also Appendix A of Riisager (2014) for further discussions of this topic. We utilize such calculations in this work to define the feeding factors for bound states and to compare our results with previous studies in the literature. Note also that  $\beta$ -delayed particle emission is easily implemented using the alternate  $R$ -matrix parameterization; all that is required is the replacement

$$\sum_{\lambda\mu} B_{\lambda x} \gamma_{\mu c} A_{\lambda\mu} \rightarrow \sum_{\lambda\mu} \tilde{B}_{\lambda x} \tilde{\gamma}_{\mu c} \tilde{A}_{\lambda\mu}, \quad (84)$$

where the relation of the alternative feeding factors  $\tilde{B}_{\lambda x}$  to the  $B_{\lambda x}$  is given by Brune (2002). Finally, since only Gamow-Teller transitions are allowed for  $^{16}\text{N}(\beta\alpha)^{12}\text{C}$ , we drop the  $x$  index from the labeling of the  $\beta$ -decay feeding parameters for this case.

### F. $R$ -matrix phenomenology

$R$ -matrix theory can be used for the phenomenological analysis of nuclear reaction data by adjusting the parameters to optimize the agreement with experimental data. More

specifically, this means adopting channel radii and adjusting the parameters  $E_\lambda$  and  $\gamma_{\lambda c}$  that determine the scattering matrix in nuclear channels. These parameters can also define the energies and ANC's of final states in radiative capture. If radiative capture data and/or  $\beta$ -delayed particle data are included in the analysis, then the photon reduced widths  $\gamma_{\lambda p}$  and/or the feeding factors  $B_{\lambda x}$  would also be adjusted.

One significant approximation in the phenomenological  $R$ -matrix approach is that the sums over levels must be truncated. Typically, the known levels up to a certain excitation energy are included and the remainder of the spectrum is modeled with one or more “background” pole terms for each spin and parity. This has been the standard technique for some time (Breit, 1940), but the exact implementation varies. This approach is utilized in the present work and its effect on the fit is discussed in Sec. VII.C. In addition, it is also generally necessary to truncate the sums over channels in a phenomenological  $R$ -matrix analysis. Channels that are strongly closed energetically are typically neglected, as they are expected to have very little influence (LT, Sec. X.2). Channels with large orbital angular momenta are likewise typically excluded, as their influence is suppressed by the angular momentum barrier.

The choice of channel radius warrants some discussion. According to formal  $R$ -matrix theory, the channel radius should be large enough so that at and beyond the channel radius, nuclear forces are negligible and Coulomb wave functions are a good approximation. However, increasing the channel radius increases the density of background poles, as can be seen from LT (Sec. IV.3.3b) for the case of zero nuclear potential. In a phenomenological analysis, choosing too large of a radius leads to problems with the background poles becoming overly complicated. For example, multiple background poles might be required to cancel most of the large hard-sphere elastic scattering phase shift (which increases along with the channel radius).

In practice, phenomenological  $R$ -matrix fits must use channel radii which enclose most but not all of the nuclear interactions. As an example, the *ab initio* calculation of Nollett *et al.* (2007) using realistic nuclear forces found that a radius of 9 fm was required for nuclear interactions in the neutron plus  $\alpha$  system to become negligible. However, a radius this large would be impractical for phenomenological fitting; see, for example, Hale, Brown, and Jarmie (1987), where 3 fm was used for this radius in a phenomenological description. As a consequence of some nuclear interactions beyond the channel radius, the phenomenological reduced-width amplitudes must be considered to be in some sense to be renormalized quantities.  $R$ -matrix fits should, however, be fairly insensitive to the specific value of the channel radius for a reasonable range of values. As the radius increases, the penetrability factor becomes larger and the reduced-width amplitudes decrease to preserve the physical width. It is thus good practice to explore the sensitivity of the phenomenological fit to the channel radius (or radii). If a strong variation in the fit quality exists, this can often indicate that background poles have not been sufficiently considered.

The phenomenological  $R$ -matrix approach derives much of its power from the fact that it automatically produces a

scattering matrix that is unitary and symmetric, even with the truncations mentioned. Unitarity is a particularly powerful constraint when data are available from multiple reaction channels. A related statement is that a single set of  $R$ -matrix parameters should be able to simultaneously describe essentially all low-energy nuclear reaction and nuclear structure data relating to a given compound nucleus. Our implementation of a phenomenological  $R$ -matrix analysis of data relevant to the  $^{12}\text{C}(\alpha, \gamma)^{16}\text{O}$  reaction is discussed next.

### G. $R$ -matrix strategy

As described in Sec. II, the energy range of the  $^{12}\text{C}(\alpha, \gamma)^{16}\text{O}$  cross section that is needed to calculate the reaction rate for astrophysical environments is very low ( $E_{\text{c.m.}} = 300$  keV), well below the limits of current experimental sensitivity ( $\sigma \approx 2 \times 10^{-17}$  b). Therefore, while there is a significant amount of data at higher energies, an extrapolation to low energy must be made. This is the primary reason that the phenomenological model must be employed. Further, from a more fundamental theory stand point, the different contributions to the cross section are calculated independently (see Secs. III.B and IV.A). Therefore, it provides further constraint to the phenomenological model if each of the individual contributions, as well as their sum, is measured independently as well. Further, as emphasized in Sec. VI, measurements over a wide energy range, up to several MeV above the  $\alpha$  threshold, are also very useful since they help constrain both the interference patterns and the background contributions of the different components, both of which can result in a large source of uncertainty in the cross section extrapolation.

Because low-energy measurements of the  $^{12}\text{C}(\alpha, \gamma)^{16}\text{O}$  reaction are greatly hindered by the Coulomb barrier, indirect techniques are extremely valuable. In particular, these techniques can be used to deduce the level parameters (i.e., energies, ANC's, lifetimes) that can then be used in  $R$ -matrix or other reaction models. These types of measurements have proven the most useful in constraining the contributions to the cross section from the subthreshold states. In particular, it is the  $1^-$  level at  $E_x = 7.12$  MeV ( $E_{\text{c.m.}} = -45$  keV) and the  $E_x = 2^+$  level at 6.92 MeV ( $E_{\text{c.m.}} = -245$  keV) that have the greatest contribution to the total cross section at  $E_{\text{c.m.}} = 300$  keV. The energies and lifetimes (or  $\gamma$  widths) are well known for these states, but the ANC's (or reduced widths) have proven difficult to determine accurately until recently (see Sec. VI.F).

So far, the most successful indirect methods include measurements of the  $\alpha$  spectrum from  $^{16}\text{N}(\beta\alpha)^{12}\text{C}$  decay, the differential cross section of  $^{12}\text{C}(\alpha, \alpha_0)^{12}\text{C}$  elastic scattering, and  $\alpha$ -transfer reactions. All can be used to determine or constrain one or both of the ANC's of the  $1^-$  and  $2^+$  subthreshold states. One limitation of elastic scattering is that, as shown by Eq. (34), the Coulomb amplitude dominates elastic scattering at low energies. Thus for energies below  $E_{\text{c.m.}} \approx 2.0$  MeV, the elastic scattering cross section is essentially indistinguishable from Rutherford scattering. In the case of  $^{16}\text{N}(\beta\alpha)^{12}\text{C}$ , the spectrum is suppressed at low  $\alpha + ^{12}\text{C}$  relative energies by the Coulomb barrier but the Coulomb

amplitude is not present. This spectrum has been measured to below  $E_{\text{c.m.}} = 1$  MeV, i.e., closer to the subthreshold states.

As compound nucleus reactions, the data from the  $^{16}\text{N}(\beta\alpha)^{12}\text{C}$  decay and  $^{12}\text{C}(\alpha, \alpha_0)^{12}\text{C}$  reaction can be fit directly in the  $R$ -matrix analysis. These data have the added benefit that they give constraints on other important level parameters as well. On the other hand, as a direct reaction, the  $\alpha$ -transfer data are analyzed using a distorted wave Born approximation (DWBA) analysis. The ANCs are deduced from a DWBA analysis, then the values and associated uncertainties can be used in the  $R$ -matrix model (Mukhamedzhanov and Tribble, 1999; Mukhamedzhanov, Gagliardi, and Tribble, 2001).

However, greatly complicating the issue, the subthreshold resonances interfere with other higher-lying broad resonances. These interferences are implemented in the  $R$  matrix by the relative signs of the reduced-width amplitudes in Eqs. (17) and (58); note the relation between the reduced width and the ANC is given in Eq. (44). The relative signs determine if the amplitudes of the cross section from the different resonances will add or subtract, which can give drastically different values for the cross section in off-resonance regions. This is because when two components of the cross section ( $\sigma_1$  and  $\sigma_2$ ) interfere with one another the magnitude goes as

$$\sigma_{\text{interference}} \propto 2\sqrt{\sigma_1\sigma_2}. \quad (85)$$

Therefore even if one of the cross section components is small, the interference term can still be significant compared to the total. It is into just such an off-resonance region where the extrapolation must be made to reach the stellar energy range. Therefore a reliable and precise extrapolation hinges on the determination of both the magnitude of the level parameters and their relative signs (see Sec. VII.B). This means that detailed measurements of the  $^{12}\text{C}(\alpha, \gamma)^{16}\text{O}$  cross section over, experimentally accessible, off-resonance regions at higher energies are very valuable in constraining the extrapolation to low energy.

It should also be emphasized that there are two different general types of interference effects seen in nuclear reactions. One type is when levels of the same  $J^\pi$  combine to produce energy-dependent interference effects. Another type is when processes with different  $J^\pi$  values combine to produce angle-dependent effects [see Eq. (34)]. Both types of interference are important for understanding the  $^{12}\text{C}(\alpha, \gamma)^{16}\text{O}$  reaction, the former being particularly critical for the low-energy extrapolation of the cross section as just discussed. The latter are critical in disentangling the  $E1$  and  $E2$  contributions to the cross section (see Sec. VI.B). Practical experimental considerations may allow for only an angle integrated and differential cross section measurement in a single setup. This reemphasizes the need to combine many different kinds of experimental results since different types of data are critical to the  $R$ -matrix analysis and have different types of uncertainties associated with them.

The general  $R$ -matrix strategy is then to utilize as much experimental data as possible in order to provide as much physical constraint as possible to the phenomenological model. While low-energy measurements of the  $^{12}\text{C}(\alpha, \gamma)^{16}\text{O}$  cross

section are critical, so too are indirect measurements and those at higher energies. It is only by combining this wide array of experimental data that the phenomenological model can be constrained to the point that it can yield an extrapolated cross section approaching the desired accuracy of nuclear astrophysics applications. With this clearly in mind, a summary of these many and diverse experimental endeavors is in order.

## V. EXPERIMENTAL MEASUREMENTS

The study of the  $^{12}\text{C}(\alpha, \gamma)^{16}\text{O}$  reaction can be naturally divided into three eras: first measurements, the push to low energies, and a return to indirect methods. The division of these eras is marked by some drastic improvement or new discovery in the experimental measurements.

Early measurements sought to investigate the low-energy cross section, not for nuclear astrophysics motivations, but to study the effects of isospin breaking of  $T = 0$  transitions (as discussed in Sec. I). In these investigations many different experimental techniques, nearly all of the indirect methods used today, were developed to study the properties of the compound nucleus. Many of these experiments simply suffered from the immaturity of the field, in both experimental techniques and theoretical interpretation. The capstones for this first period were the unprecedented measurement of the low-energy capture cross section around the  $1^-$  resonance at  $E_{\text{c.m.}} = 2.68$  MeV by Dyer and Barnes (1974) and the multilevel-multichannel  $R$ -matrix analysis of Barker (1971) that utilized capture, scattering, and  $\beta$ -delayed  $\alpha$  emission data.

Once the capture cross section was actually measured, a race began to push the measurements to lower energies, closer to the range of astrophysical interest ( $E_{\text{c.m.}} \approx 300$  keV). A host of experimental improvements and new techniques were developed, including highly  $^{13}\text{C}$  depleted and stable targets, high purity target chambers, recoil separators, inverse kinematic measurements with pure helium gas targets, and high-energy resolution detectors. Despite the extraordinary efforts, the rapid drop in the low-energy cross section made lower energy measurements hard won. The major discovery of this period was that not only  $E1$ , but also  $E2$  multipolarity, perhaps even in almost equal amplitudes, make up the dominating ground state transition cross section at stellar energies. Further theoretical methods to interpret the higher precision data were also more thoroughly explored. As it became more apparent that direct techniques would be extremely difficult to improve upon, there was a return to indirect methods. While the transition to the next period is not so clear cut, the works of Buchmann *et al.* (1993) and Zhao *et al.* (1993) serve as a reasonable division point, as they mark one of the early remeasurements of the  $\beta$ -delayed  $\alpha$  emission spectrum of  $^{16}\text{N}$  and Azuma *et al.* (1994) made one of the most detailed global analyses of the time. These measurements dramatically decrease the uncertainty in the  $E1$  cross section.

While measurements of the low-energy capture cross section continued, attempting improved measurements as new detectors or techniques were developed, many efforts have been made to revive the original indirect methods of transfer, scattering, and  $\beta$ -delayed  $\alpha$  emission of  $^{16}\text{N}$ .

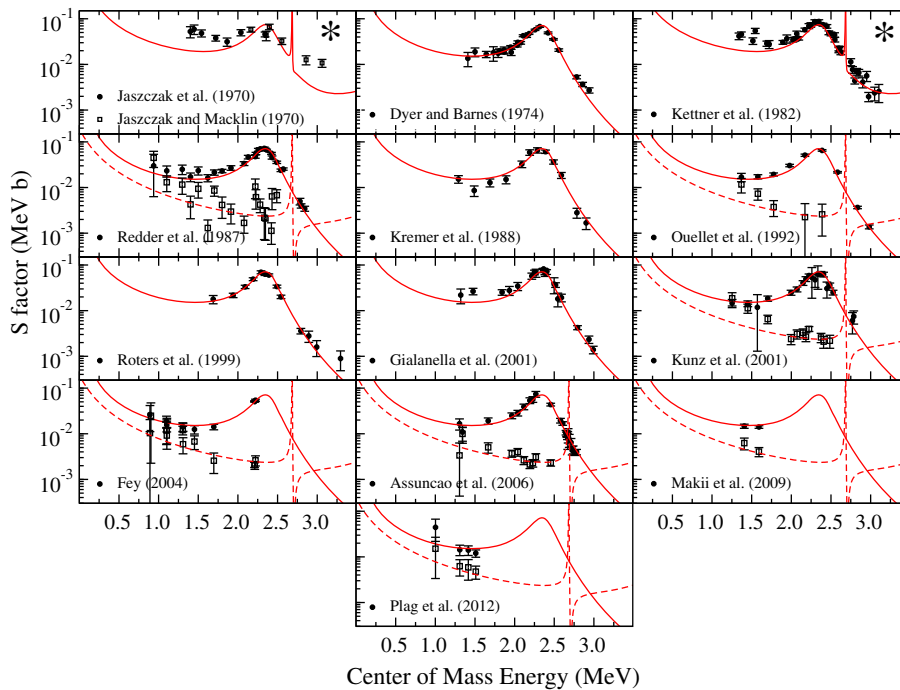


FIG. 3. Comparison of all  $E1$  and  $E2$  cross sections measured to date. The early works of [Jaszczak, Gibbons, and Macklin \(1970\)](#), [Jaszczak and Macklin \(1970\)](#), and [Kettner \*et al.\* \(1982\)](#) give only total cross sections. These are demarcated by an \*. As a standard for comparison, the  $R$ -matrix fit described later in this work is also shown. The solid red lines show the  $E1$  contributions (except where only the total is given) while the dashed red lines give the  $E2$  contributions. No normalization factors have been applied to the data. Note that the region of astrophysical interest is at roughly  $E_{c.m.} \approx 300$  keV, far below the lowest energy measurements at  $E_{c.m.} \approx 1$  MeV.

Transfer reaction studies have probably benefited the most from theoretical and experimental developments, allowing new measurements to achieve an unprecedented level of consistency. New measurements of the  $\beta$ -delayed  $\alpha$  emission spectra also continued in an effort to reach greater sensitivity and achieve improved accuracy. New scattering and recoil separator measurements were made that covered a wide energy range with high precision, providing a strong underpinning for the  $R$ -matrix analyses. Increases in computational power also brought about improvements in the sophistication of analysis methods, allowing large amounts of data to be utilized simultaneously to better constrain phenomenological fits and making Monte Carlo uncertainty methods viable. Because of its complexity, additional efforts are always underway to tackle this difficult problem. New indirect methods such as photodisintegration and Coulomb excitation are underway. New theoretical models are under development, with *ab initio* calculations on the horizon ([Elhatisari \*et al.\*, 2015](#)).

To aid the following discussions, Fig. 3 compares all the  $E1$  and  $E2$   $^{12}\text{C}(\alpha, \gamma)^{16}\text{O}$  ground state cross section data reported over the low-energy range. While the  $R$ -matrix fit, described later in this work, represents one of the more detailed phenomenological analyses to date, its use in this section is to simply provide a standard for comparison of the different data sets. This is most helpful when the data are difficult to compare on a one-to-one basis, for example, when experimental effects are significant or the cross section data are presented using different representations.

Since this figure is intended to illustrate an unbiased comparison between the different data sets, no scaling factors have been applied to the data.

Experimental techniques have improved significantly over the years and several different techniques have been explored. One of the most significant improvements has been target quality and stability or the use of a helium gas target for inverse kinematics. As a summary, Table II collects this information for the capture measurements.

#### A. First measurements (1955–1974)

The first published attempt at a direct measurement of the low-energy  $^{12}\text{C}(\alpha, \gamma)^{16}\text{O}$  cross section was made by [Allan and Sarma \(1955\)](#) at Imperial College in London with the sole goal of simply detecting a signal from the capture reaction. The experiment was performed with an  $\alpha$  beam of 1.6 MeV, a thick target (of unspecified thickness) made of natural carbon (98.9%  $^{12}\text{C}$ , 1.1%  $^{13}\text{C}$  by mole fraction), and a NaI detector. Like all subsequent experiments using forward kinematics, it was greatly hindered by a background produced from the high cross section  $^{13}\text{C}(\alpha, n)^{16}\text{O}$  reaction. Indeed several studies were made simply to characterize this reaction ([Jones and Wilkinson, 1953](#)), which is a background for all  $\alpha$  induced reaction studies. A comparison of the cross sections is shown in Fig. 4 where it can be seen that that of the  $^{12}\text{C}(\alpha, \gamma)^{16}\text{O}$  reaction, on top of the lowest energy  $1^-$  resonance, is more than 6 orders of magnitude smaller than that of the  $^{13}\text{C}(\alpha, n)^{16}\text{O}$  reaction. Only upper limits were determined

TABLE II. Summary of target details for different  $^{12}\text{C}(\alpha, \gamma)^{16}\text{O}$  experiments.

Reference	Target	Backing	Thickness	$^{13}\text{C}$ depletion or gas purity
Larson and Spear (1964)	Cracking acetylene	Ta (0.025 cm)	96 $\mu\text{g}/\text{cm}^2$ and thinner	Factor of 10 $^{13}\text{C}$ depletion
Jaszczak, Gibbons, and Macklin (1970)	Cracking of acetylene	Ta (0.025 cm)	98–178 $\mu\text{g}/\text{cm}^2$	99.94% $^{12}\text{C}$
Dyer and Barnes (1974)	Cracking of methyl alcohol	Ta (0.008 cm)	150–200 $\mu\text{g}/\text{cm}^2$	99.945% $^{12}\text{C}$
Kettner <i>et al.</i> (1982)	He gas target		10 torr	< 1 ppm
Redder <i>et al.</i> (1987)	Ion implantation	Au	80 keV at 2.68 MeV	$^{13}\text{C}/^{12}\text{C} \approx 10^{-4}$
Kremer <i>et al.</i> (1988)	He gas target		3.6(2) $\mu\text{g}/\text{cm}^2$	Recoil separator
Ouellet <i>et al.</i> (1992, 1996)	Ion implantation	Au	3–5 $\times 10^{18}$ atoms/ $\text{cm}^2$	Factor of $10^3$ $^{13}\text{C}$ depletion
Roters <i>et al.</i> (1999)	He gas target		9.1 torr	0.0001%
Gialanella <i>et al.</i> (2001)	He gas target		20 torr	0.0001%
Kunz <i>et al.</i> (2001)	Ion implantation	Au	2–3 $\times 10^{18}$ atoms/ $\text{cm}^2$	Factor of $10^3$ $^{13}\text{C}$ depletion
Fey (2004)	Ion deposition	Au	$\approx 2 \times 10^{18}$ atoms/ $\text{cm}^2$	
Schürmann <i>et al.</i> (2005)	He gas target		4.21(14) $\times 10^{17}$ atoms/ $\text{cm}^2$	Recoil separator
Assunção <i>et al.</i> (2006)	Ion implantation	Au	0.5–11 $\times 10^{18}$ atoms/ $\text{cm}^2$	Factor of $10^3$ $^{13}\text{C}$ depletion
Matei <i>et al.</i> (2006)	He gas target		4–8 torr	Recoil separator
Makii <i>et al.</i> (2009)	Cracking of methane gas	Au	250–400 $\mu\text{g}/\text{cm}^2$	99.95% $^{12}\text{C}$
Schürmann <i>et al.</i> (2011)	He gas target		4 $\times 10^{17}$ atoms/ $\text{cm}^2$	Recoil separator
Plag <i>et al.</i> (2012)	Ion deposition	Au	30–120 $\mu\text{g}/\text{cm}^2$	$^{13}\text{C}/^{12}\text{C} < 10^{-4}$

by Allan and Sarma (1955), not surprising in hindsight, as it is now known that the capture cross section at  $E_\alpha = 1.6$  MeV is about 0.2 nb.

An estimate for the astrophysical  $^{12}\text{C}(\alpha, \gamma)^{16}\text{O}$  cross section was given soon after by Burbidge *et al.* (1957), using the most basic kind of resonance theory: a single-level Breit-Wigner (Breit and Wigner, 1936). The analysis was limited to only the contribution from the  $1^-$  subthreshold state at  $E_x = 7.12$  MeV with the  $\gamma$ -ray width measured by Swann and Metzger (1956) and assuming  $\theta_\alpha^2(7.12) = 0.1$ . This result was later updated by Fowler, Caughlan, and Zimmerman (1967) using an improved resonance energy,  $\gamma$ -ray width (Swann and Metzger, 1957), and a theoretical calculation of  $\theta_\alpha^2(7.12)$  (Stephenson, 1966)

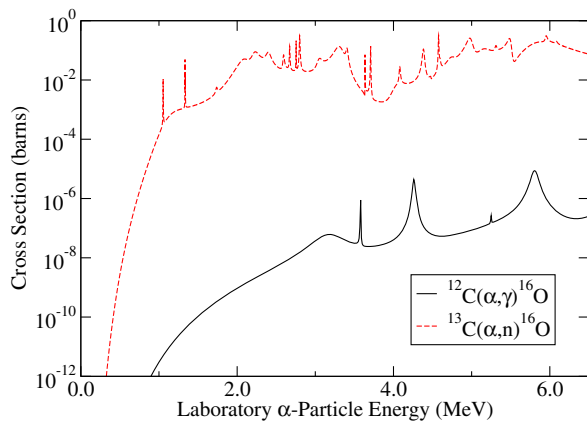


FIG. 4. Comparison of the cross section of the  $^{12}\text{C}(\alpha, \gamma)^{16}\text{O}$  reaction (this work) to that of the  $^{13}\text{C}(\alpha, n)^{16}\text{O}$  reaction. Because of the large difference in cross sections, even trace amounts of  $^{13}\text{C}$  in target materials and beam line elements can create large backgrounds in the  $\gamma$ -ray spectra of  $^{12}\text{C}(\alpha, \gamma)^{16}\text{O}$  measurements. These backgrounds are chiefly the result of  $(n, n'\gamma)$  and  $(n, \gamma)$  reactions on the detector materials themselves and nearby beam line components. Level parameters used to calculate the  $^{13}\text{C}(\alpha, n)^{16}\text{O}$  cross section have been taken from Sayer *et al.* (2002) and Leal *et al.* (2016).

that was in reasonable agreement with the result of the first  $\alpha$ -transfer reaction experiment (Loebenstein *et al.*, 1967).

Bloom, Toppel, and Wilkinson (1957) at Brookhaven National Laboratory were the first to resolve a signal from the  $^{12}\text{C}(\alpha, \gamma)^{16}\text{O}$  reaction. This was done by subtracting out the large background produced by the  $^{13}\text{C}(\alpha, n)^{16}\text{O}$  reaction. A thick target (450  $\mu\text{g}/\text{cm}^2$ ) technique was used and measurements were made over an  $\alpha$  energy range from 3.00 to 3.45 MeV. These measurements were associated with decays of  $\gamma$  rays from the  $E_x = 9.59$  MeV state, whose  $\gamma$  decay width was of great interest at the time to test theoretical predictions of isospin mixing of  $T = 1$  contributions into the predominantly  $T = 0$  state. The main result was the measurement of the ground state  $\gamma$  width of the state as  $\Gamma_{\gamma_0} \approx 6$  meV, about a factor of 2–3 smaller than the accepted value today.

Measurements were then extended to higher energies by Meads and McIlldowie (1960) at the Atomic Energy Research Establishment in Harwell, UK who were the first to study the ground state  $\gamma$  decay widths of the  $2^+$  levels at  $E_x = 9.85$  and 11.50 MeV, comparing their Weisskopf widths to that of the  $E_x = 6.92$  MeV state measured by Swann and Metzger (1957). The experiment was also the first to use targets depleted in  $^{13}\text{C}$  in order to suppress the neutron induced background. Great effort was also made to limit additional carbon buildup on the target, resulting from contamination in the beam line, by both target heating and the use of a cold trap. Angular distribution measurements were made for the first time to verify the multipolarities of the transitions.

An ambitious measurement campaign was then carried out by Larson and Spear (1964) at the California Institute of Technology (Cal Tech) who measured the  $^{12}\text{C}(\alpha, \gamma)^{16}\text{O}$  excitation function over an unprecedented energy range from  $E_\alpha = 2.8$  to 8.3 MeV. While this experiment was motivated by further structure studies, for the first time it also sought to investigate the cross section for nuclear astrophysics purposes. Building on the experience of the previous studies, the experiment utilized a depleted  $^{13}\text{C}$  target, a cold trap, and oil free pumps to limit background. While very successful at

higher energies, even measuring  $\gamma$ -ray angular distributions, yields at low energies were still insufficient to map the resonance corresponding to the  $1^-$  state at  $E_x = 9.59$  MeV. The state's properties were still investigated but a thicker target ( $96 \mu\text{g}/\text{cm}^2$ ) was necessary. A new larger value for the  $\gamma$  width of  $\Gamma_\gamma = 22(5)$  meV was found, in good agreement with current measurements. A more detailed account of the experiment can be found in [Larson \(1965\)](#). This project was suggested by Willie Fowler, with advising from Charles Lauritsen, Ward Whaling, Charlie Barnes, and Ralph Kavanagh, and with additional discussions with Tom Tombrello and Fred Barker.

A rather unique measurement testing time-reversal invariance was made by [Wimmersperg \*et al.\* \(1970\)](#) using measurements of the  $^{12}\text{C}(\alpha, \gamma_0)^{16}\text{O}$  reaction and its inverse  $^{16}\text{O}(\gamma, \alpha_0)^{12}\text{C}$  over a  $E1/E2$  mixed region at  $E_x \approx 13.1$  MeV. A detailed balance was used to test the consistency of the forward and backward asymmetry of the angular distribution at this energy. No significant deviation was observed.

The first excitation curve measurement of the lowest energy  $1^-$  resonance in the  $^{12}\text{C}(\alpha, \gamma)^{16}\text{O}$  reaction was reported by [Jaszczak, Gibbons, and Macklin \(1970\)](#) at the Oak Ridge National Laboratory (ORNL) [although preliminary measurements had also been reported at Cal Tech ([Adams \*et al.\*, 1968](#))]. Highly  $^{13}\text{C}$  depleted targets for the time were utilized (99.94%  $^{12}\text{C}$ ) with thicknesses ranging from 98 to  $178 \mu\text{g}/\text{cm}^2$ . The now typical precautions were taken to avoid carbon buildup on the target and limit background. The experiment was further notable in that it was one of the first to use a bunched helium beam for the time of flight [[Adams \*et al.\* \(1968\)](#) had also used this technique] to separate the  $\gamma$  rays from the neutron background signals. The measurements were limited to the low-energy side of the resonance ranging from  $E_\alpha = 1.86$  to  $3.20$  MeV but were extended up to  $E_\alpha = 4.2$  MeV by [Jaszczak and Macklin \(1970\)](#). No attempt was made to extrapolate the cross section to stellar energies.

With the extreme difficulty of directly measuring the capture cross section, indirect studies pursued the determination of the reduced  $\alpha$  widths. [Loebenstein \*et al.\* \(1967\)](#) also at Cal Tech made  $\alpha$  transfer measurements covering the ground state and the first five excited states of  $^{16}\text{O}$  using the  $^6\text{Li}(^{12}\text{C}, d)^{16}\text{O}$  reaction. While the experiments were performed at relatively low energies of  $E_{\text{c.m.}} = 7$  MeV, they were still not low enough to avoid the effects of compound nucleus contributions to the cross section. Because the cross sections were known to be a mixture of direct and compound nucleus formation processes, the data were difficult to interpret with theory, and the uncertainties of the extracted  $\theta_\alpha^2$  values were difficult to quantify. A range of values were given for many of the low lying states in  $^{16}\text{O}$  including the  $E_x = 6.05$  MeV  $0^+$  ( $0.14 < \theta_\alpha^2 < 0.30$ ), the  $E_x = 6.92$  MeV  $2^+$  ( $0.15 < \theta_\alpha^2 < 0.27$ ), and the  $E_x = 7.12$  MeV  $1^-$  states ( $0.06 < \theta_\alpha^2 < 0.14$ ), but this did not include any contributions to the uncertainties from theory. [Pühlhofer \*et al.\* \(1970\)](#) made similar measurements except using the  $^{12}\text{C}(^7\text{Li}, t)^{16}\text{O}$  reaction, but encountered similar complications in the interpretation of the data.

Just as in the capture data, the  $E_x = 7.12$  MeV state appears as a subthreshold state in  $\alpha$  scattering on  $^{12}\text{C}$ . While the

Rutherford cross section masks the low-energy subthreshold compound nucleus contributions, it was realized that there should be a measurable effect even at higher energies if  $\theta_\alpha^2$  was large enough. A detailed scattering measurement was performed at Australia National University by [Clark, Sullivan, and Treacy \(1968\)](#) and the effect of the subthreshold state was subsequently analyzed by [Clark \(1969\)](#) using a multilevel  $R$ -matrix analysis. While the effect of the subthreshold state was shown to significantly contribute to the scattering cross section, the uncertainty in the extracted phase shifts, and the need for a large background pole in the  $R$ -matrix analysis, resulted in a large uncertainty in  $\theta_\alpha^2(7.12 \text{ MeV})$  of  $0.71^{+0.37}_{-0.18}$ . Further, the results differed greatly from those of the transfer measurements.

Another compound nucleus reaction that can populate the  $E_x = 7.12$  and  $9.59$  MeV states is  $\beta$ -delayed  $\alpha$  emission from  $^{16}\text{N}$ . This decay almost exclusively populates the  $E_x = 9.59$  MeV state through an allowed Gamow-Teller transition, but should also weakly populate the high-energy tail of the  $E_x = 7.12$  MeV subthreshold state just as in the  $E1$  component of the capture reaction. This reaction had already been carefully investigated in order to observe the weak parity forbidden decay to the  $2^-$  state in  $^{16}\text{O}$  at  $E_x = 8.87$  MeV by [Hättig \*et al.\* \(1969\)](#) and [Hättig, Hünchen, and Wäffler \(1970\)](#) at the Max-Planck-Institute in Mainz. [Wertz \(1971\)](#) subsequently analyzed the spectrum using an  $R$ -matrix fit and showed that the data were sensitive to contributions from the subthreshold state constraining  $\theta_\alpha^2(7.12 \text{ MeV})$ . In a similar manner as the scattering data, it was found that unconstrained contributions from background states resulted in a large uncertainty. However, the range of  $0.013 < \theta_\alpha^2 < 0.105$  was found to be in good agreement with values determined from the transfer reaction data, but in disagreement with those of the scattering. The data sets resulting from these measurements were never published and only a subset of the data has survived; they are commonly referred to in the literature as the “Wäffler data.”

As a culmination of these early measurements, [Barker \(1971\)](#) performed the first comprehensive  $R$ -matrix analysis by iteratively fitting the scattering phase shifts of [Jones \*et al.\* \(1962\)](#), [Clark, Sullivan, and Treacy \(1968\)](#), and [Morris, Kerr, and Ophel \(1968\)](#), the  $\beta$ -delayed  $\alpha$  data of [Hättig, Hünchen, and Wäffler \(1970\)](#), and the capture cross section data of [Jaszczak and Macklin \(1970\)](#). The main goal was to reanalyze all of the data within a self-consistent analysis in an effort to resolve the inconsistent determinations of  $\theta_\alpha^2(7.12 \text{ MeV})$ . [Barker \(1971\)](#) found that the large value deduced by [Clark \(1969\)](#) was in error because of the invalid approximation of using a single-level  $R$  matrix and an improper treatment of the boundary conditions. The analysis found that in fact a general consistency could be obtained for the value of  $\theta_\alpha^2(7.12 \text{ MeV})$  (see [Table III](#)). The uncertainty estimate resulted in a range of the extrapolated capture  $S$  factor at  $E_{\text{c.m.}} = 300$  keV of  $50 < S(300 \text{ keV}) < 330$  keV b, with a best fit value of  $S(300 \text{ keV}) = 150$  keV b. Note that this uncertainty band includes both interference solutions for the low-energy  $E1$  capture cross section, which the data could not differentiate between. A similar analysis was soon performed by [Weisser, Morgan, and Thompson \(1974\)](#), which included the much

TABLE III. Summary of the subthreshold state reduced  $\alpha$  widths (prior to the convention of using asymptotic normalization coefficients). Here  $E1$  and  $E2$  refer to the ground state transition. Note that the reduced widths are radius dependent, which has caused some confusion in the past. Values of  $r_\alpha \approx 5.5$  fm are typical.

Reference	$\theta_{\alpha,6.92}^2$	$\theta_{\alpha,7.12}^2$	$\theta_{\alpha,7.12}^2/\theta_{\alpha,9.59}^2$	Data considered
Loebenstein <i>et al.</i> (1967)	0.15–0.27	0.06–0.14	0.07–0.16 <sup>b</sup>	$^6\text{Li}(^{12}\text{C}, d)^{16}\text{O}$
Clark (1969)		0.71 <sup>a</sup>		$^{12}\text{C}(\alpha, \alpha)^{12}\text{C}$
Pühlhofer <i>et al.</i> (1970)	0.18	0.025		$^7\text{Li}(^{12}\text{C}, t)^{16}\text{O}$
Wernitz (1971)		0.013–0.105		$^{16}\text{N}(\beta\alpha)^{12}\text{C}$
Barker (1971)		0.047–0.176		$^{12}\text{C}(\alpha, \gamma)^{16}\text{O}(E1)$ , $^{12}\text{C}(\alpha, \alpha)^{12}\text{C}$ , $^{16}\text{N}(\beta\alpha)^{12}\text{C}$
Weisser, Morgan, and Thompson (1974)		0.11		$^{12}\text{C}(\alpha, \gamma)^{16}\text{O}(E1)$ , $^{12}\text{C}(\alpha, \alpha)^{12}\text{C}$
Koonin, Tombrello, and Fox (1974)		0.18 $_{-0.10}^{+0.14}$	0.19 $_{-0.11}^{+0.16}$	$^{12}\text{C}(\alpha, \gamma)^{16}\text{O}(E1)$ , $^{12}\text{C}(\alpha, \alpha)^{12}\text{C}$
Coburn, Pisano, and Parker (1976)			0.1–0.2 <sup>b</sup>	$^{12}\text{C}(^7\text{Li}, t)^{16}\text{O}$
Becchetti, Flynn <i>et al.</i> (1978)			0.35(13)	$^{12}\text{C}(^7\text{Li}, t)^{16}\text{O}$
Becchetti, Jänecke, and Thorn (1978)			$\sim 0.4^b$	$^{12}\text{C}(^6\text{Li}, d)^{16}\text{O}$
Becchetti <i>et al.</i> (1980)			0.3–0.6	$^{12}\text{C}(^6\text{Li}, d)^{16}\text{O}$
Kettner <i>et al.</i> (1982)	1.0 $_{-0.3}^{+0.4}$	0.19 $_{-0.08}^{+0.14}$		$^{12}\text{C}(\alpha, \gamma)^{16}\text{O}(E1, E2, \&6.92)$ , $^{12}\text{C}(\alpha, \alpha)^{12}\text{C}$
Descouvemont, Baye, and Heenen (1984)	0.10(2)	0.09(2)		$^{12}\text{C}(\alpha, \gamma)^{16}\text{O}(E1, E2, \&6.92)$
Langanke and Koonin (1985)	$\approx 0.17$			$^{12}\text{C}(\alpha, \gamma)^{16}\text{O}(E1, \text{total}, \sigma_{E2}/\sigma_{E1}, 6.92)$
Barker and Kajino (1991)	0.730	0.114	0.14	$^{12}\text{C}(\alpha, \gamma)^{16}\text{O}(E1, E2, 6.92, 7.12)$ $^{12}\text{C}(\alpha, \alpha)^{12}\text{C}$ , $^{16}\text{N}(\beta\alpha)^{12}\text{C}$

<sup>a</sup>Corrected by Barker (1971) to 0.11.

<sup>b</sup>Recalculated by Barnes, Clayton, and Schramm (1982).

more accurate capture data of Dyer and Barnes (1974). A similar best fit value of  $S(300 \text{ keV}) = 170 \text{ keVb}$  was obtained. Although model uncertainties were investigated thoroughly, no overall uncertainty range was given.

At long last, the first accurate low-energy measurement of the  $^{12}\text{C}(\alpha, \gamma)^{16}\text{O}$  ground state cross section was made by Dyer and Barnes (1974) at Cal Tech. The experiment was also notable because it was the first observation of interference between a subthreshold and unbound  $1^-$  state, a phenomenon predicted several years before by Marion and Fowler (1957). The experiment utilized a target very similar to that of Jaszczak, Gibbons, and Macklin (1970) and a clean target chamber setup. Only  $E1$  and  $E2$  multiplicities are allowed from the decays of the  $1^-$  and  $2^+$  excited states to the  $0^+$  ground state of  $^{16}\text{O}$ ; therefore these multiplicities are expected to dominate the cross section. To simplify the interpretation of the data, measurements were made primarily at  $90^\circ$  to the beam axis because the  $E1$  and  $E2$  angular distributions are such that the  $E1$  cross section is both maximum and the  $E2$  cross section is zero at this angle as shown by Fig. 5. The  $E1$  cross section can be written in a simple form as (Dyer and Barnes, 1974)

$$\sigma_{E1} = 4\pi \left(\frac{2}{3}\right) \left(\frac{d\sigma}{d\Omega}\right)_{90^\circ}. \quad (86)$$

Angular distributions were also measured for the first time over this low-energy region. The angular distribution data are critical in extracting the  $E2$  cross section (as described in Sec. VI.B) since, as shown in Fig. 5, there is no angle where the  $E2$  cross section can be isolated. A detailed discussion of the different contributions to the  $E1$  cross section is given, noting, in particular, the large uncertainty that is found from the interferences of higher-energy states, modeled using a single background pole, with two explicitly

defined  $E_x = 7.12 \text{ MeV}$  subthreshold state and the  $E_x = 9.59 \text{ MeV}$  unbound state.

It was found that  $\theta_\alpha^2(7.12 \text{ MeV})$  was not well constrained by the capture data, strongly reinforcing the motivation for indirect studies. The technique of a three level  $R$ -matrix calculation to model the  $E1$  capture used by Dyer and Barnes (1974) would become the standard for many years to follow. The direct capture contribution (dominated by  $E2$  multipolarity) was modeled using the formalism found in Tombrello and Phillips (1961) and Tombrello and Parker (1963), which would later be expanded by Barker and Kajino (1991) into the external capture model. In addition, a hybrid  $R$ -matrix model was also investigated following the work of Koonin, Tombrello, and Fox (1974). In this case, the potential model gives the contribution from single-particle states, including those at higher energies, which could drastically

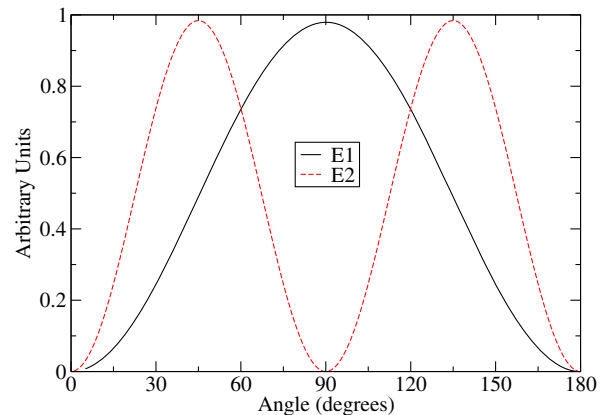


FIG. 5. Theoretical calculation comparing the  $E1$  and  $E2$  angular distributions for the ground state transition of the  $^{12}\text{C}(\alpha, \gamma)^{16}\text{O}$  reaction.

decrease the uncertainty in the extrapolation of the cross section, but this depends again on the reliability of the potential model and its likewise phenomenologically determined parameters. With limited angular distribution data, it was incorrectly assumed that the small  $E2$  component observed in the angular distributions came from direct capture. No contribution from the  $2^+$  subthreshold state at  $E_x = 6.92$  MeV was considered.

The significant progress in studying the level structure and compound nucleus cross sections of  $^{16}\text{O}$  was not limited to these very low energies. Continuing the work of Larson and Spear (1964), the  $^{12}\text{C}(\alpha, \gamma)^{16}\text{O}$  cross section was investigated above the proton separation energy  $S_p = 12.13$  MeV by Mitchell and Ophel (1964), Kernel, Mason, and Wimmersperg (1971), and Brochard *et al.* (1973). These studies were complemented by other  $^{12}\text{C} + \alpha$  reaction measurements by Mitchell and Ophel (1965) and Morris, Kerr, and Ophel (1968). The motivation for most of these studies was to understand the increasingly complicated level structure of  $^{16}\text{O}$  at these higher energies. However, it was also realized that these measurements provided an indirect way of studying the  $^{15}\text{N}(p, \gamma)^{16}\text{O}$  and  $^{15}\text{N}(p, \alpha)^{12}\text{C}$  reactions, where Bethe (1939) had pointed out as being of great interest for nucleosynthesis as they form the branch point of the CNO cycle. A study of the  $^{15}\text{N}(p, \gamma)^{16}\text{O}$  reaction had been made by Hebbard (1960) and several measurements of the  $^{15}\text{N}(p, \alpha_0)^{12}\text{C}$  and  $^{15}\text{N}(p, \alpha_1)^{12}\text{C}$  reactions by Barnes, James, and Neilson (1952), Schardt, Fowler, and Lauritsen (1952), Cohen and French (1953), Neilson, James, and Barnes (1953), Hagedorn and Marion (1957), and Bashkin, Carlson, and Douglas (1959). Hagedorn (1957) and Bashkin, Carlson, and Douglas (1959) also studied the proton scattering cross section. These measurements confirmed that the  $^{12}\text{C}(\alpha, \gamma)^{16}\text{O}$  cross section over the energy range just above  $S_p$  is dominated by two broad  $1^-$  resonances ( $E_x = 12.45$  and  $13.09$  MeV) and angular distributions hinted at a weak contribution from a broad  $2^+$  state ( $E_x = 12.95$  MeV). While these resonances are a few MeV above the astrophysical energy range of interest for the  $^{12}\text{C}(\alpha, \gamma)^{16}\text{O}$  reaction, their large widths can produce significant interference effects that impact the cross section even at low energies.

## B. The push to lower energies (1974–1993)

Despite the successful work by Dyer and Barnes (1974), their hard won success marks the beginning of a gap in capturing cross section measurements of nearly a decade. When they were finally picked up again in the early 1980s, a more focused set of experiments would emerge, with the primary goal of pushing the cross section data to ever lower energies.

In an attempt to avoid the large background problems from the  $^{13}\text{C}(\alpha, n)^{16}\text{O}$  reaction that plagued earlier measurements, the experiment of Kettner *et al.* (1982) (Claus Rolfs' Münster group, experiment performed at Bochum) was performed for the first time in inverse kinematics using a high-intensity  $^{12}\text{C}$  beam ( $50 \mu\text{A}$ ) on a windowless extended helium gas target. The gas target allowed for the use of higher beam intensities, since the destruction of the target was no longer an issue and

avoided the issue of carbon buildup on the target. However, a new set of complications presented themselves that were largely related to interpretation of the yield from the extended geometry gas target. The end result was a measurement of the low-energy total ground state capture cross section down to  $E_{\text{c.m.}} = 1.34$  MeV, about 0.1 MeV below the measurements of Dyer and Barnes (1974) but not as low as the measurements of Jaszczak, Gibbons, and Macklin (1970). It was found that the cross section at low energies was in better agreement with that of Jaszczak, Gibbons, and Macklin (1970) than that of Dyer and Barnes (1974), but the comparison was not straightforward since the data of Dyer and Barnes (1974) represent only the  $E1$  component while that of Kettner *et al.* (1982) represented an angle-integrated cross section. The most notable result of the experiment was the realization that the ground state  $E2$  cross section could make a sizable contribution to the low-energy cross section through the high-energy tail of the  $2^+$  subthreshold state at  $E_x = 6.92$  MeV, perhaps even with an amplitude equal to that of the  $E1$  cross section at  $E_{\text{c.m.}} = 300$  keV.

Because of the successful suppression of the background from the  $^{13}\text{C}(\alpha, n)^{16}\text{O}$  reaction, Kettner *et al.* (1982) achieved another first, measurements of the cascade transitions at low energies. An excitation curve of the  $E_x = 6.92$  MeV transition is given, where it is assumed that the  $E_x = 6.92$  MeV transition dominates over the  $E_x = 7.12$  MeV transition (the two individual  $\gamma$  lines could not be resolved in the NaI detectors used). It was found later that this was not a good assumption as both transitions have comparable cross sections over the reported energy range (Redder *et al.*, 1987). This highlights a continued issue with the observation of the individual cascade transitions. The  $E_x = 6.05$  and  $6.13$  MeV first and second excited states in  $^{16}\text{O}$  are only 80 keV apart and the  $E_x = 6.92$  and  $7.12$  MeV third and fourth excited states are separated only by 100 keV. Thus either a detector with high  $\gamma$ -ray energy resolution or a detailed unfolding simulation is required in order to extract their individual contributions.

Measurements were then made by Redder *et al.* (1987) (again Rolfs' Münster group, this time at Stuttgart), but now switching back to forward kinematics. Major experimental improvements included implanted targets and the first use of high-energy resolution germanium detectors Ge(Li). The targets were made by implanting  $^{12}\text{C}$  ions into a gold backing, drastically decreasing the amount of  $^{13}\text{C}$  contamination. The gold backing was further soldered onto a copper back plate that allowed for better cooling, through its enhanced thermal conductivity. This was combined with flowed water cooling. These targets were estimated to now be depleted in  $^{13}\text{C}$  by 2 orders of magnitude (earlier experiments were about 1 order of magnitude). Up until this point all previous experiments had been performed with NaI detectors, but the improved low level of neutrons allowed for the use of Ge(Li) detectors. The improved energy resolution over NaI detectors allowed for better separation of background peaks and for the  $\gamma$ -ray secondary peaks of the  $E_x = 6.92$  and  $7.12$  MeV cascade transitions to be clearly distinguished. The measurements were made over the course of three different experimental campaigns using different accelerators and different arrangements of NaI and Ge(Li) detectors. Angular distributions were

measured at an unprecedented eight angles from  $E_{\text{c.m.}} = 1.7$  to 2.84 MeV. The lowest energy measurements were extended to  $E_{\text{c.m.}} = 0.94$  MeV, now the record for the lowest energy, with the cross section at a minuscule 48 pb. Even at the lowest energies, angular distributions were measured, but with only three Ge(Li) detectors. Most significantly, the angular distribution measurements showed a substantial  $E2$  component to the cross section, confirming that this multipolarity is quite significant at stellar energies. Again, the energy dependence of the cross section at low energies was found to be higher than that of Dyer and Barnes (1974).

The improved angular distribution measurements by Redder *et al.* (1987) provided more sensitivity to the  $E2$  ground state cross section triggered by several theoretical calculations to model this previously neglected component of the cross section. For the first time Descouvemont, Baye, and Heenen (1984) made use of a microscopic model using the generator coordinate method. Langanke and Koonin (1983) updated their hybrid  $R$ -matrix calculations taking into account the new capture data and then refining the calculations again in Langanke and Koonin (1985), correcting some previous errors. Now including the  $E2$  cross section, Barker (1987) updated his calculations as well, using purely  $R$ -matrix calculations for both the  $E1$  and  $E2$  cross sections. Further, several calculations were made for the  $E_x = 6.92$  MeV cascade contribution. All agreed that its contribution to the total capture  $S$  factor should be small ( $< 15$  keV b) at stellar energies. The general result was that the  $^{12}\text{C}(\alpha, \gamma)^{16}\text{O}$  cross section at stellar energies should be significantly larger, 2–5 times of the value estimated by Dyer and Barnes (1974), but the recommended values varied widely as summarized in Table IV. History gives us a valuable lesson here. While several experiments were in apparent contradiction to Dyer and Barnes (1974), later measurements would find that these measurements were in fact erroneously large, perhaps the result of insufficient background subtraction.

The Cal Tech (Kremer *et al.*, 1988) group now looked to reinvestigate the  $^{12}\text{C}(\alpha, \gamma)^{16}\text{O}$  reaction but this time using another novel technique for the first time: a recoil separator. By detecting the  $\gamma$  rays in coincidence with the recoiling  $^{16}\text{O}$ , nearly background free spectra could be obtained. Because of the acceptance of the CTAG separator, the  $90^\circ$  placement of the NaI detectors, and the much different angular distributions of  $E1$  and  $E2$  radiation (see Fig. 5), the efficiency for detecting the  $E2$  component was only 50%–65% of that for the  $E1$  component. Theoretical values of the  $E1/E2$  cross section ratio from Langanke and Koonin (1983, 1985) were necessary to extract the  $E1$  cross section over the range from  $E_{\text{c.m.}} = 1.29$  to 3.00 MeV so the results were somewhat theory dependent. The  $E1$  cross section was found to be in good agreement with that of Dyer and Barnes (1974), reinforcing the tension between the different measurements.

To try to resolve these differences, a new measurement was then performed by the Queen's University group. The data were first reported by Ouellet *et al.* (1992) but the results were subsequently revised by Ouellet *et al.* (1996). The experiment was performed in forward kinematics using water cooled implanted targets very similar to those of Redder *et al.* (1987). The beam was also wobbled over the target surface to insure

even beam coverage lessening the sensitivity of the experiment to any target inhomogeneity. With the low neutron background, six germanium detectors were used to measure angular distributions over an energy range from  $E_{\text{c.m.}} = 1.37$  to 2.98 MeV. The data turned out to split the difference between those of Redder *et al.* (1987) and Kremer *et al.* (1988), providing no solution to the issue. In the analysis of Ouellet *et al.* (1996), the  $E1$  data along with that of Dyer and Barnes (1974), Redder *et al.* (1987), and Kremer *et al.* (1988) were fitted simultaneously using a three level  $R$ -matrix fit along with the newly measured  $^{16}\text{N}(\beta\alpha)^{12}\text{C}$  data of Azuma *et al.* (1994) and the elastic scattering phase shift data of Plaga *et al.* (1987). The  $E2$  data were fitted separately using a cluster model method. Note that in Ouellet *et al.* (1992) the destructive solution between the  $1^-$  subthreshold state ( $E_x = 7.12$  MeV) and the broad resonance corresponding to the  $1^-$  level at  $E_x = 9.59$  MeV was reported to produce the best  $\chi^2$  fit. However, in the revised analysis of Ouellet *et al.* (1996), they concluded that, considering all the capture data, the constructive solution was in fact favored and the destructive one was statistically ruled out.

While it has been neglected in all analyses, a high-energy measurement of the ground state transition cross section, in the range  $12 < E_x < 28$  MeV, was made by Snover, Adelberger, and Brown (1974). The cross section data were obtained in order to measure the  $E2$  strength of the giant dipole resonance and hence were decomposed into  $E1$  and  $E2$  components. While the measurement was made for purely structure motivations, these data could provide valuable upper limits on the high-energy background contributions of phenomenological  $R$ -matrix fits at lower energies for the dominant ground state transition. This topic is revised in Sec. VII.C.

Several measurements continued to study the properties of the  $^{16}\text{O}$  compound nucleus in the energy region just above  $S_p$ . And several measurements were made to continue in the investigation of the astrophysically important CNO branch point reactions  $^{15}\text{N}(p, \alpha)^{12}\text{C}$  (Pepper and Brown, 1976; Bray *et al.*, 1977; Zyskind and Parker, 1979; Redder *et al.*, 1982) and  $^{15}\text{N}(p, \gamma)^{16}\text{O}$  (Rolfs and Rodney, 1974). Improved measurements of  $^{12}\text{C} + \alpha$  scattering were also made by D'Agostino-Bruno *et al.* (1975).

### C. Return to indirect techniques (1993–present)

The last 20 years have witnessed a continued, and even increasingly, intense effort to study the  $^{12}\text{C}(\alpha, \gamma)^{16}\text{O}$  reaction. With the seeming impasse of a capture experiment reaching the stellar energy range, there has been a renewed interest in indirect techniques. While many direct measurements continue to be made, the development of improved theoretical and experimental methods for interpreting transfer reaction data, continued development of more accurate  $^{16}\text{N}(\beta\alpha)^{12}\text{C}$  measurements, improved recoil separators, and more sophisticated analyses have arguably produced the greatest impact.

Plaga *et al.* (1987) (Rolfs' group) measured the scattering cross section at 35 angles covering a wide angular range from  $\theta_{\text{lab}} = 22^\circ$  to  $163^\circ$  at 51 energies between  $E_{\text{c.m.}} = 0.75$  and 5.0 MeV. Phase shifts were extracted for angular momentum

TABLE IV. Extrapolations of the  $^{12}\text{C}(\alpha, \gamma)^{16}\text{O}$   $S$  factor to  $E_{\text{c.m.}} = 300$  keV categorized by either cluster model calculations or phenomenological fits. The abbreviations used below are for the generalized coordinate method (GCM) and potential model (PM) for the theoretical works and Breit-Wigner (BW),  $R$  matrix ( $R$ ), and  $K$  matrix ( $K$ ) for the phenomenological calculations. Hybrid  $R$ -matrix (HR) models have also been used in an effort to connect the phenomenological calculations more closely to more fundamental theory.

Reference	$E1$	$E2$	$S(300 \text{ keV})$ (keV b)		Model
			Cascades	Total	
Cluster models					
Descouvemont, Baye, and Heenen (1984)	300	90			GCM
Langanke and Koonin (1985)	160–280	70	$< 10^{\text{a}}$	230–350	HR & PM
Funck, Langanke, and Weiguny (1985)		100			PM
Redder <i>et al.</i> (1987)	$140_{-80}^{+120}$	$80 \pm 25$	$7 \pm 3^{\text{a}}$	$1.3_{-1.0}^{+0.5\text{b}}$	$R$ & PM
Descouvemont and Baye (1987)	160	70			GCM
Ouellet <i>et al.</i> (1992)	$1_{-1}^{+6}$	$40 \pm 7$			$R$ & PM
Descouvemont (1993)		90			GCM
Ouellet <i>et al.</i> (1996)	$79 \pm 16$	$36 \pm 6$		$120 \pm 40$	$R, K, PM$
Dufour and Descouvemont (2008)		$42 \pm 2$			GCM
Katsuma (2012)	$\approx 3$	$150_{-17}^{+41}$	$18.0 \pm 4.5^{\text{c}}$	$171_{-22}^{+46}$	PM
Xu <i>et al.</i> (2013) (NACRE2)	$80 \pm 18$	$61 \pm 19$	$6.5_{-2.2}^{+4.7\text{c}}$	$148 \pm 27$	PM
Burbidge <i>et al.</i> (1957)	340			340	BW
Barker (1971)	50–330			50–330	$R$
Koonin, Tombrello, and Fox (1974)	$80_{-40}^{+50}$			$80_{-40}^{+50}$	HR
Dyer and Barnes (1974)	$140_{-40}^{+140}$			$140_{-40}^{+140}$	$R$ & HR
Weisser, Morgan, and Thompson (1974)	170			170	$R$
Humblet, Dyer, and Zimmerman (1976)	$80_{-70}^{+140}$			$80_{-70}^{+140}$	$K$
Kettner <i>et al.</i> (1982)	250	180	$12(2)^{\text{a,b}}$	$420_{-120}^{+160}$	BW
Langanke and Koonin (1983)	150 or 340	$< 4\%$ of $E1$		150 or 340	HR
Barker (1987)	$150_{-60}^{+140}$	$30_{-30}^{+50}$			$R$
Kremer <i>et al.</i> (1988)	0–140				$R$ & HR
Filippone, Humblet, and Langanke (1989)	0–170	5–28		0–170	$K$
Barker and Kajino (1991)	$150_{-70}^{+170}$ or $260_{-160}^{+140}$	$120_{-70}^{+60}$	$10^{\text{a}}$	$280_{-140}^{+230}$ or $390_{-230}^{+200}$	$R$
Humblet, Filippone, and Koonin (1991)	$43_{-16}^{+20}$	$7_{-5}^{+24}$		$50_{-20}^{+30}$	$K$
Humblet, Filippone, and Koonin (1993)	$45_{-6}^{+5}$				$K$
Azuma <i>et al.</i> (1994)	$79 \pm 21$ or $82 \pm 26$				$R$ & $K$
Buchmann <i>et al.</i> (1996)	$79 \pm 21$	$70 \pm 70$	$16 \pm 16^{\text{a,b,d}}$	$165 \pm 75$	$R$ & $K$
Hale (1997)	20				$R$
Trautvetter <i>et al.</i> (1997)	79	14.5			BW
Brune <i>et al.</i> (1999)	$101 \pm 17$	$42_{-23}^{+16}$			$R$
Roters <i>et al.</i> (1999)	$79 \pm 21$				$R$
Angulo and Descouvemont (2000)		190–220			$R$
Gialanella <i>et al.</i> (2001)	$82 \pm 16$ or $2.4 \pm 1.0$				$R$
Kunz <i>et al.</i> (2001)	$76 \pm 20$	$85 \pm 30$	$4 \pm 4^{\text{c}}$	$165 \pm 50$	$R$
Tischhauser <i>et al.</i> (2002)		$53_{-18}^{+13}$			$R$
Hammer <i>et al.</i> (2005b)	$77 \pm 17$	$81 \pm 22$		$162 \pm 39$	$R$
Buchmann and Barnes (2006)			$5_{-4.5}^{+7}$ $7_{-4}^{+13\text{a}}$		$R$
Matei <i>et al.</i> (2006)			$25_{-15}^{+16\text{d}}$		$R$
Matei, Brune, and Massey (2008)			$7.1 \pm 1.6^{\text{a}}$		$R$
Tang <i>et al.</i> (2010)	$86 \pm 22$				$R$
Schürmann <i>et al.</i> (2011)			$< 1^{\text{d}}$		$R$
Schürmann <i>et al.</i> (2012)	83.4	73.4	$4.4^{\text{c}}$	$161 \pm 19_{-2}^{+8(\text{stat})}$	$R$
Oulebsir <i>et al.</i> (2012)	$100 \pm 28$	$50 \pm 19$		$175_{-62}^{+63}$	$R$
Sayre <i>et al.</i> (2012)		$62_{-6}^{+9}$			$R$
Avila <i>et al.</i> (2015)			$1.96 \pm 0.30$ or $4.36 \pm 0.45^{\text{d}}$ $0.12 \pm 0.04$ or $1.44 \pm 0.12^{\text{e}}$		$R$
An <i>et al.</i> (2015)	$98.0 \pm 7.0$	$56 \pm 4.1$	$8.7 \pm 1.8^{\text{c}}$	$162.7 \pm 7.3$	$R$
This work	86.3	45.3	$7^{\text{c}}$	$140 \pm 21_{-11}^{+18(\text{MC})}$	$R$

<sup>a</sup>6.92 MeV transition.<sup>b</sup>7.12 MeV transition.<sup>c</sup>Sum of all cascade transitions.<sup>d</sup>6.05 MeV transition.<sup>e</sup>6.13 MeV transition.

$l = 0$  to 6 using a multilevel  $R$ -matrix fit. One of the main findings was that the reduced  $\alpha$  widths were highly correlated with the background pole parameters, a problem observed before, resulting in large model uncertainties. This issue seems to be a limiting factor in the determination of sub-threshold reduced widths from scattering data in general.

A major step forward was the measurements of the  $\alpha$ -particle energy spectrum from  $^{16}\text{N}(\beta\alpha)^{12}\text{C}$  in the 1990s. The first results were reported from an experiment performed at TRIUMF by Buchmann *et al.* (1993), with a more complete description given by Azuma *et al.* (1994). The  $^{16}\text{N}(\beta\alpha)^{12}\text{C}$  spectrum was concurrently measured by the Yale group of Zhao *et al.* (1993). These measurements were subsequently extended by France *et al.* (1997). Another  $^{16}\text{N}(\beta\alpha)^{12}\text{C}$  measurement was performed by the Seattle group shortly after but the results were not published. The spectrum can be found in the later work of France *et al.* (2007).

These measurements were highly motivated by the theoretical calculations of Baye and Descouvemont (1988), Ji *et al.* (1990), and Humblet, Filippone, and Koonin (1991) that predicted a characteristic interference pattern at low energies. This is the result of the interference between the  $1^-$  levels at  $E_x = 7.12$  and 9.59 MeV. It is very sensitive to the relative values of the reduced  $\alpha$  widths and the  $\beta$ -decay branching ratios of the two states. However, the interpretation of the spectrum is complicated by the presence of an  $l = 3$  component coming from the  $3^-$  subthreshold state at  $E_x = 6.13$  MeV. Nevertheless, the interference pattern was in fact observed and marked a drastic improvement in the constraint of the  $E1$  ground state capture cross section.

The  $\beta$ -delayed  $\alpha$ -particle spectrum provided for a high level of constraint on the reduced  $\alpha$  width of the  $1^-$  subthreshold state. A detailed global analysis was presented by Azuma *et al.* (1994), where the TRIUMF  $^{16}\text{N}(\beta\alpha)^{12}\text{C}$  data were fitted simultaneously with the scattering phase shifts of Plaga *et al.* (1987) and the  $E1$  capture data of Dyer and Barnes (1974), Redder *et al.* (1987), Kremer *et al.* (1988), and Ouellet *et al.* (1992). It was found that the  $^{16}\text{N}(\beta\alpha)^{12}\text{C}$  data significantly improved the constraint on the  $E1$  cross section, by way of the  $1^-$  subthreshold state's ANC, over the capture data. It was noted, however, that the general shape of the capture data were still critical because only they can determine the interference pattern between the two  $1^-$  resonances, which greatly influences the low-energy cross section.

A global analysis of the capture, scattering, and  $^{16}\text{N}(\beta\alpha)^{12}\text{C}$  data was performed by Buchmann *et al.* (1996) and several important conclusions were made. One focus of the analysis was to look at biases that had developed because of the historical convention of dividing the ground state cross section into  $E1$  and  $E2$  cross sections. Two general techniques were used. The first was to measure the angular distributions and perform a fit to a theoretically motivated angular distribution function. While this technique has been widely used, it also has its pitfalls. One issue is that it can be difficult to measure differential cross sections at several angles given the very low yields. These low yields are often influenced by systematic uncertainties that can be difficult to quantify and can be easily overlooked. Further, the fitting also requires a phase that either can be left free in the fitting or can be constrained by scattering

data. The second method uses a large diameter detector also centered at  $90^\circ$  but placed in very close geometry to the target to measure the angle-integrated cross section over approximately  $2\pi$ , effectively measuring  $\sigma_{\text{total}}/2$ . Then the  $E2$  cross section can be deduced as  $\sigma_{\text{total}} - \sigma_{E1} = \sigma_{E2}$ . Both of these techniques require assumptions and simulations, allowing more opportunities for errors to be made. For these reasons, Buchmann *et al.* (1996) advocated that global analysis should instead rely on “primary” data, meaning either the actual differential cross sections that were measured or the total cross section for a close geometry setup. Unfortunately, many of the early measurements reported only the deduced  $E1$  and  $E2$  cross sections, not the differential data. Another important conclusion was that while the  $E1$  cross section seemed to be fairly consistent over different measurements, the  $E2$  cross section showed large fluctuations. This seems to be because analyses are attempting to extract a small  $E2$  contribution over most of the experimentally accessible energy region, i.e., over the broad low-energy  $1^-$  resonance. The uncertainties of this process seem to have often been underestimated.

Buchmann *et al.* (1996) also predicted through simulation that high-precision scattering measurements could be used to improve the constraint of the fits. In direct response, Tischhauser *et al.* (2002) performed a detailed measurement of the scattering cross section. Measurements were made from  $E_{\text{c.m.}} = 2.0$  to 6.1 MeV in energy steps of approximately 10 keV and at 32 angles ranging from  $\theta_{\text{lab}} = 24^\circ$  to  $166^\circ$ . The measurement sought to place stronger constraints on both the  $\alpha$  widths of the unbound states and the reduced widths of the subthreshold states. In particular, the goal was an improved constraint on the reduced width of the  $2^+$  subthreshold state, which is not constrained by the  $^{16}\text{N}(\beta\alpha)^{12}\text{C}$  reaction. However, because of the issues of background pole contributions in the  $R$ -matrix analysis, the constraint was not as great as expected. Additionally, because of issues with the target thickness varying due to carbon buildup on the target, the data were analyzed as ratios of the yields instead of as absolute cross sections. It was, however, demonstrated that this still provides significant constraint on the  $R$ -matrix fit while greatly reducing systematic uncertainties that are difficult to quantify. A more complete description of the experiment and analysis, together with an extraction of the phase shifts, was later given by Tischhauser *et al.* (2009). An  $R$ -matrix fit including data above  $S_p$ , which included  $^{12}\text{C}(\alpha, \alpha_1)^{12}\text{C}$  and  $^{12}\text{C}(\alpha, p)^{15}\text{N}$  data, was subsequently given by deBoer, Couture *et al.* (2012).

As noted, transfer reactions can provide information about reduced widths. In general, the interpretation of these experiments is subject to uncertainties in the optical potentials and the reaction mechanism (direct transfer versus multistep processes and/or compound-nuclear fusion). Sub-Coulomb measurements, where the energies in the entrance and exit channels are below the Coulomb barrier, provide a powerful way to minimize these uncertainties. For sub-Coulomb kinematics, other reaction mechanisms are suppressed relative to direct transfer and the Coulomb potentials dominate, leading to little dependence on the nuclear parts of the optical potentials. Because of the proximity of the 6.92-MeV  $2^+$  state and 7.12-MeV  $1^-$  state to the  $\alpha$  threshold, these states are ideal

for application of the sub-Coulomb  $\alpha$  transfer technique. While not quite as ideal, the 6.05-MeV  $0^+$  state and 6.13-MeV  $3^-$  state are still well suited for it. For the  $^{16}\text{O}$  ground state, it is unfortunately impossible to realize the kinematics required for sub-Coulomb transfer to be applicable, due to the large positive  $Q$  value for  $\alpha$ -transfer reactions to this state.

Brune *et al.* (1999) performed the first sub-Coulomb  $^{12}\text{C}(^6\text{Li}, d)^{16}\text{O}$  and  $^{12}\text{C}(^7\text{Li}, t)^{16}\text{O}$  experiments. Further, it was realized that analyzing the transfer cross section to determine the model-independent ANC, rather than the spectroscopic factor, removed unnecessary model dependence from the results. The ANC can be related to the reduced width for a particular channel radius by Eq. (44). The experiment determined the ANCs of the  $1^-$  and  $2^+$  subthreshold states with greatly reduced uncertainties and an  $R$ -matrix fit was used to deduce the impact on the capture extrapolation. The result was a greatly reduced uncertainty on the  $E2$  cross section and a value for the  $E1$  cross section that was roughly consistent with that deduced from the high-precision  $^{16}\text{N}(\beta\alpha)^{12}\text{C}$  spectrum.

Another low-energy cross section measurement was made by Rolfs's group at Bochum (Roters *et al.*, 1999). The experiment was performed again in inverse kinematics on a helium gas target similar to that used by Kettner *et al.* (1982) but also used by bismuth germanate detectors for the first time. The bismuth germanium oxide (BGO) detectors were 3 times as efficient compared to NaI detectors of equal size, allowing a further geometry measurement with the same statistics for a given beam time, reducing angular resolution effects. The setup was used to measure the  $E1$  cross section in far geometry at  $\theta_{\text{lab}} = 90^\circ$  and the angle-integrated cross section by placing a larger BGO in close geometry. An  $R$ -matrix fit was performed and the extrapolation predicted about an equal contribution from  $E1$  and  $E2$  multipolarities at  $E_{\text{c.m.}} = 300$  keV.

Gialanella *et al.* (2001) performed a measurement similar to that of Roters *et al.* (1999). The main result of this work was that a detailed Monte Carlo uncertainty analysis was performed for the  $R$ -matrix fit for the first time. The analysis highlighted the systematic differences between the different  $E1$  data sets. The main result was, that depending on which low-energy data were included in the fit, the destructive  $E1$  solution could not be statistically ruled out.

The first in a series of detailed angular distribution studies at Stuttgart was performed by Kunz *et al.* (2001). The measurements covered an energy range from  $E_{\text{c.m.}} = 0.95$  to 2.8 MeV at 20 energies and was notable because measurements were made at up to nine different angles and used high purity germanium detectors HPGe for the first time. The experiment benefited greatly from high background suppression provided by a BGO array allowing for reasonable statistics with less beam time than similar previous setups. Subsequent experiments were performed using the EUROGRAM and GANDI arrays. The EUROGRAM measurements covered an energy range from  $E_{\text{c.m.}} = 1.3$  to 2.78 MeV and are published in Assunção *et al.* (2006). The "turntable experiment" data are available in full only in the Ph.D. thesis of Fey (2004), but some details and data are given in Hammer *et al.* (2005a, 2005b). These measurements represent the largest set of angular distribution data currently

available, but their limited peer-review publication and apparently underestimated systematic errors (Brune and Sayre, 2013) have brought their validity into question.

Fleurot *et al.* (2005) developed a new indirect approach using Coulomb dissociation of the reaction  $^{208}\text{Pb}(^{16}\text{O}, ^{16}\text{O}^*)^{208}\text{Pb}$  for the first time. A preliminary experiment was performed at Kernfysisch Versneller Instituut KVI using the big bite spectrometer. The method should be more sensitive to the  $E2$  cross section, offering a complementary indirect approach to the  $\beta$ -delayed  $\alpha$  emission measurements. Reminiscent of high-energy transfer reaction studies, the reaction mechanism is quite complicated, requiring models for both the nuclear and Coulomb amplitudes of the cross section. The  $2^+$  states at  $E_x = 9.84$  and 11.52 MeV were populated and angular distributions were extracted. However, some of the angular distributions showed large systematic deviations from their expected values at certain angles. The results are encouraging but significant development in the technique and theory is likely required before reliable data can be obtained.

A detailed recoil separator measurement was made at DRAGON (Hutcheon *et al.*, 2003) at the TRIUMF-ISAC facility by Matei, Brune, and Massey (2008). The experiment covered a wide energy range from  $E_{\text{c.m.}} = 2.22$  to 5.42 MeV. This measurement focused on the  $E_x = 6.05$  MeV cascade transition and an  $R$ -matrix analysis of the data reported that this contribution was much larger ( $25_{-16}^{+15}$  keV b) at  $E_{\text{c.m.}} = 300$  keV than previously estimated. However, the interpretation of the data was later found to be in error and the later measurements of Schürmann *et al.* (2011) and Avila *et al.* (2015) confirmed a smaller value ( $\sim 2$ – $5$  keV b). In addition to the  $E_x = 6.05$  MeV transition, the total cross section was evaluated but is only available in the thesis of Matei (2006). Other cascade transition data were observed in the spectra but remain unanalyzed.

A remeasurement of the  $^{16}\text{N}(\beta\alpha)^{12}\text{C}$  spectrum was made by France *et al.* (2007) (Yale group) in an attempt to clarify the inconsistency issues in the different data sets. By convoluting the  $R$ -matrix fits of the previous data with the experimental resolution functions, it was reasserted that the TRIUMF data (Azuma *et al.*, 1994) were inconsistent with both their measurement and that of the Seattle measurement. In addition, the data from the previously unpublished experiments at Mainz (Hättig *et al.*, 1969; Hättig, Hünchen, and Wäffler, 1970; Neubeck, Schober, and Wäffler, 1974) and Seattle were made available, a very valuable service to the community.

Another measurement of the  $^{16}\text{N}(\beta\alpha)^{12}\text{C}$  spectrum was made soon after at Argonne National Laboratory by Tang *et al.* (2010). This experiment attempted to lessen the effects of  $\beta$  background and contaminant reactions by using the in-flight technique (Harss *et al.*, 2000) to create the  $^{16}\text{N}$  beam. To minimize the energy convolution of the spectrum by the catcher, thin carbon foils were used with thicknesses of only  $17(2) \mu\text{g}/\text{cm}^2$ . The resulting spectrum is similar to that of Azuma *et al.* (1994), but there are some very significant differences as discussed further in Sec. VI.D.

A low-energy measurement of the  $^{12}\text{C}(\alpha, \gamma)^{16}\text{O}$  reaction was made at the Research Laboratory for Nuclear Reactors at the Tokyo Institute of Technology by Makii *et al.* (2009). The

experiment concentrated on a very low-energy range, measuring at just two energies of  $E_\alpha = 2.000$  and  $2.270$  MeV. However, the goal of the experiment was a high accuracy measurement of the  $E1$  and  $E2$  cross sections at these energies where past experiments had showed considerable disagreement, especially in the  $E2$  cross section. This was accomplished by measuring at three critical angles,  $\theta_{\text{lab}} = 40^\circ, 90^\circ,$  and  $130^\circ,$  and in far geometry with small solid angles (as reflected by the  $Q$  coefficients) using time of flight. Compton suppressed NaI detectors were utilized, and targets were obtained by cracking  $^{13}\text{C}$  depleted methane gas. Additionally, the time-of-flight capability facilitated a detailed study of the different sources of background. These were primarily found to be secondary  $(n, \gamma)$  and  $(n, n'\gamma)$  reactions induced by neutrons from the  $^{13}\text{C}(\alpha, n)^{16}\text{O}$  reaction (Makii *et al.*, 2005). The deduced  $\sigma_{E1}$  and  $\sigma_{E2}$  cross sections were found with the smallest uncertainties to date in this region. They also showed significantly less scatter than many previous measurements, and in general are somewhat lower in overall cross section. Their energy dependence, albeit with only two data points, is in excellent agreement with previous  $R$ -matrix fits.

Sayre *et al.* (2012) used a novel method (Brune, 2001) of determining the  $E2$  interferences by measuring the energy integrated differential yield over the narrow low-energy  $2^+$  resonance, corresponding to the state at  $E_x = 9.85$  MeV, in the  $^{12}\text{C}(\alpha, \gamma)^{16}\text{O}$  reaction. The result was that the number of possible interference solutions with this resonance from the  $2^+$  subthreshold and the next higher-energy state at  $E_x = 11.51$  MeV could be reduced to two. These interference solutions will be discussed further in Sec. VII.B.

The measurement of Plag *et al.* (2012) investigated the low-energy cross section of  $^{12}\text{C}(\alpha, \gamma)^{16}\text{O}$  using a standard forward kinematics setup but using a nearly  $4\pi$  BaF<sub>2</sub> detector array for the first time. The BaF<sub>2</sub> detectors have the advantage that they are less sensitive to neutrons than HPGe detectors and are more efficient. Their disadvantage is a decreased energy resolution compared to HPGe's. The array is segmented in such a way that angular distributions at 12 angles can be extracted. The angular information was used to separate the  $E1$  and  $E2$  components using the traditional procedure of fitting to Legendre polynomials. In addition, the measurement also reported the sum of the cascade transition and therefore could give the total capture cross section.

A dedicated experimental campaign is ongoing at the Kyushu University Tandem Laboratory (KUTL) (Ikeda *et al.*, 2003) to measure the  $^{12}\text{C}(\alpha, \gamma)^{16}\text{O}$  reaction. The experiment aims at a direct measurement of the capture cross section down to  $E_{\text{c.m.}} = 0.7$  MeV using an inverse kinematics setup, time of flight, and a recoil separator. A windowless helium gas target is used with a pressure of  $\approx 25$  torr and beam intensities in excess of  $10 \mu\text{A}$ . The experimental development has steadily progressed with an ever improving setup. Total cross section measurements have been made at  $E_{\text{c.m.}} = 2.4$  and  $1.5$  MeV, and measurements are ongoing for  $E_{\text{c.m.}} = 1.2$  MeV (Yamaguchi *et al.*, 2014).

Significantly improved measurements have not been limited to the  $^{12}\text{C}(\alpha, \gamma)^{16}\text{O}$  reaction. The  $^{15}\text{N}(p, \gamma)^{16}\text{O}$  reaction has been the subject of several recent measurements at the

LUNA facility and the University of Notre Dame's nuclear science laboratory (Bemmerer *et al.*, 2009; LeBlanc *et al.*, 2010; Cacioli *et al.*, 2011; Imbriani *et al.*, 2012). This was highly motivated by new measurements of the bound-state proton ANCs in  $^{16}\text{O}$  (Mukhamedzhanov *et al.*, 2008), which gave strong evidence that the measurement of Rolfs and Rodney (1974) overestimated the low-energy cross section, a common theme. These complementary measurements resulted in a significant improvement in the uncertainty of this reaction at stellar energies (now at the  $\approx 5\%$  level). The  $^{15}\text{N}(p, \alpha)^{12}\text{C}$  reaction has also been reinvestigated using the Trojan Horse method (La Cognata *et al.*, 2007). Additional proton scattering data have been measured by deBoer, LeBlanc *et al.* (2012). The work of deBoer *et al.* (2013) combined the vast majority of the data above  $S_p$  and obtained a combined fit for all open reaction channels up to  $E_x \approx 14$  MeV. Preliminary fits were also made to a very limited set of  $^{12}\text{C}(\alpha, \gamma)^{16}\text{O}$  data.

The sub-Coulomb transfer reaction experiment of Avila *et al.* (2015) has reconfirmed the earlier measurements of the  $\alpha$  ANCs for the levels at  $E_x = 6.92$  ( $2^+$ ) and  $7.12$  ( $1^-$ ) MeV and additionally measured those of the  $E_x = 6.05$  ( $0^+$ ) and  $6.13$  ( $3^-$ ) MeV states for the first time. These measurements reconfirmed the assertion of Schürmann *et al.* (2011) that the large value for the low-energy  $S$  factor of the  $E_x = 6.05$  MeV transition given in Matei *et al.* (2006) was incorrect. However, the value found in Avila *et al.* (2015) is also in disagreement with that of Schürmann *et al.* (2011) since their assumed ANC was significantly smaller than that measured by Avila *et al.* (2015). These issues are discussed in detail in Sec. VI.C.

Another study was recently performed at KVI where the goal was to determine the total  $\beta\alpha$  branching ratio (Refsgaard *et al.*, 2016) for  $^{16}\text{N}(\beta\alpha)^{12}\text{C}$  decay. A value of  $[1.49 \pm 0.05(\text{stat})_{-0.10}^{\text{+0.0}}(\text{syst})] \times 10^{-5}$  was obtained, a 24% increase over the literature value of  $1.20(5) \times 10^{-5}$ . If correct, this could have an effect on the analysis of the  $^{16}\text{N}(\beta\alpha)^{12}\text{C}$  spectrum. The implications have not yet been fully explored.

Four recent comprehensive analyses of the  $^{12}\text{C}(\alpha, \gamma)^{16}\text{O}$  reaction are conspicuously absent from this section, those of Oulebsir *et al.* (2012), Schürmann *et al.* (2012), and Xu *et al.* (2013) (NACRE2), and An *et al.* (2015). A review of each of these analyses has been reserved for Sec. VIII, so that more detailed comparisons can be made with the present global analysis presented in Sec. VI.

#### D. Upcoming experiments

An experiment long under development is the measurement of the inverse photodisintegration reaction  $^{16}\text{O}(\gamma_0, \alpha)^{12}\text{C}$ . While this method has the limitation of being sensitive only to the ground state transition, this is the most important transition for the  $^{12}\text{C}(\alpha, \gamma)^{16}\text{O}$  reaction at stellar energies. Two independent groups have attempted to tackle the measurement using quite different measurement apparatuses but so far at the same beam facility, the high-intensity  $\gamma$ -ray source (HI $\gamma$ S) has been successful (Weller *et al.*, 2009). One setup uses a bubble chamber to detect the recoiling  $\alpha$  particles (DiGiovine *et al.*, 2015). The superheated liquid used in the chamber acts as both target and detection medium. A successful proof of

principle experiment was performed using a  $\text{C}_4\text{F}_{10}$  liquid by Ugalde *et al.* (2013) for the  $^{19}\text{F}(\gamma_0, \alpha)^{15}\text{N}$  reaction. Continued measurements are now taking place at Jefferson Laboratory.

Another experiment was proposed using an optical time projection chamber as described by Gai (2012). A successful experiment was performed to extract cross section data for the  $^{12}\text{C}(\gamma_0, \alpha)^8\text{Be}$  reaction as reported by Zimmerman *et al.* (2013). One great advantage of this setup is that it allows for the extraction of very detailed angular distributions. Both types of experiments are limited in their energy resolution by available  $\gamma$ -ray beams (resolution at HI $\gamma$ S  $\sim 200$  keV at these energies, for example). If the experimental techniques can be further developed, inverse measurements may be the best way to probe the low-energy cross section since the photodisintegration cross section is about 50 times larger than the capture cross section. Plans are also underway to perform these kinds of experiments at the upcoming Extreme Light Infrastructure–Nuclear Physics (ELI-NP) facility (Balabanski, 2015) where a significantly higher  $\gamma$  flux will be available.

Several recoil separator measurements are also planned for the  $^{12}\text{C}(\alpha, \gamma)^{16}\text{O}$  reaction. Further measurements have already begun at TRIUMF's DRAGON facility (Hutcheon *et al.*, 2003). The European recoil separator for the nuclear astrophysics ERNA recoil separator has also been recommissioned at the center for isotopic research on the cultural and environmental heritage CIRCE laboratory in Caserta, Italy. A reinvestigation of the  $^{12}\text{C}(\alpha, \gamma)^{16}\text{O}$  reaction is planned in order to improve upon the previously successful experimental campaigns (Schürmann *et al.*, 2005, 2011) in Bochum, Germany. In addition, the St. George recoil separator (Couder *et al.*, 2008) is currently in the commissioning phase and  $^{12}\text{C}(\alpha, \gamma)^{16}\text{O}$  is a reaction of primary interest.

Underground experimental facilities have also yet to weigh in. At LUNA (Costantini *et al.*, 2009),  $\alpha$  particle beams have been prohibited in the past due to the risk of creating background signals in other nearby experiments. This ban was lifted, however, and measurements of the  $^{12}\text{C}(\alpha, \gamma)^{16}\text{O}$  reaction are in the planning phase. However, the current LUNA facility can create only helium beams of up to  $E_\alpha = 400$  keV, a very difficult point at which to start the measurements. Therefore the first measurements may have to wait until the instillation of the new higher-energy LUNA MV facility is completed (scheduled for operation in 2019).

The compact accelerator system for performing astrophysical research CASPAR (Robertson *et al.*, 2016) is also nearing completion. This new underground facility located at the Sanford underground research facility in Lead, South Dakota will be the first underground nuclear astrophysics facility in the United States. At present a 1 MV KN accelerator has been installed and commissioning is underway. While the neutron producing reactions  $^{13}\text{C}(\alpha, n)^{16}\text{O}$  and  $^{22}\text{Ne}(\alpha, n)^{25}\text{Mg}$  are the planned flagship experiments, the  $^{12}\text{C}(\alpha, \gamma)^{16}\text{O}$  reaction will certainly be investigated in the future.

The Jinping underground laboratory is also currently under construction in Sichuan, China. The facility will have a high current (pA) 400 kV accelerator with an ECR source able to accelerate  $^4\text{He}^{++}$  beams up to  $E_\alpha = 800$  keV. One of the flagship experiments for the facility is to measure the  $^{12}\text{C}(\alpha, \gamma)^{16}\text{O}$  reaction at this energy ( $E_{\text{c.m.}} = 600$  keV). The

current goal is to perform this measurement by the end of 2019 (Liu, 2016).

As a final point, as experimental data are obtained with greater precision and at higher energies, experiments may soon become sensitive to less probable second order reaction channels. Some candidate decay channels are forbidden  $\beta$ ,  $(e^-e^+)\pi$ , internal conversion, and simultaneous multiple  $\gamma$  emission. While it is likely that most of these processes remain below current experimental detection thresholds, care should be taken to not forget they are possible. Some of these reactions could be used to further indirectly constrain the capture cross section. For example, detection of the  $\pi$  decay of the  $E_x = 6.05$  MeV transition is already being planned at the CIRCE laboratory (Guerro *et al.*, 2014; Tabassam and Mehboob, 2015).

### E. World data set

The previous sections described the many experimental endeavors that have provided a wealth of data for the understanding of the  $^{12}\text{C}(\alpha, \gamma)^{16}\text{O}$  reaction. Figure 3 shows how the capture data have evolved over time. Because the  $E1$  cross section dominates over much of the experimentally accessible region, these measurements are in reasonable agreement (barring some of the earliest measurements). While the agreement between the different  $E2$  data sets has certainly improved, there are still large disagreements between both different data sets and with theory. There are two major trends, a large scatter in the data in regions where the cross section should be smooth, and an increase in the cross section at low energy. Both of these phenomena are very common to measurements that push the limits of the experimental techniques employed. What is encouraging to see is that both these problems have lessened with more recent measurements. The trend of the data shows that attention should be made in determining accurate measurements of the  $E2$  cross section, since the  $E1$  is fairly well established. If the  $E2$  data can be improved to a level of consistency similar to the  $E1$ , this could lead to a significant reduction in the overall uncertainty in the extrapolation to low energy.

Reflecting back over the experimental data, two issues clearly stand out. The first is that of the overall normalization of the data. Future measurements will likely attempt to push to lower energies, yet it is important to remember that new measurements should not be limited to the lowest energy ranges. In particular, it is always useful to have at least one measurement near the maximum of the broad resonance at  $E_{\text{c.m.}} = 2.2$  MeV. In this way, so long as all the data can be considered to share the same overall systematic uncertainties, the normalization and shape of the data provide significantly better constraint on the extrapolation. The second issue is the splitting of the  $E1$  and  $E2$  data into separate cross sections. While this makes sense from a theory point of view, it leads to further assumptions in the analysis of the experimental data. This procedure may be responsible for the large scatter of the  $E2$  data. It also emphasizes the point that the differential cross section measurements (and even spectra) should be retained, since if these data were available, it would likely provide a better understanding of what caused these problems.

TABLE V. Summary of experimental data considered in the present analysis. The data included are in addition to what was already presented in Table I of deBoer *et al.* (2013). The reaction, the multipolarity of the  $\gamma$  rays measured, the source of the data, and the systematic uncertainty for each data set is noted. For several of the data sets, the absolute cross section was found by normalizing to previous data, so these entries are left blank as represented by the ellipses.

Reference	Reaction(s)	Source	$\sigma_{\text{syst}}$ (%)
Dyer and Barnes (1974)	$^{12}\text{C}(\alpha, \gamma_0)^{16}\text{O}$ , E1	Table 2, Fig. 6	10
Redder <i>et al.</i> (1987)	$^{12}\text{C}(\alpha, \gamma_{0,6,92,7,12})^{16}\text{O}$ , E1 and E2	Tables 1, 2, 3, Fig. 5	6
Kremer <i>et al.</i> (1988)	$^{12}\text{C}(\alpha, \gamma_0)^{16}\text{O}$ , E1	Private communication <sup>a</sup>	15
Buchmann <i>et al.</i> (1993) and Azuma <i>et al.</i> (1994)	$^{16}\text{N}(\beta\alpha)^{12}\text{C}$	Table 1	6
Ouellet <i>et al.</i> (1992) and Ouellet <i>et al.</i> (1996)	$^{12}\text{C}(\alpha, \gamma_0)^{16}\text{O}$ , E1 and E2	Tables 3, 4	...
Roters <i>et al.</i> (1999)	$^{12}\text{C}(\alpha, \gamma_0)^{16}\text{O}$ , E1 and E2	Table 1	...
Gialanella <i>et al.</i> (2001)	$^{12}\text{C}(\alpha, \gamma_0)^{16}\text{O}$ , E1	Table 2	9
Kunz <i>et al.</i> (2001)	$^{12}\text{C}(\alpha, \gamma_0)^{16}\text{O}$ , E1 and E2	Table 1, Fig. 3	...
Fey (2004)	$^{12}\text{C}(\alpha, \gamma_0)^{16}\text{O}$ , E1 and E2	Tables E1, E2, Figs. D1–D13	...
Schürmann <i>et al.</i> (2005)	$^{12}\text{C}(\alpha, \gamma)^{16}\text{O}$	Table 1	6.5
Assunção <i>et al.</i> (2006), and Brune and Sayre (2013)	$^{12}\text{C}(\alpha, \gamma_0)^{16}\text{O}$ , E1 and E2	Table 1 (3 parameters), Fig. 10	...
Makii <i>et al.</i> (2009)	$^{12}\text{C}(\alpha, \gamma_0)^{16}\text{O}$ , E1 and E2	Table 7	... <sup>b</sup>
Tischhauser <i>et al.</i> (2009)	$^{12}\text{C}(\alpha, \alpha)^{12}\text{C}$	EXFOR <sup>c</sup>	...
Tang <i>et al.</i> (2010)	$^{16}\text{N}(\beta\alpha)^{12}\text{C}$	Table 1	2
Schürmann <i>et al.</i> (2011)	$^{12}\text{C}(\alpha, \gamma_{\text{all}})^{16}\text{O}$	Table 1	6.5
Plag <i>et al.</i> (2012)	$^{12}\text{C}(\alpha, \gamma_{\text{all}})^{16}\text{O}$	Table III	< 10

<sup>a</sup>Data available in Supplemental Material [410].

<sup>b</sup>Statistical and systematic uncertainties combined.

<sup>c</sup>Data available as both yields (C1461002) and cross sections (C1461014).

For this review, a global  $R$ -matrix analysis has been performed in order to facilitate a better comparison of the different capture data sets and combine several recent results that have not yet been considered relative to other data. The method provides a standard framework to interpret the impact and gauge the level of agreement between all the types of measurements, both direct and indirect, on the extrapolation of the capture cross section. An attempt has been made to consider as much of the relevant experimental data as possible. However, there are a few cases in which the experimental data are clearly in very poor agreement and are therefore excluded from the analysis.

Most of the past data sets are found to be in reasonable agreement. The few that are excluded are the ground state capture data of Jaszczak, Gibbons, and Macklin (1970) and Jaszczak and Macklin (1970), both the ground state and cascade capture data of Kettner *et al.* (1982), the E2 data of Redder *et al.* (1987), and the  $E_x = 6.05$  MeV transition data of Matei *et al.* (2006). Further, the  $\beta$ -delayed  $\alpha$  data sets of Neubeck, Schober, and Wäffler (1974) and France *et al.* (2007), that is the Yale, Mainz, and Seattle data, are also excluded because not enough information regarding the target effect corrections has been given to perform a reanalysis of these data sets. This is discussed in more detail in Sec. VI.D. There have been several  $\alpha$  scattering experiments that have all been largely consistent only with improved uncertainties. For this reason only the most comprehensive data set of Tischhauser *et al.* (2009) is considered here. Further, the data reported by Assunção *et al.* (2006) are replaced by the corrected data presented by Brune and Sayre (2013).

Table V summarizes the data considered in the energy region below  $S_p$  in  $^{16}\text{O}$ , but the higher-energy data given in

Table I of deBoer *et al.* (2013) are also included. The table also summarizes where the actual numerical values of the data for each of the measurements were obtained. It is fortuitous that most of the E1 and E2 data, below  $S_p$ , have been made available in tabular form and therefore few had to be digitized from figures. Note that this was not true for the data from Jaszczak, Gibbons, and Macklin (1970) and Jaszczak and Macklin (1970), but these data have been excluded from the analysis as mentioned. Unfortunately much of the angular distribution data did have to be digitized. The figures for these data were obtained as listed in Table V. For ease of reference, Table II also summarizes the different kinds of targets that have been used in the various capture measurements.

## VI. R-MATRIX ANALYSIS OF $^{12}\text{C}(\alpha, \gamma)^{16}\text{O}$

As described in Sec. IV, the phenomenological  $R$ -matrix method is currently the preferred method for the analysis of the  $^{12}\text{C}(\alpha, \gamma)^{16}\text{O}$  reaction. This method has been used to simultaneously fit the experimental measurements that populate the  $^{16}\text{O}$  compound nucleus at energies below  $E_x \approx 14$  MeV (see Fig. 2). A modified version of the  $R$ -matrix code AZURE2 (Azuma *et al.*, 2010; Uberseder and deBoer, 2015) has been used. The code implements the generalized mathematical formalism described in Sec. IV.A including the alternate  $R$ -matrix formalism of Brune (2002) in order to more conveniently utilize level parameters from the literature. Another convince of this alternate parametrization is that boundary conditions are eliminated. However, the channel radii still need to be specified. In principle a different radius can be chosen for each channel, but it is common practice to only choose different radii for different partitions. For the best

TABLE VI. Masses and particle separation energies used in the  $R$ -matrix calculation. The quantities  $S_\alpha$ ,  $S_p$ , and  $S_{\alpha_1}$  represent the separation energies of an  $\alpha$  particle, a proton, and an  $\alpha$  particle with  $^{12}\text{C}$  in its first excited state, respectively. Masses are in atomic mass units. From Audi, Wapstra, and Thibault, 2003.

Parameter	Value
$S_\alpha$	7.161 92(1) MeV
$S_p$	12.127 41(1) MeV
$S_{\alpha_1}$	11.600 83(31) MeV
$m_p$	1.007 825 032 07(10)
$m_\alpha$	4.002 603 254 15(6)
$m(^{12}\text{C})$	12
$m(^{15}\text{N})$	15.000 108 898 23(15)
$m(^{16}\text{N})$	16.006 101 658(2815)
$m(^{16}\text{O})$	15.994 914 619 56(16)

fit, values of  $a_{\alpha_0} = a_{\alpha_1} = 5.43$  fm and  $a_{p_0} = 5.03$  fm were found. Discussion of the sensitivity of the fit to the choice of channel radii is given in Sec. VII.C.

Several physical quantities have uncertainties much smaller than those from other sources and are treated as constants in the analysis. These are summarized in Table VI. Entrance channel angular momenta were considered up to  $l = 8$ . Unless specifically labeled otherwise, all quantities are given in the center-of-mass reference frame.

The present work is an extension of the  $R$ -matrix analysis given by deBoer *et al.* (2013). In that work, a global  $R$ -matrix fit was achieved for data belonging to all the open channels above the first excited state  $\alpha$  particle ( $S_{\alpha_1} = 11.60$  MeV) and proton ( $S_p = 12.13$  MeV) separation energies and below  $E_x \approx 14.0$  MeV in  $^{16}\text{O}$  (see Fig. 2). In the present analysis, all the previous channels and data are again considered, but, in addition, the lower energy data for the  $\alpha$  capture reaction and the  $^{16}\text{N}(\beta\alpha)^{12}\text{C}$  spectra are included. This global, simultaneous, analysis considers over 15 000 data points, the majority of the data available in the literature. In addition to the primary aim of facilitating a comparison between the different data sets, this global analysis has the potential to place more stringent constraints on the extrapolation of the  $^{12}\text{C}(\alpha, \gamma)^{16}\text{O}$  reaction to stellar energies. This is mainly the result of the inclusion of the higher-energy data and the extension of the phenomenological model to those energies. While the resonances at higher energy do not have a strong impact on the low-energy cross section, an explicit fitting to these higher energies places much more stringent limits on possible low-energy tail contributions of even higher-lying resonances. As will be described, this has been, and remains, one of the largest uncertainties in the extrapolation of the cross section to stellar energies.

#### A. “Best fit” procedure

One of the main reasons that the  $^{12}\text{C}(\alpha, \gamma)^{16}\text{O}$  cross section has such large uncertainties in the extrapolation is that there are different possible fit solutions, corresponding to the different relative interference patterns of the different resonances, depending on different assumptions and interpretations of the data. However, as more and more measurements

have been undertaken, these ambiguities have steadily decreased. Here the assumptions of this analysis are described and a large amount of the remainder of this work details what happens when these assumptions are bent or broken in order to more fully gauge the uncertainties.

As with most analyses of this kind, the path to the final solution was not a straightforward procedure but was an iterative process. In this section the details of the “best fit” are given. This was not the fit with the lowest overall  $\chi^2$ , nor was it the fit that allowed all possible parameters to vary freely, but it is believed to be the most physically reasonable one. In principle a  $\chi^2$  minimization should lead to the best solution, but this assumes that all of the uncertainties have been correctly quantified in the data, and this is certainly not the case. While the  $\chi^2$  minimization also includes a term for a constant systematic uncertainty, and often this is a dominant contribution, energy and angular dependent systematic uncertainties are also present, which may or may not have been quantified. These usually have a smaller effect, but in some cases, especially when the statistical uncertainties become very small, it is very likely that these are the cause of poorer quality fits.

The assumptions that brought about the best fit are as follows:

- (•) The ANCs, as determined from modern transfer reactions, are reliable and their values are fixed in the fit.
- (•)  $\gamma$ -ray widths of the subthreshold states are reliable and are fixed in the fit.
- (•) Fits are unacceptable if the normalization factors of all data sets in a given channel systematically deviate (the exception to this rule is the  $E2$  ground state transition data).

Important conclusions brought about by a thorough review of the data and the  $R$ -matrix fits are as follows:

- (•) The  $^{12}\text{C}(\alpha, \gamma)^{16}\text{O}$   $E2$  ground state transition cross section data show large deviations between one another.
- (•) Background pole contributions are negligible for the  $^{12}\text{C}(\alpha, \gamma)^{16}\text{O}$  capture data for all transitions.
- (•) For the ground state  $^{12}\text{C}(\alpha, \gamma)^{16}\text{O}$  data, the low-energy measurements yielding larger cross sections are more likely to be affected by unreported systematic uncertainties.

These assumptions and conclusions were in most cases not assumed *a priori*, but came about through the iteration of many test calculations. Of course these assumptions, although logically motivated, are still somewhat subjective and may have (in fact have greatly) varied from one evaluator to the next over the years. Therefore it is of the utmost importance that these assumptions are tested rigorously and the sensitivity of the fit must be gauged for each one. This is what much of Sec. VII is devoted to, a quantification of these assumptions into uncertainties on the extrapolation of the cross section to stellar energies. Throughout this work there are discussions of these different assumptions but a brief discussion of all of them is first given here.

While ANCs can be determined, in theory, through compound nucleus reactions such as scattering, capture, and  $\beta$ -delayed particle emission, there are nearly always

complications. These analyses are usually performed using a phenomenological  $R$ -matrix analysis but are often complicated by the presence of broad resonance contributions and the need for background contributions. It is our experience that unless a capture cross section can be described well using only the external capture model (i.e., no broad resonances are present) it can be difficult to extract a reliable value for ANC's from this type of data. For scattering it is nearly always the case that many background poles are needed to compensate for the potential phase shift that is only approximately reproduced by the hard-sphere phase shifts. The situation is similar for  $^{16}\text{N}(\beta\alpha)^{12}\text{C}$  data where again background contributions are often required. Further, even small errors in the corrections of the data for experimental effects can affect the ANC determinations.

Transfer reactions have their own issues, namely, that there are theoretical uncertainties that can be difficult to quantify, but recent sub-Coulomb measurements seem to have succeeded in limiting these effects so that ANC's can be extracted reliably to about the 10% uncertainty level. This has been confirmed by measurements by different groups using different experimental setups that yield consistent results. Certainly more experiments need to be performed to better verify this claim, but at this time they seem to be the most reliable and accurate method.

The only  $\gamma$ -ray widths of subthreshold states that have a large impact on the cross section determination are the ground state widths of the  $E_x = 6.92$  and  $7.12$  MeV states which make strong subthreshold contributions to the ground state  $E2$  and  $E1$  cross sections, respectively. These widths are known to better than 5% total uncertainty and have been verified by several different measurements, although they have not been studied recently.

Unless there is some reason to suspect that all data for a specific reaction suffer from a shared systematic uncertainty, it seems reasonable to assume that the weighted average of different measurements should be very close to 1. This has been found to be true for all of the reaction channels studied here except for the  $^{12}\text{C}(\alpha, \gamma)^{16}\text{O}$   $E2$  ground state data. These data show large scatter that is not reflected by the experimental error bars and has been found to be systematically too large in value. These issues have lessened with more recent measurements. The issue here has always been the attempt to determine a small  $E2$  component from a cross section that is dominated by the broad  $E1$  resonance at  $E_x = 9.59$  MeV.

With the addition of the higher-energy states in this analysis, a reasonable fit can be achieved for both the  $E1$  and  $E2$  ground state capture transition data without any background contributions. This does not mean that the present  $R$ -matrix analysis does not have any background poles, several are still required to fit the  $^{12}\text{C}(\alpha, \alpha_0)^{12}$ ,  $^{15}\text{N}(p, p_0)^{15}\text{N}$ , and  $^{16}\text{N}(\beta\alpha)^{12}\text{C}$  reaction data. The physical justification for this is seen in the higher-energy  $^{12}\text{C}(\alpha, \gamma)^{16}\text{O}$  data of [Snover, Adelberger, and Brown \(1974\)](#) where it was shown that the cross section, for both  $E1$  and  $E2$  multipolarities, becomes weak at high energies and does not show any resonances that compare in strength to those that correspond to the  $1^-$  levels  $E_x = 12.45$  and  $13.09$  MeV. Since these two strong higher-energy states are now included

explicitly, they should account for the majority of the higher-energy background contributions.

For the  $E2$  ground state transition data, more recent measurements have achieved significantly more consistent measurements ([Makii \*et al.\*, 2009](#); [Plag \*et al.\*, 2012](#)). This is also true for the  $E1$  ground state transition data, but to a lesser extreme. This can be seen clearly in [Fig. 3](#). From [Jaszczak, Gibbons, and Macklin \(1970\)](#) to [Plag \*et al.\* \(2012\)](#), there has been a general decrease in the values given for the cross sections on the low-energy side of the  $1^-$  resonance. In general, background contaminations are often underestimated for the yield extraction in low statistics measurements and this trend is quite prevalent in the literature.

### 1. Systematic uncertainty $\chi^2$ term

Every data set has some systematic uncertainty, which represents the experimentalist's best estimate of contributions to the uncertainty that come from sources that are not statistical. In many cases these uncertainties are approximated by a constant factor (e.g., target thickness, beam intensity, efficiency, etc.) that affects the entire data set. However, as measurements become more precise, the quantification of the systematic uncertainties often becomes increasingly complicated.

As the first step, it is critical to separate the uncertainties into contributions from point-to-point and overall systematic uncertainties in order to perform the  $\chi^2$  minimization accurately. For analyses that consider multiple data sets, each with independent systematic uncertainties, this becomes even more crucial. This has been shown some time ago by [Dodder \*et al.\* \(1977\)](#), yet has been neglected even in some relatively recent and comprehensive analyses ([Hammer \*et al.\*, 2005b](#)). Further, it was shown that the method of introducing the systematic uncertainty term into the  $\chi^2$  fitting solves Peelle's pertinent puzzle or at least makes the effect negligible ([Hale, 2004](#); [Carlson \*et al.\*, 2009](#)).

For the approximation that the systematic uncertainty of an individual data set can be treated as constant, it is included in the  $\chi^2$  fit using the method described in [Dodder \*et al.\* \(1977\)](#), [D'Agostini \(1994\)](#), and [Schürmann \*et al.\* \(2012\)](#) and is given by

$$\chi^2 = \sum_i \left( \sum_j R_{ij}^2 + \frac{(n_i - 1)^2}{\sigma_{\text{sys},i}^2} \right), \quad (87)$$

$$R_{ij} = \frac{f(x_{i,j}) - n_i y_{i,j}}{n_i \sigma_{i,j}}, \quad (88)$$

where  $n_i$  is the normalization factor of an individual data set,  $f(x_{i,j})$  is the value of the cross section from the  $R$ -matrix fit,  $y_{i,j}$  is the experimental cross section of a given data point,  $\sigma_{i,j}$  is the statistical uncertainty of the data point, and  $\sigma_{\text{sys},i}^2$  is the overall fractional systematic uncertainty of the data set. A summary of the systematic uncertainties of the different experiments is listed in [Table V](#). Since several of the capture measurements were normalized to earlier measurements, several lack independent normalizations (indicated by the  $\dots$  in [Table V](#)). In these cases, the normalizations of the data

TABLE VII. Normalization factors ( $n_i$ ),  $\chi^2$ , and number of data points ( $N$ ) for excitation curve data resulting from the  $R$ -matrix fit. Note the reasonable scattering in the normalizations of the  $E1$  data compared to the much larger scatter present in the  $E2$  data. Additionally, note that the reduced  $\chi^2$  values for the  $^{16}\text{N}(\beta\alpha)^{12}\text{C}$  and  $^{12}\text{C}(\alpha, \alpha_0)^{12}\text{C}$  data sets are significantly greater than 1. The effect of this on the uncertainty estimate of the extrapolated cross section is discussed in Sec. VII.F.

Reaction	Reference	$\sigma_{\text{sys},i}$ %	Norm. ( $n_i$ )	$\chi^2$	$L^{-1}$	$N$
$^{12}\text{C}(\alpha, \gamma_0)^{16}\text{O}$	Brune and Sayre (2013)	9	1.12	20.3	14.0	16
$^{12}\text{C}(\alpha, \gamma_0)^{16}\text{O}$ ( $28^\circ$ )	Ouellet <i>et al.</i> (1996)	...	1.200	18.4	14.9	15
( $60^\circ$ )	Ouellet <i>et al.</i> (1996)	...	0.970	91.7	20.7	16
( $90^\circ$ )	Ouellet <i>et al.</i> (1996)	...	1.046	78.6	18.0	16
( $90^\circ$ )	Ouellet <i>et al.</i> (1996)	...	0.957	86.7	18.7	16
( $120^\circ$ )	Ouellet <i>et al.</i> (1996)	...	1.068	45.3	14.5	15
( $143^\circ$ )	Ouellet <i>et al.</i> (1996)	...	1.117	28.7	15.6	15
( $40^\circ$ )	Makii <i>et al.</i> (2009)	...	1.085	1.55	2.23	2
( $90^\circ$ )	Makii <i>et al.</i> (2009)	...	0.926	0.527	1.81	2
( $130^\circ$ )	Makii <i>et al.</i> (2009)	...	0.842	1.982	2.50	2
$^{12}\text{C}(\alpha, \gamma_0)^{16}\text{O}$ ( $E1$ )	Dyer and Barnes (1974)	10	1.031	55.9	25.2	24
	Redder <i>et al.</i> (1987)	6	1.006	72.8	29.3	26
	Kremer <i>et al.</i> (1988)	15	1.110	18.4	13.1	12
	Ouellet <i>et al.</i> (1996)	...	0.957	44.8	11.6	9
	Roters <i>et al.</i> (1999)	...	1.092	15.4	12.0	13
	Gialanella <i>et al.</i> (2001)	9	0.913	27.3	18.5	20
	Kunz <i>et al.</i> (2001)	...	1.011	12.4	15.6	19
	Fey (2004)	...	1.000	16.9	8.3	11
	Makii <i>et al.</i> (2009)	...	0.959	0.43	1.47	2
	Schürmann <i>et al.</i> (2011)	6.5	0.994	0.605	0.95	1
	Plag <i>et al.</i> (2012)	12–21	1.017	2.01	3.25	4
$^{12}\text{C}(\alpha, \gamma_0)^{16}\text{O}$ ( $E2$ )	Ouellet <i>et al.</i> (1996)	...	0.883	3.42	5.70	5
	Roters <i>et al.</i> (1999)	...	1.698	0.246	1.54	2
	Kunz <i>et al.</i> (2001)	...	1.065	23.2	13.6	11
	Fey (2004)	...	1.364	15.1	12.8	12
	Makii <i>et al.</i> (2009)	...	1.095	0.46	1.63	2
	Schürmann <i>et al.</i> (2011)	6.5	0.958	29.4	8.0	7
	Plag <i>et al.</i> (2012)	30–61	1.016	0.342	2.93	5
$^{12}\text{C}(\alpha, \gamma_{6.05})^{16}\text{O}$ ( $E1$ )	Schürmann <i>et al.</i> (2011)	6.5	1.00	1.71	1.08	1
( $E2$ )	Schürmann <i>et al.</i> (2011)	6.5	1.19	16.5	9.4	6
$^{12}\text{C}(\alpha, \gamma_{6.13})^{16}\text{O}$	Schürmann <i>et al.</i> (2011)	6.5	1.03	8.9	5.2	7
$^{12}\text{C}(\alpha, \gamma_{6.92})^{16}\text{O}$	Redder <i>et al.</i> (1987)	...	0.261	26.4	42.8	25
	Kunz (2002)	...	0.644	9.0	21.0	12
	Schürmann <i>et al.</i> (2011)	6.5	0.993	18.1	12.7	7
$^{12}\text{C}(\alpha, \gamma_{7.12})^{16}\text{O}$	Redder <i>et al.</i> (1987)	...	0.265	52.4	29.5	24
	Kunz (2002)	...	0.469	8.3	16.7	12
	Schürmann <i>et al.</i> (2011)	6.5	1.00	3.64	6.6	7
$^{12}\text{C}(\alpha, \gamma_{\text{total}})^{16}\text{O}$	Schürmann <i>et al.</i> (2005)	6.5	0.926	301	136	76
	Plag <i>et al.</i> (2012)	8–21	1.08	4.90	4.18	4
	Yamaguchi <i>et al.</i> (2014)	...	0.972	0.982	6.2	3
$^{16}\text{N}(\beta\alpha)^{12}\text{C}$	Azuma <i>et al.</i> (1994)	5	0.91	496	122	87
	Tang <i>et al.</i> (2010)	2	1.13	545	135	88
$^{12}\text{C}(\alpha, \alpha)^{12}\text{C}$	Tischhauser <i>et al.</i> (2009)	...	...	56 021	11 775	9728

are allowed to vary freely in the fitting. Table VII lists the normalization factors for the excitation curve data resulting from the  $R$ -matrix fit and compares them to the experimental systematic uncertainties.

Ideally all parameters of the  $R$ -matrix fit could be varied simultaneously to achieve the best fit, but this situation could not be realized. The current analysis has 64 fit parameters not including the normalization parameters. These parameters correspond to the partial widths and energies of the 12 particle unbound states in  $^{16}\text{O}$  that were used to describe the broad energy structure of the reaction cross sections. An additional

seven background poles were necessary, primarily to reproduce the scattering reaction data. However, the best fit contains no background poles for the  $^{12}\text{C}(\alpha, \gamma)^{16}\text{O}$  reaction, for any of the transitions. Five subthreshold states and five levels corresponding to narrow resonances were also included, with their ANCs or partial particle widths and  $\gamma$ -decay widths fixed to values from the literature. Tables XXI and XXII in Appendix A give the  $R$ -matrix parameters necessary to reproduce the best fit of this analysis. The parameters in bold indicate those actually used for the fitting. Other parameters were fixed at values taken from the literature. Additionally,

Table XXIV gives the reduced-width amplitudes associated with the  $\gamma$ -ray widths, subdivided into their internal end channel contributions. Note that these are not additional fitting parameters.

It should be mentioned here that many different fitting combinations were investigated and are discussed, but for clarity and practicality only the details of the best fit are given in Tables XXI, XXII, and XXIII. For example, in the subsequent sections that investigate the uncertainties in the fitting, background poles for the  $^{12}\text{C}(\alpha, \gamma)^{16}\text{O}$  reaction are introduced, but these are absent from the parameter tables since they are not included in the best fit.

With such a complicated fitting, it is reasonable to question whether the fit is unique. That is, can a similar quality fit be obtained but with a very different parameter set? For levels in the  $R$  matrix that correspond to physical levels, it is believed that these values are in fact unique and well defined, at least to within their uncertainties. This can be said with some confidence because of the unitarity condition of the  $R$ -matrix theory, but this does apply only for the particle channels. Further, it is often the case that only the partial width that corresponds to the lowest orbital angular momentum channel is used in the fitting. Higher orbital angular momentum channels have been investigated but had values consistent with zero for the present experimental data. When more precise data are obtained, this assumption should be reinvestigated.

For the  $\gamma$ -ray channels, unitarity is not enforced, as this reaction mechanism is introduced into the theory as a perturbation. This is well satisfied in the current case because the capture cross sections are always much smaller than the nuclear ones. However, because the particle width(s) of a given level are always much larger than the  $\gamma$ -ray widths, they determine the resonance's total width while the  $\gamma$ -ray widths effectively determine only the height of the resonance. In this way the capture data uniquely constrain the total  $\gamma$ -ray widths. However, it is sometimes possible that more than one  $\gamma$ -ray multipolarity can contribute and may be of similar intensity. This is especially true for the well-known case when  $E2$  and  $M1$  decays are both possible and it is often true that the data may not uniquely determine the multipolarity. Therefore the values of the total  $\gamma$ -ray widths are likely unique, but their multiplicities should be viewed as tentative assignments. Additionally, similar to the particle channels, higher order multiplicities may also be possible. The fit was tested for sensitivities to these higher order terms but again they were found to not be significant considering the uncertainties of the current data.

What are more ambiguous are the interference combinations that are possible for the capture data. The ground state inference patterns appear to now be well known as discussed in Sec. VII.B, but some of these assignments are based on only a single measurement or only a few data points. The ambiguity is much greater for the cascade transitions. Very few data exist for these transitions and often the interference signs have been deduced based on a few number of data points and the constraint imposed by the total capture cross section measurements. The situation is even worse above  $S_p$ ; here the interference signs are only constrained by their effects on the lower energy data.

However, since the cascade transitions are dominated by external capture at low energies, these different solutions have a negligible effect on the low-energy extrapolation.

Finally, the values of the background poles are certainly not unique. This is perfectly acceptable since their energies are rather arbitrary. The only condition is that these energies should be significantly larger than the highest energy data points so that they can provide an approximately energy-independent underlying background that represents the sum of the low-energy tails of all higher-lying resonances. What is unique is the magnitude of the underlying background provided by the background poles, and this contribution can be produced many different equivalent ways. For example, the background poles are often placed at  $E_x = 20$  MeV for the best fit, but an investigation of the extension of the capture cross section to higher energies necessitates moving the background poles up to  $E_x = 40$  MeV. While the values of the partial widths for these poles are of course much different than those at lower energy, the cross section that they produce at low energy is relatively unchanged.

## 2. Corrections for experimental effects

It is a simple fact that measurements made in the laboratory are never actually the true cross sections, statistical variations aside. Even for arguably the simplest of experimental data, for example,  $^{12}\text{C}(\alpha, \alpha_0)^{12}\text{C}$ , the reported quantities are often expressed as yields instead of actual cross sections. Even quantities labeled as cross sections in the literature are often only normalized yields, which may or may not have been subjected to any number of different deconvolution techniques and other corrections for experimental effects. A general formula relating the experimental yield  $Y(E_b)$  at mean beam-particle energy  $E_b$  to true cross section  $\sigma(E)$  is

$$Y(E_b) = \int_{E_b-\Delta}^{E_b} \int_0^{\infty} \frac{\sigma(E)}{\epsilon(E'_b)} g(E - E'_b) dE dE'_b. \quad (89)$$

Here the function  $g(E - E_b)$  describes the spreading of the beam-particle energy around the mean energy,  $\epsilon(E_b)$  is the stopping power that describes the energy loss of the beam particles as they pass through the target material, and  $\Delta$  is the total energy loss in the target. Other effects, such as energy straggling, may also be important depending on the experimental conditions, but Eq. (89) serves as a general enough example. As is commonly implemented in the case of charged-particle beams, the spreading function is approximated by a Gaussian function

$$g(E - E_b) = \frac{1}{\sqrt{2\pi\sigma_b^2}} \exp\left[-\frac{(E - E_b)^2}{2\sigma_b^2}\right], \quad (90)$$

where  $\sigma_b$  defines the energy width of the beam.

In this analysis, Eq. (89) is used to approximately correct for the resolution of the experimental measurements, as most of the data under analysis assumes this sort of convolution function. It should be kept in mind that this is an approximate method and that for data with very small uncertainties this simple method may not prove accurate enough. In this

analysis a good example is the  $\beta$ -delayed  $\alpha$  emission data. Possible failings of the deconvolution method have been discussed by [Buchmann, Ruprecht, and Ruiz \(2009\)](#) and are described further in Sec. VI.D.

## B. Ground state transition

The largest contribution to the  $^{12}\text{C}(\alpha, \gamma)^{16}\text{O}$  cross section at low energy ( $E_{\text{c.m.}} \approx 300$  keV) is the ground state transition. This is illustrated in Fig. 6.<sup>1</sup> The  $E1$  and  $E2$  multipoles dominate the low-energy cross section in nearly equal amplitudes as discussed in Sec. III. At higher energies, high order multipoles could become significant, although this has not yet been observed. A prime candidate is the ground state  $E3$  decay of the broad  $3^-$  level at  $E_x = 11.49$  MeV.

The separation of the ground state capture cross section into  $E1$  and  $E2$  multipoles ( $\sigma_{E1}$  and  $\sigma_{E2}$ ) dates back to [Dyer and Barnes \(1974\)](#). As discussed in Sec. V, at that time  $\sigma_{E1}$  was thought to dominate the low-energy cross section, which was determined by decay through the  $1^-$  subthreshold state and its interference with the unbound level at  $E_x = 9.59$  MeV. The  $E1$  cross section was also easily isolated experimentally by measuring at  $90^\circ$  where  $\sigma_{E2}$  and the interference terms are zero (see Sec. V.A). This then also greatly simplifies the mathematics of the analysis, which at the time was usually a three level  $R$ -matrix fit. Complications arose when it was found that  $\sigma_{E2}$  was also significant (see Sec. V.B). From an experimental standpoint, the immediate difficulty was that there is no angle where  $\sigma_{E1}$  is zero and  $\sigma_{E2}$  is not, therefore  $\sigma_{E2}$  must be deduced indirectly. The traditional technique is to measure the differential cross section at several angles, spanning a wide angular range, and then perform a fit to a theory motivated function representing the angular distribution. If only  $E1$  and  $E2$  multipoles contribute to the cross section, the differential cross section can be written as ([Dyer and Barnes, 1974](#))

$$\begin{aligned}
 4\pi \left( \frac{d\sigma}{d\Omega} \right) (E, \theta_\gamma) &= \sigma_{E1}(E) [1 - Q_2 P_2(\cos \theta_\gamma)] \\
 &+ \sigma_{E2}(E) \left[ 1 + \frac{5}{7} Q_2 P_2(\cos \theta_\gamma) - \frac{12}{7} Q_4 P_4(\cos \theta_\gamma) \right] \\
 &+ 6 \cos \phi(E) \sqrt{\frac{\sigma_{E1}(E) \sigma_{E2}(E)}{5}} [Q_1 P_1(\cos \theta_\gamma) \\
 &- Q_3 P_3(\cos \theta_\gamma)], \tag{91}
 \end{aligned}$$

where  $P_n \cos(\theta_\gamma)$  are the Legendre polynomials,  $Q_n$  are the geometric correction factors ([Rose, 1953](#)), and  $\phi$  is the difference in phase between the  $E1$  and  $E2$  transition matrix elements. The phase difference can be written as

<sup>1</sup>While the  $E1$  constructive solution is shown here, this statement is true even for a destructive  $E1$  solution, since the  $E2$  cross section still dominates over the cascade transition contributions. There is no  $E2$  interference pattern that has been considered viable that makes its contribution of similar magnitude or smaller than the cascade contributions.

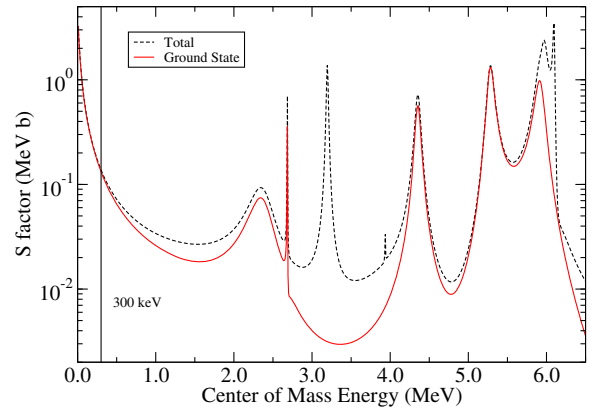


FIG. 6. The total  $^{12}\text{C}(\alpha, \gamma)^{16}\text{O}$   $S$  factor (dashed black line) compared to the ground state transition (red line) based on the  $R$ -matrix analysis of this work. The ground state transition dominates at stellar energies.  $E_{\text{c.m.}} = 300$  keV is indicated by the vertical black line. Experimental measurements of the ground state transition have reached as low as  $E_{\text{c.m.}} \approx 1$  MeV.

$$\cos \phi = \cos[\delta_{\alpha 1} - \delta_{\alpha 2} - \tan^{-1}(\eta/2)], \tag{92}$$

where  $\delta_{\alpha l, 2}$  are the angular momentum  $l = 1$  and  $2\alpha$  scattering phase shifts [see Eq. (25)] and  $\eta$  is the Sommerfeld parameter. As discussed in Sec. IV.D, Eq. (92) is very general and is a consequence of Watson's theorem. It is also fully consistent with the  $R$ -matrix formalism used here. This simply illustrates the connection between the scattering cross section, from which the phase shifts can be extracted, and the capture cross section. Since the scattering cross section is large, the phase shifts can be easily and accurately measured and used to constrain  $\cos \phi$  up to an overall sign ([Brune, 2001](#)). If  $\sigma_{E1}$  is then determined from measurements at  $90^\circ$ , then  $\sigma_{E2}$  is essentially the only undetermined quantity. In principle this provides a straightforward way of obtaining  $\sigma_{E2}$  but there are complications. The main issue is that  $\sigma_{E1}$  is much larger than

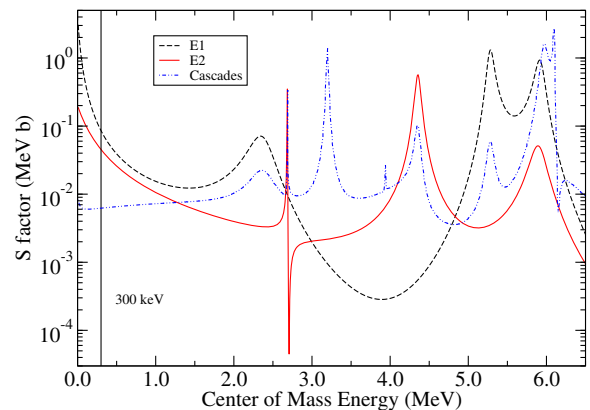


FIG. 7. Comparison of predicted  $E1$  (dashed black line),  $E2$  (solid red line), and the sum of the cascade transitions (dot-dot-dashed blue line) cross sections. Over much of the low-energy range covered by most measurements, the broad resonance corresponding to the  $E1$  decay of the  $1^-$  level at  $E_x = 9.59$  MeV dominates over the  $E2$  contribution. This has made the experimental determination of the  $E2$  cross section extremely challenging.

$\sigma_{E2}$  over much of the experimentally accessed low-energy range because the cross section is dominated by the broad resonance corresponding to the  $1^-$  level at  $E_x = 9.59$  MeV as illustrated in Fig. 7. The fact that the interference term is proportional to  $\sqrt{\sigma_{E1}\sigma_{E2}}$  increases the sensitivity to the small  $E2$  component, but in practice this approach has yielded a large scatter in the  $\sigma_{E2}$  data as shown in Figs. 3 and 9. The scatter is far outside the acceptable statistical range and suggests that systematic errors in the radiative capture measurements have been underestimated.

One way to understand the sign ambiguity in  $\cos \phi$  is that the nuclear phase shifts and arctangent function in Eq. (92) are ambiguous by multiples of  $\pi$ . However, in our  $R$ -matrix formalism, the sign of  $\cos \phi$  is determined by the phases of the transition matrix elements which are ultimately determined by the signs of the reduced-width amplitudes (phase shifts are inherently ambiguous and are not used in the calculations). Note also that a generalization of Watson's theorem still applies when inelastic scattering and reaction channels are open, such as is the case shown in Fig. 22. In this situation, the phases of the radiative capture transition matrix elements are determined by the  $R$ -matrix parameters for the nuclear channels, as shown by Eq. (75), which can be constrained if sufficient data in the nuclear channels are available.

For the  $E1$  data, only decays from  $1^-$  levels can contribute because the spins of the entrance channel particles and the final state are all zero. The different levels that are considered are the subthreshold state at  $E_x = 7.12$  MeV and the unbound states at  $E_x = 9.59$ , 12.45, and 13.10 MeV. While the two higher-lying states are 3 to 4 MeV above the lowest energy resonance, their large total widths and ground state  $\gamma$ -ray decay widths make their contributions significant even at low energies. The different contributions used to reproduce the cross section data are shown in Fig. 8. This  $E1$  ground state cross section is unique in that it has a very weak external capture contribution [see Sec. IV.D, Eq. (62)]. It does, however, have a strong subthreshold contribution from the  $E_x = 7.12$  MeV state. The  $\text{ANC}_\alpha$  together with the energy and the  $\Gamma_{\gamma_0}$  of this state characterize the strength of the subthreshold contribution. A discussion of the subthreshold state parameters is deferred to Sec. VI.F. Also note that the magnitudes of the contributions from the subthreshold state and all three unbound states are similar at  $E_{\text{c.m.}} \approx 1.2$  MeV. The cross section that is shown in the figures of this work is the result of the choice of the constructive  $E1$  interference solution. A discussion of why this particular solution has been chosen is given in Sec. VII.B.

The situation is similar for the  $E2$  data where only  $2^+$  states can contribute. The states that are considered explicitly are the subthreshold at  $E_x = 6.92$  MeV and two unbound ones at  $E_x = 11.51$  and 12.96 MeV. The narrow state at  $E_x = 9.84$  MeV is also included but its energy and partial widths are all fixed to the values in the literature (Tilley, Weller, and Cheves, 1993). Further, as suggested by Sayre *et al.* (2012), experimental data in the vicinity of this state ( $2 < E_{\text{c.m.}} < 3$  MeV) have been excluded because the deconvolution of these data from yield to cross sections is unreliable (see Figs. 3 and 9). The interference sign is also fixed to the one determined by Sayre *et al.* (2012). The different

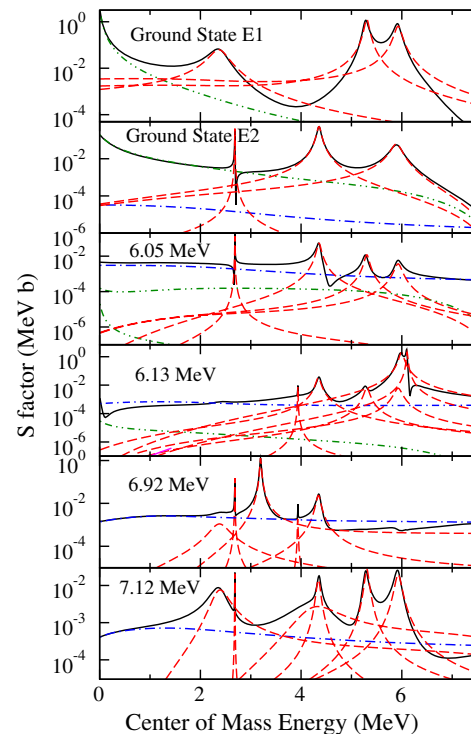


FIG. 8.  $S$  factors of the different transitions that make up the total  $^{12}\text{C}(\alpha, \gamma)^{16}\text{O}$  cross section. The ground state is further divided into  $E1$  and  $E2$  multiplicities. Dashed red lines indicate individual resonance contributions (single-level calculation), dash-dotted blue lines are the hard-sphere contributions to the external capture, dash-dot-dotted green lines are subthreshold contributions, and the solid black lines represent the total with interferences included (i.e., individual contributions summed coherently).

reaction components used for the fit are shown in Fig. 8. The subthreshold state completely dominates at low energy and is a slowly varying function of energy. Note that it is dominant all the way up to  $E_{\text{c.m.}} \approx 3.5$  MeV. Only one experimental measurement has been made at these higher energies, that of Schürmann *et al.* (2011). There is a small  $E2$  external capture contribution that is present but because of interference terms it can have a significant effect on the  $E2$  cross section in certain isolated regions. In fact it is just in the region near  $E_{\text{c.m.}} \approx 3.5$  MeV that the effect is maximal since the other resonances make their smallest relative contributions here (see Fig. 8). Therefore the lowest energy  $E2$  ground state transition data of Schürmann *et al.* (2011) have the somewhat unexpected ability to constrain the ground state external capture contribution. However, it is only the two lowest energy data points that have any significant sensitivity. Further discussions of the subthreshold state parameters are given in Sec. VI.F.

Ideally, the  $R$ -matrix fit would be made directly to primary data.<sup>2</sup> This is done when the data are available, but in several instances only the derived  $E1$  and  $E2$  cross sections are given,

<sup>2</sup>That is, the data that are most closely related to the yields that are measured.

TABLE VIII. Summary of  $Q$  coefficients for extended detector geometry corrections. In cases where the coefficients were not reported they have been approximated using a GEANT4 simulation and the details of the geometry presented in the reference; the source for these cases is indicated as “this work.”

Reference	Detector	$Q_1$	$Q_2$	$Q_3$	$Q_4$	Source
Larson and Spear (1964)		0.897	0.719	0.509	0.311	This work
Kernel, Mason, and Wimmersperg (1971)		0.989	0.968	0.937	0.896	This work
Dyer and Barnes (1974)		0.955	0.869	0.750	0.610	Table 5.5 of Sayre (2011)
Ophel <i>et al.</i> (1976)		0.990	0.969	0.948	0.900	This work
Ouellet <i>et al.</i> (1996)	28°	0.9719	0.9173	0.8395	0.7431	Table 1
	60°	0.9675	0.9047	0.8162	0.7061	
	90°	0.9541	0.8670	0.7474	0.6068	
	90°	0.9543	0.8675	0.7486	0.6091	
	120°	0.9762	0.9296	0.8672	0.7787	
	143°	0.9831	0.9500	0.9017	0.8400	
Redder <i>et al.</i> (1987)			0.92		0.75	In text
Assunção <i>et al.</i> (2006)		0.989(2)	0.968(4)	0.936(8)	0.895(14)	In text
Makii <i>et al.</i> (2009)	40°	0.980	0.947	0.898	0.837	Table VI
	90°	0.980	0.946	0.897	0.835	
	130°	0.980	0.948	0.901	0.841	
Plag <i>et al.</i> (2012)		0.948	0.927	0.862	0.775	Eq. (2)

and the original angular distributions are not reported. Differential cross section measurements below  $S_p$  are available only for the ground state transition and only in the limited energy range around the broad lowest energy  $1^-$  resonance that corresponds to the level at  $E_x = 9.59$  MeV (Dyer and Barnes, 1974; Redder *et al.*, 1987; Ouellet *et al.*, 1996; Fey, 2004; Assunção *et al.*, 2006; Makii *et al.*, 2009). These data are used to determine the relative interference between the  $E1$  and  $E2$  components of the cross section, but it is possible that measurements over other regions, where the two components are closer in magnitude, would provide better constraint. Above  $S_p$ , measurements are available in Larson and Spear (1964) and Kernel, Mason, and Wimmersperg (1971) over the broad states at  $E_x = 12.45$  ( $1^-$ ),  $12.96$  ( $2^+$ ), and  $13.10$  ( $1^-$ ) MeV. The  $Q$  coefficients (Rose, 1953; Longland *et al.*, 2006) used to correct for the extended geometry of the  $\gamma$ -ray detectors are listed in Table VIII.

The best fit to the  $^{12}\text{C}(\alpha, \gamma_0)^{16}\text{O}$  angle-integrated data of Brochard *et al.* (1973), Dyer and Barnes (1974), Kettner *et al.* (1982), Redder *et al.* (1987), Kremer *et al.* (1988), Ouellet *et al.* (1996), Roters *et al.* (1999), Gialanella *et al.* (2001), Kunz *et al.* (2001), Fey (2004), Assunção *et al.* (2006), Makii *et al.* (2009), Schürmann *et al.* (2011), and Plag *et al.* (2012) is shown in Fig. 9. The simultaneous fit to the ground state angular distribution differential cross section data (Dyer and Barnes, 1974; Redder *et al.*, 1987; Fey, 2004; Assunção *et al.*, 2006) is shown in Fig. 10 and the differential excitation curves of Ouellet *et al.* (1996) and Makii *et al.* (2009) are shown in Fig. 11.

### C. Cascade transitions

While the cascade cross sections make a small contribution to the total low-energy cross section ( $\approx 5\%$  at  $E_{\text{c.m.}} = 300$  keV), at higher energies they can dominate as shown in Figs. 6 and 7. However, another compelling reason for their accurate measurement would be to constrain the ANCs of the subthreshold states, in particular, those of the  $E_x = 6.92$  and

7.12 MeV states, through their external capture contributions. The  $E_x = 6.13$  MeV transition capture cross section, which is external capture dominated, is also connected to the  $\beta$ -delayed  $\alpha$  emission spectrum through its ANC as discussed further in Sec. VI.D.

Cascade transition excitation curves for the  $^{12}\text{C}(\alpha, \gamma)^{16}\text{O}$  reaction have been measured by Kettner *et al.* (1982), Redder *et al.* (1987), Matei *et al.* (2006), and Schürmann *et al.* (2011). The measurements of these transitions are complicated experimentally by the close energy spacing of the bound states at

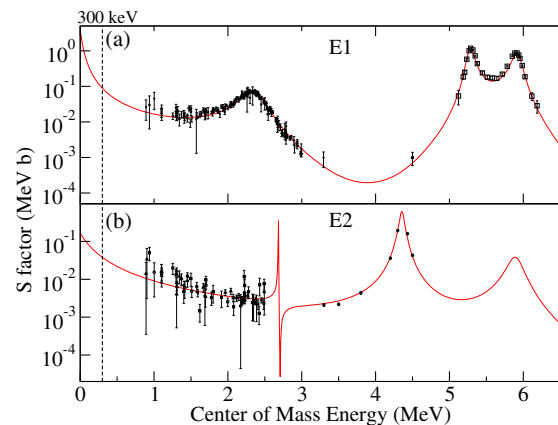


FIG. 9. Fit to the  $^{12}\text{C}(\alpha, \gamma_0)^{16}\text{O}$  cross section. (a) The  $E1$  contribution from Dyer and Barnes (1974), Redder *et al.* (1987), Kremer *et al.* (1988), Ouellet *et al.* (1996), Roters *et al.* (1999), Gialanella *et al.* (2001), Kunz *et al.* (2001), Fey (2004), Assunção *et al.* (2006), Makii *et al.* (2009), Schürmann *et al.* (2011), and Plag *et al.* (2012). (b) The  $E2$  contribution from Redder *et al.* (1987), Ouellet *et al.* (1996), Roters *et al.* (1999), Kunz *et al.* (2001), Fey (2004), Assunção *et al.* (2006), Makii *et al.* (2009), Schürmann *et al.* (2011), and Plag *et al.* (2012). (a) The angle-integrated cross section data of Brochard *et al.* (1973) are also shown at high energy for comparison as they are dominated by  $E1$  capture. Note that the data have been subjected to overall normalizations as determined by the fitting procedure.

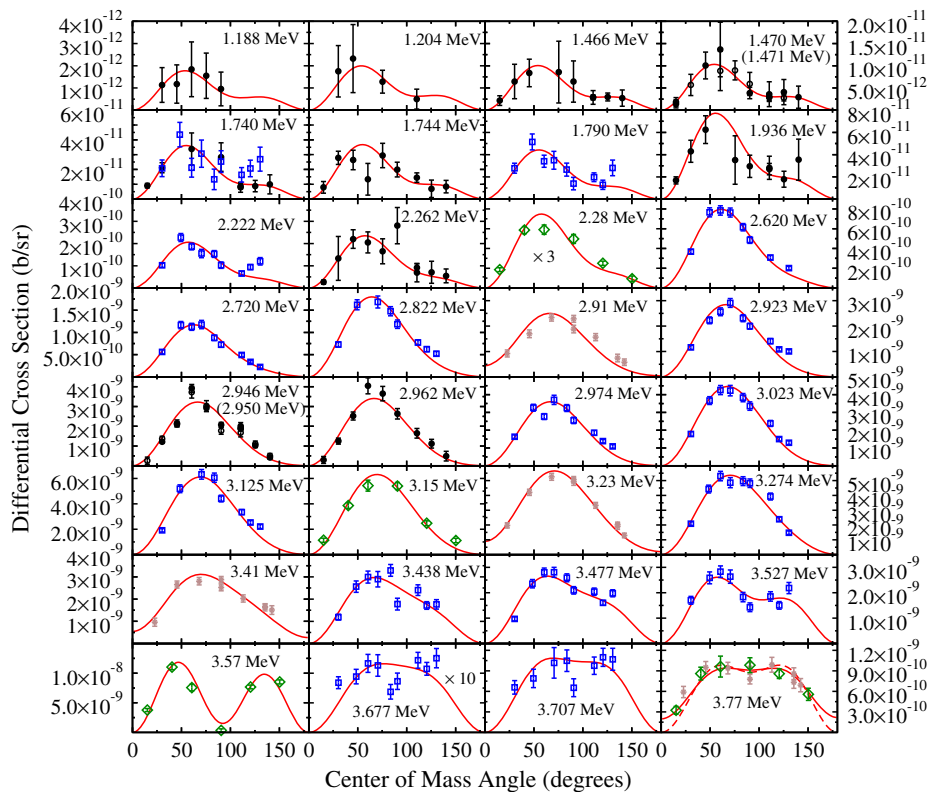


FIG. 10. Comparison of the  $R$ -matrix fit to the angular distribution data of Dyer and Barnes (1974) (green diamonds), Redder *et al.* (1987) (brown stars), Assunção *et al.* (2006) (black circles), and Fey (2004) (blue squares). Note that the data at  $E_\alpha = 2.28$  and 3.677 MeV have been scaled for plotting convenience. The data from Fey (2004) show a systematic deviation from the  $R$ -matrix fit and other data sets at backward angles. This is most clearly visible at  $E_\alpha = 1.740$  MeV where the data from Fey (2004) and Assunção *et al.* (2006) were measured at the same energy.

$E_x = 6.05$  ( $0^+$ ) and 6.13 ( $3^-$ ) MeV and those at  $E_x = 6.92$  ( $2^+$ ) and 7.12 ( $1^-$ ) MeV. This can make separating the individual contributions difficult when using sodium iodide, barium fluoride, or lanthanum bromide detectors, which have poorer energy resolution than a germanium detector. For example, Kettner *et al.* (1982) first reported measurements of the transition to the  $E_x = 6.92$  MeV state but in Redder *et al.* (1987), where Ge(Li) detectors were used, it was clarified that the measurement was actually the sum of the deexcitations through the  $E_x = 6.92$  and 7.12 MeV states. The combined cross section,  $E_x = 6.92 + 7.12$  MeV transition, of Kettner *et al.* (1982) is shown in Fig. 12 compared to the sum of the cross sections for each transition from the  $R$ -matrix fit. While the data are in rough agreement, the shape is distorted in the vicinity of the  $4^+$  level at  $E_x = 10.36$  MeV. Further, while the  $E_x = 6.92$  and 7.12 MeV data of Redder *et al.* (1987) are in agreement as far as their energy dependence, their absolute scale is about a factor of 2 larger than recent measurements by Kunz (2002) [see Table VII and Schürmann *et al.* (2012)]. Note that the data of Kettner *et al.* (1982) are excluded from the fitting. Further measurements of these cascade transitions at low energy are needed in order to understand these discrepancies.

There has been a great deal of interest and contradictory results regarding the cascade cross section measurements of the  $E_x = 6.05$  MeV transition. The measurement of Matei *et al.* (2006) reported an excitation curve for this transition

over a wide energy range. Further, in that work an  $R$ -matrix fit was made to these data that gave a much larger low-energy contribution than previously estimated. A subsequent measurement by Schürmann *et al.* (2011) over a more limited higher-energy range claimed that their data were inconsistent with those of Matei *et al.* (2006) and their  $R$ -matrix fit predicted the opposite extreme that the transition's contribution was lower than previously estimated. A reanalysis of the data of Schürmann *et al.* (2011) by deBoer *et al.* (2013) found a value in between the two, which was closer to previous estimates. Finally, Avila *et al.* (2015) measured the ANCs of the  $E_x = 6.05$  and 6.13 MeV transitions and arrived at values very close to those deduced by deBoer *et al.* (2013). Several details of the analysis of this transition have not been explained fully in the literature. For this reason they are addressed here in some detail.

The first issue is that the  $R$ -matrix fit presented by Matei *et al.* (2006) is erroneous. An error was made in the code used for the fit that allowed for a larger  $E1$  contribution. Proper calculations show that the large  $E1$  component is impossible to reproduce.

Second, Schürmann *et al.* (2011) showed that their  $E_x = 6.05$  MeV cascade data are inconsistent with those of Matei *et al.* (2006). This is true if the data are taken at face value. However, the experiment of Matei *et al.* (2006) measured not only the cascade transition to the  $E_x = 6.05$  MeV state, but also the total cross section. Unfortunately these data have

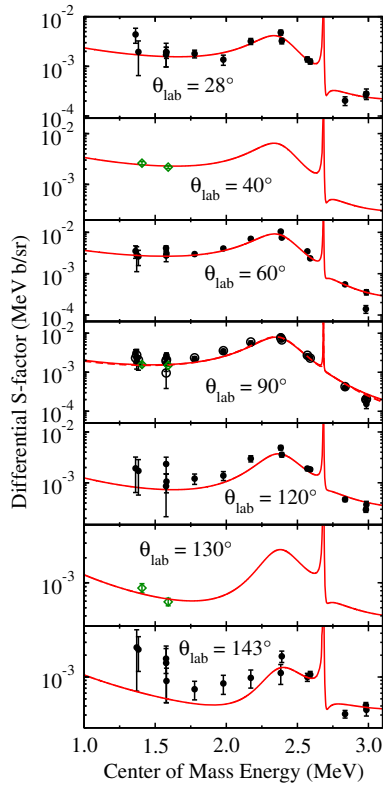


FIG. 11. Fits to the differential excitation curve data of [Ouellet \*et al.\* \(1996\)](#) (solid black points) and [Makii \*et al.\* \(2009\)](#) (green diamonds). At  $\theta_{\text{lab}} = 90^\circ$  two measurements were made by [Ouellet \*et al.\* \(1996\)](#) but with different detectors on opposite sides of the target. This second data set is represented by open black points. This is also the only angle where both experiments measured the cross section at the same angle.

never been published and are available only in the thesis of [Matei \(2006\)](#). A comparison of the fit from this work with both the total and the  $E_x = 6.05$  MeV transition cross section is shown in Fig. 13. The total cross section data from [Matei](#)

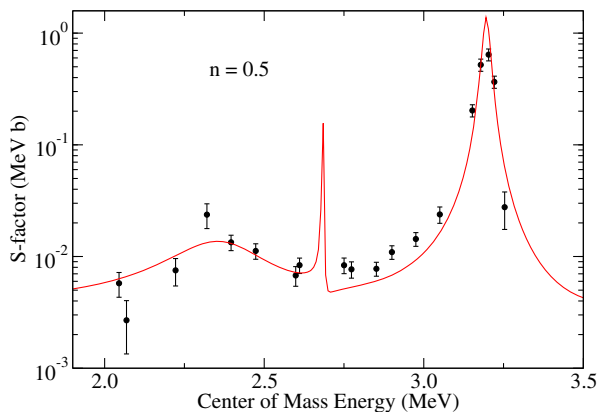


FIG. 12. Data for the sum of the  $E_x = 6.92$  and  $7.12$  MeV transitions for the  $^{12}\text{C}(\alpha, \gamma)^{16}\text{O}$  data of [Kettner \*et al.\* \(1982\)](#). The data have been normalized by a factor of 0.5 to match the  $R$ -matrix fit. The agreement is reasonably good at low energies but above the narrow resonance corresponding to the  $2^+$  level at  $E_x = 9.845$  MeV the agreement worsens. These data were not included in the global fit.

(2006) are not in immediately good agreement with the fit, but become so if multiplied by a factor of  $\approx 1.2$  ( $n_1$  in Fig. 13). This normalization factor is well within the quoted experimental systematic uncertainty of  $+31\% / -25\%$ . The data are in excellent agreement with the fit over the entire energy range except for three points at  $E_{\text{c.m.}} = 2.41, 4.29,$  and  $4.32$  MeV. However, if the cross sections of these three points are all multiplied by a factor of 3 ( $n_2$  in Fig. 13), they are in excellent agreement with the total cross section data of [Schürmann \*et al.\* \(2011\)](#).

Turning back to the  $E_x = 6.05$  MeV transition, it was found that the data of [Matei \*et al.\* \(2006\)](#) deviated from those of [Schürmann \*et al.\* \(2011\)](#) not only in normalization but also in energy dependence, albeit the comparison could be made only over the limited energy range of the data of [Schürmann \*et al.\* \(2011\)](#) ( $3.5 < E_{\text{c.m.}} < 4.5$  MeV, see Fig. 15). Further, the  $R$ -matrix analysis of [Schürmann \*et al.\* \(2011\)](#) indicated a difference in energy dependence over an even wider energy range. Both of these issues can now be addressed. As for the  $R$ -matrix fit, the energy dependence does not match over the broad energy range because a value of  $\gamma_{6.05} = 0.1^{+0.05}_{-0.01}$  (corresponding to an  $\text{ANC}_{\alpha, 6.05 \text{ MeV}} = 44^{+270}_{-44} \text{ fm}^{-1/2}$ ) was chosen, which was subsequently shown to be much too small by [Avila \*et al.\* \(2015\)](#) ( $\text{ANC}_{\alpha, 6.05 \text{ MeV}} = 1560 \pm 100 \text{ fm}^{-1/2}$ ). Since external capture dominates the  $E_x = 6.05$  MeV transition cross section over much of the energy region (see Fig. 8), this caused a significant difference in the cross section. In [Schürmann \*et al.\* \(2011\)](#), the large systematic uncertainty of [Matei \*et al.\* \(2006\)](#) was not taken into account and instead the difference in the two data sets was attributed to the data of [Matei \*et al.\* \(2006\)](#) being the sum of the  $E_x = 6.05$  and  $6.13$  MeV transitions. However, the experimental technique of [Matei \*et al.\* \(2006\)](#) used a coincidence of  $\gamma$  rays with recoils. Since the  $\gamma$ -ray decay from the  $E_x = 6.05$  MeV state to the ground state ( $0^+ \rightarrow 0^+$ ) is strictly forbidden, this explanation seems impossible. If instead the data of [Matei \*et al.\* \(2006\)](#) are

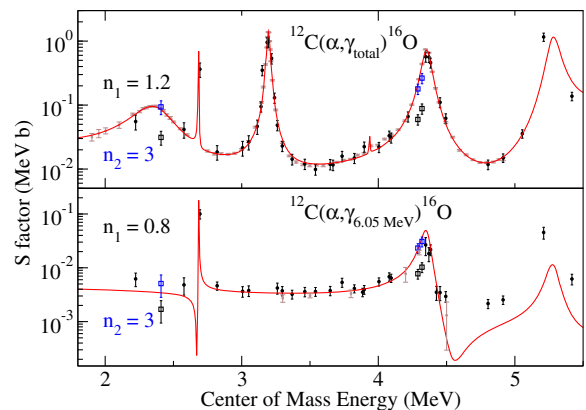


FIG. 13. Comparison of the  $^{12}\text{C}(\alpha, \gamma_{\text{total}})^{16}\text{O}$  and  $^{12}\text{C}(\alpha, \gamma_{6.05 \text{ MeV}})^{16}\text{O}$  data of [Matei \(2006\)](#) and [Matei \*et al.\* \(2006\)](#) (solid black points) and [Schürmann \*et al.\* \(2005, 2011\)](#) (brown stars) with the global  $R$ -matrix fit from this work (solid red line). The data have been renormalized by the factors  $n_1$  to match the fit. The blue square points represent the further renormalization of data points that are all systematically low by the same amount as discussed in the text.

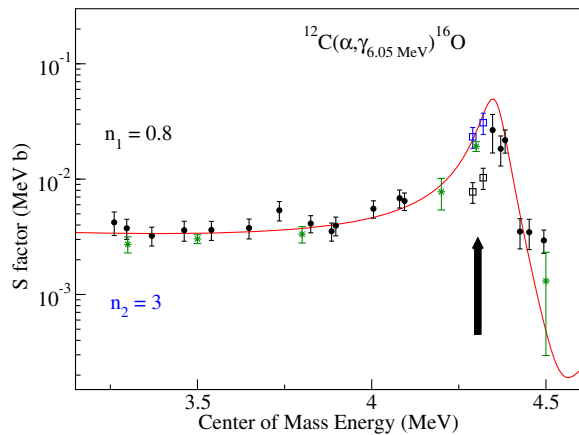


FIG. 14. Comparison between the  $E_x = 6.05$  MeV transition data of Matei *et al.* (2006) and Sukhbold *et al.* (2016) over the smaller energy range of the Schürmann *et al.* (2011) data. The data of Matei *et al.* (2006) have been normalized to those of Schürmann *et al.* (2011) with a factor of  $n_1 = 0.8$ . The cross section of the two data points at  $E_{\text{c.m.}} = 4.29$  and  $4.32$  MeV has been scaled up by the same factor of 3 used to normalize the corresponding points in the total cross section as shown in Fig. 13. The original values are indicated by the open black squares, and the scaled values by the open blue squares.

normalized to the data of Schürmann *et al.* (2011) in the off-resonance region over the range from  $3.25 < E_{\text{c.m.}} < 4.10$  MeV (normalization factor of 0.8), the agreement is much improved. The remaining deviation occurs for just two points, which happen to fall at  $E_{\text{c.m.}} = 4.29$  and  $4.32$  MeV, the very same points that were found to be too low in the total cross section data. If these points are subjected to the same normalization factor as those in the total cross section, the data are in much better agreement as shown in Fig. 14. Regarding the low-energy point at  $E_{\text{c.m.}} = 2.41$  MeV, its agreement is also much improved with the energy dependence of the  $R$ -matrix fit if subjected to this same normalization factor.

Summarizing the situation for the  $E_x = 6.05$  MeV transition, the data of Matei *et al.* (2006) and Sukhbold *et al.* (2016) are in generally good agreement if the systematic uncertainties are considered. There are a few points in the data of Matei *et al.* (2006) that appear to have some unconsidered systematic shift in their absolute scale compared to the rest of the data set. Attempts were made to reexamine the log books of the experiment but no correlation between these data points could be established. It was found that no significant  $E1$  contribution was necessary to fit the data and that the low-energy cross section is dominated by  $E2$  external capture (see Fig. 8) in contradiction to the recent reassertion in An *et al.* (2015) that this cross section is  $E1$  dominated. Finally, the ANCs measured by Avila *et al.* (2015) are found to be in good agreement with the capture data.

The  $R$ -matrix fit and the cascade data included in the global fit are shown in Fig. 15. It was found that the cascade data of Kunz (2002) ( $E_x = 6.92$  and  $7.12$  MeV transitions) require normalization factors of  $\approx 0.5$  while those of Redder *et al.* (1987) require values of  $\approx 0.25$  (see Table VII). The normalization is somewhat unexpected since this was not required in the fit of Schürmann *et al.* (2012). This may be the result of the

different ANCs used in this analysis. In addition, the value of the absolute normalization for the cascade data is highly sensitive to the normalization factor of the total cross section data. If the normalization of the total cross section data is increased by a few percent, well within their systematic uncertainty of 6.5%, more consistent normalizations can be obtained for the  $E_x = 6.92$  and  $7.12$  MeV transition data of Kunz (2002). However, at low energies the external capture dominates the cross section for both of these transitions and the data are only over the resonance region corresponding to the  $E_x = 9.59$  MeV state. Hence the fit to the data over this energy region has little effect on the extrapolation to stellar energies.

A detail that is only briefly mentioned in Schürmann *et al.* (2012) is that their data give the first evidence for  $\gamma$ -ray decays from the  $3^-$  state at  $E_x = 11.49$  MeV. In this analysis evidence is found for decays to the  $E_x = 6.13$  ( $M1/E2$ ),  $6.92$  ( $E1$ ), and  $7.12$  ( $E2$ ) MeV final states. The lowest order multipolarity has been assumed except for the  $E_x = 6.13$  MeV transition. No evidence for the  $E3$  decay through the  $E_x = 6.05$  MeV transition is observed in the data. The widths of these states can be found in Table XXII.

#### D. $\beta$ -delayed $\alpha$ emission

There have been several measurements of the  $\beta$ -delayed  $\alpha$  emission spectrum of  $^{16}\text{N}$  as discussed in Sec. V. However, the different spectra cannot be directly compared since all of them suffer from experimental resolution effects to different degrees. This point was the subject of an analysis by Gai (1998) where it was determined that the spectra of the Yale (France *et al.*, 1997), Seattle (unpublished), and Mainz (Hättig, Hünchen, and Wäffler, 1970) groups were inconsistent with that of TRIUMF (Azuma *et al.*, 1994). This began a long debate regarding the consistency between the data sets that still remains unresolved.

More recently, Buchmann, Ruprecht, and Ruiz (2009) performed another comparison between the different data sets where detailed GEANT simulations were created for several of the past setups. The Monte Carlo simulations were used to simulate the observed  $\alpha$  spectra. Many different deconvolution effects and background sources were investigated for the Mainz, Seattle, Yale, Argonne, and TRIUMF data sets. In the end, the main conclusion was that the different spectra were very sensitive to the deconvolution technique that was used. In particular, energy loss effects through the catcher foils were found to be a main factor. The claim was also made that the deconvolution technique used by France *et al.* (2007) was incorrect and that this data set may in fact be in agreement with those of Hättig, Hünchen, and Wäffler (1970) and Azuma *et al.* (1994). Unfortunately another conclusion of the work was that not enough experimental information is available to properly analyze much of the data with the degree of confidence that is desired. It remains a challenge for future measurements to produce consistent results for the measurement of the  $^{16}\text{N}(\beta, \alpha)^{12}\text{C}$  spectrum.

For the current analysis, because of the previous issues, the data are limited to that of Azuma *et al.* (1994) and Tang *et al.* (2010). These data sets have the most detailed documentation of how to simulate their remaining resolution effects and claim

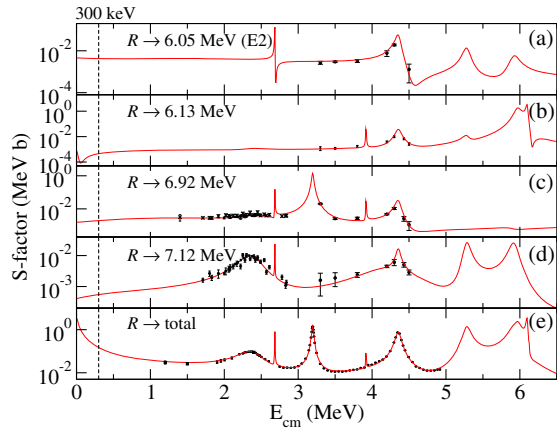


FIG. 15. (a)–(d) Transitions for primary  $\gamma$  rays to excited states in  $^{16}\text{O}$  for the  $^{12}\text{C}(\alpha, \gamma)^{16}\text{O}$  reaction. The data include those from Redder *et al.* (1987), Schürmann *et al.* (2005, 2011, 2012), Plag *et al.* (2012), and Yamaguchi *et al.* (2014). (e) The total  $S$  factor.

that they can be accurately done so using the simple method given by Eq. (90). In addition to the usual convolution term, it was also recommended that each spectrum be shifted in energy in order to agree with the more easily determined energy calibration of the scattering data. These correction factors are summarized in Table IX.

A fit to both of these  $^{16}\text{N}(\beta, \alpha)^{12}\text{C}$  data sets simultaneously, along with the rest of the data from other channels, is shown in Fig. 16. The fit includes contributions from the  $1^-$  levels at  $E_x = 7.12$  and  $9.59$  MeV, and the  $3^-$  level at  $E_x = 6.13$  MeV. Additionally, as in both Azuma *et al.* (1994) and Tang *et al.* (2010), a  $1^-$  background pole (at  $E_x = 20$  MeV) is included. The different components for the fit are shown in Fig. 17.

While the quality of the fit looks reasonable to the eye, the small error bars reveal significant differences between the two data sets even after the convolution correction to the  $R$ -matrix curve. The resulting reduced  $\chi^2$  of the fit is rather large as detailed in Table X. However, the resulting  $\log(ft_{1/2})$  values are in reasonable agreement with those given in the compilation, with the exception of the  $3^-$  subthreshold state that is too large by about 3 standard deviations.

To further investigate the differences, the spectra were fitted independently (with the rest of the data). The  $\chi^2$  value of the Tang *et al.* (2010) data decreased substantially, demonstrating the tension between the two data sets. It is interesting to note that the  $\chi^2$  of the fit to the data of Azuma *et al.* (1994) actually

TABLE IX. Summary of convolution and energy shift corrections for  $^{16}\text{N}(\beta, \alpha)^{12}\text{C}$  spectra for Azuma *et al.* (1994) and Tang *et al.* (2010). For the other measurements, the convolution parameters are estimated from the best fits to the data of Azuma *et al.* (1994) and Tang *et al.* (2010).

Reference	$\sigma$ (keV)	$\Delta E$ (keV)
Azuma <i>et al.</i> (1994) (TRIUMF)	30	−5
Tang <i>et al.</i> (2010) (Argonne)	40	−3.75
France <i>et al.</i> (2007) (Yale)	100	0
Hättig, Hünchen, and Wäffler (1970) (Mainz)	40	−10
Unpublished (Seattle)	40	−5

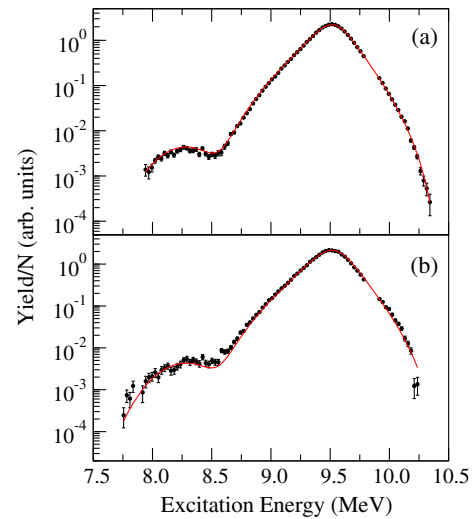


FIG. 16. Simultaneous fit including the  $^{16}\text{N}(\beta, \alpha)^{12}\text{C}$  data of both (a) Azuma *et al.* (1994) and (b) Tang *et al.* (2010). In the fitting procedure the ANCs were fixed to the values of the transfer measurements. The solid red lines represent the  $R$ -matrix cross sections convoluted with the resolution function given by Eq. (89) and the specific parameters given in Table IX.

becomes larger. This is caused by the tension between the data in the other channels. The results are given in Table XI.

What is most interesting is the large difference in the  $\log(ft_{1/2})$  values of the  $3^-$  state that result from the individual fits. This is caused by the difference in the data in the vicinity of the interference region around  $E_x \approx 8.5$  MeV. With the  $\alpha$  ANC fixed, the fit attempts to compensate this difference by changing the  $\log(ft_{1/2})$  value. Given the deconvolution methods used, it is clear that the data of Azuma *et al.*

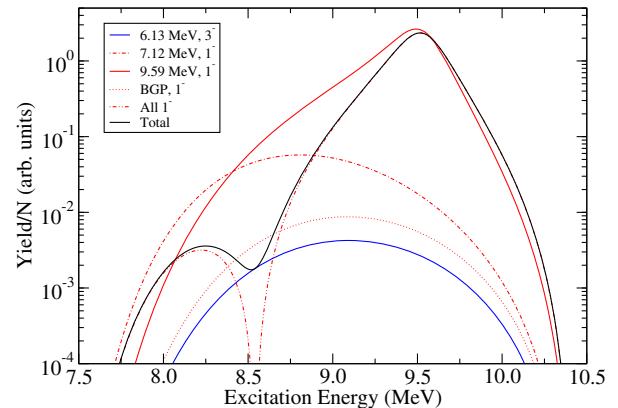


FIG. 17. Components of the  $R$ -matrix fit to the  $^{16}\text{N}(\beta, \alpha)^{12}\text{C}$  data of Azuma *et al.* (1994) and Tang *et al.* (2010). The different red curves (except the dash-dot-dotted line) represent the  $1^-$  components of the fit, which add coherently to give the interference pattern shown by the dash-dot-dotted red line. The individual  $1^-$  contributions come from the  $E_x = 7.12$  and  $9.59$  MeV, and background pole (BGP) at  $20$  MeV. An additional  $3^-$  component adds incoherently to give the total yield, which is given by the solid black line. Note the similar energy dependence of the subthreshold state and BGP contributions.

TABLE X. Summary of results for fits considering different  $^{16}\text{N}(\beta, \alpha)^{12}\text{C}$  data. The half-life of  $^{16}\text{N}$  was taken as  $t_{1/2} = 7.13(2)$  s with a  $\beta\alpha$  branching ratio of  $1.20(5) \times 10^{-5}$ . From [Tilley, Weller, and Cheves, 1993](#).

$\tilde{E}_x$ (MeV)	$J^\pi$	$\text{ANC}_\alpha$ ( $\text{fm}^{-1/2}$ ) or $\tilde{\Gamma}_\alpha$ (keV)	$\log(ft_{1/2})$	
			<a href="#">Azuma <i>et al.</i> (1994)</a> and <a href="#">Tang <i>et al.</i> (2010)</a>	<a href="#">Tilley, Weller, and Cheves (1993)</a>
6.13	$3^-$	139(9)	4.59	4.48(4)
7.12	$1^-$	$2.08(17) \times 10^{14}$	5.08	5.11(4)
9.59	$1^-$	382	6.15	6.12(5)
20 (BGP)	$1^-$	15 000	$-5.70^a$	
$\chi^2$ (N)			496 (87), 793 (88)	

<sup>a</sup>The minus sign indicates the sign of the interference on the reduced-width amplitude.

TABLE XI. Summary of fits to the  $^{16}\text{N}(\beta, \alpha)^{12}\text{C}$  data but for each spectrum individually.

$\tilde{E}_x$ (MeV)	$J^\pi$	$\text{ANC}_\alpha$ ( $\text{fm}^{-1/2}$ ) or $\tilde{\Gamma}_\alpha$ (keV)	$\log(ft_{1/2})$		
			<a href="#">Azuma <i>et al.</i> (1994)</a>	<a href="#">Tang <i>et al.</i> (2010)</a>	<a href="#">Tilley, Weller, and Cheves (1993)</a>
6.13	$3^-$	139(9)	4.44	4.80	4.48(4)
7.12	$1^-$	$2.08(17) \times 10^{14}$	5.06	5.06	5.11(4)
9.59	$1^-$	382	6.13	6.18	6.12(5)
20 (BGP)	$1^-$	15 000	$-5.73$	$-6.53$	
$\chi^2$ (N)			519 (87)	466 (88)	

(1994) are in the best agreement with the ANCs of [Avila \*et al.\* \(2015\)](#).

A comparison is made using the best fit parameters from the simultaneous fit to the data of [Azuma \*et al.\* \(1994\)](#) and [Tang \*et al.\* \(2010\)](#) with the remaining data sets from the Mainz, Seattle, and Yale experiments, where the data were taken from [France \*et al.\* \(2007\)](#). Since these three data sets retain significant experimental effects, the convolution value of each data set was varied while the  $R$ -matrix parameters were kept constant. The resulting calculations are shown in Fig. 18 and the convolution parameters are given in the bottom half of Table IX. The data are reasonably reproduced by the convolution effects except near the interference dip around  $E_x = 8.5$  MeV. Here the fit underpredicts the data for all three data sets. This seems to indicate a better agreement with the data of [Tang \*et al.\* \(2010\)](#).

These seeming contradictions in the data, that seem to place the current data into two camps, are a critical puzzle that needs to be resolved. It seems that this can be done only through future measurements considering the number of reanalyses that have been unable to resolve the issues. The  $^{16}\text{N}(\beta, \alpha)^{12}\text{C}$  spectrum could provide one of the most stringent constraints on several of the level parameters critical for the determination of the  $E1$  ground state cross section. However, with these unresolved experimental effects and contradictions between different data sets, the uncertainties are substantially increased and are difficult to quantify.

As a final point, the analysis of the  $^{16}\text{N}(\beta, \alpha)^{12}\text{C}$  spectrum utilizes  $\beta$ -decay branching ratios from the literature to constrain the values of the  $R$ -matrix  $\beta$ -decay fit parameters. In particular, these are the branching ratios to the  $E_x = 6.13$  ( $3^-$ ), 7.12 ( $1^-$ ), and 9.59 ( $1^-$ ) MeV levels in  $^{16}\text{O}$ . While the compilation ([Tilley, Weller, and Cheves, 1993](#)) reports these values with small uncertainties, it is unclear where some of them actually originated. Most of the branching ratios date

back to measurements at Brookhaven National Laboratory from the 1950s ([Alburger, Gallmann, and Wilkinson, 1959](#)). While the fact that these are older measurements does not mean they are incorrect, verification studies seem overdue since they play a rather important role in the analysis of the  $^{16}\text{N}(\beta, \alpha)^{12}\text{C}$  spectrum.

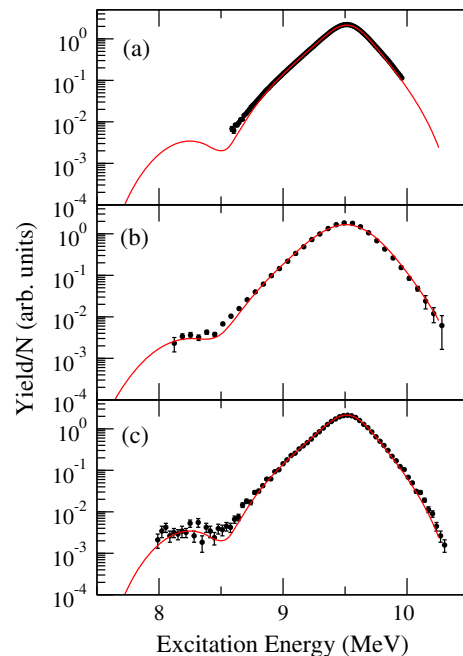


FIG. 18. Comparison of the  $^{16}\text{N}(\beta, \alpha)^{12}\text{C}$  spectra of (a) Mainz, (b) Yale, and (c) Seattle to the best fit to the data from [Azuma \*et al.\* \(1994\)](#) (TRIUMF) and [Tang \*et al.\* \(2010\)](#) (Argonne), but with the unknown convolution parameters varied to best match the data.

### E. $\alpha$ scattering

Section V describes how several scattering experiments (Clark, Sullivan, and Treacy, 1968; D'Agostino-Bruno *et al.*, 1975; Tischhauser *et al.*, 2009; Plag *et al.*, 2012) have been performed in order to constrain the values of the ANCs of the subthreshold states as well as the particle widths of the unbound states. Here only the data of Tischhauser *et al.* (2009) [the higher-energy analysis was worked out subsequently by deBoer, Couture *et al.* (2012)] are considered as they represent the most precise and accurate measurement, cover the broadest energy range, and are in good agreement with previous studies. In the present analysis, the original yield ratio data are directly fit instead of the phase shifts extracted by Tischhauser *et al.* (2009).

Some previous analysis attempted to limit the complexity of the fitting problem by considering only individual phase shifts, in particular, only the  $s$  and  $d$  waves since they are the only partial waves directly connected to the  $E1$  and  $E2$  capture cross sections. However, Buchmann *et al.* (1996) realized that this was poor practice since it neglected the statistical correlations inherent in the full set of phase shifts. This also extends to the propagation of the uncertainties from the yield ratios to the phase shifts.

However, fitting to the full set of the original data comes at a price. While the phase shift data consist only of 2814 (402 energies,  $l = 0$  to 6) data points there are 12 864 yield ratio data points since the measurements were made at 32 different angles. In addition, the  $R$ -matrix cross section must be convoluted with the function given by Eq. (89) to correct for beam energy resolution and energy loss through the target. This results in a significant increase in computation time. In order to avoid large convolution corrections, the data in the vicinity of narrow resonances, which are not fit in the analysis, have been neglected. This limits the data in the present analysis to 304 energies or 9728 data points. An example excitation yield ratio curve of this data is shown in Fig. 2.

In principle the scattering data can provide significant constraint on the value of the ANCs of the subthreshold states (see Sec. V). At the current level of precision, the data constrain only the ANCs of the  $2^+$  and  $1^-$  states, which are closest to threshold. Since the ANC of the  $1^-$  state is already strongly constrained by the  $^{16}\text{N}(\beta\alpha)^{12}\text{C}$  data, the goal of recent scattering measurements has been to better constrain that of the  $2^+$  state (see Fig. 26). However, as mentioned in Secs. V.C and VI.A, the large background poles that are necessary to fit the data also tend to lessen the constraint of the fit on the ANCs. This is because both contributions to the cross section have a similar energy dependence; hence the ANCs and the parameters of the background poles are strongly correlated.

The present fit to the scattering data does not result in as small of a  $\chi^2$  (see Table VII) as that achieved by Tischhauser *et al.* (2009). The main difference is that in the present global fit there is tension between the scattering data and other data sets for the values of the energies, widths, and ANCs. In particular, this tension has a very large effect on the  $\chi^2$  of the fit in the vicinity of the  $E_x = 10.36$  MeV ( $4^+$ ) and the  $E_x = 11.49$  ( $3^-$ ) and 11.51 MeV ( $2^+$ ) doublet. In these regions the scattering cross section changes rapidly in energy and the

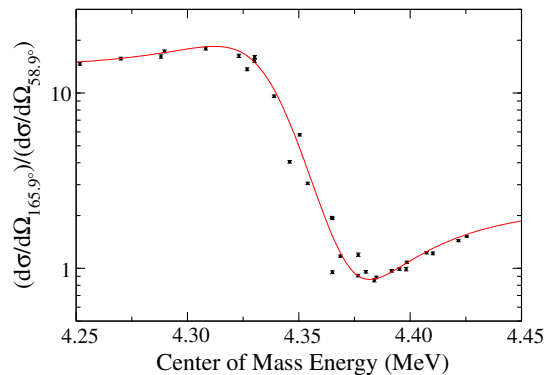


FIG. 19. Sample region of the scattering data of Tischhauser *et al.* (2009) in the vicinity of the resonances that correspond to the levels at  $E_x = 11.49$  ( $3^-$ ) and 11.51 ( $2^+$ ) MeV. The cross section ratio changes rapidly with energy, causing the effect of energy uncertainties on the  $\chi^2$  to be amplified.

uncertainties on the yield ratio data are about 2%. Further, there are some points that show significant deviations from the expected cross section ratios over these regions as shown in Fig. 19. Since this effect is less pronounced in other more slowly varying cross section regions, this may be attributed to an unaccounted for energy uncertainty that is not reflected in the yield uncertainties.

### F. Subthreshold states

In the previous sections the importance of the bound states of  $^{16}\text{O}$  have been stressed. This section is devoted to a discussion of the current understanding of these states. The parameters that are of interest are the energies,  $\gamma$  widths, and ANCs of the five bound states of  $^{16}\text{O}$ .

All the energies of the bound states are known with a precision of at least 1 keV (Tilley, Weller, and Cheves, 1993). These uncertainties propagate into small uncertainties in the cross sections. Additionally, the separation energies of  $^{16}\text{O}$  (listed in Table VI) all have uncertainties that are less than a keV.

All of the bound states of  $^{16}\text{O}$  decay with nearly 100% probability to the ground state. Except for the first excited  $0^+$  state at  $E_x = 6.05$  MeV, the primary decay mode is single  $\gamma$ -ray emission. Because both the ground state and first excited state of  $^{16}\text{O}$  are  $0^+$ , the state cannot decay by single  $\gamma$  emission. Its primary decay mode is therefore through  $e^+e^-$  emission (or  $\pi$  decay) (Fowler and Lauritsen, 1939). The  $\gamma$ -ray widths of the bound-state levels are necessary in order to calculate the subthreshold state capture contribution through different transitions. While the ground state  $\gamma$  decays through the  $E_x = 6.92$  and 7.12 MeV subthreshold states have the most significant contribution to the total capture cross section, small branching to other excited states make contributions to some of the cascade cross sections.

Several measurements have been made to investigate the ground state  $\gamma$  widths of the  $E_x = 6.92$  and 7.12 MeV subthreshold states by way of inelastic electron scattering (Stroetzel, 1968; Miska *et al.*, 1975) and nuclear resonance fluorescence (Evers *et al.*, 1968; Swann, 1970; Moreh *et al.*, 1985). The values are in relatively good agreement and the

TABLE XII. Summary of the known  $\gamma$ -decay widths for the bound states of  $^{16}\text{O}$ . Where values are averaged, the compilation is quoted.

$E_i$ ( $J^\pi$ ) (MeV)	$E_f$ (MeV)	$\Pi L$	$\Gamma_\gamma$ (eV)	Reference
6.05 ( $0^+$ )	G.S.	$E0$	Forbidden	
6.13 ( $3^-$ )	G.S.	$E3$	$2.60(13) \times 10^{-5}$	Miska <i>et al.</i> (1975)
	6.05	$E3$	Unobserved	
6.92 ( $2^+$ )	G.S.	$E2$	0.097(3)	Tilley, Weller, and Cheves (1993)
	6.05	$E2$	$2.7(3) \times 10^{-5}$	Tilley, Weller, and Cheves (1993)
	6.13	$E1$	$< 7.8 \times 10^{-6a}$	Wilkinson, Alburger, and Lowe (1968)
7.12 ( $1^-$ )	G.S.	$E1$	0.055(3)	Tilley, Weller, and Cheves (1993)
	6.05	$E1$	$< 3.3 \times 10^{-7}$	Lowe, Alburger, and Wilkinson (1967)
	6.13	$E2$	$4.6(3) \times 10^{-5a}$	Matei, Brune, and Massey (2008)
	6.92	$E1$	$< 1.1 \times 10^{-6a}$	Matei, Brune, and Massey (2008)

<sup>a</sup>Calculated from branching ratio and  $\Gamma_{\gamma 0}$ .

compilation (Tilley, Weller, and Cheves, 1993) adopts a weighted average of all the past measurements. This results in uncertainties of 3.1% and 5.4% for the  $\gamma$  widths of the  $E_x = 6.92$  and 7.12 MeV states, respectively. For the latest discussion, see Moreh *et al.* (1985).

Past measurements of the different cascade  $\gamma$  rays have been made by Fuchs, Hagemann, and Gaarde (1965), Lowe, Alburger, and Wilkinson (1967), Wilkinson, Alburger, and Lowe (1968), and Miska *et al.* (1975). A recent measurement by Matei, Brune, and Massey (2008) investigated the branching ratios of the decay from  $E_x = 7.12$  MeV state, giving a more accurate value for the

branching to the  $E_x = 6.13$  MeV state and an upper limit to the  $E_x = 6.92$  MeV state. The  $\gamma$ -ray decay widths that lead to significant subthreshold contributions to the cross section have been measured to a precision that is smaller than or competitive with other uncertainties as summarized in Table XII.

At present, what seems to be the most reliable method of determining the  $\alpha$  ANCs of bound states is via sub-Coulomb transfer reactions (see Sec. V). Recent measurements of the  $\alpha$  ANCs of the  $E_x = 7.12$  ( $1^-$ ) and 6.92 ( $2^+$ ) MeV states were made by Brune *et al.* (1999), Belhout *et al.* (2007), and Oulebsir *et al.* (2012) using the  $\alpha$  transfer reactions

TABLE XIII. Summary of  $\alpha$  particle asymptotic normalization coefficients of the two subthreshold states at  $E_x = 6.92$  and 7.12 MeV. Because the CN reaction data do not place strong constraints on the ANCs (and are sometimes inconsistent), the values obtained from transfer studies are adopted as the best estimates for this analysis. For comparison, theoretical values and those deduced from  $R$ -matrix analysis are also shown.

Reference	ANC $_\alpha$ (fm $^{-1/2}$ )	
	6.92 MeV, $2^+$	7.12 MeV, $1^-$
<i>Theory</i>		
Descouvemont (1987)	$1.34 \times 10^{5a}$	
Sparenberg (2004)	$1.445(85) \times 10^5$	
Dufour and Descouvemont (2008)	$1.26(5) \times 10^5$	
<i>R matrix</i>		
Barker and Kajino (1991)	$3.19 \times 10^{5b}$	
Azuma <i>et al.</i> (1994)		$1.90 \times 10^{14}$
Angulo and Descouvemont (2000)	$4.02 \times 10^{5a}$	
Buchmann (2001)	$2.28^{+33}_{-37} \times 10^{5a}$	
Matei, Brune, and Massey (2008)	$2.3(4) \times 10^5$	
Tischhauser <i>et al.</i> (2009)	$1.54(18) \times 10^{5a}$	
Tang <i>et al.</i> (2010)	$1.67 \times 10^5$	$1.96 \times 10^{14}$
Schürmann <i>et al.</i> (2012)	$1.5 \times 10^5$	$1.94 \times 10^{14}$
Sayre <i>et al.</i> (2012)	$1.59 \times 10^5$	
<i>Transfer</i>		
Brune <i>et al.</i> (1999)	$1.14(10) \times 10^5$	$2.08(20) \times 10^{14}$
Belhout <i>et al.</i> (2007)	$1.40(50) \times 10^{5c}$	$1.87(54) \times 10^{14}$
Oulebsir <i>et al.</i> (2012)	$1.44(28) \times 10^5$	$2.00(35) \times 10^{14}$
Avila <i>et al.</i> (2015)	$1.22(7) \times 10^5$	$2.09(14) \times 10^{14}$

<sup>a</sup> $\gamma_\alpha$  transformed to ANC $_\alpha$  by Sparenberg (2004).

<sup>b</sup> $\gamma_\alpha$  transformed to ANC $_\alpha$  by Dufour and Descouvemont (2008).

<sup>c</sup>Renormalized by Oulebsir *et al.* (2012).

TABLE XIV. Asymptotic normalization coefficients for the  $E_x = 6.05$  MeV bound state in  $^{16}\text{O}$ .

Reference	$\text{ANC}_\alpha$ (fm $^{-1/2}$ )
<i>R matrix</i>	
Schürmann <i>et al.</i> (2011)	$44_{-44}^{+270}$
deBoer <i>et al.</i> (2013)	1800
<i>Transfer</i>	
Avila <i>et al.</i> (2015)	1560(100)

TABLE XV. Asymptotic normalization coefficients for the  $E_x = 6.13$  MeV bound state in  $^{16}\text{O}$ .

Reference	$\text{ANC}_\alpha$ (fm $^{-1/2}$ )
<i>R matrix</i>	
Azuma <i>et al.</i> (1994)	121–225
Tang <i>et al.</i> (2010)	191–258
deBoer <i>et al.</i> (2013)	150
<i>Transfer</i>	
Avila <i>et al.</i> (2015)	139(9)

$^{12}\text{C}(^6\text{Li}, d)^{16}\text{O}$  and  $^{12}\text{C}(^7\text{Li}, t)^{16}\text{O}$  and were found to be in excellent agreement as summarized in Table XIII.

The ANCs of the  $E_x = 6.05$  and 6.13 MeV states have received less attention because the  $E_x = 6.13$  MeV state is too weak to have a significant ground state subthreshold state contribution and the  $E_x = 6.05$  MeV to ground state transition is forbidden. However, the  $E_x = 6.13$  MeV ( $3^-$ ) state makes a weak yet important contribution to the  $^{16}\text{N}(\beta\alpha)^{12}\text{C}$  spectrum just in the sensitive interference region between the  $E_x = 7.12$  and 9.59 MeV  $1^-$  states. These ANCs were recently measured for the first time using sub-Coulomb transfer by Avila *et al.* (2015). Their effects on fits to the capture data and the  $\beta$ -delayed  $\alpha$  spectrum are discussed in Secs. VI.C and VI.D, respectively. The past values are summarized in Tables XIV and XV.

The ground state  $\alpha$  ANC is outside the kinematic window for sub-Coulomb transfer but it can be deduced by other means, such as sequential breakup reactions (Adhikari and Basu, 2009). Morais and Lichtenthaler (2011) also investigated the use of the scattering reaction  $^{12}\text{C}(^{16}\text{O}, ^{12}\text{C})^{16}\text{O}$ . In addition, the  $R$ -matrix analysis of Sayre *et al.* (2012) contends that the ground state  $E2$  external capture makes a significant contribution to that cross section and has given a value based on an  $R$ -matrix fit to ground state transition  $E2$  data. The measurements giving estimates of the ground state  $\alpha$  ANC are summarized in Table XVI. In this work, a much smaller value has been obtained (see Table XXI). The data that constrain the value are primarily the  $E2$  ground state data of Schürmann *et al.* (2011) in the off-resonance region near  $E_{c.m.} \approx 3.5$  MeV (see Fig. 9).

This section has summarized the best fit for the  $R$ -matrix analysis and has described the wide range of experimental measurements that have been used to constrain the phenomenological model parameters. The parameters for the best fit can be found in Tables XXI, XXII, and XXIII of Appendix A. For convenience, the main contributions to the low-energy cross section are summarized in Table XVII to aid in a quick

TABLE XVI. Summary of previous measurements of the  $\alpha$  particle asymptotic normalization coefficient of the ground state of  $^{16}\text{O}$ . The scatter in the values combined with different favored solutions of the data represents a systematic uncertainty in the  $E2$  cross section. See text for details.

Reference	$\text{ANC}_\alpha$ (fm $^{-1/2}$ )
<i>R matrix</i>	
Sayre <i>et al.</i> (2012)	709
<i>Transfer</i>	
Adhikari and Basu (2009)	13.9(24)
	1200 (WS2)
Morais and Lichtenthaler (2011)	4000 (WS1)
	750 (FP)

TABLE XVII. Summary of the critical parameters necessary to reproduce the total  $^{12}\text{C}(\alpha, \gamma)^{16}\text{O}$  low-energy cross section at  $E_{c.m.} = 300$  keV with about 7% deviation (lower) from the full parameter set. Signs on the partial widths indicate the sign of the corresponding reduced-width amplitude. See Tables XXI and XXII of Appendix A for further details.

$J^\pi$	$E_x$ (MeV)	$\Gamma_\alpha$ (keV)/ANC (fm $^{-1/2}$ )	$\Gamma_{\gamma_0}$ (meV)
$0^+$	0	58	
$0^+$	6.05	1560	
$2^+$	6.92	$1.14 \times 10^5$	97
$1^-$	7.12	$2.08 \times 10^{14}$	55
$1^-$	9.586	382	-15
$2^+$	11.5055	83	-490

reproduction of the low-energy cross section. Yet for any analysis of this kind, the best fit is only the beginning, the real challenge is the estimation of the uncertainties. In particular, how are the systematic differences in the data and the ambiguities inherent in the model dealt with?

## VII. UNCERTAINTY ANALYSIS

The total uncertainty of the capture cross section, and subsequent reaction rate, resulting from the  $R$ -matrix analysis has significant contributions from both the experimental observables and the phenomenological model. In the following sections, investigations of these uncertainties are made by way of different sensitivity studies.

The studies begin with an examination of the sensitivity of the fit to different sets of data. Then the uncertainties stemming from the model are explored (i.e., background poles, channel radii, goodness of fit estimate). A frequentist Monte Carlo analysis (Gialanella *et al.*, 2001; deBoer *et al.*, 2014) is then performed to estimate the contributions from the statistical and overall systematic uncertainties of the data. The uncertainties from quantities that were fixed in the fitting, primarily the ANCs and  $\gamma$  widths of the subthreshold states, are now varied so that their uncertainties can be propagated through the Monte Carlo analysis.

Throughout this section the results of different fits that test the uncertainty of the  $R$ -matrix analysis are compared to the  $S$  factor of the best fit at  $E_{c.m.} = 300$  keV by giving the deviation  $\Delta S_{300 \text{ keV}}$  (see the bottom of Table IV for the best fit

value of this work). This is a shorthand comparison since different solutions produce different deviations from the best fit as a function of energy, but it serves to give a good measure of the effect at the region of greatest interest (see Table XIX for a summary). The full excitation curves were recorded for each different test calculation and then used for the total cross section and reaction rate uncertainties.

### A. Sensitivity to different data sets

In Sec. VI.B it was shown that the ground state  $E2$  data are not always well reproduced by the  $R$ -matrix fit and that they show significant discrepancies between one another. Since the global fit includes data for the total cross section, the ground state  $E1$ , and all cascade transitions, the  $E2$  cross section should be highly constrained even with no  $E2$  cross section data (i.e.,  $\sigma_{\text{total}} - \sigma_{\text{G.S.E1}} - \sigma_{\text{cascades}} = \sigma_{\text{G.S.E2}}$ ). In practice, this is with the caveat that the  $E2$  cross section is significant compared to the total cross section compared to the uncertainties of the data, which it is over several regions, especially at higher energies. When the  $E2$  data were completely neglected in the fit, a similar result was obtained ( $\Delta S_{300 \text{ keV}} = -0.6 \text{ keV b}$ ). This is largely because the  $E2$  cross section is dominated by the subthreshold state at  $E_x = 6.92 \text{ MeV}$ . Since the parameters that describe these contributions are highly constrained by other types of data, it does not change significantly.

The ground state angular distribution data also show discrepancies, both between one another and with the fit at certain energies and angles (see Fig. 10). Another test was made by completely eliminating the ground state angular distribution data from the fit, leaving only the derived  $E1$  and  $E2$  excitation curve data. This had a somewhat more pronounced effect resulting in a lower value in the extrapolation ( $\Delta S_{300 \text{ keV}} = -5.2 \text{ keV b}$ ). Finally both the  $E1$  and  $E2$  excitation curve data were removed, fitting only to the angular distribution data for the ground state transition. Again, only a small deviation ( $\Delta S_{300 \text{ keV}} = -0.9 \text{ keV b}$ ) was observed from the standard fit.

### B. Limiting interference solutions

One of the largest sources of uncertainty in an  $R$ -matrix analysis can come from different possible interference solutions that cannot be ruled out by the data. These different solutions are a result of the different possible signs for the reduced-width amplitudes. When more than one level is present in the sum of Eq. (17), the difference in the sign of each element can produce drastically different values for the cross section. This sign cannot usually be predicted by theory, therefore experimental capture data are critical. However, limiting the solutions is often challenging because the cross section must usually be measured in off-resonance regions where the experimental yields are small. For the case of the  $^{12}\text{C}(\alpha, \gamma)^{16}\text{O}$  reaction, different interference solutions have been proposed for both the  $E1$  and  $E2$  ground state transition and can produce large differences in the extrapolated value of  $S_{300 \text{ keV}}$ . Different interference solutions have also been proposed for the cascade transitions and these are not as well established as the ground state transition. At this stage, the

data have limited the possible solutions, at least over the lower energy range, to only a few.

Starting with the ground state  $E2$  cross section data, Sayre *et al.* (2012) made an extensive reanalysis of this low-energy data where a statistical criterion was used to eliminate outlying data points. Further, Sayre *et al.* (2012) analyzed the narrow resonance region in order to determine the relative interference signs of the  $E2$  contributions to the cross section. The main result of Sayre *et al.* (2012) was to limit the  $E2$  interferences to two possible solutions. If the subsequent higher-energy data from Schürmann *et al.* (2011) are now considered, only one interference solution remains viable as shown in Fig. 20. This then gives a final interference pattern for the  $E2$  cross section, at least between the  $2^+$  subthreshold state, the narrow  $2^+$  at  $E_x = 9.84 \text{ MeV}$ , the first broad resonance at  $E_x = 11.51 \text{ MeV}$ , and the  $E2$  external capture.

As an aside, in the analysis of Sayre *et al.* (2012) the  $R$ -matrix fit was performed to only the ground state  $E2$  data allowing the ANCs of the ground state and  $E_x = 6.92 \text{ MeV}$  subthreshold state to vary freely. The fit resulted in values of 709 and  $1.59 \times 10^5 \text{ fm}^{-1/2}$  for the ANCs of the ground state and  $2^+$  subthreshold state, respectively. This can be compared to the values of 14 (Adhikari and Basu, 2009) or 750–4000 (Morais and Lichtenthäler, 2011) for the ground state and  $1.14(10) \times 10^5$  (Brune *et al.*, 1999)  $-1.22(7) \times 10^5$  (Avila *et al.*, 2015)  $\text{fm}^{-1/2}$  for the  $2^+$  subthreshold state. The two components interfere with each other destructively and can result in a range of values that produce a similar  $E2$  cross section over the energy range of the data. The analysis of Sayre *et al.* (2012) was made before the data of Schürmann *et al.* (2011) were available that significantly increase the sensitivity of the fit to the  $E2$  data, especially the external capture that has a maximum effect in the off-resonance region at  $E_{\text{c.m.}} \approx 3 \text{ MeV}$ . A measurement of the ground state ANC taken together with the capture data would then provide a consistency check for the value of the  $2^+$  subthreshold state ANC. Since large systematic differences occur for the  $E2$  cross section, another method of verification is highly desirable (see Secs. VI.B and VI.F).

Now turning to the  $E1$  cross section, a large source of uncertainty can come from the ambiguity in the interference

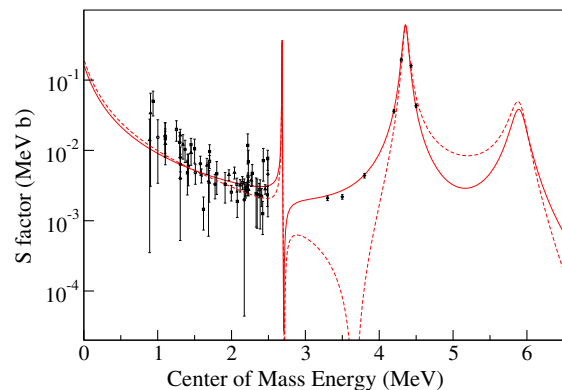


FIG. 20. Comparison of the two allowed  $E2$  interference solutions determined by Sayre *et al.* (2012). If the higher-energy data of Schürmann *et al.* (2011) are also considered, only one solution remains viable.

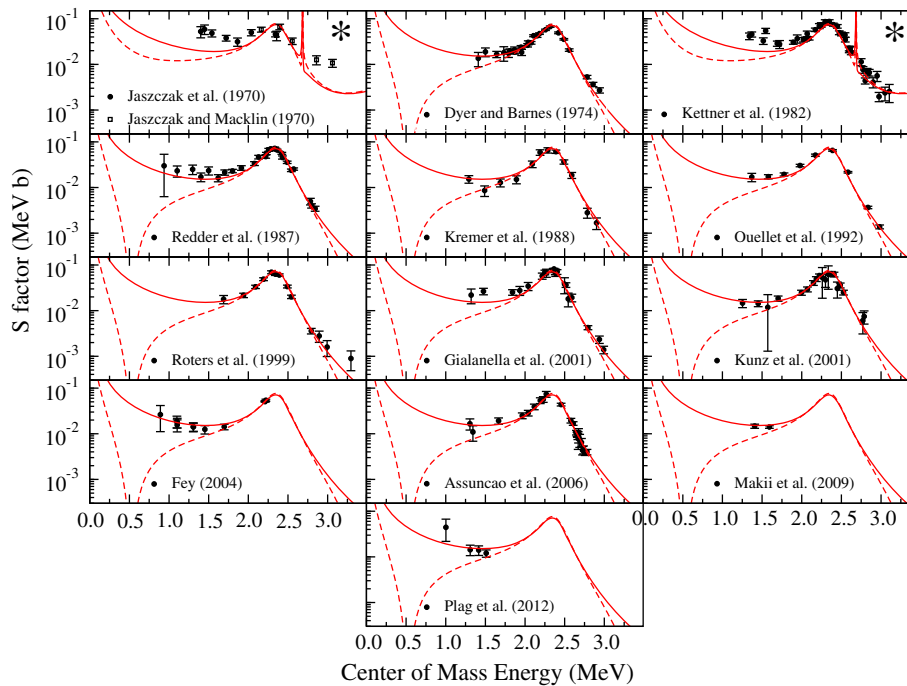


FIG. 21. Comparison of destructive (dashed red lines) and constructive (solid red lines)  $E1$  solutions. A  $1^-$  background pole is included in the ground state  $\gamma$ -ray channel in these cases. The energy of the pole is held constant in both cases and the fitted  $\alpha$  widths are very similar. For the constructive case  $\Gamma_{\gamma_0} = 1.8$  eV, while the destructive case gives 21.7 eV.

sign between the  $1^-$   $E_x = 7.12$  MeV subthreshold state and the unbound state at  $E_x = 9.59$  MeV. Most analyses have concluded (or assumed) that the constructive solution is favored, but most also do not provide detailed quantitative support for this decision. A few analyses, those of [Ouellet \*et al.\* \(1992\)](#),<sup>3</sup> [Hale \(1997\)](#), and [Gialanella \*et al.\* \(2001\)](#), have either ruled in favor or determined that the destructive solution cannot be dismissed. Here the  $E1$  destructive solution is investigated in detail in light of the present analysis and the most current data.

The situation was investigated in detail by [Kunz \(2002\)](#), [Fey \(2004\)](#), and [Hammer \*et al.\* \(2005b\)](#). However, approximations were made in these analyses that can now be improved upon and in fact are very significant to the analysis. The first is the neglect of the overall systematic uncertainties. This resulted in greatly inflated  $\chi^2$  values for the fits of those works, regardless of the interference solution. This is because the systematic uncertainties are quite large compared to the statistical ones, at least near the peak of the low-energy  $1^-$  resonance. The second issue is that the contributions from the two  $1^-$  levels at  $E_x = 12.45$  and  $13.10$  MeV are not explicitly included but are instead treated as a single background pole (the classic three level  $E1$  fit). The single pole assumption leads to fits to the low-energy data that are now found to be unphysical when the added constraints of the higher-energy data are imposed. The last improvement is that the transfer reaction measurements have provided much tighter constraints

on the values of the ANCs, further limiting the number of viable solutions.

These further constraints have a strong impact on the  $E1$  destructive and constructive solutions. In fact, they limit the destructive solution to only one possibility, and it will be shown that this is also ruled out, in favor of the constructive one. Figure 21 shows the result of an analysis of the destructive solution compared to the constructive one. In this fit, the ANC of the  $1^-$  subthreshold state has been fixed to a value of  $2.08(20) \times 10^{14} \text{ fm}^{-1/2}$  ([Brune \*et al.\*, 1999](#)). This has been done because if it is allowed to vary freely, tension from other data sets causes the destructive solution result in unphysical values for the ANC. This on its own is one hint that this solution may not be viable. In particular, the fit would favor a very small ANC, many sigma removed from the value of [Brune \*et al.\* \(1999\)](#). Considering only the  $\chi^2$  from the  $E1$  data (165 data points), the constructive solution gives  $\chi^2 = 259.8$  and the destructive solution gives  $\chi^2 = 583.8$ , a difference of  $\Delta\chi^2 = 324.0$  (see Table XVIII). The difference in  $\chi^2$  for a  $5\sigma$  deviation for 78 fit parameters is  $\Delta\chi^2_{5\sigma} = 169$ . Hence the destructive solution is ruled out under these conditions, and the ANC would have to be changed to a value far outside the acceptable range of the transfer measurements to recover a  $\chi^2$  of less than  $5\sigma$ .

At higher energies, the possible interference combinations are further limited by the stronger  $E1/E2$  interference in the angular distributions. This uniquely defines the interferences at high energy between the  $1^-$  levels at  $E_x = 12.45$  and  $13.10$  MeV and the  $2^+$  level at  $E_x = 12.97$  MeV. A similar situation exists for the  $^{15}\text{N}(p, \alpha_0)^{12}\text{C}$  data. Examples of these different interference solutions are shown in Fig. 22 for the

<sup>3</sup>However, this seems to have been retracted in a subsequent publication ([Ouellet \*et al.\*, 1996](#)).

TABLE XVIII. Comparison of  $\chi^2$  values for different  $E1$  interference solutions. Only the data of [Kremer \*et al.\* \(1988\)](#) favor a destructive solution.

Reference	$N$	$\chi^2$	
		Constructive	Destructive
Dyer and Barnes (1974)	24	69.6	135.9
Redder <i>et al.</i> (1987)	26	67.5	146.2
Kremer <i>et al.</i> (1988)	12	18.2	16.9
Ouellet <i>et al.</i> (1992)	9	29.2	82.6
Roters <i>et al.</i> (1999)	13	13.6	26.5
Gialanella <i>et al.</i> (2001)	20	22.9	58.0
Kunz <i>et al.</i> (2001)	19	12.1	36.8
Fey (2004)	11	4.5	39.0
Assunção <i>et al.</i> (2006)	24	19.4	26.3
Makii <i>et al.</i> (2009)	2	0.2	5.5
Plag <i>et al.</i> (2012)	4	1.9	5.2
All	164	259.8	583.8

$^{12}\text{C}(\alpha, \gamma_0)^{16}\text{O}$  reaction and Fig. 50 of [deBoer \*et al.\* \(2013\)](#) for the  $^{15}\text{N}(p, \alpha_0)^{12}\text{C}$  reaction.

Turning to the cascade transitions, in [Avila \*et al.\* \(2015\)](#), ANCs were measured for the  $E_x = 6.05, 6.13, 6.92,$  and  $7.12$  MeV bound states, with the  $E_x = 6.05$  and  $6.13$  MeV ANCs being measured for the first time via sub-Coulomb transfer. ANCs similar to those deduced in the global  $R$ -matrix fit of [deBoer \*et al.\* \(2013\)](#), where the capture data of [Schürmann \*et al.\* \(2011\)](#) were fitted to constrain the ANCs, were found. An interference ambiguity in the low-energy  $S$  factor for these two transitions was still left undefined in [Avila \*et al.\* \(2015\)](#). If the external capture determined by these ANCs is combined with the higher-energy capture data of [Schürmann \*et al.\* \(2011\)](#) the interference combination can be uniquely determined for the  $E_x = 6.05$  MeV transition and is suggestive of a solution for the  $E_x = 6.13$  MeV transition as shown in Fig. 23.

The most important result of this section is that only one viable interference solution is possible for both the  $E1$  and  $E2$

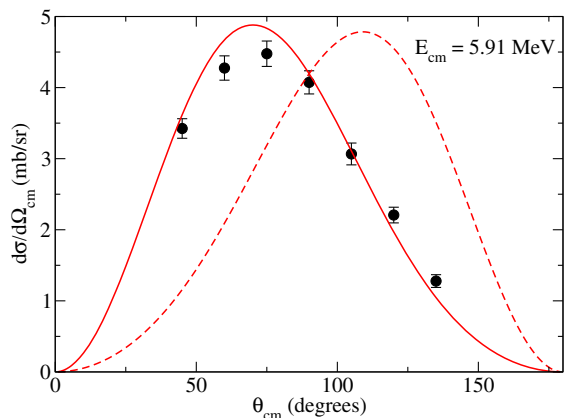


FIG. 22. Example angular distribution for the  $^{12}\text{C}(\alpha, \gamma_0)^{16}\text{O}$  reaction at  $E_{\text{c.m.}} = 5.91$  MeV ( $E_x = 13.07$  MeV). The solid red line shows the differential cross section with the preferred interference pattern while the dashed red line shows the differential cross section with the relative interference sign between the  $E1$  and  $E2$  contributions switched. From [Kernel, Mason, and Wimmersperg, 1971](#).

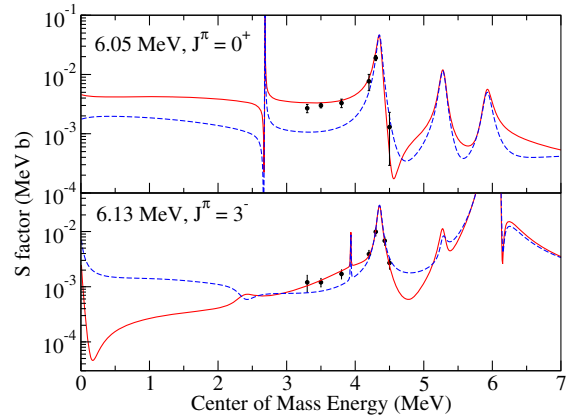


FIG. 23. Comparison of the different possible interference solutions for the  $E_x = 6.05$  and  $6.13$  MeV transition capture cross sections as purposed by [Avila \*et al.\* \(2015\)](#). The different solutions are compared with the higher-energy data of [Schürmann \*et al.\* \(2011\)](#), the only data available for these transitions. For the  $E_x = 6.05$  MeV transition, the constructive solution at low energy is highly favored. For the  $E_x = 6.13$  MeV transition, the destructive solution is favored but there is more ambiguity, especially since the  $3^-$  state at  $E_x = 11.49$  MeV can contribute to the cross section over the energy range of the data. The calculation shows that additional measurements at just slightly higher energy than those of [Schürmann \*et al.\* \(2011\)](#) could provide a more definitive solution.

ground state cross sections. This drastically decreases the uncertainty, by ruling out the destructive  $E1$  solution. While there is a limited amount of data for the cascade transitions, the current data seem to constrain the major interference solutions. However, because of the limited data it is certainly possible that some of the solutions here are incorrect. The situation worsens at higher energy where the data become even more sparse. For the cascade transitions there is almost no data above  $S_p$ . While these different solutions do not have a direct effect on the low-energy cross section determination, they may affect the extrapolation indirectly since the overall fit is quite sensitive to the total cross section data at higher energies. Hence further studies of the cascade data are highly desirable.

### C. Channel radius and background poles

A long-standing complication with  $R$ -matrix theory is that it requires two sets of model parameters: channel radii and background poles. What complicates the situation is that these two sets of model parameters are correlated to one another, hence there is a range of viable solutions.

A phenomenological  $R$ -matrix fit must then be tested for its sensitivity to the choice of both the channel radii<sup>4</sup> and the

<sup>4</sup>Even the choice of how many different channel radii will be used is different for different  $R$ -matrix analyses. In principle a different channel radius can be chosen for each  $s-l$  channel. While this is sometimes done, many analyses restrict themselves to different channel radii only for different particle partitions. That is the approach taken here.

background poles. The radius and the number of levels included in the analysis are closely linked as discussed in Sec. IV.A. In the strict  $R$ -matrix theory, the fit should be completely insensitive to the choice of channel radius, but this is in the limit of an infinite number of levels. It is also important to note that the channel radius does not correspond to a real nuclear radius, although the value used in phenomenological analyses is often rather close, which has caused much confusion over the issue. In practice the number of levels in an  $R$ -matrix calculation is truncated to only a few or even just one. Even if the tails of higher-energy resonances do have an effect, their contributions can often be reproduced, up to some level of precision, with only a single background pole (for each  $J^\pi$ ). However, as the data become more precisely measured, especially in the interference regions between resonances, it may be possible that more than one background pole is required.

While the sensitivity of the fit to the channel radius and background poles are closely linked, each is discussed separately in order to try to gauge their contributions. Further, while it is not often explicitly stated, the many sensitivity tests that were made involved several different combinations of both radii and number and value of background poles.

A strong sensitivity in  $\chi^2$  to the channel radius exists for the present fit. This is primarily the result of the fit to the scattering data and was detailed previously by Tischhauser *et al.* (2002). This was interpreted as a positive result by Tischhauser *et al.* (2002), giving a constraint on the radius that should be used. However, this is in direct conflict with the previous discussion, where it was argued that the value of the channel radius should be insensitive to the fit. This represents one of the remaining puzzles to be solved, not only for this case, but for the phenomenological  $R$ -matrix technique in general.

It should be possible to decrease the sensitivity of the fit on the channel radius by adding more background poles. This procedure was performed, yet the sensitivity remained almost unchanged. Therefore, to gauge the sensitivity of the fit to the extrapolated value of the capture cross section, different fits were made at different channel radii varying between 4.5 and 6.5 fm and using various numbers and combinations of background poles. A radius of 5.43 fm was found to be the best fit value, in excellent agreement with the value of  $5.42^{+0.16}_{-0.27}$  of Tischhauser *et al.* (2002). Despite a rather large change in the overall  $\chi^2$  of the fit, the extrapolated value of the  $S$  factor changed only by  $\pm 8$  keV b. This is because the sensitivity in  $\chi^2$  comes mainly from the scattering data, while that of the capture data is much less so.

Turning now to the background poles, one of the assertions of this analysis is that a reasonable fit can be obtained for the  $^{12}\text{C}(\alpha, \gamma)^{16}\text{O}$  data with no background pole contributions in the capture partition (they remain very necessary for the scattering partition). The reason for this assertion is that no strong higher-energy resonances have been observed in the capture data up to  $E_{\text{c.m.}} \approx 20$  MeV (Snover, Adelberger, and Brown, 1974). This is the main reason for explicitly including the two  $1^-$  levels at  $E_x = 12.45$  and 13.09 MeV, which

correspond to the final two strong  $E1$  resonances observed in  $^{12}\text{C}(\alpha, \gamma_0)^{16}\text{O}$ , at least up to  $E_x \approx 20$  MeV. It is therefore expected that higher-energy background contributions will be weak for the ground state.

However, adding additional background poles is allowed by the data and does improve the quality of the fit. The question becomes whether the improvement is physically reasonable or is it simply the result of adding more free parameters to the fit. Additionally the improvement results largely from achieving a better fit to the very low-energy data, but there are strong hints that much of these data may overestimate the cross section (see Sec. VI.A).

Ground state background contributions were considered for both the  $E1$  and  $E2$  cross sections using  $J^\pi = 1^-$  and  $2^+$  poles, respectively. The  $J^\pi = 1^-$  background pole contribution resulted in a significant improvement in the fit of the low-energy  $^{12}\text{C}(\alpha, \gamma)^{16}\text{O}$  data. For example, it decreased the  $\chi^2$  from 436 to 203 for the 164 data points considered in the low-energy  $E1$  capture data. This ambiguity in the strength of the  $1^-$  background pole is one of the most significant uncertainties in the fitting, producing a value of  $S(300 \text{ keV}) = 15.2 \text{ keV b}$  larger than the fit without. Inclusion of a  $J^\pi = 2^+$  background pole had only a small effect.

One way to obtain further constraint on the background pole contributions is to continue to fit to higher energies. This becomes increasingly difficult in practice as the numbers of levels and channels increase quickly at higher energies. Even so, a test can be made to see if the magnitude of the background contributions is reasonable. There is one measurement by Snover, Adelberger, and Brown (1974) which extends the ground state transitions cross section to much higher energies. The data show that the ground state cross section decreases substantially above the two strong  $1^-$  resonances at  $E_x = 12.45$  and 13.09 MeV. In Fig. 24 the data of Snover, Adelberger, and Brown (1974) are shown together with a fit that has all

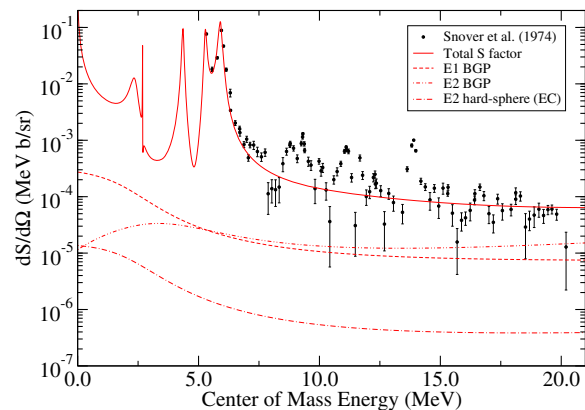


FIG. 24. Differential  $S$  factor of the data ( $\theta_{\text{lab}} = 52^\circ$ ) of Snover, Adelberger, and Brown (1974). The  $R$ -matrix fit was made with the data fixed at the reported cross sections in order to test whether the amplitude of the free background poles were reasonable. The extrapolated values of the  $S$  factor using the two different methods proved to be very similar. In the legend,  $E2$  hard-sphere (EC) refers to the hard-sphere contribution to the external capture.

of the background poles placed now at higher energies ( $E_x = 40$  MeV). The fit gives a background contribution that is roughly consistent with these data in that it follows the off-resonance trend of the data. This produced a value for  $S(300 \text{ keV}) = 155.3 \text{ keV b}$ , very similar to the value of  $153.7 \text{ keV b}$  found with out this higher-energy data (with the lower energy background poles), demonstrating that this additional background contribution is at least physically reasonable.

It is somewhat surprising that such good fits can also be obtained for the cascade transitions without background poles. There is no higher-energy data for these transitions so their higher-energy behavior is unknown. In fact the higher-energy (above  $S_p$ ) constraint of this fit comes indirectly from  $^{15}\text{N}(p, \gamma)^{16}\text{O}$  cascade transition data (Imbriani *et al.*, 2012), and these have large uncertainties. One likely reason for such good fits is that external capture is the dominant contribution to the cascade transitions at low energy, lessening the effects of resonance interference.

#### D. Different fitting methods

In principle, if the data were expressed as true cross sections, were consistent with each another, and the uncertainties were completely characterized, performing a standard  $\chi^2$  fit would be all that was required to achieve the best fit and accurate extrapolation of the low-energy cross section. Unfortunately these conditions are hardly ever met in practice and therefore a blind  $\chi^2$  fitting is likely to lead to an erroneous result. This is the reason why many different experimental approaches are critical; by examining the reaction mechanism through different methods, hidden systematic errors can be more readily revealed.

While a standard  $\chi^2$  fit analysis has been used as the standard fit procedure for this analysis, other methods have been investigated to check the robustness of the fitting and the uncertainty estimates. In particular, the tension between different data sets and the background pole contributions has the effect that the subthreshold parameters need to be fixed during the normal fitting.

An alternative fitting method investigated here is to base the goodness of fit on the reduced  $\chi^2$  of each data set. The idea is based on that presented by Dodder *et al.* (1977), where a similar analysis involving many data sets was made. Equation (87) is modified to

$$\chi^2 = \sum_i \left( \frac{\sum_j R_{ij}^2}{N_i - \nu} \right) + \frac{(n_i - 1)^2}{\sigma_{\text{sys},i}^2}, \quad (93)$$

where  $N_i$  is the total number of data points in the  $i$ th data set and  $\nu$  is the number of fit parameters. Fitting to the reduced  $\chi^2$  puts each data set on a more equal footing regardless of the number of data points in that set. This is statistically incorrect, but has the result of putting each data set on a more equal footing, even if that data set has many experimental points. From a purely statistical view this does not make much sense, but from a practical standpoint this can be reasonable since it will lessen any systematic bias of a single data set over the rest, especially if that single data set has many points with small uncertainties.

In the current analysis the scattering data of Tischhauser *et al.* (2009) dominate the normal  $\chi^2$  function because they contain, by far, the largest number of data points and have small statistical uncertainties (see Sec. VI.E). If the data were a perfect representation of the true cross section, this would be ideal because this would reflect the experimenter's ability to easily access this cross section. However, it is known that the data of Tischhauser *et al.* (2009) require experimental resolution corrections, which are quite significant at the statistical uncertainty level of the data points, particularly in regions where the cross section changes rapidly. If the method used for this correction is not precise enough or if there are any unaccounted for uncertainties in the data this will result in a bias in the fit from this data set. This issue undoubtedly exists in the data considered and is not limited to the scattering data. The other main data sets where this effect is most likely are in the  $^{16}\text{N}(\beta, \alpha)^{12}\text{C}$  spectrum measurements of Azuma *et al.* (1994) and Tang *et al.* (2010).

Another different approach would be to also include the uncertainties on the subthreshold parameters in the  $\chi^2$  fitting. This can be done by adding additional terms to the  $\chi^2$  function

$$\chi^2 = \sum_i \left( \frac{\sum_j R_{ij}^2}{N_i} \right) + \frac{(n_i - 1)^2}{\sigma_{\text{sys},i}^2} + \sum_k \frac{(P_{\text{fit},k} - P_{\text{exp},k})^2}{\sigma_{\text{exp},k}^2}, \quad (94)$$

where  $P_{\text{fit},k}$  is the parameter value varied in the fit,  $P_{\text{exp},k}$  is the experimentally determined value, and  $\sigma_{\text{exp},k}$  is the experimental uncertainty.

This method, combined with using the reduced  $\chi^2$  method, results in much more reasonable fits than the standard  $\chi^2$  fitting when the subthreshold state parameters are allowed to vary freely. Using this approach the fit favors a larger ANC for the  $1^-$  subthreshold state ( $\text{ANC} = 2.6 \times 10^{14} \text{ fm}^{-1/2}$ ,  $\Gamma_{\gamma_0} = 48 \text{ meV}$ ) and a smaller one for the  $2^+$  ANC ( $\text{ANC} = 0.84 \times 10^5 \text{ fm}^{-1/2}$ ,  $\Gamma_{\gamma_0} = 98.0 \text{ meV}$ ). This is a reflection of the tension between the  $^{16}\text{N}(\beta, \alpha)^{12}\text{C}$ , transfer, and elastic scattering measurements. The increasing  $1^-$  ANC and decreasing  $2^+$  ANC have canceling effects in the ground state cross section and in the cascade cross sections, resulting in a somewhat larger value for the total capture cross section of  $S(300 \text{ keV}) = 152.1 \text{ keV b}$ .

In any analysis that contains a large amount of data there tend to be outlier data points. It has been shown that certain data sets are plagued by this problem in the current analysis. There are various methods of testing the sensitivity of fits to these points. For example, Sayre *et al.* (2012) used Chauvenet's criterion to reject outliers in the  $E2$  ground state data. Instead of outright rejection of data points, there are different methods of modifying the  $\chi^2$  function to give less weight to outlier data. These methods are similar to increasing the uncertainties on the data points. One example is the method given by Sivia and Skilling (2006) where instead of minimizing  $\chi^2$ , the function

$$L = \sum_j \log \left[ \frac{1 - e^{-R_{ij}^2/2}}{R_{ij}^2} \right] \quad (95)$$

is maximized. This alternative function has a broader probability density function leading to more conservative uncertainty estimates than the standard  $\chi^2$  function. Fitting with this alternative approach produced a very similar fit as the standard  $\chi^2$  method [ $S(300 \text{ keV}) = 146.2 \text{ keV b}$ ] demonstrating that outlier data points have a minimal effect on the central value obtained for fit. However, as shown in the next section, the effect on the uncertainty estimation is quite significant.

### E. Monte Carlo uncertainty analysis

The best fit resulting from the  $R$ -matrix analysis was subjected to a MC uncertainty analysis. From the MC analysis, uncertainty contributions from the statistical and the overall systematic uncertainties of the experimental data were obtained for the fit parameters, the  $^{12}\text{C}(\alpha, \gamma)^{16}\text{O}$  cross section, and corresponding reaction rate. However, in order for the fit to yield accurate uncertainties, the reduced  $\chi^2$  of the fit should be approximately 1. Given that this is not the case, as detailed in Table VII, the alternative goodness of the fit method given by Eq. (95) was employed. In this way, the uncertainty from outlying data points and discrepant data sets can be better estimated. At  $E_{\text{c.m.}} = 300 \text{ keV}$ , the difference in the uncertainty calculated with the standard  $\chi^2$  function of Eq. (87) versus the  $L$  estimator of Eq. (95) was quite significant, inflating the uncertainty from about 10% to about 15%. Indeed, over other energy regions, especially near the low cross section area in the vicinity of  $E_{\text{c.m.}} \approx 3 \text{ MeV}$ , the increase in the uncertainty was even more dramatic.

The MC technique was adapted from those of Gialanella *et al.* (2001), Schürmann *et al.* (2012), and deBoer *et al.* (2014). The following assumptions and steps were taken for this analysis:

- (1) The best fit from the  $R$ -matrix analysis is taken as the most probable description of the data. The  $L$  method of Eq. (95) is used to define the goodness of the fit.
- (2) The data are then subjected to a random variation based on their uncertainties. The data are varied, assuming a Gaussian probability density function, around the best fit cross section value. The uncertainty on the data point is scaled by the square root of the ratio of the cross section of the fit divided by the cross section of the Gaussian randomized cross section.
- (3) The systematic overall uncertainty for each experimental data set is also varied assuming a Gaussian probability density function.
- (4) The ANCs and  $\gamma$  widths of the subthreshold states are also allowed to vary. Their uncertainty contributions are included using Eq. (94).
- (5) Background poles for  $E1$  and  $E2$  multipolarities are introduced to the capture channels to give further freedom in the fit.
- (6) The  $R$ -matrix fit (the  $L$  maximization) is then performed again. The initial values of the parameters are those from the original best fit.
- (7) Steps 3–6 are then repeated many times (referred to as the “MC iterations”). For each of the MC iterations, an extrapolation of the cross section can be made using

the best fit parameters from that iteration. This cross section is then numerically integrated to calculate the reaction rate as a function of temperature.

Histograms were then created from the MC procedure for the cross sections and reaction rates at specific energies or temperatures, respectively. The lower and upper uncertainties were then defined by the 16% and 84% quantiles. The central value is defined as the 50% quantile.

The uncertainty in the cross section derived from the MC analysis is shown in Fig. 25. At low energies, the uncertainty budget is dominated by the uncertainties in the ANCs of the subthreshold states and is about 15% at  $E_{\text{c.m.}} = 300 \text{ keV}$ . In the region above  $E_{\text{c.m.}} = 5.0 \text{ MeV}$ , the cross section is determined mainly indirectly through a combination of the  $^{15}\text{N}(p, \gamma)^{16}\text{O}$ ,  $^{12}\text{C}(\alpha, \alpha_0)^{12}\text{C}$ , and  $^{15}\text{N}(p, \alpha_0)^{12}\text{C}$  data. In this region the uncertainty becomes much smaller and was found to be in good agreement with that obtained from a standard  $\chi^2$  analysis. At the highest energies, where the experimental data taper off, the uncertainty begins to increase again.

Therefore, using Eq. (95), it is believed that a conservative estimate of the uncertainty stemming from the experimental uncertainties has been obtained. Taking the approach considered here, where a large portion of the experimental data is considered, it is useful to compare with the other extreme where only a small subset of well-defined data is considered as in Schürmann *et al.* (2012). Each approach has its advantages and drawbacks. Foremost among them, the method considered here likely errs on the side of including a significant amount of data that is incompatible, yet it is not subject to the bias of choosing the best data. On the other hand, choosing a small subset of data can yield a smaller uncertainty that may be accurate; however, the entire analysis hinges on choosing the “correct” data.

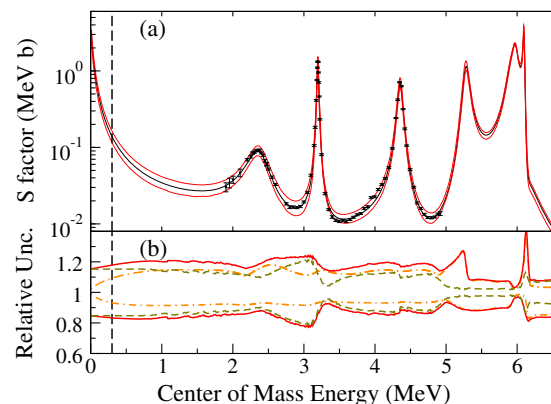


FIG. 25. (a) The uncertainty in the  $S$  factor as derived by combining the MC analysis (which includes the subthreshold state uncertainties) and the model uncertainties. The data from Schürmann *et al.* (2005) are shown for comparison. (b) The uncertainties relative to the best fit value for the Monte Carlo analysis (dashed olive line) and the uncertainties derived from the model (dot-dashed orange line). The total uncertainty, taken as the MC and model uncertainties summed in quadrature, is shown by the solid red line. The black vertical dashed line marks the region of typical astrophysical interest at  $E_{\text{c.m.}} = 300 \text{ keV}$ .

TABLE XIX. Summary of the systematic uncertainties that were considered and their affects on  $S(300 \text{ keV})$ .

Source	Systematic uncertainty contribution (keV b)
Inclusion of $Q$ coefficients	+1.2
Relativistic $\gamma$ -ray angular distribution correction	-0.3
Fixed energy of $E_x = 9.5779 \text{ MeV}$	-1.2
Different fitting functions	+7.7
Fixed Kunz (2002) cascade data normalizations	-0.5
Fixed Schürmann <i>et al.</i> (2005, 2011) data normalizations	+1.1
No ground state $^{12}\text{C}(\alpha, \gamma)^{16}\text{O}$ $E2$ excitation curve data	-0.6
No ground state $^{12}\text{C}(\alpha, \gamma)^{16}\text{O}$ $E1$ or $E2$ excitation curve data	-0.9
No ground state $^{12}\text{C}(\alpha, \gamma)^{16}\text{O}$ angular distribution data	-5.2
$1^-$ ground state $^{12}\text{C}(\alpha, \gamma)^{16}\text{O}$ $E1$ BGP	+15.2
$2^+$ ground state $^{12}\text{C}(\alpha, \gamma)^{16}\text{O}$ $E2$ BGP	-3.0
$\alpha_0$ channel radius variation	$\pm 8$
Alternative fitting approaches	+13.1

Both the uncertainties from the experimental data and the uncertainties from the model have been estimated. These results are now combined to give a best estimate of the total uncertainty on the  $^{12}\text{C}(\alpha, \gamma)^{16}\text{O}$  reaction rate.

#### F. Summary and total uncertainty estimate

The previous sections have investigated different sources of uncertainty in the extrapolation of the  $^{12}\text{C}(\alpha, \gamma)^{16}\text{O}$  cross section to the stellar energy range. The uncertainty analysis is complicated by data sets that lack good statistical agreement and by ambiguities inherent in the phenomenological model. For added clarification, the key results of these sections are summarized here.

- The reaction data now provide definitive solutions for the ground state interference patterns of both the  $E1$  and  $E2$  cross sections, eliminating a large source of uncertainty. However, many of the  $E2$  measurements show large scatter with respect to one another as well as the  $R$ -matrix prediction for the cross section that far exceeds their quoted uncertainties. The  $E1$  data are in better agreement but still produce a reduced  $\chi^2$  significantly greater than 1.
- The reduced  $\chi^2$  values for the  $\beta$ -delayed  $\alpha$  emission spectra and the scattering data are also significantly greater than 1, likely a result of only approximate modeling of the remaining experimental effects reported in the data. This may even suggest that there are additional unaccounted for uncertainties in the data or, very likely, that the models used to correct for remaining experimental effects in the data are insufficiently accurate.
- If experimental measurements and uncertainties are taken at face value and model uncertainties are ignored, and the uncertainty in the extrapolation of the  $R$  matrix to low energy is calculated, an uncertainty of only a few percent is obtained. However, the large reduced  $\chi^2$  values found for such a fit indicate that this method would significantly underestimate the uncertainty. For this reason a more conservative uncertainty estimator, that of Eq. (95), was used for the MC analysis. Additionally, several sources of known model uncertainty were

explored and found to make a significant contribution to the overall uncertainty budget.

- The properties of the subthreshold states seem to be well known at present, both  $\gamma$  widths and ANCs. Since the development of sub-Coulomb transfer measurements, different experimental measurements have yielded consistent results for the ANCs. In view of the previous points, the uncertainties in the ANCs and  $\gamma$  widths of the subthreshold states have been included in the fitting and uncertainty analysis using Eq. (94).

The total uncertainty has thus been estimated by combining the uncertainties from the experimental data via the MC analysis and the model uncertainties summarized in Table XIX. This produces a total uncertainty of 15% to 20% when both contributions are summed in quadrature over most of the energy region. The results of this analysis are compared to previous results of  $S(300 \text{ keV})$  in Table IV and Fig. 26. With the fitting and uncertainties discussed in detail,

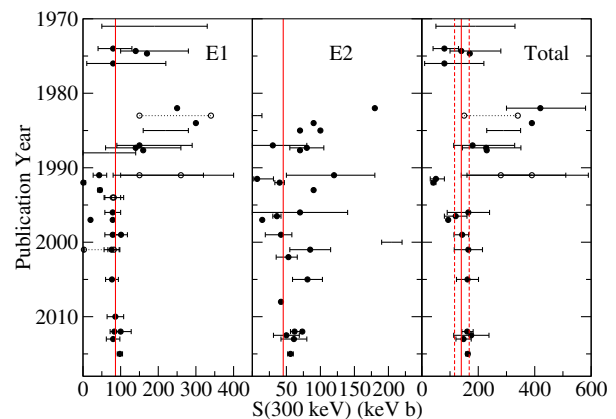


FIG. 26. Plot of  $S(300 \text{ keV})$  values for all past estimates in the literature back to 1970. For the  $E1$  extrapolation, the uncertainty is quite large before the early 1990s. The dramatic decrease is due to the greatly improved constraint on the  $1^-$  subthreshold contribution provided by  $\beta$ -delayed  $\alpha$  emission data and later from sub-Coulomb transfer experiments. The extrapolation of the  $E2$  data still has a somewhat larger spread but it too has seen significant reduction in its uncertainty thanks to high-precision scattering and sub-Coulomb transfer experiments.

the discussion can turn back to several important recent works that were neglected in Sec. V.C.

### VIII. DISCUSSION OF RECENT WORKS

Figure 26 gives an idea of the difficulty encountered in analyzing and then extrapolating the cross section of the  $^{12}\text{C}(\alpha, \gamma)^{16}\text{O}$  reaction to low energy by the wide range of values for  $S(300 \text{ keV})$  that have been estimated over the course of many works. As discussed in Sec. V.A, from the outset, Barker (1971) realized the importance of a comprehensive analysis and it is an impressive feat that even his first work on the subject contains the key elements of the most sophisticated analyses published today: fit to capture, scattering,  $\beta$ -delayed  $\alpha$  spectrum, and consideration of the reduced  $\alpha$  widths from transfer reactions. However, the complexity involved in having to include data from many different reaction types is also why many analyses have considered only a subset of the data (or reactions). Even today, making a general analysis code that can simultaneously fit all of the data is quite challenging and simply compiling all of the experimental data is no small task.

Note that even the implementation of the  $R$ -matrix methods used over the years has undergone significant development. This is for the most part limited to the  $\gamma$ -ray channels, but it is important to realize that extrapolations using the  $R$  matrix have not always been the same. In Sec. III.C it was described how the hybrid  $R$ -matrix model was used for some time but fell out of favor because it was unable to fit the scattering data as well as the standard theory. A significant improvement to the modeling of the external component of the capture cross section was provided by Barker and Kajino (1991), as discussed in detail in Sec. IV.D. Yet even after this work, several analyses continued to neglect the external contributions.

Figure 27 demonstrates the effect of including external capture in the ground state transition of the  $^{12}\text{C}(\alpha, \gamma_0)^{16}\text{O}$  reaction in the  $R$ -matrix analysis. Since the  $\alpha$  particle ANC of the ground state of  $^{16}\text{O}$  remains quite uncertain, a moderate value of  $100 \text{ fm}^{-1/2}$  has been chosen for an example calculation. Figure 27(a) demonstrates that the  $E1$  external capture can be neglected to a good approximation given the data presently available. At  $E_{\text{c.m.}} = 300 \text{ keV}$  the effect is only about 2% for the ANC used. The effect is maximum,  $\approx 35\%$  difference, in the off-resonance region at  $E_{\text{c.m.}} \approx 4 \text{ MeV}$ . Therefore if experimental measurements do access this region  $E1$  external capture does become a necessary part of the calculation.

Figure 27(b) shows that the  $E2$  external capture is much more significant. Here the effect is maximum,  $\approx 30\%$ , in the region in the range  $2 \lesssim E_{\text{c.m.}} \lesssim 3.5 \text{ MeV}$ . Here certainly the  $E2$  external capture cannot be neglected since data have been measured throughout this region with uncertainties much less than 30% in many cases. The effect lessens at  $E_{\text{c.m.}} = 300 \text{ keV}$ , but is still  $\approx 10\%$ . Therefore, if  $E2$  external capture is neglected, a fit may try to compensate by increasing the  $2^+$  subthreshold  $\alpha$  particle ANC, which produces a similar energy dependence in the cross section from the tail of the subthreshold state. This results in what would seem to be a

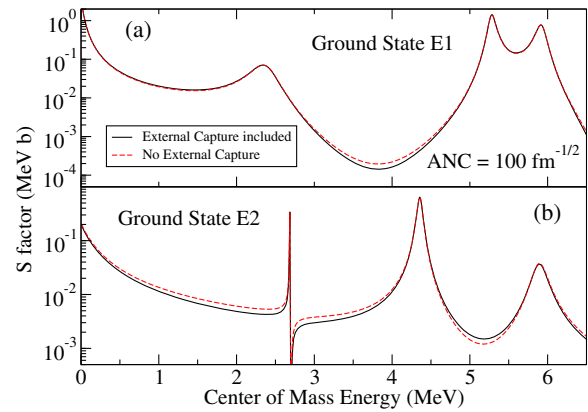


FIG. 27. Comparison of calculations of the ground state transition capture  $S$  factor made with (solid black line) and without (dashed red line) an external capture contribution to the  $R$  matrix. Here no external capture signifies that only the internal part of Eq. (56) is considered. A moderate value of  $100 \text{ fm}^{-1/2}$  has been used as the value of the ground state ANC (see Table XVI). (a) As expected, the  $E1$  external capture is negligible over much of the energy range. Only in the very low  $S$ -factor region around  $E_{\text{c.m.}} \approx 3.75 \text{ MeV}$  is there a significant effect. However, this energy range has proved largely experimentally inaccessible. (b) For the  $E2$  external capture, the lack of low-energy resonances makes its contribution more important. Its interference with the subthreshold  $2^+$  resonance can produce a change in the  $S$  factor significant compared to the uncertainties of the data. As shown in Fig. 8, all of the cascade transitions have very significant hard-sphere contributions, making the inclusion of external capture critical for their modeling. The significance of the external capture for the different transitions is also reflected in the relative contributions of the internal and channel portions of the total reduced-width amplitude as given in Table XXIV.

tension between the ANC measured via transfer reaction and that deduced from the fit to the  $E2$  capture data.

Further, as the main subject of Barker and Kajino (1991), the cascade transition cross sections cannot be analyzed without external capture since it dominates the cross section over a wide energy range (see Fig. 8). Therefore any analysis that is making a global analysis of the  $^{12}\text{C}(\alpha, \gamma)^{16}\text{O}$  reaction must include a model for the direct capture process.

This section now returns to the aforementioned recent works that were not discussed in Sec. V.C, those of Oulebsir *et al.* (2012), Schürmann *et al.* (2012), Xu *et al.* (2013) (NACRE2) and An *et al.* (2015). Each of these different works was made by a different research group and has performed an independent comprehensive analysis of the  $^{12}\text{C}(\alpha, \gamma)^{16}\text{O}$  reaction.

#### A. Schürmann *et al.* (2011)

The global analysis of Schürmann *et al.* (2012) is based on a long history of measurements and analyses performed by Claus Rolf's research group in Münster (Kettner *et al.*, 1982; Redder *et al.*, 1987; Roters *et al.*, 1999; Gialanella *et al.*, 2001; Schürmann *et al.*, 2005, 2011) and Wolfgang Hammer's group at Stuttgart (Kunz *et al.*, 2001; Hammer *et al.*, 2005a, 2005b; Assunção *et al.*, 2006). Much of the basis for the global

$R$ -matrix analysis was developed by Ralf Kunz and was published in [Kunz \*et al.\* \(2002\)](#) with many further details of the analysis in [Kunz \(2002\)](#). Note that this work was done with a completely independent  $R$ -matrix code to the one used here. This extremely comprehensive work was the first to push the  $R$ -matrix calculations up above the proton separation energy. There were several approximations that were made at that time that were subsequently improved upon in [Schürmann \*et al.\* \(2012\)](#). Important improvements have been an external capture calculation of the  $E2$  ground state transition and a systematic uncertainty term in the  $\chi^2$  function. However, even in [Schürmann \*et al.\* \(2012\)](#), the analysis does not include the proton and  $\alpha_1$  partitions at higher energies.

The main difference from the present analysis is that a stringent rejection criterion for the data was adopted. This highlights a common philosophical difference in data analysis. On the one hand, the experimenter knows the details of his own data on a first hand basis, but must often rely on only the details of a publication for the reanalysis of other work. In [Schürmann \*et al.\* \(2012\)](#) the criteria for their data analysis was so stringent that in effect only data measured by that group could be retained. On the other hand, despite the experimenter's confidence in their own data, it is often hard to justify why one measurement is correct over another.

Another major difference is that [Schürmann \*et al.\* \(2012\)](#) did not directly consider the transfer reaction results for the ANC's in their analysis. They were instead treated as fit parameters. However, unlike in the current analysis, because only a very limited amount of data was considered, the tension between different data sets was greatly reduced and their fitted values did not vary as widely as observed here. This may also be because only the phase shifts from [Tischhauser \*et al.\* \(2009\)](#) were used, and the fewer number of data points then lessened the tension between the scattering data and other data sets. Also, only the  $\beta$ -delayed  $\alpha$  data of [Azuma \*et al.\* \(1994\)](#) were considered eliminating the tension between those different data sets.

For the ground state transition, a larger value for the ANC of the  $1^-$  level than those of the higher precision transfer reactions of [Brune \*et al.\* \(1999\)](#) and [Avila \*et al.\* \(2015\)](#) was found. This is in general agreement with what was found here as well when the ANC's are allowed to vary freely (see Sec. VII.D). For the  $2^+$  ANC, excellent agreement was achieved (see Table XIII). The agreement with transfer is quite poor for the  $E_x = 6.05$  MeV  $\alpha$  ANC, as was discussed in Sec. VI.C.

For the final uncertainty analysis a Monte Carlo analysis similar to the one performed here [and originally applied to the case of  $^{12}\text{C}(\alpha, \gamma)^{16}\text{O}$  by [Gialanella \*et al.\* \(2001\)](#)] was performed. Systematic uncertainties were also explored but few details were given regarding the details. In the end, a value of  $S(300 \text{ keV}) = 161 \pm 19_{\text{stat}}^{+8}_{-2} \text{ syst}$  was found.

This central value is very close to the upper 68% confidence level of the current analysis. However, it is difficult to understand the values of  $S(300 \text{ keV})$  for the  $E1$  and  $E2$  contributions compared to the present results. The  $E1$  values are very close ([Schürmann \*et al.\*, 2012](#)) 83.4, current work 86.3 keV b. While naively these values are in good agreement, they should not be, since the  $1^-$  ANC used by [Schürmann](#)

*et al.* (2012) is significantly larger than that used here. Further, and equally perplexing, the  $E2$  value is much larger than that deduced here ([Schürmann \*et al.\*, 2012](#)) 73.4, current work 45.3 keV b, yet the  $2^+$  ANC's are nearly identical for the two analyses. Unfortunately [Schürmann \*et al.\* \(2012\)](#) gave few details as to the resonance parameters that were used so it is impossible to make an exact comparison. One explanation could be that different background pole contributions were used. Since [Schürmann \*et al.\* \(2012\)](#) did not include data at higher energies, more freedom should have been possible for their background contributions.

The overall uncertainty quoted by [Schürmann \*et al.\* \(2012\)](#) for  $S(300 \text{ keV})$  is  $\sim 13\%$ . Given the comparison with this work, this value seems reasonable, if one accepts that all of the data used are correct. It may also be that some of the systematic uncertainties discussed here were overlooked since there are not many details given regarding this in [Schürmann \*et al.\* \(2012\)](#).

## B. Oulebsir *et al.* (2012)

A global  $R$ -matrix analysis was performed as part of the transfer reaction study of [Oulebsir \*et al.\* \(2012\)](#). Besides the analysis being performed from a transfer reaction experimental point of view, this analysis was chosen for comparison because it represents the most recent calculations with Pierre Descouvemont's  $R$ -matrix code DREAM ([Mountford \*et al.\*, 2014](#)), another  $R$ -matrix code developed completely independently from the AZURE2 code used here. While this analysis is limited to the more typical lower-energy range, it considers all of the ground state transition  $E1$  and  $E2$  data. None of the cascade data are considered however. The fits do include some higher-energy resonances explicitly in the  $R$ -matrix calculation with their parameters fixed to values in the compilation. This analysis follows a similar analysis technique as the best fit of the present work in that the ANC's were treated as fixed parameters. However, in addition, all the resonance parameters of the unbound states were fixed to previously determined values. Only the background pole contribution widths were allowed to vary. Given that one of the largest uncertainties in the  $R$ -matrix analysis stems from the background poles, this seems to be a reasonable approximation.

The fitting technique was done iteratively, first fitting to the scattering data to constrain the energy and  $\alpha$  widths, then fitting to the capture data to constrain the ground state  $\gamma$  widths of the background poles. Only  $l = 1$  and  $2$  phase shifts were fit instead of the actual scattering yields, which may cause difficulties in the uncertainty propagation as described by [Buchmann \*et al.\* \(1996\)](#). The  $^{16}\text{N}(\beta\alpha)^{12}\text{C}$  spectrum was not fit but a comparison of the  $l = 1$  contributions was performed showing reasonable agreement.

The extrapolated  $S$  factors are in good agreement with the current analysis. This should be expected because one of the primary methodologies of the analysis is the same, fixing the subthreshold state ANC's to the value measured through transfer reactions. The values for the  $E1$  and  $E2$   $S$  factors [100(28) and 50(19) keV b, respectively] are systematically larger than the best fit values of this work (86.3 and

45.3 keV b, respectively), although in good agreement considering the uncertainties.

This difference is likely because there are no background poles included in the current best fit and inclusion of the poles has only been found to increase the low-energy cross section. For tests with background poles in this work, the extrapolated value  $S(300 \text{ keV})_{E1}$  is nearly identical with the one found here (101.5 keV b). For  $S(300 \text{ keV})_{E2}$  the value found here remains nearly the same, actually slightly decreasing to 42 keV b. This may be a result of the greater constraint imposed on the background poles by the inclusion of the higher-energy data.

The uncertainty in the  $S$  factor quoted by [Oulebsir \*et al.\* \(2012\)](#) is significantly larger than that of the current analysis. This results from the larger uncertainties obtained in the ANCs from their transfer experiment ( $\sim 20\%$ ) over those of either [Brune \*et al.\* \(1999\)](#) or [Avila \*et al.\* \(2015\)](#) that have been adopted in this work ( $\sim 10\%$ ) (see Table XIII). Further, the lack of higher-energy data, in particular, the total cross section data of [Schürmann \*et al.\* \(2005\)](#), results in significantly more freedom in the background contributions.

### C. Xu *et al.* (2013) (NACRE2)

The analysis presented as part of [Xu \*et al.\* \(2013\)](#) (NACRE2) provides an interesting comparison because it uses a PM calculation instead of a phenomenological  $R$ -matrix method to predict the low-energy  $S$  factor. While still a phenomenological procedure, the PM method tries to take a step in a more fundamental direction by defining real Woods-Saxon potentials for each  $J^\pi$ . The parameters that define the potential, its magnitude, radius, and diffuseness are treated as free parameters in the fit to match the resonances and binding energies of the experimental data. This has the advantage that it may lead to less fit parameters than the standard phenomenological  $R$ -matrix approach but it comes at the cost of less flexibility. Further, some states cannot be produced by the potential model, as discussed in Sec. III.B, and have been parametrized separately using approximate Breit-Wigner formulas. Interference between resonances must also be introduced *ad hoc*. The direct capture contribution to the cross section is modeled in a similar manner as that proposed by [Rolf \*et al.\* \(1973\)](#). Additionally, each transition is fit independently, and this includes the different ground state  $E1$  and  $E2$  fits. The phase shifts and the  $^{16}\text{N}(\beta, \alpha)^{12}\text{C}$  data are not considered in the model.

It is clear from Fig. 64 of NACRE2 that the PM model used is not able to reproduce the experimental data to the same degree as the phenomenological  $R$ -matrix fits. However, considering the added constraints and approximations that are imposed, the reproduction of the data is impressive. While a  $\chi^2$  fit to the data was likely made, the value is not given so an exact comparison is not possible. The final value of the extrapolated  $S$  factor [ $S_{\text{total}} = 148(27)$ ,  $S_{E1} = 80(18)$ , and  $S_{E2} = 61(19)$  keV b] is similar to that deduced here, although with all the considerations pointed out, this may be somewhat coincidental. The total uncertainty is quoted as about  $\sim 18\%$ , but the details of how this is calculated are not given.

### D. An *et al.* (2015)

Previous to the current work, [An \*et al.\* \(2015\)](#) considered the largest amount of data over the broadest energy range. While a phenomenological  $R$ -matrix analysis was performed, it seems that the capture formalism was limited to that of internal contributions. The analysis is performed using the  $R$ -matrix code RAC, which has been used previously for evaluations of neutron capture data ([Carlson \*et al.\*, 2009](#)). The neglect of external contributions for the ground state  $E1$  cross section has been justified ([Barker and Kajino, 1991](#)). However, for the ground state  $E2$  cross section, which has an appreciable external capture component, this approximation is not valid for a high-precision analysis as shown earlier in this section. Further, the cascade transition cross sections all have significant external contributions. Additionally, no mention was made of the corrections for experimental effects, which are quite important for the  $^{16}\text{N}(\beta\alpha)^{12}\text{C}$  and scattering data sets.

[An \*et al.\* \(2015\)](#) made the bold claim that the low-energy  $S$  factor has been constrained to 4.5%. However, the lack of an investigation of systematic effects and approximations that seem to have been made in the theory make this difficult to defend. The uncertainty determination that was used is an iterative fitting procedure that involves inflating the experimental error bars in order to achieve a fit with a reduced  $\chi^2$  that approaches 1. However, this has the underlying assumption that the average value of all of the data gives the best estimate of the cross section and it is far from clear that is the case. In this work it has been found that capture data likely overestimate the low-energy cross section and that there is tension between the  $^{16}\text{N}(\beta\alpha)^{12}\text{C}$ , scattering, and transfer reaction data that translates into different preferred values for the subthreshold ANCs and by extension the low-energy cross section. The results of the transfer reaction measurements of the ANCs were also not considered.

It is also unclear how or if the experimental systematic uncertainties are included in the fit, since no  $\chi^2$  function is given. A related issue is that the normalizations of some data sets were fixed and it is unclear how or if these uncertainties were propagated through into the final uncertainty budget. It is also unclear if systematic effects of the  $R$ -matrix model were investigated. It is stated that a channel radius of 6.5 fm was used for the fitting but there is no discussion of how different channel radii affect the fit and there is no discussion of how the background poles affect the fitting and extrapolation. The qualities of the fits to the scattering data are also rather poor compared to the quality of a similar  $R$ -matrix analysis made by [deBoer \*et al.\* \(2013\)](#). The reason for this is not discussed. Further, the definition of the  $\gamma$ -ray fit parameters given in Table IV are unclear making a recalculation of the fit impossible.

In the end, not enough details are given by [An \*et al.\* \(2015\)](#) to understand the fitting or uncertainty estimate procedure. It appears as though the many systematic uncertainties identified in the current work were neglected. In fact, if the model uncertainties and the tension between different data sets are ignored in the Monte Carlo uncertainty analysis described here, a result similar to the 4.5% uncertainty of [An \*et al.\* \(2015\)](#) is obtained.

## IX. STELLAR REACTION RATE AND IMPLICATIONS

The stellar reaction rate for  $^{12}\text{C}(\alpha, \gamma)^{16}\text{O}$  was calculated as a sum of nonresonant, or broad resonant,  $S$ -factor contributions that were determined through the  $R$ -matrix analysis by numerical integration of Eq. (2), and narrow resonance contributions that were calculated through a Breit-Wigner approximation using Eq. (6). This separation was made to avoid numerical integration problems for the narrow resonances and because their uncertainties were better quantified experimentally as uncertainties on their strengths  $\omega\gamma$  (see Sec. II.E). The uncertainties in the rate were calculated from the MC analysis (see Sec. VII.E) and from the model uncertainties (see Sec. VII) discussed previously. The experimental uncertainties in the energies and the strengths were likewise used to propagate the uncertainties stemming from the narrow resonances.

Figure 28 shows the Gamow window [see Eqs. (4) and (5)] and the integrand of the  $S$  factor with the Maxwell-Boltzmann energy distribution [the integrand of Eq. (2)] for a range of temperatures. This depicts how different energy ranges of the cross section contribute to the reaction rate at different stellar temperatures.

The narrow resonance contributions ( $\Gamma_{\text{total}} \lesssim 1$  keV) are from the  $2^+$  resonance corresponding to the state at  $E_x = 9.8445(5)$  MeV [ $\Gamma_\alpha = 0.62(10)$  keV,  $\Gamma_\gamma = 9.8(8)$  meV] and the  $4^+$  at  $E_x = 11.0967(16)$  MeV [ $\Gamma_\alpha = 0.28(5)$  keV,  $\Gamma_\gamma = 5.6(14)$  meV] (Tilley, Weller, and Cheves, 1993). There is an additional narrow  $0^+$  state at  $E_x = 12.049(2)$  MeV [ $\Gamma_{\text{total}} = 1.5(5)$  keV]. Its strength was reported for the first time by Schürmann *et al.* (2005) [ $\omega\gamma = 11.2(15)$  meV].

The narrow resonance contributions and their uncertainties have been calculated using STARLIB (Sallaska *et al.*, 2013). As

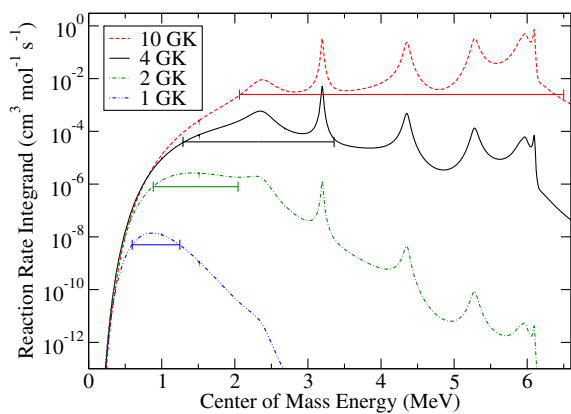


FIG. 28. The reaction rate integrand as a function of c.m. energy for  $T = 1, 2, 4,$  and  $10$  GK. At larger temperatures above  $T = 1$  GK several resonance contributions begin to dominate the rate. Above  $T \approx 4$  GK it is estimated that higher-lying resonance contributions (at  $E_{\text{c.m.}} > 6.5$  MeV) not included in the present analysis could have a significant contribution compared to the quoted uncertainty. While the ground state transition has been shown to be fairly weak at these higher energies, limited information is available for the cascade transitions, and they may make significant contributions. For comparison, the Gaussian Gamow energy windows described by Eqs. (4) and (5) are indicated by the horizontal error bars.

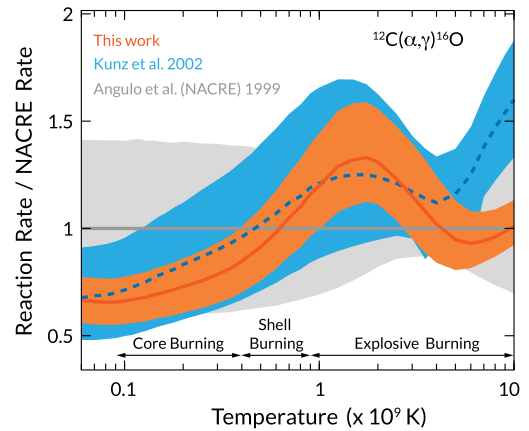


FIG. 29. Comparison of the reaction rate and uncertainty calculated in this work (orange band, solid central line) and that from Kunz *et al.* (2002) (blue band, dashed central line) normalized to the adopted value from Angulo *et al.* (1999) (NACRE compilation) (gray band, solid central line). The deviations at higher temperature are the result of the different narrow resonance and cascade transitions that were considered in the different works.

these resonances are narrow, their interferences with the broad states can be neglected to within the uncertainty of this analysis. The uncertainties are combined by summing (incoherently) the rate probability density functions (PDFs) from the  $R$ -matrix Monte Carlo procedure with those from the Monte Carlo Breit-Wigner narrow resonance approximation calculations from STARLIB.

Of the narrow resonances, only the  $2^+$  has a significant effect on the rate. It makes a contribution of  $> 2\%$  at  $T > 1.75$  GK with a maximum contribution of  $15\%$  at  $T = 3.5$  GK. It is estimated that this resonance can have a  $> 2\%$  contribution up to  $T \approx 9$  GK. It is estimated that the  $4^+$  resonance has a maximum contribution of  $\approx 1\%$  at  $T \approx 6$  GK. The  $0^+$  resonance is too weak to make a significant contribution even at  $T = 10$  GK.

The total reaction rate is compared to the NACRE rate (Angulo *et al.*, 1999) in Fig. 29. The present rate is within the uncertainties of Angulo *et al.* (1999) except at  $T \approx 2$  GK, where the present rate is larger because of the inclusion of the narrow  $2^+$  resonance and the cascade transitions. The uncertainty band is significantly smaller at low temperatures but is similar at higher temperatures reflecting the significantly increased constraint on the subthreshold parameters imposed by transfer reactions since the NACRE publication. The rate from Kunz *et al.* (2002) is also shown in Fig. 29 for additional comparison. The reaction rate of this work is given in Table XXV of Appendix B.

With the revised reaction rate in hand, investigations can now be made to ascertain the effect of the smaller central value and smaller uncertainty band on stellar model calculations.

## X. ASTROPHYSICS IMPLICATIONS

Returning at last to the discussions of Sec. II, the  $^{12}\text{C}(\alpha, \gamma)^{16}\text{O}$  reaction is responsible for the origin of oxygen in the Universe and for setting the profile of the carbon to

oxygen ratio in stars. This, in turn, affects subsequent stellar evolution and determines the nucleosynthesis phases of quiescent and explosive burning events.

Attention is focused on models of a single star, with solar metallicity, and zero-age main-sequence masses of  $3M_{\odot}$ ,  $15M_{\odot}$ , and  $25M_{\odot}$ . These three masses are representative of different stellar evolution and nucleosynthesis paths. The  $3M_{\odot}$  models are of interest because they produce CO white dwarf masses near the  $M \approx 0.6M_{\odot}$  peak of the observed DA (hydrogen-dominated atmosphere) and DB (helium dominated atmosphere) white dwarf mass distributions (Eisenstein *et al.*, 2006; Kepler *et al.*, 2007, 2015, 2016). The  $15M_{\odot}$  models are chosen because, for a classical Salpeter initial mass function with slope  $\Gamma = -1.35$  (Salpeter, 1955; Scalo, 1986; Maschberger, 2013), the average supernova mass by number is  $\langle M_{SN} \rangle = (1/2)^{1/\Gamma} M_L$  (here  $M_L$  is the lower mass limit for stars that become core-collapse supernovae). For  $M_L = 9M_{\odot}$ , this yields  $\langle M_{SN} \rangle = 15M_{\odot}$ . Finally, the  $25M_{\odot}$  models are motivated by their representation of the average nucleosynthesis supernova for a Salpeter initial mass function; that is, the average supernova mass by number weighted by the mass fraction ejected in heavy elements.

The stellar models are evolved using the Modules for Experiments in Stellar Astrophysics software instrument (MESA, version 3372 for  $3M_{\odot}$  models and version 7624 for  $15M_{\odot}$  and  $25M_{\odot}$  models (Paxton *et al.*, 2011, 2013, 2015). The  $3M_{\odot}$  models were computed from the pre-main sequence to the AGB phase and through several thermal pulses (He-shell flashes). The  $15M_{\odot}$  and  $25M_{\odot}$  models were calculated from the pre-main sequence to extinction of core He burning, defined as the time when the central mass fraction of He has fallen below  $1 \times 10^{-5}$ . Other than the specified  $^{12}\text{C}(\alpha,\gamma)^{16}\text{O}$  reaction rate, models with the same initial mass assume identical input physics assumptions (Jones *et al.*, 2015; Farmer *et al.*, 2016; Fields *et al.*, 2016). An overview of the model results using the  $^{12}\text{C}(\alpha,\gamma)^{16}\text{O}$  reaction rate from this work is given in Table XX.

Throughout this section a comparison to the rate from this work is made to that of Kunz *et al.* (2002), as they are propagated through different stellar models. The Kunz *et al.* (2002) rate has been chosen because it has been widely accepted as one of the most accurate determinations of the

TABLE XX. Overview of the MESA stellar models.  $M_{\text{ini}}$  is the initial mass in solar masses,  $\lambda_{12\alpha\gamma}$  is the lower (L), adopted (A), and upper (U)  $^{12}\text{C}(\alpha,\gamma)^{16}\text{O}$  reaction rates from this work.  $M_{\text{CO}}$  is the carbon-oxygen core mass at the end of core helium burning.  $X_c(^{12}\text{C})$  and  $X_c(^{16}\text{O})$  are the central mass fractions of  $^{12}\text{C}$  and  $^{16}\text{O}$ , respectively.

Model	$M_{\text{ini}}$	$\lambda_{12\alpha\gamma}$	$M_{\text{CO}}$	$X_c(^{12}\text{C})$	$X_c(^{16}\text{O})$	$X_c(^{12}\text{C})/X_c(^{16}\text{O})$
m3l	3	L	0.189	0.35	0.62	0.56
m3a	3	A	0.180	0.34	0.64	0.53
m3u	3	U	0.190	0.27	0.71	0.38
m15l	15	L	3.07	0.30	0.67	0.45
m15a	15	A	3.03	0.25	0.72	0.35
m15u	15	U	3.08	0.22	0.75	0.29
m25l	25	L	6.40	0.25	0.72	0.34
m25a	25	A	6.45	0.20	0.76	0.27
m25u	25	U	6.45	0.16	0.80	0.21

$^{12}\text{C}(\alpha,\gamma)^{16}\text{O}$  reaction rate and has been used for several years in many rate libraries such as JINA Reaclib (Cyburt *et al.*, 2010). As illustrated in Fig. 29, the rates of Angulo *et al.* (1999) (NACRE), Kunz *et al.* (2002), and the present work are all in agreement, but their central values trend lower as do their uncertainties, respectively.

### A. Aspects of $^{12}\text{C}(\alpha,\gamma)^{16}\text{O}$ on $3M_{\odot}$ stellar models

Figure 30 summarizes some of the key differences between using the  $^{12}\text{C}(\alpha,\gamma)^{16}\text{O}$  reaction rate of this work and that of Kunz *et al.* (2002). The  $x$  axis is the lower, adopted, and upper reaction rates for each source of the  $^{12}\text{C}(\alpha,\gamma)^{16}\text{O}$  rate. The left  $y$  axis is the percentage difference in the central  $^{12}\text{C}/^{16}\text{O}$  mass fraction ratio at the end of helium burning. The right  $y$  axis is the percentage difference in the surface  $^{12}\text{C}/^{16}\text{O}$  molar abundance ratio for two thermal pulses. A molar abundance is related to the mass fraction by the atomic weight (see Fig. 1 caption). For both  $y$  axes the percentage difference is relative to Kunz *et al.* (2002) [i.e.,  $\Delta A = 100(A_{\text{this work}} - A_{\text{Kunz}})/A_{\text{Kunz}}$ ].

One of the key features shown in Fig. 30 is that the central  $^{12}\text{C}/^{16}\text{O}$  mass fraction ratio is  $\approx 30\%$  larger when using the adopted or upper rates from this work compared to those of Kunz *et al.* (2002). This is because the latter reaction rates are larger than those from this work at the relevant temperatures (see Fig. 29). The trend is opposite, a  $\approx -10\%$  decrease, for the lower limits because the rate from this work is larger than that of Kunz *et al.* (2002). The red arrow along the left  $y$  axis in Fig. 30 gives the range of  $X_c(^{12}\text{C}/^{16}\text{O})$ ,  $\approx 35\%$ , resulting from the use of the lower and upper  $^{12}\text{C}(\alpha,\gamma)^{16}\text{O}$  rates of this work.

Also highlighted in Fig. 30 is the impact of thermal pulses on the surface abundances, which can be measured with stellar spectroscopy (Smith and Lambert, 1990; Abia *et al.*, 2002).

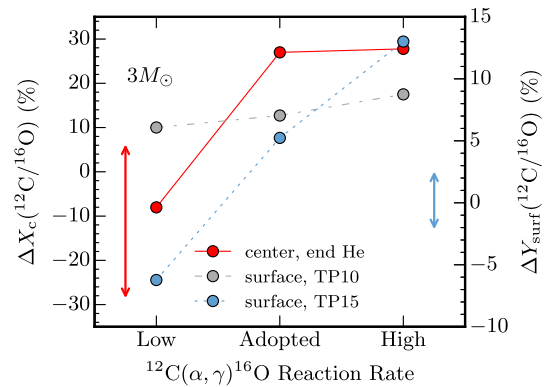


FIG. 30. Ratio of  $^{12}\text{C}$  and  $^{16}\text{O}$  mass fractions at the stellar center at the end of core He burning (left axis, red circles) and number ratios at the surface (right axis, gray and blue circles) during the tenth and 15th thermal pulses (He shell flashes) in the  $3M_{\odot}$  models. The points connected by lines are differences arising in the models when using the  $^{12}\text{C}(\alpha,\gamma)^{16}\text{O}$  rate of this work and that of Kunz *et al.* (2002). The red arrow along the left  $y$  axis spans the range of  $X_c(^{12}\text{C}/^{16}\text{O})$  resulting from the uncertainty in the rate of this work. The blue arrow along the right  $y$  axis is the equivalent range of  $Y_{\text{surf}}(^{12}\text{C}/^{16}\text{O})$  during the 15th thermal pulse.

After a thermal pulse the products of shell He burning are brought to the surface regions by convection. A larger  $^{12}\text{C}(\alpha, \gamma)^{16}\text{O}$  rate results in more  $^{16}\text{O}$  and less  $^{12}\text{C}$  during helium burning. Every time the convective envelope dredges freshly burned helium up to the surface, it mixes more  $^{16}\text{O}$  and less  $^{12}\text{C}$  with the existing surface composition, decreasing the  $^{12}\text{C}/^{16}\text{O}$  ratio.

At the tenth thermal pulse (gray circles), the differences between the  $^{12}\text{C}(\alpha, \gamma)^{16}\text{O}$  rate of this work and that of [Kunz \*et al.\* \(2002\)](#) are in the range between  $\approx 5\%$ – $9\%$ . At the 15th thermal pulse (blue circles), the differences become  $\approx -5\%$  and  $+13\%$ . Both thermal pulses show a linear trend toward larger differences as the two rates are varied across their respective low, adopted, and high values. Finally, the blue arrow along the right y axis shows the range,  $\approx 5\%$  spread, of  $Y_{\text{Surf}}(^{12}\text{C}/^{16}\text{O})$ , which represents the uncertainty in the MESA stellar models for the surface abundance ratio, given the uncertainty range of the rate from this work.

The treatment of convective-boundary mixing in stellar models for the thermal pulses has a major role on the surface abundances of  $^{12}\text{C}$ ,  $^{16}\text{O}$ , and *s*-process elements, but remains uncertain ([Straniero \*et al.\*, 1995](#); [Gallino \*et al.\*, 1998](#); [Herwig, 2005](#); [Herwig \*et al.\*, 2007](#); [Karakas and Lattanzio, 2014](#); [Cristallo \*et al.\*, 2015](#); [Pignatari \*et al.\*, 2016](#)). Several physics mechanisms have been proposed that could dominate convective-boundary mixing including overshooting ([Herwig \*et al.\*, 1997](#)), exponential decay of convective velocities ([Cristallo \*et al.\*, 2001](#)), internal gravity waves ([Denissenkov and Tout, 2003](#); [Battino \*et al.\*, 2016](#)), and magnetic buoyancy ([Trippella \*et al.\*, 2016](#)). A consensus on the solution to this puzzle has not yet been reached.

### B. Aspects of $^{12}\text{C}(\alpha, \gamma)^{16}\text{O}$ on $15M_{\odot}$ and $25M_{\odot}$ models

Figure 31 shows the percent differences between using the  $^{12}\text{C}(\alpha, \gamma)^{16}\text{O}$  rate from this work and that of [Kunz \*et al.\* \(2002\)](#) on the CO core mass  $\Delta M_{\text{CO}}$  and the central carbon/oxygen ratio  $\Delta X_{\text{C}}(^{12}\text{C}/^{16}\text{O})$  for the  $15M_{\odot}$  and  $25M_{\odot}$  MESA models. The core masses are measured as the mass coordinate where  $X(^4\text{He}) < 0.01$  and  $X(^{12}\text{C}) > 0.1$  when  $X_{\text{C}}(^4\text{He})$  reaches  $1 \times 10^{-5}$ . For the  $15M_{\odot}$  models,  $\Delta M_{\text{CO}}$  (red circles) ranges from  $\approx 1.2\%$  for the respective low rates to  $\approx -0.5\%$  for the respective adopted and high rates. For the  $25M_{\odot}$  models,  $\Delta M_{\text{CO}}$  ranges from  $\approx 1.7\%$  for the respective low rates to  $\approx 1.0\%$  for the respective adopted rates and  $\approx -0.5\%$  for the respective high rates. See Table XX for the absolute values of the CO core masses resulting from the  $^{12}\text{C}(\alpha, \gamma)^{16}\text{O}$  rate from this work. The red arrow along the left y axis in Fig. 31 is the range of  $M_{\text{CO}}$  resulting from the uncertainty in the rate from this work. The central CO core masses have a spread of  $\approx 1.5\%$  for the  $15M_{\odot}$  models and  $\approx 0.7\%$  for the  $25M_{\odot}$  models.

The  $15M_{\odot}$  and  $25M_{\odot}$  models show CO mass fraction profiles that are nearly flat, due to convective mixing, from the center to the inner edge of the shell He-burning region. For the  $15M_{\odot}$  models,  $\Delta X_{\text{C}}(^{12}\text{C}/^{16}\text{O})$  ranges from  $\approx -30\%$  for the respective low rates through  $\approx 0\%$  for the respective adopted rates to  $\approx 30\%$  for the respective high rates. For the  $25M_{\odot}$  models,  $\Delta X_{\text{C}}(^{12}\text{C}/^{16}\text{O})$  ranges from  $\approx 20\%$  for the respective

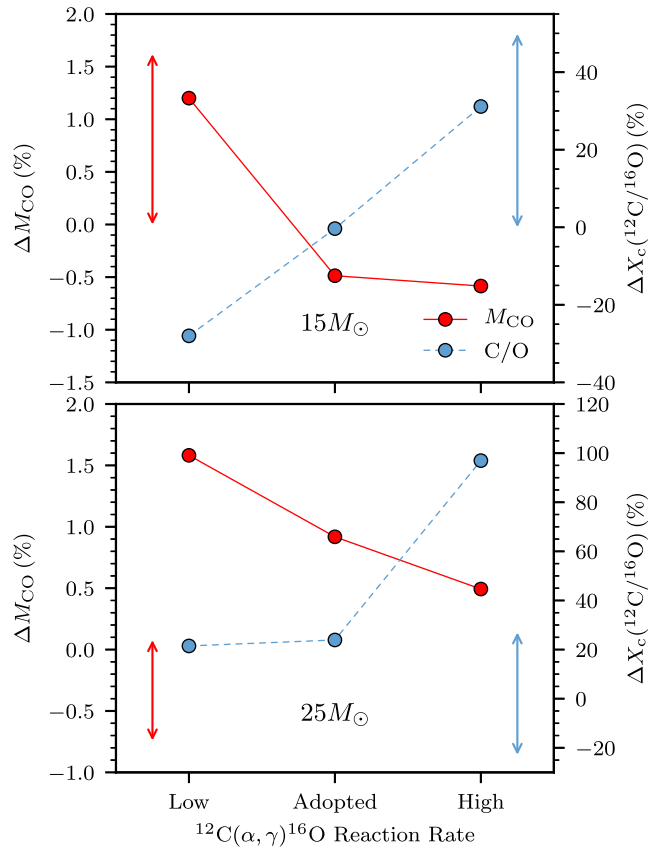


FIG. 31. Percent difference in the carbon-oxygen core mass  $\Delta M_{\text{CO}}$  (left axis, red circles), and the central carbon/oxygen ratio  $\Delta X_{\text{C}}(^{12}\text{C}/^{16}\text{O})$  (right axis, blue circles), between using the  $^{12}\text{C}(\alpha, \gamma)^{16}\text{O}$  rate of this work and that of [Kunz \*et al.\* \(2002\)](#) for  $15M_{\odot}$  (top panel) and  $25M_{\odot}$  (bottom panel) MESA models at core He depletion (defined as when the central He mass fraction falls below  $10^{-5}$ ). The x axis gives the low, adopted, and high  $^{12}\text{C}(\alpha, \gamma)^{16}\text{O}$  rates for the respective rate selection. The red arrow along the left axis is the range of  $M_{\text{CO}}$  resulting from the uncertainty in the rate of this work. The blue arrow along the right y axis is the equivalent range for the central carbon mass fraction.

low and adopted rates to  $\approx 100\%$  for the respective high rates. The difference in the trends between these  $15M_{\odot}$  and  $25M_{\odot}$  MESA models is driven by the  $15M_{\odot}$  models having a larger electron degeneracy in the core than the  $25M_{\odot}$  models, and nonlinear couplings between the shell-burning regions and the core as the helium fuel depletes. The blue arrow along the right y axis is the spread of central carbon mass fraction achieved when using the lower, adopted, and upper rates from this work, and shows larger spreads,  $\approx 50\%$  for the  $15M_{\odot}$  models and  $\approx 45\%$  for the  $25M_{\odot}$  models.

The mass fractions of  $^{12}\text{C}$  and  $^{16}\text{O}$  in the core at the end of the He-burning phase for the models using the rate from this work are listed in Table XX. The models using the highest rate have the lowest  $^{12}\text{C}$  abundance at the end of core He burning. This results in a smaller convective C-burning core in the subsequent evolution which will in turn change slightly where the various shell-burning episodes will ignite. Both the  $15M_{\odot}$  and  $25M_{\odot}$  models exhibit higher central C/O ratios using the upper limit for the rate of this work compared with the upper

limit of [Kunz \*et al.\* \(2002\)](#), because the latter rate is faster (see Fig. 29). The converse statement is true for the lower limits.

The nucleosynthesis from the  $15M_{\odot}$  stellar models was computed by postprocessing the thermodynamic evolution of the models with a 1107-isotope nuclear reaction network and mixing the species after every network time step by solving the diffusion equation using the diffusion coefficient from the MESA model. For this, the NuGrid software instruments were used ([Pignatari and Herwig, 2012](#); [Jones \*et al.\*, 2015](#)). In Fig. 32 the abundances of elements with  $26 < Z < 42$  (Fe–Mo) that are affected by the weak  $s$  process are shown at the end of the core He-burning phase. The top panel shows the mass-weighted average of the elemental mass fractions in the innermost  $2M_{\odot}$  of the star as so-called overabundances (i.e., the abundance of each element is normalized to the solar abundance, which in this case was the initial composition of the models). Both models exhibit the familiar weak  $s$ -process pattern that is made when  $^{56}\text{Fe}$ , the seed isotope, is depleted as it captures neutrons being released by the  $^{22}\text{Ne}(\alpha, n)^{25}\text{Mg}$  reaction, producing the elements up to the neutron shell closure at  $N = 50$  (Sr, Y, Zr).

The bottom panel in Fig. 32 shows the differences, as percentages, in the abundances of the elements in the CO core

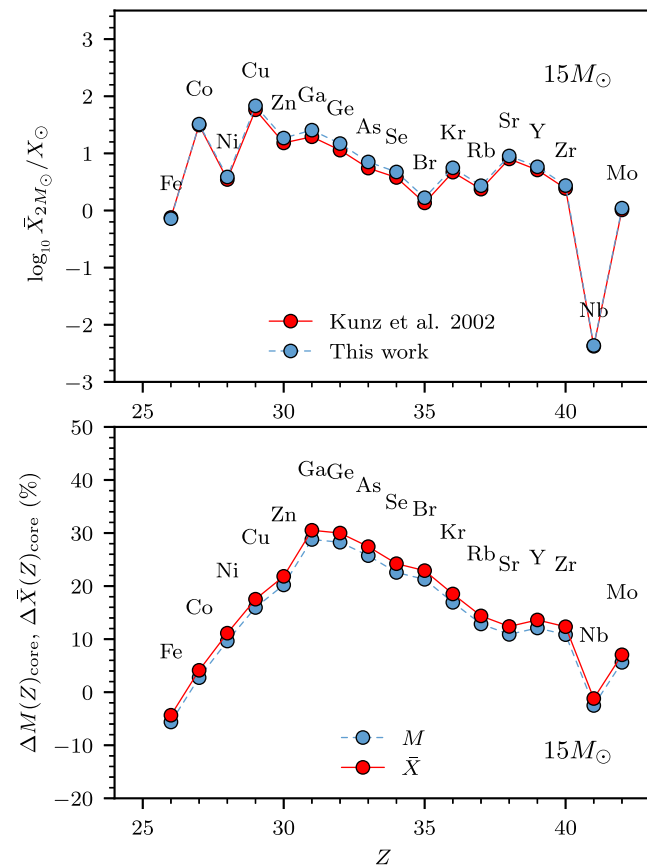


FIG. 32. Top: Mass-averaged mass fractions of the weak  $s$ -process elements in the central  $2M_{\odot}$  of the  $15M_{\odot}$  models at the end of core He burning using the  $^{12}\text{C}(\alpha, \gamma)^{16}\text{O}$  rate of this work and that of [Kunz \*et al.\* \(2002\)](#). Bottom: Percentage difference in weak  $s$ -process production at the end of core He burning as both total elemental masses and mass-averaged mass fractions for the  $15M_{\odot}$  models using the rates of this work and [Kunz \*et al.\* \(2002\)](#).

at the end of core He burning when using the  $^{12}\text{C}(\alpha, \gamma)^{16}\text{O}$  reaction rate of this work compared with that of [Kunz \*et al.\* \(2002\)](#). The differences are shown for both the total masses of the elements in the CO core ( $M$ , blue circles) and the average mass fractions across the CO core ( $\bar{X}$ , red circles). The two lines are similar, indicating that the difference in the actual CO core masses resulting from the different  $^{12}\text{C}(\alpha, \gamma)^{16}\text{O}$  rates has no strong influence on the weak  $s$ -process element production, as for instance the  $\alpha$  capture rates on the neutron source  $^{22}\text{Ne}$  [see, e.g., for a recent impact study [Talwar \*et al.\* \(2015\)](#)]. The weak  $s$ -process production is more efficient in the model that uses the adopted  $^{12}\text{C}(\alpha, \gamma)^{16}\text{O}$  rate from this work because the rate is slower and therefore  $^{12}\text{C}$  is less of a competitor for  $\alpha$  particles than  $^{22}\text{Ne}$ , the neutron source. This can also be seen by simply noting that  $\Delta M(\text{Fe}) < 0$  or  $\Delta \bar{X}(\text{Fe})_{\text{core}} < 0$  in the bottom panel of Fig. 32, i.e., the element Fe—comprised mostly of the  $s$ -process seed isotope  $^{56}\text{Fe}$ —is further depleted in the model with the adopted rate of the present work than in the model with the [Kunz \*et al.\* \(2002\)](#) rate.

The difference in the weak  $s$ -process production arising from the different  $^{12}\text{C}(\alpha, \gamma)^{16}\text{O}$  rates [this work versus [Kunz \*et al.\* \(2002\)](#)] is significant and is as much as  $\approx 30\%$  in the total masses of Ga and Ge that are produced. The variation in the weak  $s$ -process production that is due to the uncertainty of the  $^{12}\text{C}(\alpha, \gamma)^{16}\text{O}$  rate from this work (not shown in Fig. 32) is on the order of 20%–30%.

## XI. SUMMARY AND OUTLOOK

The  $^{12}\text{C}(\alpha, \gamma)^{16}\text{O}$  reaction has remained one of the most challenging problems in nuclear astrophysics. This is because it is extremely difficult to access experimentally, it cannot be accurately predicted with theory, and even its impact on stellar environments is so convoluted with other uncertainties that its exact effect is difficult to quantify. Yet there is no doubt that it remains one of the most critical reactions for our understanding of nucleosynthesis and stellar evolution, and attempts to address these issues have remained at the forefront across the field. The major experimental improvements have been made through indirect techniques such as improved measurements of the  $\beta$ -delayed  $\alpha$  emission spectra of  $^{16}\text{N}$  and sub-Coulomb transfer. This is apparent in Fig. 26 where  $^{16}\text{N}(\beta\alpha)^{12}\text{C}$  measurements drastically decreased the  $E1$  uncertainties in the early 1990s and the transfer measurements resulted in a large decrease in the  $E2$  uncertainty around the early 2000s. The combination of these measurements together with a large amount of low-energy data and the inclusion of higher-energy data in the  $R$ -matrix analysis has thus reduced the uncertainty in the extrapolation for  $S(300 \text{ keV})$  to  $\approx 20\%$  uncertainty level. However, improvements in the uncertainty are now hindered by the tension produced by inconsistencies between different measurements. This issue now bars the way to the smaller uncertainty level reflected by the statistical uncertainties of the individual measurements. To move forward, these inconsistencies must be resolved.

With the uncertainty in the rate suggested by this work and other recent global analyses, is there still a real need for improvement? Some stellar modelers have indicated that if the uncertainty in the  $^{12}\text{C}(\alpha, \gamma)^{16}\text{O}$  rate reaches the 10% level, it

will be on par with other non-nuclear physics uncertainties as well as that of the  $3\alpha$  reaction rate. However, it was pointed out that for AGB stars the impact of the present level of the uncertainty in the  $^{12}\text{C}(\alpha, \gamma)^{16}\text{O}$  reaction rate is smaller than other sources of uncertainties, e.g., the convective-boundary mechanisms active at the He intershell, during the AGB phase. Yet for massive stars the required level of precision must be at this level of about 10% since the posthelium burning evolution is strongly affected by the  $^{12}\text{C}(\alpha, \gamma)^{16}\text{O}$  rate. For example, in this work it was suggested that relevant structure differences are at the  $\approx 2\%$  uncertainty level in the carbon-oxygen core mass, at the  $\approx 15\%$  level in the carbon and oxygen mass fractions, and at the  $\approx 30\%$  level in the weak  $s$ -process yields. These estimates are only for a limited number of stellar models, and we encourage the community to more thoroughly investigate the impacts of this work's  $^{12}\text{C}(\alpha, \gamma)^{16}\text{O}$  reaction rate.

So how should we proceed? Of course any new method that allows for the more precise and accurate determination of the various different experimental data will improve the situation. For now we conclude finally with some suggestions for specific experimental measurements that could improve our knowledge of the  $^{12}\text{C}(\alpha, \gamma)^{16}\text{O}$  reaction that can likely be done with existing experimental techniques.

- (•) Measurement of ground state angular distributions to higher energies ( $E_{\text{c.m.}} > 3$  MeV), specifically in off-resonance regions, to place more stringent upper limits on  $E1$  background terms and verify both  $E1$  and  $E2$  interference patterns.
- (•) Further verification of  $\alpha$  ANC's from transfer reactions, perhaps by systematic studies of additional kinds of transfer reactions.
- (•) Reinvestigation of  $^{16}\text{N}(\beta\alpha)^{12}\text{C}$  spectrum measurements until constant measurements can be achieved.
- (•) Consistent measurements of  $\text{ANC}_{\text{G.S.}}^{\alpha}$ .
- (•) Recoil separator measurements to lower energy ( $E_{\text{c.m.}} < 2$  MeV) and to higher energies, continuing above  $S_p$  ( $E_{\text{c.m.}} > 5$  MeV).
- (•) Cascade transition measurements over wide energy ranges.
- (•) Reporting of differential cross sections, not just  $E1$  and  $E2$  cross sections if the experiment permits.
- (•) Scattering measurements using thinner targets and covering a wide energy and angular range.

## ACKNOWLEDGMENTS

The authors acknowledge many useful discussions with M. Avila (ANL), A. DiLeva (INFN), H. O. U. Fynbo (AU), G. Imbriani (INFN), L. Gialanella (CIRCE), G. Hale (LANL), A. Heger (Monash U.), C. Matei (NPL), M. Paris (LANL),

A. Roberts (USD), G. V. Rogachev (TAMU), D. Schürmann (CIRCE), O. Straniero (INAF Teramo), F. Strieder (SDSMT), and A. Villano (UMN). R. J. D., M. W., and J. G. gratefully acknowledge funding by the National Science Foundation through Grant No. Phys-0758100 and the Joint Institute for Nuclear Astrophysics through Grant No. Phys-0822648. R. J. D. also acknowledges support from the Notre Dame Center for Research Computing and the hospitality of the INFN during a portion of this work. M. P. and S. J. acknowledge significant support from NuGrid via NSF Grants No. PHY 02-16783 and No. PHY 09-22648 (Joint Institute for Nuclear Astrophysics, JINA), NSF Grant No. PHY-1430152 (JINA Center for the Evolution of the Elements), and the EU MIRG-CT-2006-046520. M. P. acknowledges support from the “Lendulet-2014” Programme of the Hungarian Academy of Sciences, the SNF (Switzerland), and the UK BRIDGCE network. NuGrid data are served by Canfar/CADC. S. J. is supported by the Alexander von Humboldt Foundation and acknowledges support from the Klaus Tschira Stiftung. M. P. also acknowledges PRACE, through its Distributed Extreme Computing Initiative, for resource allocations on Sisu (CSC, Finland), Archer (EPCC, UK), and Beskow (KTH, Sweden) and the support of STFC's DiRAC High Performance Computing Facilities. Ongoing resource allocations on the University of Hull's High Performance Computing Facility—viper—are gratefully acknowledged. The work of C. R. B. was supported in part by the U.S. Department of Energy, Grants No. DE-FG02-88ER40387 and No. DE-NA0002905. C. E. F. acknowledges partial support from a Predoctoral Fellowship administered by the National Academies of Sciences, Engineering, and Medicine on behalf of the Ford Foundation and an Edward J. Petry Graduate Fellowship from Michigan State University.

## APPENDIX A: $R$ -MATRIX FIT PARAMETERS

The  $R$ -matrix parameters in this section represent the best fit of this work. Note that this fit does not include any background poles for the capture channels, although it does for the particle channels. The value of  $S_{\text{total}}(300 \text{ keV})$  for the  $^{12}\text{C}(\alpha, \gamma)^{16}\text{O}$  reaction resulting from these parameters is 140 keV b. The fit used channel radii  $a_{\alpha_0} = a_{\alpha_1} = 5.43$  fm and  $a_{p_0} = 5.03$  fm. No boundary conditions must be defined since the alternate parametrization of Brune (2002) is utilized.

The comprehensive fit used in this work is also quite complicated and includes many parameters. In order to aid in the reproduction of the results of this work, an AZURE2 input file is provided in the Supplemental Material [410]. The AZURE2 code is open source and can be obtained at [azure.nd.edu](http://azure.nd.edu).

TABLE XXI. Observable energies and particle widths (or ANCs) used for the  $R$ -matrix fit [see Eqs. (43) and (44)]. Parameters marked in bold were treated as fit parameters. All others were held constant at their central or nominal values. For the uncertainty analysis, fixed parameters with uncertainties were varied assuming a Gaussian PDF. Minus signs on the partial widths correspond to the sign of the corresponding reduced-width amplitude. Uncertainties are given in the form (central value) $^{+(\text{stat. syst})}_{-(\text{stat. syst})}$ .

$J^\pi$	(keV or fm $^{-1/2}$ )							
	$\tilde{E}_x$ (MeV)		$\tilde{\Gamma}_{\alpha_0}$ or ANC $_{\alpha}$		$\tilde{\Gamma}_{p_0}$ or ANC $_p$		$\tilde{\Gamma}_{\alpha_1}$	
	This work	Lit.	This work	Lit.	This work	Lit.	This work	Lit.
0 $^-$	<b>12.7954</b> $^{(4,0)}_{(3,0)}$	12.7937			<b>40.9</b> $^{(15,1)}_{(15,2)}$	40		
0 $^+$		0.0	58			13.9(19)		
0 $^+$		6.0494(10)		1560(100)				
0 $^+$		12.049(2)		1.5(5)				
0 $^+$	15 (BGP)		<b>-11.900</b> $^{(220,50)}_{(165,110)} \times 10^3$		<b>420</b> $^{(37,70)}_{(47,20)}$			
1 $^-$		7.1165(14)		$2.08(20) \times 10^{14}$		0.98(12)		
1 $^-$	<b>9.586</b> $^{(1,0)}_{(1,8)}$	9.585(11)	<b>382</b> $^{(3,0)}_{(3,4)}$	420(20)				
1 $^-$	<b>12.4493</b> $^{(8,2)}_{(8,0)}$	12.440(2)	<b>99.2</b> $^{(11,2)}_{(8,2)}$	91(6)	<b>1.73</b> $^{(4,2)}_{(4,20)}$	1.1	<b>-0.031</b> $^{(2,4)}_{(2,2)}$	0.025
1 $^-$	<b>13.094</b> $^{(1,2)}_{(1,0)}$	13.090(8)	<b>-29.9</b> $^{(1,0)}_{(1,6)}$	45	<b>110.4</b> $^{(2,5)}_{(2,0)}$	100	<b>0.636</b> $^{(27,5)}_{(43,0)}$	1
1 $^-$	17.09 (BGP)		500					
1 $^-$	20 (BGP)		<b>15.6</b> $^{(7,1)}_{(4,2)} \times 10^3$		<b>270</b> $^{(61,15)}_{(30,170)}$			
1 $^+$	<b>13.6646</b> $^{(7,0)}_{(7,2)}$	13.664(3)			<b>-10.3</b> $^{(2,1)}_{(4,3)}$	8(3)	<b>61.1</b> $^{(23,4)}_{(17,2)}$	55(3)
2 $^+$		6.9171(6)		$1.14(20) \times 10^5$		0.45(13)		
2 $^+$		9.8445(5)		0.62(10)				
2 $^+$	<b>11.5055</b> $^{(3,0)}_{(5,1)}$	11.520(4)	<b>83.0</b> $^{(6,1)}_{(3,0)}$	71(3)				
2 $^+$	<b>12.9656</b> $^{(14,5)}_{(28,2)}$	13.02(1)	<b>-349</b> $^{(8,2)}_{(3,3)}$	150(10)	<b>1.82</b> $^{(8,4)}_{(8,18)}$		<b>-4.0</b> $^{(7,0)}_{(9,0)}$	
2 $^+$	15		<b>5.5</b> $^{(5,2)}_{(5,2)} \times 10^3$		<b>-8.1</b> $^{(20,0)}_{(15,5)}$			
3 $^-$		6.129 89(4)		139(9)		1.88(23)		
3 $^-$	<b>11.5058</b> $^{(28,0)}_{(19,7)}$	11.60(2)	<b>902</b> $^{(5,1)}_{(6,1)}$	800(100)				
3 $^-$	<b>13.1412</b> $^{(10,3)}_{(13,0)}$	13.129(10)	<b>72.9</b> $^{(42,9)}_{(24,8)}$	90(14)	<b>-1.11</b> $^{(2,1)}_{(3,2)}$	1	<b>20.5</b> $^{(13,0)}_{(16,1)}$	20
3 $^-$	13.2650	13.259(2)	<b>12.8</b> $^{(6,2)}_{(4,2)}$	9(4)	<b>3.66</b> $^{(10,1)}_{(8,2)}$	4.1	<b>11.74</b> $^{(33,1)}_{(54,1)}$	8.2(11)
3 $^-$	20 (BGP)		<b>-22</b> $^{(1,2)}_{(2,0)} \times 10^3$					
4 $^+$	<b>10.3581</b> $^{(1,0)}_{(1,1)}$	10.356(3)	<b>26.13</b> $^{(25,3)}_{(15,3)}$	26(3)				
4 $^+$		11.0967(16)		0.28(5)				
4 $^+$	15 (BGP)		<b>2.57</b> $\times 10^3$ $^{(22,2)}_{(14,4)}$					
5 $^-$	14.66 (BGP)		<b>1.22</b> $\times 10^3$ $^{(10,12)}_{(6,9)}$		8			

TABLE XXII. Observable  $\gamma$ -ray widths of the best fit of the  $R$ -matrix analysis as defined by Eq. (77). Excitation energies are in MeV and correspond to those of Table XXI.

		(meV)									
		$\tilde{\Gamma}_{\gamma_0}$		$\tilde{\Gamma}_{\gamma_{6.05}}$		$\tilde{\Gamma}_{\gamma_{6.13}}$		$\tilde{\Gamma}_{\gamma_{6.92}}$		$\tilde{\Gamma}_{\gamma_{7.12}}$	
$J^\pi$	$\tilde{E}_x$	This work	Lit.	This work	Lit.	This work	Lit.	This work	Lit.	This work	Lit.
$0^-$	12.80	$3.28_{(19,2)}^{(24,2)} \times 10^3$									
$1^-$	7.12		55(3)		$3.3 \times 10^{-4}$		0.046		$1 \times 10^{-3}$		
$1^-$	9.59	$-15_{(2,2)}^{(1,3)}$	15.6(12)					$0.5_{(2,0)}^{(3,7)}$	1.4(14)	$4.2_{(4,2)}^{(9,30)}$	7.8(16)
$1^-$	12.45	$5.6_{(2,9)}^{(2,0)} \times 10^3$	$9.5(17) \times 10^3$	$-53_{(16,4)}^{(18,8)}$	120(60)	$30_{(18,9)}^{(15,2)}$				$118_{(15,2)}^{(16,15)}$	
$1^-$	13.09	$42_{(1,8)}^{(2,0)} \times 10^3$	$44(8) \times 10^3$	244		-400					$1.35(4) \times 10^3$
$1^-$	17.09		$500 \times 10^3$								
$2^+$	6.92		97(3)		-0.027(3)				< 0.0078		
$2^+$	9.84		-5.7(6)		-1.9(4)				2.2(4)		0.3
$2^+$	11.51	$-490_{(70,30)}^{(40,100)}$	610(20)	$49_{(23,0)}^{(27,19)}$	30(5)	$-33_{(4,5)}^{(5,1)}$		$24_{(5,0)}^{(7,5)}$	29(7)	$14.0_{(4,6)}^{(4,1)}$	< 5
$2^+$	12.97	$-560_{(60,190)}^{(120,0)}$	700								
$3^-$	6.13		0.0260(13)								
$3^-$	11.51	$0.20_{(18,20)}^{(20,64)}$ <sup>a</sup>				$8_{(3)}^{(3)}$		$8_{(5,8)}^{(7,10)}$ <sup>a</sup>		$21_{(4,7)}^{(4,7)}$	
$3^-$	13.14	10				8000					
$3^-$	13.26					$-5.2_{(6,0)}^{(6,3)} \times 10^3$					
$4^+$	10.36		$5.6(20) \times 10^{-5}$		< 1.0			$42.7_{(6,2)}^{(2,7)}$	62(6)		
$4^+$	11.10						3.1(13)		2.5(6)		

<sup>a</sup>Consistent with zero and should be treated as an upper limit.

TABLE XXIII.  $\beta$ -delayed  $\alpha$ -decay parameters resulting from the  $R$ -matrix fit. The half-life of  $^{16}\text{N}$  was taken as  $t_{1/2} = 7.13(2)$  s with a  $\beta\alpha$  branching ratio of  $1.20(5) \times 10^{-5}$  (Tilley, Weller, and Cheves, 1993).  $\beta$ -decay feeding factors  $\tilde{B}_\lambda$  are those defined by Brune (2002) and can be compared directly with those found in Table I of that work.  $\log f t_{1/2}$  values were calculated using Eq. (83).

$J^\pi$	$\tilde{E}_x$ (MeV)	$\tilde{B}_\lambda$	$\log f t_{1/2}$	
			This work	Tilley, Weller, and Cheves (1993)
$3^-$	6.13	2.54	$4.59_{(24,25)}^{(16,0)}$	4.48(4)
$1^-$	7.12	1.27	$5.08_{(2,2)}^{(0,1)}$	5.11(4)
$1^-$	9.59	0.451	$6.15_{(2,0)}^{(2,1)}$	6.12(5)
$1^-$	20 (BGP)	-0.618	$-5.70_{(4,1)}^{(6,1)}$	

TABLE XXIV. The internal reduced-width amplitudes  $\tilde{\gamma}_p$  and the external reduced-width amplitudes  $\tilde{\gamma}_p(\text{ch})$  calculated using Eq. (77) from which the  $\gamma$  widths in Table XXII were calculated. Bold internal reduced-width amplitudes correspond to the partial widths that were treated as fit parameters in Table XXII (i.e., they are not additional fit parameters). External reduced-width amplitudes were always fixed as they correspond to fixed ANCs. Excitation energies are in MeV.

$J^\pi$	$\tilde{E}_x$	$(\text{MeV}^{1/2})$							
		$E_f = 0$	$E_f = 6.05$	$E_f = 6.13$	$E_f = 6.92$	$E_f = 7.12$			
		$\tilde{\gamma}_p$	$\tilde{\gamma}_p(\text{ch})$	$\tilde{\gamma}_p$	$\tilde{\gamma}_p(\text{ch})$	$\tilde{\gamma}_p$	$\tilde{\gamma}_p(\text{ch})$	$\tilde{\gamma}_p$	$\tilde{\gamma}_p(\text{ch})$
$0^-$	12.80	<b>0.295</b>							
$1^-$	7.12	0.0188	0.00567 +i0.0						
$1^-$	9.59	<b>-0.00986</b>	$-(3.8 + i0.6) \times 10^{-5}$						
$1^-$	12.45	<b>0.0588</b>	$(639 + i0.69) \times 10^{-4}$	<b>-0.0321</b>	$-(0.82 + i1.35) \times 10^{-4}$	<b>0.368</b>	$0.399 + i0.109$	<b>1.022</b>	$1.125 + i0.472$
$1^-$	13.09	0.233	$0.0610 + i0.0047$	<b>0.0563</b>	$(4.0 + i7.6) \times 10^{-5}$	<b>-2.316</b>	$0.234 - i0.0124$	<b>2.23</b>	$0.109 + i0.158$
$1^-$	17.09	0.587	$0.0338 + i0.0194$					<b>5.54</b>	$-(0.0449 + i0.0742)$
$2^+$	6.92	0.974	$0.0157 + i0.0$	<b>-3.31</b>	$0.401 + i0.0$	$2.27 \times 10^{-3}$	$(5.81 + i0.0) \times 10^{-3}$		
$2^+$	9.84	<b>-0.0987</b>	$(9.54 + i1.06) \times 10^{-4}$	<b>-0.650</b>	$0.0497 + i0.0132$			$1.181$	$0.0560 + i0.0163$
$2^+$	11.51	<b>-0.610</b>	$(5.42 + i2.05) \times 10^{-3}$	<b>0.991</b>	$0.230 + i0.171$	<b>-0.0287</b>	$-(5.0 + i3.8) \times 10^{-5}$	<b>1.057</b>	$0.252 + i0.195$
$2^+$	12.97	<b>-0.512</b>	$0.0243 - i0.0038$					<b>0.0254</b>	$-(3.4 + i4.2) \times 10^{-5}$
$3^-$	6.13	0.691							
$3^-$	11.51	<b>0.242</b>	$0.0 + i0.0(E3)$	<b>-0.138</b>	$0.543 + i0.221$			<b>0.0113</b>	$-(4.22 + i2.95) \times 10^{-4}$
$3^-$	13.14	<b>1.07</b>	$0.0 + i0.0(E3)$	9.70	$0.0144 + i0.0600$				
$3^-$	13.26			<b>-7.09</b>	$0.130 + i0.0252$				
$4^+$	10.36							<b>3.18</b>	$0.729 + i0.0819$
$4^+$	11.10			$9.87 \times 10^{-3}$	$-(6 + 1) \times 10^{-6}$			0.500	$0.0416 + i0.0094$

## APPENDIX B: TABULATED REACTION RATE

The tabulated reaction rate is calculated at the same temperatures as in [Angulo \*et al.\* \(1999\)](#) (NACRE) for ease of comparison. In addition, the rate has been parametrized using the format recommended by JINA ReacLib ([Cyburt \*et al.\*, 2010](#)). In order to fit the rate in the range  $0.06 < T_9 < 10$  GK to a precision of better than 5%, two instances of the rate parametrization formula,

$$N_A \langle \sigma v \rangle = \exp \left[ a_0 + \sum_{i=1}^5 a_i T_9^{(2i-5)/3} + a_6 \ln T_9 \right], \quad (\text{B1})$$

were necessary: a nonresonant and a resonance term (i.e.,  $N_A \langle \sigma v \rangle_{\text{total}} = N_A \langle \sigma v \rangle_{\text{nonresonant}} + N_A \langle \sigma v \rangle_{\text{resonance}}$ ). The first follows the suggested format for a charged particle induced nonresonance contribution, while the second represents a single isolated narrow resonance term. The parameters are given in [Table XXVI](#). Note that the parameter values do not necessarily correspond to physical quantities.

TABLE XXV. The rate of the  $^{12}\text{C}(\alpha, \gamma)^{16}\text{O}$  reaction. Uncertainties are calculated using a combination of Monte Carlo analysis and investigation of systematic contributions from both data and model sources and are listed separately.

$T$ (GK)	Adopted rate	Lower rate	Upper rate
0.06	$6.78 \times 10^{-26}$	$5.69 \times 10^{-26}$	$7.90 \times 10^{-26}$
0.07	$3.28 \times 10^{-24}$	$2.76 \times 10^{-24}$	$3.83 \times 10^{-24}$
0.08	$8.00 \times 10^{-23}$	$6.71 \times 10^{-23}$	$9.35 \times 10^{-23}$
0.09	$1.18 \times 10^{-21}$	$9.91 \times 10^{-22}$	$1.38 \times 10^{-21}$
0.1	$1.20 \times 10^{-20}$	$1.00 \times 10^{-20}$	$1.40 \times 10^{-20}$
0.11	$9.03 \times 10^{-20}$	$7.55 \times 10^{-20}$	$1.06 \times 10^{-19}$
0.12	$5.38 \times 10^{-19}$	$4.50 \times 10^{-19}$	$6.31 \times 10^{-19}$
0.13	$2.65 \times 10^{-18}$	$2.21 \times 10^{-18}$	$3.11 \times 10^{-18}$
0.14	$1.11 \times 10^{-17}$	$9.28 \times 10^{-18}$	$1.30 \times 10^{-17}$
0.15	$4.08 \times 10^{-17}$	$3.41 \times 10^{-17}$	$4.80 \times 10^{-17}$
0.16	$1.34 \times 10^{-16}$	$1.12 \times 10^{-16}$	$1.58 \times 10^{-16}$
0.18	$1.09 \times 10^{-15}$	$9.11 \times 10^{-16}$	$1.29 \times 10^{-15}$
0.2	$6.64 \times 10^{-15}$	$5.53 \times 10^{-15}$	$7.83 \times 10^{-15}$
0.25	$2.43 \times 10^{-13}$	$2.02 \times 10^{-13}$	$2.87 \times 10^{-13}$
0.3	$3.73 \times 10^{-12}$	$3.10 \times 10^{-12}$	$4.43 \times 10^{-12}$
0.35	$3.28 \times 10^{-11}$	$2.72 \times 10^{-11}$	$3.90 \times 10^{-11}$
0.4	$1.96 \times 10^{-10}$	$1.62 \times 10^{-10}$	$2.33 \times 10^{-10}$
0.45	$8.82 \times 10^{-10}$	$7.30 \times 10^{-10}$	$1.05 \times 10^{-9}$
0.5	$3.22 \times 10^{-9}$	$2.66 \times 10^{-9}$	$3.85 \times 10^{-9}$
0.6	$2.70 \times 10^{-8}$	$2.23 \times 10^{-8}$	$3.23 \times 10^{-8}$
0.7	$1.47 \times 10^{-7}$	$1.21 \times 10^{-7}$	$1.76 \times 10^{-7}$
0.8	$5.92 \times 10^{-7}$	$4.90 \times 10^{-7}$	$7.11 \times 10^{-7}$
0.9	$1.92 \times 10^{-6}$	$1.59 \times 10^{-6}$	$2.31 \times 10^{-6}$
1	$5.30 \times 10^{-6}$	$4.40 \times 10^{-6}$	$6.38 \times 10^{-6}$
1.25	$4.10 \times 10^{-5}$	$3.42 \times 10^{-5}$	$4.93 \times 10^{-5}$
1.5	$2.03 \times 10^{-4}$	$1.70 \times 10^{-4}$	$2.43 \times 10^{-4}$
1.75	$7.65 \times 10^{-4}$	$6.46 \times 10^{-4}$	$9.14 \times 10^{-4}$
2	$2.40 \times 10^{-3}$	$2.04 \times 10^{-3}$	$2.86 \times 10^{-3}$
2.5	$1.57 \times 10^{-2}$	$1.32 \times 10^{-2}$	$1.88 \times 10^{-2}$
3	$6.66 \times 10^{-2}$	$5.51 \times 10^{-2}$	$8.10 \times 10^{-2}$
3.5	$2.09 \times 10^{-1}$	$1.71 \times 10^{-1}$	$2.55 \times 10^{-1}$
4	$5.31 \times 10^{-1}$	$4.37 \times 10^{-1}$	$6.48 \times 10^{-1}$
5	$2.38 \times 10^0$	$2.02 \times 10^0$	$2.84 \times 10^0$
6	$7.93 \times 10^0$	$6.96 \times 10^0$	$9.22 \times 10^0$
7	$2.11 \times 10^1$	$1.89 \times 10^1$	$2.41 \times 10^1$
8	$4.64 \times 10^1$	$4.20 \times 10^1$	$5.26 \times 10^1$
9	$8.75 \times 10^1$	$7.96 \times 10^1$	$9.86 \times 10^1$
10	$1.46 \times 10^2$	$1.33 \times 10^2$	$1.64 \times 10^2$

TABLE XXVI. The sum of two instances of Eq. (B1) are necessary to fit the reaction rate to better than 5% accuracy over the range  $0.06 < T < 10$  GK and the parameters given here reproduce the recommended rate to better than 3.5%. Not all parameters are necessary for the fitting and these have been set to zero. Parameters that were adjusted for the fit are set in bold.

Term	$a_0$	$a_1$	$a_2$	$a_3$	$a_4$	$a_5$	$a_6$
Nonresonant	<b>24.1</b>	0	<b>-32</b>	<b>-5.9</b>	<b>1.8</b>	<b>-0.17</b>	$-2/3$
Resonance	<b>7.4</b>	<b>-30</b>	0	0	0	0	$-3/2$

## REFERENCES

- Abel, T., G. L. Bryan, and M. L. Norman, 2002, *Science* **295**, 93.
- Abia, C., M. Busso, R. Gallino, I. Domínguez, O. Straniero, and J. Isern 2001, *Astrophys. J.* **559**, 1117.
- Abia, C., I. Domínguez, R. Gallino, M. Busso, S. Masera, O. Straniero, P. de Laverny, B. Plez, and J. Isern 2002, *Astrophys. J.* **579**, 817.
- Adams, A., M. H. Shapiro, C. A. Barns, E. G. Adelberger, and W. M. Denny, 1968, *Bull. Am. Phys. Soc.* **13**, 698.
- Adhikari, S., and C. Basu, 2009, *Phys. Lett. B* **682**, 216.
- Aerts, C., and T. M. Rogers, 2015, *Astrophys. J. Lett.* **806**, L33.
- Alburger, D. E., A. Gallmann, and D. H. Wilkinson, 1959, *Phys. Rev.* **116**, 939.
- Allan, H. R., and N. Sarma, 1955, *Proc. Phys. Soc. London Sect. A* **68**, 535.
- An, Z.-D., Z.-P. Chen, Y.-G. Ma, J.-K. Yu, Y.-Y. Sun, G.-T. Fan, Y.-J. Li, H.-H. Xu, B.-S. Huang, and K. Wang, 2015, *Phys. Rev. C* **92**, 045802.
- Angulo, C., and P. Descouvemont, 2000, *Phys. Rev. C* **61**, 064611.
- Angulo, C., and P. Descouvemont, 2001, *Nucl. Phys. A* **690**, 755.
- Angulo, C., *et al.*, 1999, *Nucl. Phys. A* **656**, 3.
- Assunção, M., *et al.*, 2006, *Phys. Rev. C* **73**, 055801.
- Audi, G., A. Wapstra, and C. Thibault, 2003, *Nucl. Phys. A* **729**, 337.
- Avila, M. L., G. V. Rogachev, E. Koshchiy, L. T. Baby, J. Belarge, K. W. Kemper, A. N. Kuchera, A. M. Mukhamedzhanov, D. Santiago-Gonzalez, and E. Uberseder, 2015, *Phys. Rev. Lett.* **114**, 071101.
- Azuma, R. E., *et al.*, 1994, *Phys. Rev. C* **50**, 1194.
- Azuma, R. E., *et al.*, 2010, *Phys. Rev. C* **81**, 045805.
- Balabanski, D. L. (the ELI-NP Science Team), 2015, *J. Phys. Conf. Ser.* **590**, 012005.
- Barker, F. C., 1967, *Aust. J. Phys.* **20**, 341.
- Barker, F. C., 1969, *Aust. J. Phys.* **22**, 293.
- Barker, F. C., 1994a, *Phys. Lett. B* **322**, 17.
- Barker, F. C., 1994b, *Nucl. Phys. A* **575**, 361.
- Barker, F. C., 1995, *Nucl. Phys. A* **588**, 693.
- Barker, F. C., 1971, *Aust. J. Phys.* **24**, 771.
- Barker, F. C., 1987, *Aust. J. Phys.* **40**, 25.
- Barker, F. C., and T. Kajino, 1991, *Aust. J. Phys.* **44**, 369.
- Barker, F. C., and E. K. Warburton, 1988, *Nucl. Phys. A* **487**, 269.
- Barker, F. O., 1972, *Aust. J. Phys.* **25**, 341.
- Barnes, C., D. Clayton, and D. Schramm, 1982, Eds., *Essays on Nuclear Astrophysics* (Cambridge University Press, Cambridge, England).
- Barnes, C. A., D. B. James, and G. C. Neilson, 1952, *Can. J. Phys.* **30**, 717.
- Bashkin, S., R. R. Carlson, and R. A. Douglas, 1959, *Phys. Rev.* **114**, 1543.
- Battino, U., *et al.*, 2016, *Astrophys. J.* **827**, 30.
- Baye, D., and P. Descouvemont, 1988, *Nucl. Phys. A* **481**, 445.
- Becchetti, F., E. Flynn, D. Hanson, and J. Sunier, 1978, *Nucl. Phys. A* **305**, 293.
- Becchetti, F. D., J. Jänecke, and C. E. Thorn, 1978, *Nucl. Phys. A* **305**, 313.
- Becchetti, F. D., D. Overway, J. Jänecke, and W. Jacobs, 1980, *Nucl. Phys. A* **344**, 336.
- Beck, C., 2010, Ed., *Clusters in Nuclei* (Springer-Verlag, Berlin/Heidelberg), Vol. 818.
- Beck, C., 2012, Ed., *Clusters in Nuclei* (Springer-Verlag, Berlin/Heidelberg), Vol. 848.
- Beck, C., 2014, Ed., *Clusters in Nuclei* (Springer-Verlag, Berlin/Heidelberg), Vol. 875.
- Beers, T. C., G. W. Preston, and S. A. Sackett, 1985, *Astron. J.* **90**, 2089.
- Beers, T. C., G. W. Preston, and S. A. Sackett, 1992, *Astron. J.* **103**, 1987.
- Belhout, A., *et al.*, 2007, *Nucl. Phys. A* **793**, 178.
- Bemmerer, D., *et al.* (LUNA Collaboration), 2009, *J. Phys. G* **36**, 045202.
- Bessell, M. S., and J. Norris, 1984, *Astrophys. J.* **285**, 622.
- Bethe, H. A., 1939, *Phys. Rev.* **55**, 434.
- Bloch, C., 1957, *Nucl. Phys.* **4**, 503.
- Bloom, S. D., B. J. Toppel, and D. H. Wilkinson, 1957, *Philos. Mag.* **2**, 57.
- Boggs, S. E., *et al.*, 2015, *Science* **348**, 670.
- Bond, H. E., 1981, *Astrophys. J.* **248**, 606.
- Bond, J. R., W. D. Arnett, and B. J. Carr, 1984, *Astrophys. J.* **280**, 825.
- Bonifacio, P., *et al.*, 2015, *Astron. Astrophys.* **579**, A28.
- Bray, K. H., A. D. Frawley, T. R. Ophel, and F. C. Barker, 1977, *Nucl. Phys. A* **288**, 334.
- Breit, G., 1940, *Phys. Rev.* **58**, 1068.
- Breit, G., and E. Wigner, 1936, *Phys. Rev.* **49**, 519.
- Brochard, F., P. Chevallier, D. Disdier, V. Rauch, and F. Scheibling, 1973, *J. Phys. (Paris)* **34**, 363.
- Brown, G. E., and A. M. Green, 1966, *Nucl. Phys.* **75**, 401.
- Brune, C. R., 1996, *Nucl. Phys. A* **596**, 122.
- Brune, C. R., 2001, *Phys. Rev. C* **64**, 055803.
- Brune, C. R., 2002, *Phys. Rev. C* **66**, 044611.
- Brune, C. R., W. H. Geist, R. W. Kavanagh, and K. D. Veal, 1999, *Phys. Rev. Lett.* **83**, 4025.
- Brune, C. R., and D. B. Sayre, 2013, *Nucl. Instrum. Methods Phys. Res., Sect. A* **698**, 49.
- Buchmann, L., 2001, *Phys. Rev. C* **64**, 022801.
- Buchmann, L., R. E. Azuma, C. A. Barnes, J. Humblet, and K. Langanke, 1996, *Phys. Rev. C* **54**, 393.
- Buchmann, L., G. Ruprecht, and C. Ruiz, 2009, *Phys. Rev. C* **80**, 045803.
- Buchmann, L., *et al.*, 1993, *Phys. Rev. Lett.* **70**, 726.
- Buchmann, L. R., and C. A. Barnes, 2006, *Nucl. Phys. A* **777**, 254.
- Burbidge, E. M., G. R. Burbidge, W. A. Fowler, and F. Hoyle, 1957, *Rev. Mod. Phys.* **29**, 547.
- Cacioli, A., *et al.*, 2011, *Astron. Astrophys.* **533**, A66.
- Calder, A. C., D. M. Townsley, I. R. Seitenzahl, F. Peng, O. E. B. Messer, N. Vladimirova, E. F. Brown, J. W. Truran, and D. Q. Lamb, 2007, *Astrophys. J.* **656**, 313.
- Cannon, R. D., 1970, *Mon. Not. R. Astron. Soc.* **150**, 111.
- Carlson, A., *et al.*, 2009, *Nucl. Data Sheets* **110**, 3215.
- Carr, B. J., and M. J. Rees, 1979, *Nature (London)* **278**, 605.
- Castellani, V., A. Chieffi, and O. Straniero, 1992, *Astrophys. J. Suppl. Ser.* **78**, 517.
- Caughlan, G. R., and W. A. Fowler, 1988, *At. Data Nucl. Data Tables* **40**, 283.
- Chatzopoulos, E., S. M. Couch, W. D. Arnett, and F. X. Timmes, 2016, *Astrophys. J.* **822**, 61.
- Christlieb, N., 2008, in *Reviews in Modern Astronomy*, edited by R. E. Schielicke (WILEY-VCH GmbH), pp. 191–206.
- Christy, R., and I. Duck, 1961, *Nucl. Phys.* **24**, 89.
- Clark, G. J., 1969, *Aust. J. Phys.* **22**, 289.
- Clark, G. J., D. J. Sullivan, and P. B. Treacy, 1968, *Nucl. Phys. A* **110**, 481.
- Coburn, M. E., D. J. Pisano, and P. D. Parker, 1976, *Phys. Rev. C* **14**, 491.
- Cohen, A., and A. French, 1953, *Philos. Mag. J. Sci.* **44**, 1259.

- Cook, C. W., W. A. Fowler, C. C. Lauritsen, and T. Lauritsen, 1957, *Phys. Rev.* **107**, 508.
- Costantini, H., A. Formicola, G. Imbriani, M. Junker, C. Rolfs, and F. Strieder, 2009, *Rep. Prog. Phys.* **72**, 086301.
- Costantini, H., *et al.*, 2010, *Phys. Rev. C* **82**, 035802.
- Couch, S. M., E. Chatzopoulos, W. D. Arnett, and F. X. Timmes, 2015, *Astrophys. J. Lett.* **808**, L21.
- Couder, M., G. Berg, J. Grres, P. LeBlanc, L. Lamm, E. Stech, M. Wiescher, and J. Hinnefeld, 2008, *Nucl. Instrum. Methods Phys. Res., Sect. A* **587**, 35.
- Creevey, O. L., *et al.*, 2015, *Astron. Astrophys.* **575**, A26.
- Cristallo, S., C. Abia, O. Straniero, and L. Piersanti, 2015, *Astrophys. J.* **801**, 53.
- Cristallo, S., O. Straniero, R. Gallino, F. Herwig, A. Chieffi, M. Limongi, and M. Busso, 2001, *Nucl. Phys. A* **688**, 217.
- Cybur, R. H., *et al.*, 2010, *Astrophys. J. Suppl. Ser.* **189**, 240.
- D'Agostini, G., 1994, *Nucl. Instrum. Methods Phys. Res., Sect. A* **346**, 306.
- D'Agostino-Bruno, M., I. Massa, A. Uguzzoni, G. Bannini, E. Verondini, and A. Vitale, 1975, *Nuovo Cimento A* **27**, 1.
- D'Antona, F., 1982, *Astron. Astrophys.* **115**, L1 [<http://adsabs.harvard.edu/abs/1982A%26A...115L...1D>].
- deBoer, R. J., A. Couture, R. Detwiler, J. Görres, P. Tischhauser, E. Uberseder, C. Ugalde, E. Stech, M. Wiescher, and R. E. Azuma, 2012, *Phys. Rev. C* **85**, 045804.
- deBoer, R. J., J. Görres, G. Imbriani, P. J. LeBlanc, E. Uberseder, and M. Wiescher, 2013, *Phys. Rev. C* **87**, 015802.
- deBoer, R. J., J. Görres, K. Smith, E. Uberseder, M. Wiescher, A. Kontos, G. Imbriani, A. Di Leva, and F. Strieder, 2014, *Phys. Rev. C* **90**, 035804.
- deBoer, R. J., P. J. LeBlanc, S. Falahat, G. Imbriani, J. Görres, S. O'Brien, E. Uberseder, and M. Wiescher, 2012, *Phys. Rev. C* **85**, 038801.
- Delgado-Inglada, G., M. Rodríguez, M. Peimbert, G. Stasińska, and C. Morisset, 2015, *Mon. Not. R. Astron. Soc.* **449**, 1797.
- Denissenkov, P. A., and C. A. Tout, 2003, *Mon. Not. R. Astron. Soc.* **340**, 722.
- Descouvemont, P., 1987, *Nucl. Phys. A* **470**, 309.
- Descouvemont, P., 1993, *Phys. Rev. C* **47**, 210.
- Descouvemont, P., and D. Baye, 1987, *Phys. Rev. C* **36**, 1249.
- Descouvemont, P., and D. Baye, 2010, *Rep. Prog. Phys.* **73**, 036301.
- Descouvemont, P., D. Baye, and P.-H. Heenen, 1984, *Nucl. Phys. A* **430**, 426.
- DiGiovine, B., D. Henderson, R. Holt, R. Raut, K. Rehm, A. Robinson, A. Sonnenschein, G. Rusev, A. Tonchev, and C. Ugalde, 2015, *Nucl. Instrum. Methods Phys. Res., Sect. A* **781**, 96.
- Dodder, D., G. Hale, N. Jarmie, J. Jett, P. Keaton, R. Nisley, and K. Witte, 1977, *Phys. Rev. C* **15**, 518.
- Doherty, C. L., P. Gil-Pons, L. Siess, J. C. Lattanzio, and H. H. B. Lau, 2015, *Mon. Not. R. Astron. Soc.* **446**, 2599.
- Dohet-Eraly, J., and D. Baye, 2013, *Phys. Rev. C* **88**, 024602.
- Dufour, M., and P. Descouvemont, 2008, *Phys. Rev. C* **78**, 015808.
- Dyer, P., and C. Barnes, 1974, *Nucl. Phys. A* **233**, 495.
- Eisenstein, D. J., *et al.*, 2006, *Astrophys. J. Suppl. Ser.* **167**, 40.
- Eldridge, J. J., and C. A. Tout, 2004, *Mon. Not. R. Astron. Soc.* **353**, 87.
- El Eid, M. F., K. J. Fricke, and W. W. Ober, 1983, *Astron. Astrophys.* **119**, 54 [<http://adsabs.harvard.edu/abs/1983A%26A...119...54E>].
- El Eid, M. F., B. S. Meyer, and L.-S. The, 2004, *Astrophys. J.* **611**, 452.
- Elhatisari, S., D. Lee, G. Rupak, E. Epelbaum, H. Krebs, T. A. Lähde, T. Luu, and U.-G. Meißner, 2015, *Nature (London)* **528**, 111.
- Epelbaum, E., H. Krebs, T. A. Lähde, D. Lee, U.-G. Meißner, and G. Rupak, 2014, *Phys. Rev. Lett.* **112**, 102501.
- Evers, D., G. Flügge, J. Morgenstern, T. Retz-Schmidt, H. Schmidt, J. Schmidt, and S. Skorka, 1968, *Phys. Lett. B* **27**, 423.
- Ezer, D., and A. G. W. Cameron, 1971, *Astrophys. Space Sci.* **14**, 399.
- Farmer, R., C. E. Fields, I. Petermann, L. Dessart, M. Cantiello, B. Paxton, and F. X. Timmes, 2016, *Astrophys. J. Suppl. Ser.* **227**, 22.
- Farmer, R., C. E. Fields, and F. X. Timmes, 2015, *Astrophys. J.* **807**, 184.
- Faulkner, D. J., and R. D. Cannon, 1973, *Astrophys. J.* **180**, 435.
- Fey, M., 2004, "Im Brennpunkt der Nuklearen Astrophysik: Die Reaktion  $^{12}\text{C}(\alpha, \gamma)^{16}\text{O}$ ," Ph.D. thesis (Universität Stuttgart).
- Fields, C. E., R. Farmer, I. Petermann, C. Iliadis, and F. X. Timmes, 2016, *Astrophys. J.* **823**, 46.
- Filippone, B. W., J. Humblet, and K. Langanke, 1989, *Phys. Rev. C* **40**, 515.
- Fishlock, C. K., A. I. Karakas, M. Lugaro, and D. Yong, 2014, *Astrophys. J.* **797**, 44.
- Fleurot, F., *et al.*, 2005, *Phys. Lett. B* **615**, 167.
- Fowler, W. A., 1984, *Science* **226**, 922.
- Fowler, W. A., G. R. Caughlan, and B. A. Zimmerman, 1967, *Annu. Rev. Astron. Astrophys.* **5**, 525.
- Fowler, W. A., and C. C. Lauritsen, 1939, *Phys. Rev.* **56**, 840.
- France, III, R. H., E. Wilds, N. Jevtic, J. McDonald, and M. Gai, 1997, *Nucl. Phys. A* **621**, 165.
- France, III, R. H., E. L. Wilds, J. E. McDonald, and M. Gai, 2007, *Phys. Rev. C* **75**, 065802.
- Frebel, A., A. Chiti, A. P. Ji, H. R. Jacobson, and V. M. Placco, 2015, *Astrophys. J. Lett.* **810**, L27.
- Frebel, A., *et al.*, 2005, *Nature (London)* **434**, 871.
- Freer, M., 2007, *Rep. Prog. Phys.* **70**, 2149.
- Freer, M., and H. Fynbo, 2014, *Prog. Part. Nucl. Phys.* **78**, 1.
- Fuchs, H., K. Hagemann, and C. Gaarde, 1965, *Nucl. Phys.* **66**, 638.
- Fuller, G. M., S. E. Woosley, and T. A. Weaver, 1986, *Astrophys. J.* **307**, 675.
- Fuller, J., M. Cantiello, D. Stello, R. A. Garcia, and L. Bildsten, 2015, *Science* **350**, 423.
- Funck, C., K. Langanke, and A. Weiguny, 1985, *Phys. Lett. B* **152**, 11.
- Gai, M., 1998, *J. Phys. G* **24**, 1625.
- Gai, M. (the UConn-Yale-Duke-Weizmann-PTB-UCL Collaboration), 2012, *J. Phys. Conf. Ser.* **337**, 012054.
- Gai, M., 2013, *Phys. Rev. C* **88**, 062801.
- Gallino, R., C. Arlandini, M. Busso, M. Lugaro, C. Travaglio, O. Straniero, A. Chieffi, and M. Limongi, 1998, *Astrophys. J.* **497**, 388.
- Garaud, P., M. Medrano, J. M. Brown, C. Mankovich, and K. Moore, 2015, *Astrophys. J.* **808**, 89.
- García-Berro, E., C. Ritossa, and I. Iben, Jr., 1997, *Astrophys. J.* **485**, 765.
- Garnett, D., 1997, *Nucl. Phys. A* **621**, 27.
- Gialanella, L., *et al.*, 2001, *Eur. Phys. J. A* **11**, 357.
- Girardi, L., 1999, *Mon. Not. R. Astron. Soc.* **308**, 818.
- Guenther, D. B., and P. Demarque, 1983, *Astron. Astrophys.* **118**, 262 [<http://adsabs.harvard.edu/abs/1983A%26A...118..262G>].
- Guerro, L., *et al.*, 2014, *Eur. Phys. J. A* **50**, 171.
- Hagedorn, F. B., 1957, *Phys. Rev.* **108**, 735.
- Hagedorn, F. B., and J. B. Marion, 1957, *Phys. Rev.* **108**, 1015.
- Hale, G., 1997, *Nucl. Phys. A* **621**, 177.
- Hale, G., 2004, "Some Thoughts on  $\chi^2$  Expressions," Los Alamos National Laboratory, unpublished memorandum.
- Hale, G., and D. Dodder, 1980, in *Nuclear Cross Sections for Technology: Proceedings of the International Conference on Nuclear Cross Sections for Technology*, Natl. Bur. Stand. (U.S.)

- Special Publication 594, edited by J. Fowler, C. Johnson, and C. Bowman (U.S. GPO, Washington, DC), pp. 650–658.
- Hale, G. M., R. E. Brown, and N. Jarmie, 1987, *Phys. Rev. Lett.* **59**, 763.
- Hammer, J. W., *et al.*, 2005a, *Nucl. Phys. A* **758**, 363.
- Hammer, J. W., *et al.*, 2005b, *Nucl. Phys. A* **752**, 514.
- Hansen, C. J., S. D. Kawaler, and V. Trimble, 2004, *Stellar interiors: physical principles, structure, and evolution*, edited by C. J. Hansen, S. D. Kawaler, and V. Trimble (Springer-Verlag, New York), 2nd ed.
- Hansen, T., *et al.*, 2015, *Astrophys. J.* **807**, 173.
- Hansen, T. T., J. Andersen, B. Nordström, T. C. Beers, V. M. Placco, J. Yoon, and L. A. Buchhave, 2016, *Astron. Astrophys.* **586**, A160.
- Harss, B., *et al.*, 2000, *Rev. Sci. Instrum.* **71**, 380.
- Hättig, H., K. Hünchen, P. Roth, and H. Wäffler, 1969, *Nucl. Phys. A* **137**, 144.
- Hättig, H., K. Hünchen, and H. Wäffler, 1970, *Phys. Rev. Lett.* **25**, 941.
- Hebbard, D. F., 1960, *Nucl. Phys.* **15**, 289.
- Heger, A., N. Langer, and S. E. Woosley, 2000, *Astrophys. J.* **528**, 368.
- Heger, A., and S. E. Woosley, 2002, *Astrophys. J.* **567**, 532.
- Heger, A., and S. E. Woosley, 2010, *Astrophys. J.* **724**, 341.
- Herwig, F., 2005, *Annu. Rev. Astron. Astrophys.* **43**, 435.
- Herwig, F., S. M. Austin, and J. C. Lattanzio, 2006, *Phys. Rev. C* **73**, 025802.
- Herwig, F., T. Bloeker, D. Schoenberner, and M. El Eid, 1997, *Astron. Astrophys.* **324**, L81 [<http://adsabs.harvard.edu/abs/1997A%26A...324L..81H>].
- Herwig, F., B. Freytag, T. Fuchs, J. P. Hansen, R. M. Hueckstaedt, D. H. Porter, F. X. Timmes, and P. R. Woodward, 2007, in *Why Galaxies Care About AGB Stars: Their Importance as Actors and Probes*, Astron. Soc. Pac. Conf. Ser., Vol. 378, edited by F. Kerschbaum, C. Charbonnel, and R. F. Wing (Astronomical Society of the Pacific, San Francisco), p. 43.
- Höfllich, P., J. C. Wheeler, and F. K. Thielemann, 1998, *Astrophys. J.* **495**, 617.
- Holt, R. J., H. E. Jackson, R. M. Laszewski, J. E. Monahan, and J. R. Specht, 1978, *Phys. Rev. C* **18**, 1962.
- Hosokawa, T., S. Hirano, R. Kuiper, H. W. Yorke, K. Omukai, and N. Yoshida, 2016, *Astrophys. J.* **824**, 119.
- Hoyle, F., 1954, *Astrophys. J. Suppl. Ser.* **1**, 121.
- Humblet, J., 1990, *Phys. Rev. C* **42**, 1582.
- Humblet, J., A. Csötö, and K. Langanke, 1998, *Nucl. Phys. A* **638**, 714.
- Humblet, J., P. Dyer, and B. Zimmerman, 1976, *Nucl. Phys. A* **271**, 210.
- Humblet, J., B. W. Filippone, and S. E. Koonin, 1991, *Phys. Rev. C* **44**, 2530.
- Humblet, J., B. W. Filippone, and S. E. Koonin, 1993, *Phys. Rev. C* **48**, 2114.
- Humphreys, R. M., and K. Davidson, 1994, *Publ. Astron. Soc. Pac.* **106**, 1025.
- Hutcheon, D., *et al.*, 2003, *Nucl. Instrum. Methods Phys. Res., Sect. A* **498**, 190.
- Iben, Jr., I., 1966, *Astrophys. J.* **143**, 516.
- Iben, Jr., I., 1991, *Astrophys. J. Suppl. Ser.* **76**, 55.
- Ikeda, K., N. Takigawa, and H. Horiuchi, 1968, *Prog. Theor. Phys. Suppl.* **E68**, 464.
- Ikeda, N., K. Sagara, K. Tsuruta, H. Oba, T. Ohta, Y. Noguchi, K. Ichikawa, Y. Miwa, and S. Morinobu, 2003, *Nucl. Phys. A* **718**, 558.
- Iliadis, C., K. S. Anderson, A. Coc, F. X. Timmes, and S. Starrfield, 2016, *Astrophys. J.* **831**, 107.
- Iliadis, C., R. Longland, A. Coc, F. X. Timmes, and A. E. Champagne, 2015, *J. Phys. G* **42**, 034007.
- Imbriani, G., M. Limongi, L. Gialanella, F. Terrasi, O. Straniero, and A. Chieffi, 2001, *Astrophys. J.* **558**, 903.
- Imbriani, G., *et al.*, 2012, *Phys. Rev. C* **85**, 065810.
- Jaszczak, R. J., J. H. Gibbons, and R. L. Macklin, 1970, *Phys. Rev. C* **2**, 63.
- Jaszczak, R. J., and R. L. Macklin, 1970, *Phys. Rev. C* **2**, 2452.
- Jerkstrand, A., F. X. Timmes, G. Magkotsios, S. A. Sim, C. Fransson, J. Spyromilio, B. Müller, A. Heger, J. Sollerman, and S. J. Smartt, 2015, *Astrophys. J.* **807**, 110.
- Ji, A. P., A. Frebel, and V. Bromm, 2015, *Mon. Not. R. Astron. Soc.* **454**, 659.
- Ji, X., B. W. Filippone, J. Humblet, and S. E. Koonin, 1990, *Phys. Rev. C* **41**, 1736.
- Jiang, Y.-F., M. Cantiello, L. Bildsten, E. Quataert, and O. Blaes, 2015, *Astrophys. J.* **813**, 74.
- Jiang, Y.-F., M. Cantiello, L. Bildsten, E. Quataert, and O. Blaes, 2016, [arXiv:1612.06434](https://arxiv.org/abs/1612.06434).
- Johnson, C. H., 1973, *Phys. Rev. C* **7**, 561.
- Jones, C. M., G. C. Phillips, R. W. Harris, and E. H. Beckner, 1962, *Nucl. Phys.* **37**, 1.
- Jones, G. A., and D. H. Wilkinson, 1953, *Proc. Phys. Soc. London Sect. A* **66**, 1176.
- Jones, S., R. Andrassy, S. Sandalski, A. Davis, P. Woodward, and F. Herwig, 2017, *Mon. Not. R. Astron. Soc.* **465**, 2991.
- Jones, S., R. Hirschi, M. Pignatari, A. Heger, C. Georgy, N. Nishimura, C. Fryer, and F. Herwig, 2015, *Mon. Not. R. Astron. Soc.* **447**, 3115.
- Jones, S., *et al.*, 2013, *Astrophys. J.* **772**, 150.
- Justham, S., P. Podsiadlowski, and J. S. Vink, 2014, *Astrophys. J.* **796**, 121.
- Käppeler, F., *et al.*, 1994, *Astrophys. J.* **437**, 396.
- Karakas, A. I., and J. C. Lattanzio, 2014, *Publ. Astron. Soc. Aust.* **31**, e030.
- Kashi, A., K. Davidson, and R. M. Humphreys, 2016, *Astrophys. J.* **817**, 66.
- Katsuma, M., 2012, *Astrophys. J.* **745**, 192.
- Keller, S. C., *et al.*, 2014, *Nature (London)* **506**, 463.
- Kepler, S. O., S. J. Kleinman, A. Nitta, D. Koester, B. G. Castanheira, O. Giovannini, A. F. M. Costa, and L. Althaus, 2007, *Mon. Not. R. Astron. Soc.* **375**, 1315.
- Kepler, S. O., I. Pelisoli, D. Koester, G. Ourique, A. D. Romero, N. Reindl, S. J. Kleinman, D. J. Eisenstein, A. D. M. Valois, and L. A. Amaral, 2016, *Mon. Not. R. Astron. Soc.* **455**, 3413.
- Kepler, S. O., *et al.*, 2015, *Mon. Not. R. Astron. Soc.* **446**, 4078.
- Kernel, G., W. M. Mason, and U. V. Wimmersperg, 1971, *Nucl. Phys. A* **167**, 352.
- Kettner, K. U., H. W. Becker, L. Buchmann, J. Görres, H. Kräwinkel, C. Rolfs, P. Schmalbrock, H. P. Trautvetter, and A. Vlieks, 1982, *Z. Phys. A* **308**, 73.
- Kippenhahn, R., A. Weigert, and A. Weiss, 2012, *Stellar Structure and Evolution* (Springer-Verlag, Berlin).
- Knutson, L. D., 1999, *Phys. Rev. C* **59**, 2152.
- König, S., D. Lee, and H.-W. Hammer, 2013, *J. Phys. G* **40**, 045106.
- Koonin, S. E., T. A. Tombrello, and G. Fox, 1974, *Nucl. Phys. A* **220**, 221.
- Kragh, H., 2010, *Arch. Hist. Exact Sci.* **64**, 721.
- Kremer, R. M., C. A. Barnes, K. H. Chang, H. C. Evans, B. W. Filippone, K. H. Hahn, and L. W. Mitchell, 1988, *Phys. Rev. Lett.* **60**, 1475.
- Kunz, R., M. Fey, M. Jaeger, A. Mayer, J. W. Hammer, G. Staudt, S. Harissopulos, and T. Paradellis, 2002, *Astrophys. J.* **567**, 643.

- Kunz, R., M. Jaeger, A. Mayer, J. W. Hammer, G. Staudt, S. Harissopoulos, and T. Paradellis, 2001, *Phys. Rev. Lett.* **86**, 3244.
- Kunz, R. W., 2002, “ $^{12}\text{C}(\alpha, \gamma)^{16}\text{O}$ -Die Schlüsselreaktion im Heliumbrennen der Sterne,” Ph.D. thesis (Universität Stuttgart).
- La Cognata, M., *et al.*, 2007, *Phys. Rev. C* **76**, 065804.
- Lane, A., and J. Lynn, 1960, *Nucl. Phys.* **17**, 563.
- Lane, A. M., and D. Robson, 1966, *Phys. Rev.* **151**, 774.
- Lane, A. M., and R. G. Thomas, 1958, *Rev. Mod. Phys.* **30**, 257.
- Langanke, K., and H. Friedrich, 1986, “Advances in Nuclear Physics,” *Chap. Microscopic Description of Nucleus-Nucleus Collisions* (Plenum, New York), pp. 223–363.
- Langanke, K., and S. Koonin, 1983, *Nucl. Phys. A* **410**, 334.
- Langanke, K., and S. E. Koonin, 1985, *Nucl. Phys. A* **439**, 384.
- Larson, J. D., 1965, “Gamma radiation from the alpha particle bombardment of  $^{12}\text{C}$ ,” Ph.D. thesis (California Institute of Technology).
- Larson, J. D., and R. H. Spear, 1964, *Nucl. Phys.* **56**, 497.
- Leal, L., E. Ivanov, G. Noguere, A. Plompen, and S. Kopecky, 2016, *EPJ Nucl. Sci. Technol.* **2**, 43.
- LeBlanc, P. J., *et al.*, 2010, *Phys. Rev. C* **82**, 055804.
- Lecoanet, D., J. Schwab, E. Quataert, L. Bildsten, F. X. Timmes, K. J. Burns, G. M. Vasil, J. S. Oishi, and B. P. Brown, 2016, *Astrophys. J.* **832**, 71.
- Limongi, M., and A. Chieffi, 2003, *Astrophys. J.* **592**, 404.
- Liu, W. P. (the JUNA Collaboration), 2016, “Underground nuclear astrophysics experiment juna in china,” in *Proceedings of the 14th International Symposium on Nuclei in the Cosmos (NIC2016)*, <http://journals.jps.jp/doi/pdf/10.7566/JPSCP.14.011101>.
- Loebenstein, H. M., D. W. Mingay, H. Winkler, and C. S. Zaidins, 1967, *Nucl. Phys. A* **91**, 481.
- Longland, R., C. Iliadis, A. Champagne, C. Fox, and J. Newton, 2006, *Nucl. Instrum. Methods Phys. Res., Sect. A* **566**, 452.
- Lowe, J., D. E. Alburger, and D. H. Wilkinson, 1967, *Phys. Rev.* **163**, 1060.
- Lugaro, M., A. M. Davis, R. Gallino, M. J. Pellin, O. Straniero, and F. Käppeler, 2003, *Astrophys. J.* **593**, 486.
- Lynn, J., 1968, *The Theory of Neutron Resonance Reactions* (Clarendon Press, Oxford).
- Maeder, A., and G. Meynet, 2012, *Rev. Mod. Phys.* **84**, 25.
- Makii, H., K. Mishima, M. Segawa, E. Sano, H. Ueda, T. Shima, Y. Nagai, M. Igashira, and T. Ohsaki, 2005, *Nucl. Instrum. Methods Phys. Res., Sect. A* **547**, 411.
- Makii, H., Y. Nagai, T. Shima, M. Segawa, K. Mishima, H. Ueda, M. Igashira, and T. Ohsaki, 2009, *Phys. Rev. C* **80**, 065802.
- Marchant, P., N. Langer, P. Podsiadlowski, T. M. Tauris, and T. J. Moriya, 2016, *Astron. Astrophys.* **588**, A50.
- Marigo, P., L. Girardi, C. Chiosi, and P. R. Wood, 2001, *Astron. Astrophys.* **371**, 152.
- Marion, J. B., and W. A. Fowler, 1957, *Astrophys. J.* **125**, 221.
- Martins, F., S. Simon-Diaz, R. H. Barba, R. C. Gamem, and S. Ekstroem, 2016, [arXiv:1611.05223](https://arxiv.org/abs/1611.05223).
- Maschberger, T., 2013, *Mon. Not. R. Astron. Soc.* **429**, 1725.
- Matei, C., 2006, “Nucleosynthesis of  $^{16}\text{O}$  under quiescent helium burning,” Ph.D. thesis (Ohio University).
- Matei, C., C. R. Brune, and T. N. Massey, 2008, *Phys. Rev. C* **78**, 065801.
- Matei, C., *et al.*, 2006, *Phys. Rev. Lett.* **97**, 242503.
- McKee, C. F., and J. C. Tan, 2008, *Astrophys. J.* **681**, 771.
- Meads, R. E., and J. E. G. McIlldowie, 1960, *Proc. Phys. Soc. London* **75**, 257.
- Meakin, C. A., and D. Arnett, 2007, *Astrophys. J.* **667**, 448.
- Metcalf, T. S., 2003, *Astrophys. J. Lett.* **587**, L43.
- Miles, B. J., D. R. van Rossum, D. M. Townsley, F. X. Timmes, A. P. Jackson, A. C. Calder, and E. F. Brown, 2016, *Astrophys. J.* **824**, 59.
- Miska, H., H. GrÄf, A. Richter, R. Schneider, D. SchÄll, E. Spamer, H. Theissen, O. Titze, and T. Walcher, 1975, *Phys. Lett. B* **58**, 155.
- Mitchell, I. V., and T. R. Ophel, 1964, *Nucl. Phys.* **58**, 529.
- Mitchell, I. V., and T. R. Ophel, 1965, *Nucl. Phys.* **66**, 553.
- Morais, M. C., and R. LichtenthÄler, 2011, *Nucl. Phys. A* **857**, 1.
- Moreh, R., W. C. Sellyey, D. Sutton, and R. Vodhanel, 1985, *Phys. Rev. C* **31**, 2314.
- Morris, J. M., G. W. Kerr, and T. R. Ophel, 1968, *Nucl. Phys. A* **112**, 97.
- Mountford, D., R. deBoer, P. Descouvemont, A. S. J. Murphy, E. Uberseder, and M. Wiescher, 2014, *Nucl. Instrum. Methods Phys. Res., Sect. A* **767**, 359.
- Mukhamedzhanov, A. M., C. A. Gagliardi, and R. E. Tribble, 2001, *Phys. Rev. C* **63**, 024612.
- Mukhamedzhanov, A. M., and R. E. Tribble, 1999, *Phys. Rev. C* **59**, 3418.
- Mukhamedzhanov, A. M., *et al.* 2008, *Phys. Rev. C* **78**, 015804.
- Müller, B., M. Viallet, A. Heger, and H.-T. Janka, 2016, *Astrophys. J.* **833**, 124.
- Neilson, G. C., D. B. James, and C. A. Barnes, 1953, *Phys. Rev.* **92**, 1084(A).
- Neubeck, K., H. Schober, and H. WÄffler, 1974, *Phys. Rev. C* **10**, 320.
- Nollett, K. M., S. C. Pieper, R. B. Wiringa, J. Carlson, and G. M. Hale, 2007, *Phys. Rev. Lett.* **99**, 022502.
- Nomoto, K., and I. Iben, Jr., 1985, *Astrophys. J.* **297**, 531.
- Nomoto, K., C. Kobayashi, and N. Tominaga, 2013, *Annu. Rev. Astron. Astrophys.* **51**, 457.
- Ofek, E. O., *et al.*, 2014, *Astrophys. J.* **789**, 104.
- Ophel, T. R., A. D. Frawley, P. B. Treacy, and K. H. Bray, 1976, *Nucl. Phys. A* **273**, 397.
- Ouellet, J. M. L., *et al.*, 1992, *Phys. Rev. Lett.* **69**, 1896.
- Ouellet, J. M. L., *et al.*, 1996, *Phys. Rev. C* **54**, 1982.
- Oulebsir, N., *et al.*, 2012, *Phys. Rev. C* **85**, 035804.
- Özel, F., D. Psaltis, S. Ransom, P. Demorest, and M. Alford, 2010, *Astrophys. J. Lett.* **724**, L199.
- Paetz gen. Schieck, H., 2012, *Nuclear Physics with Polarized Particles* (Springer, Berlin/Heidelberg), Vol. 842.
- Palla, F., E. E. Salpeter, and S. W. Stahler, 1983, *Astrophys. J.* **271**, 632.
- Papadopoulos, A., *et al.*, 2015, *Mon. Not. R. Astron. Soc.* **449**, 1215.
- Pavlovskii, K., N. Ivanova, K. Belczynski, and K. X. Van, 2017, *Mon. Not. R. Astron. Soc.* **465**, 2092.
- Paxton, B., L. Bildsten, A. Dotter, F. Herwig, P. Lesaffre, and F. Timmes, 2011, *Astrophys. J. Suppl. Ser.* **192**, 3.
- Paxton, B., *et al.*, 2013, *Astrophys. J. Suppl. Ser.* **208**, 4.
- Paxton, B., *et al.*, 2015, *Astrophys. J. Suppl. Ser.* **220**, 15.
- Pepper, G. H., and L. Brown, 1976, *Nucl. Phys. A* **260**, 163.
- Perego, A., M. Hempel, C. Fröhlich, K. Ebinger, M. Eichler, J. Casanova, M. Liebendörfer, and F.-K. Thielemann, 2015, *Astrophys. J.* **806**, 275.
- Perlmutter, S., *et al.* (The Supernova Cosmology Project), 1999, *Astrophys. J.* **517**, 565.
- Pignatari, M., R. Gallino, M. Heil, M. Wiescher, F. Käppeler, F. Herwig, and S. Bisterzo, 2010, *Astrophys. J.* **710**, 1557.
- Pignatari, M., and F. Herwig, 2012, *Nucl. Phys. News* **22**, 18.
- Pignatari, M., *et al.*, 2016, *Astrophys. J. Suppl. Ser.* **225**, 24.
- Plag, R., R. Reifarth, M. Heil, F. Käppeler, G. Rupp, F. Voss, and K. Wisshak, 2012, *Phys. Rev. C* **86**, 015805.
- Plaga, R., H. Becker, A. Redder, C. Rolf, H. Trautvetter, and K. Langanke, 1987, *Nucl. Phys. A* **465**, 291.

- Poelarends, A. J. T., F. Herwig, N. Langer, and A. Heger, 2008, *Astrophys. J.* **675**, 614.
- Pühlhofer, F., H. G. Ritter, R. Bock, G. Brommundt, H. Schmidt, and K. Bethge, 1970, *Nucl. Phys. A* **147**, 258.
- Quataert, E., R. Fernández, D. Kasen, H. Klion, and B. Paxton, 2016, *Mon. Not. R. Astron. Soc.* **458**, 1214.
- Raiteri, C. M., M. Busso, G. Picchio, R. Gallino, and L. Pulone, 1991, *Astrophys. J.* **367**, 228.
- Raskin, C., E. Scannapieco, C. Fryer, G. Rockefeller, S. Diehl, and F. X. Timmes, 2012, *Astrophys. J.* **746**, 62.
- Redder, A., H. W. Becker, H. Lorenz-Wirzba, C. Rolfs, P. Schmalbrock, and H. P. Trautvetter, 1982, *Z. Phys. A* **305**, 325.
- Redder, A., H. W. Becker, C. Rolfs, H. P. Trautvetter, T. R. Donoghue, T. C. Rinckel, J. W. Hammer, and K. Langanke, 1987, *Nucl. Phys. A* **462**, 385.
- Refsgaard, J., *et al.*, 2016, *Phys. Lett. B* **752**, 296.
- Riess, A. G., *et al.*, 1998, *Astron. J.* **116**, 1009.
- Riisager, K., 2014, *Nucl. Phys. A* **925**, 112.
- Ritter, J. S., C. Safranek-Shrader, M. Milosavljević, and V. Bromm, 2016, *Mon. Not. R. Astron. Soc.* **463**, 3354.
- Robertson, D., M. Couder, U. Greife, F. Strieder, and M. Wiescher, 2016, *Eur. J. Phys. Web of Conferences* **109**, 09002.
- Rogers, T. M., 2015, *Astrophys. J. Lett.* **815**, L30.
- Rogers, T. M., D. N. C. Lin, J. N. McElwaine, and H. H. B. Lau, 2013, *Astrophys. J.* **772**, 21.
- Rolfs, C., 1973, *Nucl. Phys. A* **217**, 29.
- Rolfs, C., and W. S. Rodney, 1974, *Nucl. Phys. A* **235**, 450.
- Röpke, F. K., M. Gieseler, M. Reinecke, C. Travaglio, and W. Hillebrandt, 2006, *Astron. Astrophys.* **453**, 203.
- Rose, H. J., and D. M. Brink, 1967, *Rev. Mod. Phys.* **39**, 306.
- Rose, M. E., 1953, *Phys. Rev.* **91**, 610.
- Roters, G., C. Rolfs, F. Strieder, and H. Trautvetter, 1999, *Eur. Phys. J. A* **6**, 451.
- Sacco, G. G., *et al.*, 2015, *Astron. Astrophys.* **574**, L7.
- Safronov, A. N., 2009, *Phys. At. Nucl.* **72**, 996.
- Salaris, M., A. Weiss, L. P. Cassarà, L. Piován, and C. Chiosi, 2014, *Astron. Astrophys.* **565**, A9.
- Sallaska, A. L., C. Iliadis, A. E. Champagne, S. Goriely, S. Starrfield, and F. X. Timmes, 2013, *Astrophys. J. Suppl. Ser.* **207**, 18.
- Salpeter, E. E., 1952, *Astrophys. J.* **115**, 326.
- Salpeter, E. E., 1955, *Astrophys. J.* **121**, 161.
- Salpeter, E. E., 2002, *Annu. Rev. Astron. Astrophys.* **40**, 1.
- Sayer, R., L. Leal, N. Larson, R. Spencer, and R. Wright, 2002, *J. Nucl. Sci. Technol.* **39**, 88.
- Sayre, D., 2011, "Measurement of the 2.68-MeV Resonance Interference and R-Matrix Analysis of the  $^{12}\text{C}(\alpha, \gamma)^{16}\text{O}$  Reaction," Ph.D. thesis (Ohio University).
- Sayre, D. B., C. R. Brune, D. E. Carter, D. K. Jacobs, T. N. Massey, and J. E. O'Donnell, 2012, *Phys. Rev. Lett.* **109**, 142501.
- Scalo, J. M., 1986, *Fundam. Cosm. Phys.* **11**, 1 [<http://adsabs.harvard.edu/abs/1986FCPh...11....1S>].
- Schardt, A., W. A. Fowler, and C. C. Lauritsen, 1952, *Phys. Rev.* **86**, 527.
- Schürmann, D., L. Gialanella, R. Kunz, and F. Strieder, 2012, *Phys. Lett. B* **711**, 35.
- Schürmann, D., *et al.*, 2005, *Eur. Phys. J. A* **26**, 301.
- Schürmann, D., *et al.*, 2011, *Phys. Lett. B* **703**, 557.
- Seidel, E., P. Demarque, and D. Weinberg, 1987, *Astrophys. J. Suppl. Ser.* **63**, 917.
- Seitzzahl, I. R., *et al.*, 2016, *Astron. Astrophys.* **592**, A57.
- Siess, L., 2007, *Astron. Astrophys.* **476**, 893.
- Siess, L., 2009, *Astron. Astrophys.* **497**, 463.
- Sivia, D., and J. Skilling, 2006, *Data Analysis: A Bayesian Tutorial* (Oxford University Press, New York), 2nd ed.
- Smith, N., *et al.*, 2016, *Mon. Not. R. Astron. Soc.* **458**, 950.
- Smith, V. V., and D. L. Lambert, 1990, *Astrophys. J. Suppl. Ser.* **72**, 387.
- Snover, K. A., E. G. Adelberger, and D. R. Brown, 1974, *Phys. Rev. Lett.* **32**, 1061.
- Sparenberg, J.-M., 2004, *Phys. Rev. C* **69**, 034601.
- Sparenberg, J.-M., P. Capel, and D. Baye, 2010, *Phys. Rev. C* **81**, 011601.
- Stacy, A., V. Bromm, and A. T. Lee, 2016, *Mon. Not. R. Astron. Soc.* **462**, 1307.
- Stancliffe, R. J., A. Chieffi, J. C. Lattanzio, and R. P. Church, 2009, *Pub. Astron. Soc. Aust.* **26**, 203.
- Stephenson, Jr., G. J., 1966, *Astrophys. J.* **146**, 950.
- Straniero, O., I. Domínguez, G. Imbriani, and L. Piersanti, 2003, *Astrophys. J.* **583**, 878.
- Straniero, O., R. Gallino, M. Busso, A. Chieffi, C. M. Raiteri, M. Limongi, and M. Salaris, 1995, *Astrophys. J. Lett.* **440**, L85.
- Straniero, O., R. Gallino, and S. Cristallo, 2006, *Nucl. Phys. A* **777**, 311.
- Stroetzel, M., 1968, *Phys. Lett. B* **26**, 376.
- Strotjohann, N. L., *et al.*, 2015, *Astrophys. J.* **811**, 117.
- Sukhbold, T., T. Ertl, S. E. Woosley, J. M. Brown, and H.-T. Janka, 2016, *Astrophys. J.* **821**, 38.
- Suno, H., Y. Suzuki, and P. Descouvemont, 2016, *Phys. Rev. C* **94**, 054607.
- Suwa, Y., T. Yoshida, M. Shibata, H. Umeda, and K. Takahashi, 2015, *Mon. Not. R. Astron. Soc.* **454**, 3073.
- Swann, C., 1970, *Nucl. Phys. A* **150**, 300.
- Swann, C. P., and F. R. Metzger, 1956, *Bull. Am. Astron. Soc.*, Vol. 1, p. 211.
- Swann, C. P., and F. R. Metzger, 1957, *Phys. Rev.* **108**, 982.
- Tabassam, U., and K. Mehboob, 2015, *Prob. Atomic Sci. and Tech.: Nucl. Phys. Invest.* **97**, 44 [<http://vant.kipt.kharkov.ua>].
- Talwar, R., *et al.*, 2015, [arXiv:1508.05660](https://arxiv.org/abs/1508.05660).
- Tang, X. D., *et al.*, 2010, *Phys. Rev. C* **81**, 045809.
- The, L., M. F. El Eid, and B. S. Meyer, 2007, *Astrophys. J.* **655**, 1058.
- Thomas, R. G., 1951, *Phys. Rev.* **81**, 148.
- Thomas, R. G., 1952, *Phys. Rev.* **88**, 1109.
- Tilley, D. R., H. R. Weller, and C. M. Cheves, 1993, *Nucl. Phys. A* **564**, 1.
- Timmes, F. X., S. E. Woosley, and R. E. Taam, 1994, *Astrophys. J.* **420**, 348.
- Timmes, F. X., S. E. Woosley, and T. A. Weaver, 1996, *Astrophys. J.* **457**, 834.
- Tischhauser, P., *et al.*, 2002, *Phys. Rev. Lett.* **88**, 072501.
- Tischhauser, P., *et al.*, 2009, *Phys. Rev. C* **79**, 055803.
- Tombrello, T. A., and P. D. Parker, 1963, *Phys. Rev.* **131**, 2582.
- Tombrello, T. A., and G. C. Phillips, 1961, *Phys. Rev.* **122**, 224.
- Trautvetter, H., G. Roters, C. Rolfs, S. Schmidt, and P. Descouvemont, 1997, *Nucl. Phys. A* **621**, 161.
- Trippella, O., M. Busso, S. Palmerini, E. Maiorca, and M. C. Nucci, 2016, *Astrophys. J.* **818**, 125.
- Truran, J. W., and A. G. W. Cameron, 1971, *Astrophys. Space Sci.* **14**, 179.
- Tur, C., A. Heger, and S. M. Austin, 2007, *Astrophys. J.* **671**, 821.
- Tur, C., A. Heger, and S. M. Austin, 2009, *Astrophys. J.* **702**, 1068.
- Tur, C., A. Heger, and S. M. Austin, 2010, *Astrophys. J.* **718**, 357.
- Turk, M. J., T. Abel, and B. O'Shea, 2009, *Science* **325**, 601.
- Uberseder, E., and R. J. deBoer, 2015, *AZURE2 User Manual*.

- Ugalde, C., B. DiGiiovine, D. Henderson, R. Holt, K. Rehm, A. Sonnenschein, A. Robinson, R. Raut, G. Rusev, and A. Tonchev, 2013, *Phys. Lett. B* **719**, 74.
- Umeda, H., K. Nomoto, and T. Nakamura, 2000, in *The First Stars*, edited by A. Weiss, T. G. Abel, and V. Hill (Springer, Berlin), p. 150.
- Van Dyk, S. D., C. Y. Peng, J. Y. King, A. V. Filippenko, R. R. Treffers, W. Li, and M. W. Richmond, 2000, *Publ. Astron. Soc. Pac.* **112**, 1532.
- Van Winckel, H., and M. Reyniers, 2000, *Astron. Astrophys.* **354**, 135 [<http://adsabs.harvard.edu/abs/2000A%26A...354..135V>].
- Viallet, M., C. Meakin, D. Arnett, and M. Mocák, 2013, *Astrophys. J.* **769**, 1.
- Volya, A., and Y. M. Tchuvil'sky, 2015, *Phys. Rev. C* **91**, 044319.
- Vreeswijk, P. M., *et al.*, 2014, *Astrophys. J.* **797**, 24.
- Watson, K. M., 1954, *Phys. Rev.* **95**, 228.
- Weaver, T. A., and S. Woosley, 1993, *Phys. Rep.* **227**, 65.
- Weiss, A., S. Cassisi, H. Schlattl, and M. Salaris, 2000, *Astrophys. J.* **533**, 413.
- Weisser, D. C., J. F. Morgan, and D. R. Thompson, 1974, *Nucl. Phys. A* **235**, 460.
- Weller, H. R., M. W. Ahmed, H. Gao, W. Tornow, Y. K. Wu, M. Gai, and R. Miskimen, 2009, *Prog. Part. Nucl. Phys.* **62**, 257.
- Werner, K., and F. Herwig, 2006, *Publ. Astron. Soc. Pac.* **118**, 183.
- Wertz, C., 1971, *Phys. Rev. C* **4**, 1591.
- West, C., A. Heger, and S. M. Austin, 2013, *Astrophys. J.* **769**, 2.
- Wheeler, J. A., 1937a, *Phys. Rev.* **52**, 1083.
- Wheeler, J. A., 1937b, *Phys. Rev.* **52**, 1107.
- Wheeler, J. C., D. Kagan, and E. Chatzopoulos, 2015, *Astrophys. J.* **799**, 85.
- Wiescher, M., F. Käppeler, and K. Langanke, 2012, *Annu. Rev. Astron. Astrophys.* **50**, 165.
- Wigner, E. P., and L. Eisenbud, 1947, *Phys. Rev.* **72**, 29.
- Wilkinson, D. H., D. E. Alburger, and J. Lowe, 1968, *Phys. Rev.* **173**, 995.
- Wimmersperg, U. V., G. Kernel, B. Allardyce, W. Mason, and N. Tanner, 1970, *Phys. Lett. B* **33**, 291.
- Woosley, S. E., A. Heger, and T. A. Weaver, 2002, *Rev. Mod. Phys.* **74**, 1015.
- Xu, Y., K. Takahashi, S. Goriely, M. Arnould, M. Ohta, and H. Utsunomiya, 2013, *Nucl. Phys. A* **918**, 61.
- Yamaguchi, H., K. Sagara, K. Fujita, D. Kodama, Y. Narikiyo, K. Hamamoto, T. Ban, N. Tao, and T. Teranishi, 2014, *AIP Conf. Proc.* **1594**, 229.
- Yoon, J., T. C. Beers, V. M. Placco, K. C. Rasmussen, D. Carollo, S. He, T. T. Hansen, I. U. Roederer, and J. Zeanah, 2016, *Astrophys. J.* **833**, 20.
- Yuan, F., *et al.*, 2015, *Mon. Not. R. Astron. Soc.* **452**, 3047.
- Zamora, O., C. Abia, B. Plez, I. Domínguez, and S. Cristallo 2009, *Astron. Astrophys.* **508**, 909.
- Zavagno, A., *et al.*, 2010, *Astron. Astrophys.* **518**, L101.
- Zhao, Z., R. H. France, K. S. Lai, S. L. Rugari, M. Gai, and E. L. Wilds, 1993, *Phys. Rev. Lett.* **70**, 2066.
- Zimmerman, W., *et al.*, 2013, *Phys. Rev. Lett.* **110**, 152502.
- Zyskind, J. L., and P. D. Parker, 1979, *Nucl. Phys. A* **320**, 404.
- See Supplemental Material at <http://link.aps.org/supplemental/10.1103/RevModPhys.89.035007> for the data of Kremer *et al.* (1988) and for an AZURE2 input file.